Katholieke Universiteit Leuven
Faculteit Wetenschappen

Stellar populations and dust formation in the inner Galaxy

Evelien Vanhollebeke

Leuven 2007

PROMOTORES	*dr. Joris Blommaert*	Katholieke Universiteit Leuven
	prof. Christoffel Waelkens	Katholieke Universiteit Leuven
COPROMOTOR	*dr. Martin Groenewegen*	Katholieke Universiteit Leuven
JURY	*prof. Jan Cami*	University of Western Ontario
	dr. Leo Girardi	Osservatorio Astronomico di Padova
	Em. prof. Harm Habing	Sterrewacht Leiden
	prof. André Vantomme	Katholieke Universiteit Leuven
	prof. Hans van Winckel	Katholieke Universiteit Leuven
	prof. Rens Waters	Universiteit Amsterdam
		Katholieke Universiteit Leuven

Cover illustration:
Artistic interpretation of the Institute for Astronomy's computer cluster named "pleiades". With this cluster all the models discussed in Chapter 7 were calculated, as well as many other "try-out" models that did not make this work. A creation of *Atelier Erik Broeders.*

ISBN 978-90-8649-132-2
D/2007/10.705/54

Voor mijn meter

Leer ons zó onze dage tellen,
dat wij een wijs hart bekomen.

Dankwoord

De vele fietsritjes die ik de afgelopen jaren maakte tussen ons huisje in de Brusselsestraat en het instituut waren nooit vervelend. Deze 15 minuten 's morgens behoorden steevast tot mijn creatiefste momenten van de dag. Het was dan ook tijdens een van deze ochtendlijke ritten, dat ik besefte dat het voorbereiden van een doctoraat eigenlijk wel wat lijkt op het voorbereiden van een feestmaal.

Alhoewel je een feestmaal "zelfstandig" kunt klaarmaken, maak je het toch nooit alleen. Het begint al bij de keuze van het type gerecht. Je laat je leiden door je eigen smaak, maar ook het enthousiasme van anderen kan je al op voorhand doen watertanden. Christoffel, hierin speelde je een uitermate belangrijke rol. Het enthousiasme waarmee je de lessen inleiding tot de sterrenkunde op de KULAK doceerde, werkte ongelooflijk aanstekelijk.
Voor beginnende "koks" is een kookboek onontbeerlijk. Joris en Martin, zonder jullie was dit werk er niet geweest. Jullie hebben me de afgelopen vier jaar dag na dag begeleid. Van jullie kennis en ervaring mocht ik leren en samen hebben we nieuwe kennis vergaard. Daarnaast kon ik ook altijd rekenen op de hulp van vele anderen. Arianne, Bernhard, Ciska, Els, Leo, Mathias, Ian, Jan, Peter, Rens, and Xander, you all contributed in one way or another to the contents of this work. Thank you all!
Een goed gerecht maak je ook niet zonder de nodige specerijen. Jan & Els, de tijd die ik bij jullie in Californië doorbracht was geweldig! Ik vond het ontzettend fijn dat ik bij jullie mocht logeren. Also my trip to South-Africa was one of the most memorable things during the last four years. Ian, I would like to thank you for your hospitality and although the telescope was broke and the weather was bad, I enjoyed the few hours we actually observed the GC!
Dan zijn er ook nog een heleboel mensen die hielpen om alles "computertechnisch" in goede banen te leiden. Bart, Jan, Rik en Wim, alhoewel het indirect was, hebben jullie ook ontzettend veel geholpen aan dit werk. Erik, ook jou wil ik heel graag bedanken voor de vele "tips and tricks" die uiteindelijk tot hoofdstuk 7 geleid hebben, maar ook heel speciaal voor de mooie aquarellen waaruit ik mocht kiezen om mijn kaft te versieren. Dank je wel!

De laatste groep mensen die ik wil bedanken, hebben altijd voor extra energie gezorgd. Ik zou jullie kunnen vergelijken met de vele vlammetjes van een groot gas-fornuis.
Mijn collega's op het instituut wil ik graag bedanken voor de gezellige sfeer. Mijn "de Moete-maatjes", jullie zorgden voor de noodzakelijke ontspanning tijdens de lunchpauzes en hebben mijn niet aflatend gekwetter vier jaar aanhoord. Ook de collega's die mij soms op nieuwe ideeën brachtten of andere denkpistes aanhaalden tijdens een van de SE-groep meetings, dank je wel! Leen, vijf jaar geleden leerde ik mijn eerste stapjes in het onderzoek van je, dank je wel voor je enthousiasme, gastvrijheid, en je luisterende oor! Bram en Maarten, als bureaugenoten gedurende verschillende fases van dit project, hebben jullie altijd met me mee geleefd en geluisterd, dank je wel!
Karolien, nu we beiden promoveren en we in de toekomst enkel nog vriendinnen zullen zijn en geen collega-vriendinnen meer, wil ik je heel graag bedanken. Alhoewel het voor ons beiden op het einde zeker niet gemakkelijk was, waren je vriendschap, steun, bemoedigingen en kleine attenties altijd oprecht en troffen iedere keer weer hun doel, dank je wel meid!
Bij mijn famillie, schoonfamillie en vrienden kon ik tot rust en weer op adem komen. Jullie leefden onvoorwaardelijk met me mee, alhoewel het waarschijnlijk niet altijd even duidelijk was waar ik het nu eigenlijk over had. Lief en leed kon ik met jullie delen. Zonder jullie extra steun en liefde had ik het niet gehaald.
Dieter, velen keken raar op toen ze ontdekten dat we in augustus, zo dicht bij mijn deadline, naar "de Vlaanders" verhuisden. Ze waren duidelijk niet op de hoogte van jouw ongelooflijke inzet om onze verhuis te doen slagen. Inpakken, verhuizen en uitpakken, een huzarenwerk, maar je deed het allemaal. Zo zijn er nog talloze voorbeelden van jouw enthousiasme en overgave waarmee je de dingen doet, iets waar ik alleen maar kan van leren. Jouw steun is onontbeerlijk voor me. Dank je wel dat ik je vrouw mag zijn!

En na de voorbereiding komt het eigenlijke feest zelf. Geniet ervan, smakelijk en bedankt!

Evelien
Leuven, 14 november 2007

CONTENTS

CHAPTER 1

Introduction

As time-scales inherent to stellar evolution are much longer than our human lifetime, we might not always realise it, but as it is very natural on earth that "mother nature" re-uses material, it is equally normal in the universe. Stars are born out of clouds, the remnants of earlier generations of stars. Depending on their initial mass they evolve according to different physical processes. Some stars produce during their lifetime large amounts of dust which they give back to their surroundings. Also gas is ejected into the interstellar medium by e.g. the stellar winds of massive stars. Due to the processes in the interior of the star, all this dust and gas which is now given back to the universe, is enriched. A new generation of stars will be born from the remnants of this generation. And as is also the case on earth, this cycle of life goes on and on...

In this thesis, we will present work done on the stellar populations in the inner galaxy. We will study OH/IR stars in the Galactic Centre (GC) which are believed to originate from different stellar populations (see Chapter 2). In Chapters 3 to 6 we will study a sample of the stellar population of AGB stars in the Galactic Bulge (GB) and study the dust formed around these stars, which will eventually be used to enrich the interstellar medium (ISM). And last but not least we will study the characteristics of the GB and its stellar population using a "galaxy model" (see Chapter 7).

In this chapter, we will give a general but brief introduction to the topics that cover this thesis. Unless mentioned otherwise, this introduction is based on the different chapters in Habing and Olofsson (2003).

1.1 Stellar populations

One of the keywords in the title of this thesis is *stellar populations*. A population of stars is a sample of stars that for some reason can be categorised into the same group of stars. The most often used definition of a stellar population is that of a population consisting of stars with a range of masses, all of which were formed at roughly the same time, so that they have a common age and comparable chemical composition. An example of this kind of population is e.g. stars located in a stellar cluster (see e.g. right panel in Figure 1.1).
Using the distribution of stars we can define a second definition for a stellar population in which we consider the phase-space distribution. The phase-space distribution function of stars gives the amount of stars as a function of their location in the galaxy and their velocity. If we consider the entire phase-space distribution as the composition of smaller groups of stars, than also these groups of stars can be called a stellar population. Examples of this are e.g. stars in the disk or stars in the halo.

AGB stars in particular are often used to study stellar populations as these objects can be used as tracers of the broader underlying population. The AGB stars are luminous and are therefore easily detected throughout our Galaxy, as well as in galaxies within about 10 Mpc. If a galaxy is too far away to distinguish individual stars, the presence of AGB stars may still show up in the integrated spectrum of the galaxy. Therefore, AGB stars make good probes to study galactic structure and dynamics, as well as star formation histories.

1.2 AGB stars

An important part of this thesis is dedicated to AGB stars, therefore we will give a general introduction to AGB stars, their structure and evolution, variability, and dust formation process in this section.

1.2.1 Low-mass stars: from the Main Sequence to the Asymptotic Giant Branch

The evolutionary path a single star follows, depends on its initial mass. Figure 1.1 shows two Hertzsprung-Russell diagrams (HR diagram). Depending on a star's temperature and luminosity it gets a place in the HR diagram. The left panel of Figure 1.1 shows also some evolutionary tracks, which depend on the initial mass of the star.

The majority of stars studied in this thesis are so called *low-mass stars*, meaning that these objects have an initial mass somewhere between 0.8 and 2.3 $M_{\odot}$. Therefore we will only briefly introduce the pre-AGB evolution for these stars.

Low-mass stars have similar masses as our Sun and start their life in the *Solar-like region* shown in the left panel of Figure 1.1. This phase of their life is called the *Main Sequence* (MS) and during this period hydrogen is burned into helium in the stellar core. The left panel

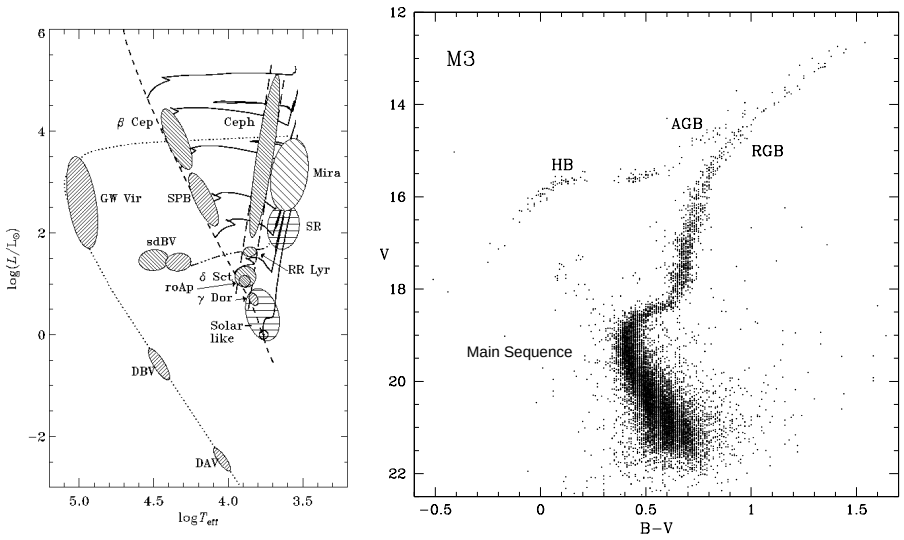

Figure 1.1: The left panel shows a theoretical Hertzsprung-Russell diagram. The *x*-axis indicates the temperature, the *y*-axis the luminosity. This figure also shows types of variable stars, among which are AGB stars (semi-regulars (SR) and Mira's). The figure on the right is an observed colour-magnitude diagram for the globular cluster M3. On the *x*-axis the $B - V$ colour is given and on the *y*-axis the *V*-band magnitude (taken from Habing and Olofsson 2003).

in Figure 1.1 shows in detail the evolutionary track these stars follow.
When the hydrogen in the core is exhausted, the star leaves the MS. Since the hydrogen burning in the stellar core stopped, there exists no energy source to counter the gravity in the stellar core and the star begins to contract. Due to this contraction the temperature rises and at a certain moment the temperature is high enough to start hydrogen burning in a thin shell around the helium core. The star is now located on the *Red Giant Branch* (RGB).
The hydrogen burning shell increases the temperature of the core until the temperature is high enough to start helium burning. Since the core of an RGB star is degenerate, the helium burning does not trigger an expansion of the star, but instead causes a helium-flash. This helium-flash lifts the degeneracy of the core and so the RGB phase ends and the star moves to the *Horizontal Branch* (HB).
When all helium in the core is burned to carbon and/or oxygen, the core contracts and heats up. Due to the rise in temperature, hydrogen shell burning occurs and the star moves up to the right in the HR diagram and starts the *Asymptotic Giant Branch* (AGB) phase.

Also the so-called *intermediate-mass* stars (with initial masses lower than $8 - 9$ $M_\odot$) eventually become AGB stars, nevertheless in a slightly different way. These objects have a helium core which is hot enough to prevent the electron gas to become degenerate as occurs for the low-mass stars. The intermediate-mass stars start helium-burning in a non-explosive way, similar to that on the HB.

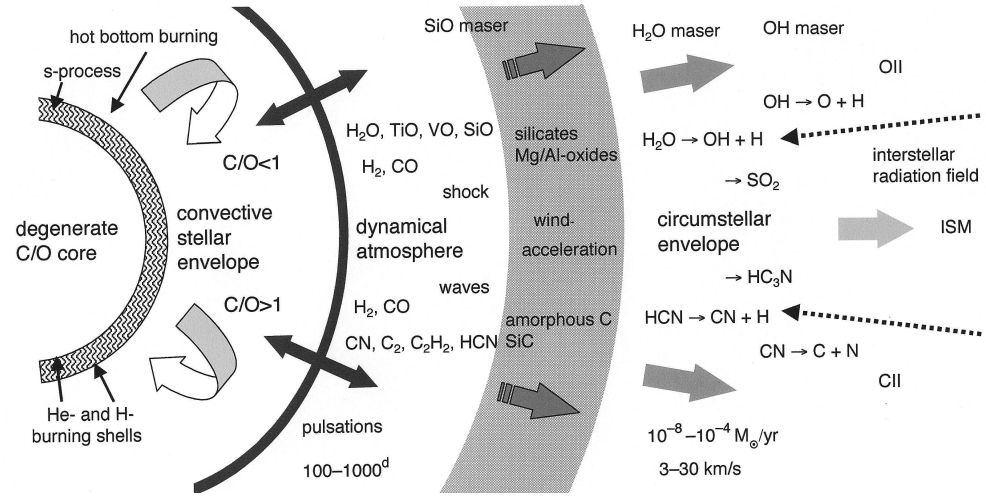

Figure 1.2: Schematic and not at scale overview of an AGB star. The division into the four major parts (the degenerate C/O core, the stellar envelope, the atmosphere, and the circumstellar envelope) and some important physical/chemical processes are indicated (adapted by J. Hron from an original idea by Th. Le Bertre).

1.2.2 Internal structure

Notwithstanding that the lifetime of a star on the AGB is very short compared to its MS lifetime, the AGB phase is a very complex and eventful phase. In general, an AGB star can be divided into four main parts: *(a)* a small, very hot, and dense core, *(b)* a large, hot, and less dense stellar envelope, *(c)* a tenuous, warm atmosphere, and *(d)* a very large, very diluted, and cool circumstellar envelope (see also Figure 1.2).

1.2.2.1 The core and stellar envelope

At the beginning of the AGB phase, the *early-AGB* (E-AGB), the material around the CO core consists of hydrogen. The temperature around the core is high enough to ignite H into He, which results in a hydrogen-burning shell. This H-burning shell produces most of the energy in the star.

The star continues to increase its luminosity and when it reaches a luminosity of about 3000 times the solar luminosity the temperature is high enough to ignite the He formed by the H-burning shell around the core. The AGB star is now able to burn both helium and hydrogen in shells. At the beginning of the *double-shell burning phase*, the He-burning shell dominates. Because the H-burning shell continues to burn H into He, the mass of the thin He layer increases, separating the core from the mantle. This causes the He-burning shell to become unstable and the He burning occurs now in a degenerate environment, causing the He-layer to burn He into C very rapidly. This is called a He-shell flash or thermal pulse, therefore this part of evolution is called the *thermally pulsing AGB phase* (TP-AGB).

Figure 1.3 shows the interior of an AGB star during the TP-AGB phase. The upper panel shows one thermal pulse in detail, the middle panel two consecutive thermal pulses, and the lower panel shows the luminosity in function of time. The *y*-axis of the two upper panels shows the mass fraction. A thermal pulse can be divided in 5 phases indicated at the top of this figure. During the "off" phase at the beginning and the end of a thermal pulse, the energy of the star is mainly created by the H-burning shell. During the "on" phase, the He-shell burns very strongly. The energy deposited by the He-burning reactions cannot be transported by radiation alone and a convective shell develops immediately above the He-burning region, the inter shell convective zone. During the "power down" phase, the He shell burning decreases and the inter shell convective zone disappears. Because of the loads of energy released by the previous inter shell convective zone, the H-shell burning zone is pushed upwards in mass fraction to lower temperatures and densities so that it is (almost) extinguished. During the next phase of the thermal pulse, the convective layers (shaded regions in Figure 1.3) reach the layers where nuclear processing takes places. These convective layers take the processed material to the stellar surface, which therefore becomes enriched. This is called a *dredge-up*.

Because of this dredge-up, especially the newly created carbon will become visible at the surface. In some stars this continues long enough so that the abundance of carbon exceeds that of oxygen and a *carbon-rich star* is born. This will not happen in all stars: stars that have sufficient mass experience *hot bottom burning* (HBB) which causes the carbon to burn into nitrogen before it can reach the surface of the star. Also in low-mass stars the conversion from oxygen-rich (O-rich) to carbon-rich (C-rich) will not occur: all the matter between the core and the stellar surface will be ejected and further evolution will be terminated before the conversion can take place. The initial mass is not the only factor playing a role here, also the metallicity is important. An AGB star with a lower metallicity has a smaller absolute difference between the amount of C and O-atoms and therefore this star needs a shorter time of dredge-up to become a carbon-rich star.

1.2.2.2 The atmosphere

The atmosphere is mostly defined as the stellar region visible from the outside. In general, the atmosphere can be considered as the region responsible for the electromagnetic emission one observes. Based on the effective temperature of a star ($T_{\rm eff}$, the temperature a black body would have if it emitted the same amount of energy per unit area as the star), it can be classified in terms of a spectral type. The oxygen-rich AGB stars studied in this work are classified as spectral type M. As these spectral classes are quite broad and contain many different objects, they are often sub-divided from categories 0 to 10, in our case from M0 to M10. The spectral classification of M-giants is generally based on absorption features (Fluks et al. 1994) such as e.g. TiO bands in the optical and near-Infrared (near-IR) spectrum. The TiO bands are sensitive to the effective temperature of the star and become stronger when the effective temperature decreases or equivalent when an M-giant evolves from M0 to M10.

Since the effective temperatures of these objects are low (around 3000 K), molecules are formed and have a larger impact on the near-IR spectra than atoms. The relative importance of different molecules determines the spectral signature of cool stars such as e.g. M giants

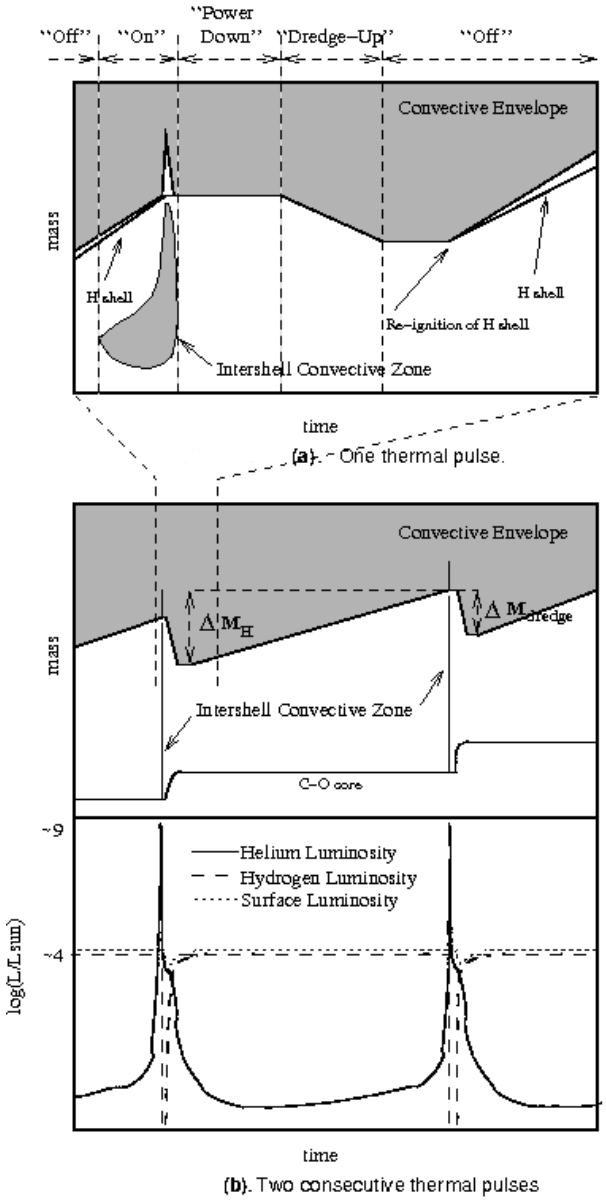

Figure 1.3: The upper panel shows some details of interior evolution during one thermal pulse, while the two lower panels show two consecutive pulses. Shaded regions are convective regions. The He-burning shell is indicated by the full line at the bottom of the middle panel. The position of H-burning shell is indistinguishable from the position of the base of the convective envelope in this panel (taken from Lattanzio and Wood 2003).

studied in this work. Decin (2000) shows based on model spectra how the relative strengths of molecular bands in the near-IR spectrum change as function of the stellar parameters such as the effective temperature. Therefore molecules such as TiO bands or CO bands can be good indicators of the effective temperature.

The atmospheres of AGB stars are unstable against convection in the deeper layers, pulsations, and the thermal pulses. These events have a large influence on the stellar atmosphere, the latter two can create (strong) shocks. Because of these shocks, grain condensation can take place in the post-shock gas at higher latitudes. Another effect of the shocks is mass-loss. In the beginning of the AGB phase, this will be at a very low rate (10^{-9} $M_{\odot}$/yr), but at the end of the AGB this can be as high as 10^{-4} $M_{\odot}$/yr.

1.2.2.3 The circumstellar envelope

Because of the mass-loss a circumstellar envelope (CSE) of escaping gas and dust particles will be formed. Depending on the temperature molecules are located in envelopes with different sizes in the CSE. The two biggest envelopes are formed by H_2 and CO. The dust grains are located much further away from the central star than the molecules. The highest temperature at which dust grains exists is about 1800 K (see also Section 1.2.4). The kind of molecules and dust grains formed is highly dependent on the C/O ratio. Oxygen-rich stars show molecules and dust grains with more oxygen than carbon, while carbon-rich stars have mainly carbon in their molecules and dust grains.

1.2.2.4 End of the AGB

At the end of the AGB phase the radius of the star becomes smaller, as the rate of ejection of matter is higher than the growth rate of the core. From now on, the mass-loss process determines the evolution. This causes the star to move in the HR diagram towards the blue. When all the matter around the core is dispersed into space, the object leaves the AGB phase and enters the *post-AGB* phase. Due to the high mass-loss at the end of the AGB phase, the inner parts of the star become more exposed. Since the inner regions of the star are hotter, it is possible that the previously lost mass becomes ionised. If this occurs, the material becomes visible as a Planetary Nebula (PN).

1.2.3 Variability

As could already be seen from the previous section, variability is a very common feature of AGB stars. Therefore, AGB stars are also often classified based on their variability type. There exists four broad groups: the irregular variables, the semi-regular variables, the Mira variables, and the dust-enshrouded infrared variables.

The irregular variables are the less evolved AGB stars and have little periodicity. The semi-regular variables are the next stage of evolution, have some definite periodicity, and

a pulsation amplitude less then 2.5 mag in the *V* band. The Mira variables have a larger pulsation amplitude (> 2.5 mag in the *V*-band) and show relatively regular variations. The dust-enshrouded infrared variables have the longest periods (> 600 d) and the highest pulsation amplitudes (in the *K*-band up to 3 mag) of the four groups. The oxygen-rich stars in this group are known as the OH/IR stars. These stars are the most evolved AGB stars and are believed to be progenitors of Planetary Nebulae (see e.g. Cohen et al. 2005; Habing 1996) (see also Section 1.2.6).

Period-Luminosity relation

Figure 1.4 shows the Period-Luminosity (PL) relation for optically visible semi-regular and Mira variables in the Large Magellanic Cloud (LMC) (Wood 2000). The figure shows four parallel PL sequences (A – D) and another sequence E.

Sequence E consists mostly of stars still on the RGB since this sequence lies below the TP-AGB minimum luminosity (see arrows in Figure 1.4). The stars in this sequence have quite regular light curves, which is an indication of some sort of binary or rotational origin.
As is indicated in Figure 1.4, the Mira variables are located at the top of sequence C and pulsate in one period. The period-luminosity relation found for large-amplitude AGB variables in the LMC coincides with sequence C. This PL-relation can be accurately reproduced by fundamental mode pulsation. Therefore objects on this sequence are believed to pulsate in the fundamental radial mode.
Sequences A, B, and the lower part of sequence C are occupied by the semi-regular variables. The pulsations of semi-regular variables located on sequences A and B can pulsate in a number of modes, often simultaneously. These objects become first, second, or third overtone pulsators.
The stars located on sequence D are invariably multi-periodic: they have one period that lies on sequence D and another that lies on sequence A, B, or sometimes C. The origin of this sequence is currently still unknown.

1.2.4 Dust formation and mass-loss mechanism

AGB stars are known to lose a significant fraction of their mass through a slow, massive wind. The oxygen-rich dust condensation sequence describes in general the order in which the dust grains could be formed in the winds of oxygen-rich AGB stars. To predict the condensation sequence one relies on the thermodynamic condensation sequences. In this section, we describe the condensation sequence starting from alumina and from silica (based on Tielens et al. 1997; Cami 2002).

For oxygen-rich stars a fairly abundant element is aluminium. Thermodynamic studies predict that dust formation for the Al condensation sequence starts with the formation of crystalline Al_2O_3 (corundum or crystalline alumina) at about 1760 K. Figure 1.5 illustrates this sequence. When corundum cools down, it reacts with gaseous SiO, Ca, and Mg to form melilite, first in the form of pure gehlenite ($Ca_2Al_2SiO_7$), later to transform gehlenite par-

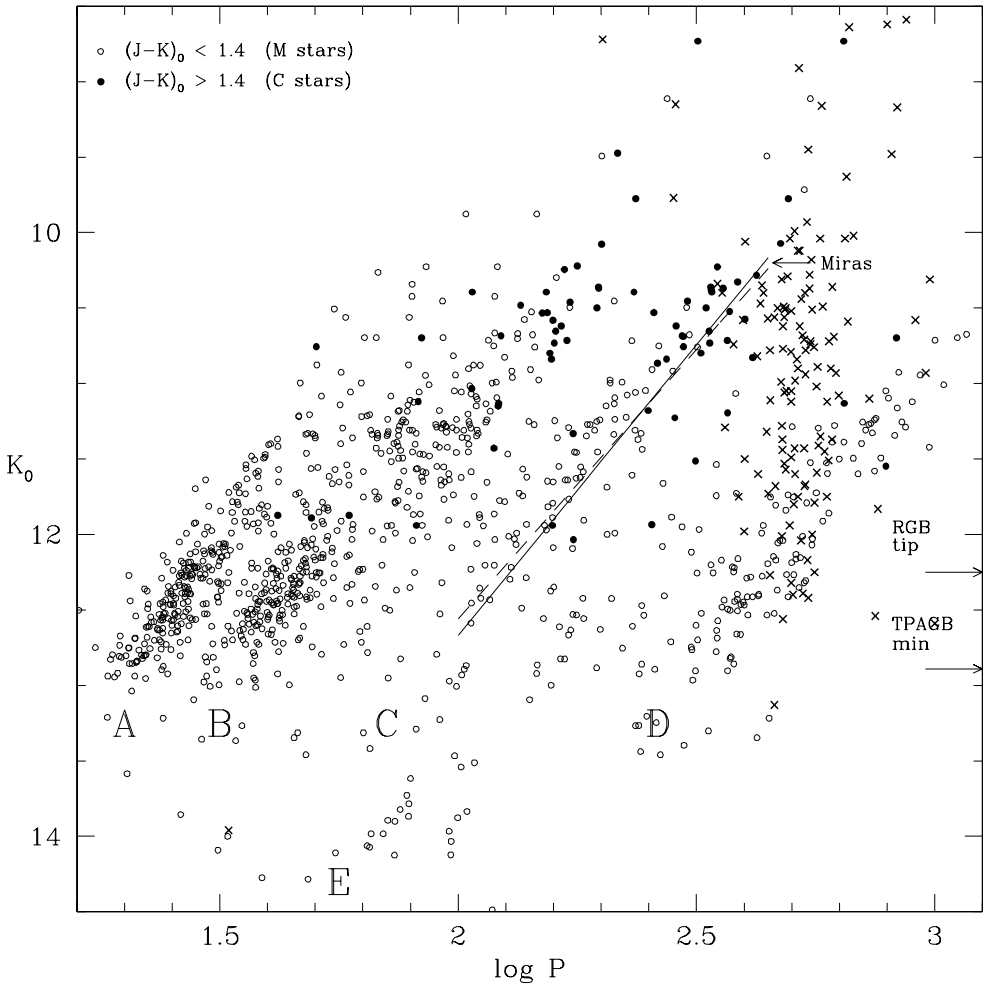

Figure 1.4: The log P vs K_0 diagram shows the period-luminosity relations for optically visible red variables in a 0.5×0.5 degree area of the LMC. The crosses are MSX-selected infrared sources from a 3×3.5 degree arc of the LMC (taken from Lattanzio and Wood 2003).

tially into akermanite ($Ca_2MgSi_2O_7$) around 1550 K, corundum (above 1510 K), and spinel ($MgAl_2O_4$) below 1510 K. At about 1450 K, melilite reacts to form diopside ($CaMgSi_2O_6$) and spinel. The latter two are then through solid-solid interactions transformed into anorthite ($CaAl_2Si_2O_8$).

Only a small fraction of the Mg and the Si is involved in this part of the condensation sequence. The main silicon bearing minerals are formed through a separate condensation sequence. Most of the silicon nucleates and condenses first at about 1440 K as forsterite (Mg_2SiO_4), which is the Mg-rich end member of the olivine family ($a_{2x}b_{2-2x}SiO_4$ with a and

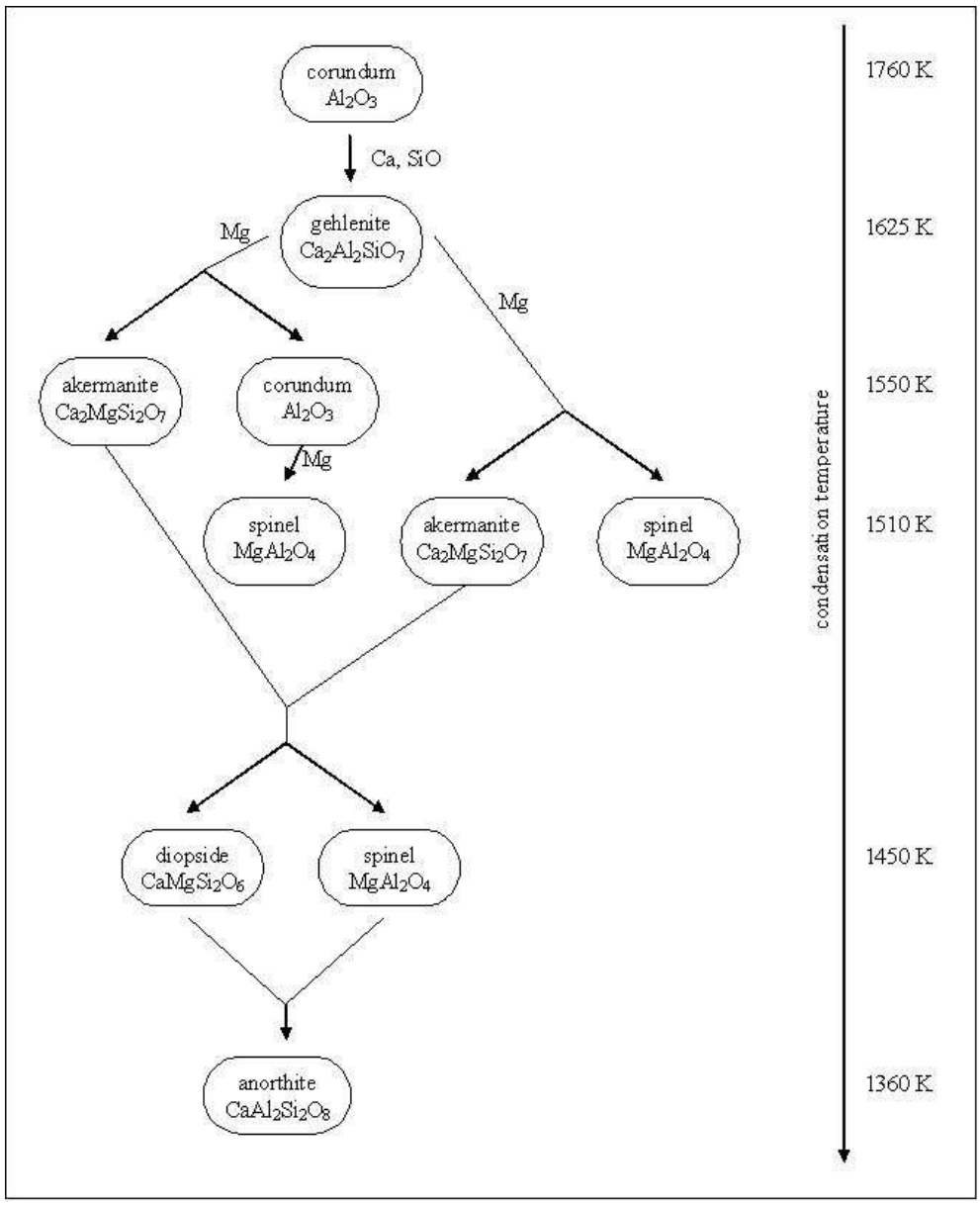

Figure 1.5: The Al condensation sequence. Based on Cami (2002).

b Mg, Fe, Mn, Co, or Zn). The excess SiO will eventually convert forsterite at about 1350 K into enstatite ($MgSiO_3$), the Mg-rich end member of the pyroxenes, which are SiO_6 chains.

What happens with Fe is not very clear in the described scenarios. Metallic iron is likely

to be formed but iron could also transform enstatite into forsterite and fayalite (Fe_2SiO_4) at 1100 K. Magnesiowüstite (MgFeO), often observed in AGB stars in the form of $Mg_{0.1}Fe_{0.9}O$, is not an expected condensate in these sequences. It is therefore not clear how this molecule fits in these oxygen-rich dust condensation sequences.

Several observations, mostly IRAS/LRS and ISO/SWS have revealed the presence of many different dust compounds in O-rich AGB stars (see e.g. Vardya et al. 1986; Onaka et al. 1989; Sloan and Price 1995; Waters et al. 1996; Speck et al. 2000; Fabian et al. 2001; Cami 2002; Posch et al. 2002; Blommaert et al. 2006). Many, but not all, of these compounds are part of the theoretical condensation sequence: AGB stars with high mass-loss rates show copious amounts of silicates, including crystalline olivines and pyroxenes, while the spectra of AGB stars with low mass-loss rates, on the other hand, show evidence for aluminium-oxide and magnesium-iron oxides. This difference in spectral structure of AGB stars is thought to reflect the rapid "freeze-out" of the dust condensation sequence, a term used to indicate that the densities in the dust formation zone are too low for certain condensation reactions to occur, and therefore the dust condensation sequence stops at the intermediate step. Thus, studying a sample of similar stars but with different mass-loss rates is a powerful way to probe the dust condensation sequence observationally, as the freeze-out will occur at different densities and therefore stop the condensation sequence at different intermediate steps. Chapters 3 to 6 will be dedicated to a sample of AGB stars in the Galactic Bulge, chosen to study the oxygen-rich dust condensation sequence.

Basically one could describe the mass-loss process as a pulsation-enhanced dust-driven wind: shock waves created by stellar pulsation lead to a dense, cool, extended stellar atmosphere, allowing for efficient dust formation. The composition in the dust grains is then determined by the elemental abundances in the stellar atmosphere, with C-rich stars forming carbon grains, and O-rich environments producing silicate particles (Höfner and Andersen 2007). The dust formed in the outflow is not only dependent on the elemental abundances in the stellar atmosphere, but also the temperature and the mass-loss rate, which depend on the evolution along the AGB, play a key-role in the entire dust formation process.

This model works very well for C-rich stars and it was assumed that it would also work for O-rich stars. Only recently, it became clear that this driving mechanism for the wind is not understood at all in the case of O-rich stars. Woitke (2006) shows that Fe is needed to have a dust-driven wind. Silicates such as Mg_2SiO_4 without Fe-contribution are unable to do this because they are almost completely transparent around 1 μm where most of the stellar flux radiates. So the role of solid iron and Fe-rich silicates is crucial for the wind driving mechanism. The drawback of this is that the Fe containing condensates are not stable with respect to the temperatures close by the star and therefore form at too large distances from the star to provide an efficient mass-loss mechanism. Gail and Sedlmayr (1999) showed that also separate grains of metallic iron are formed in the winds of AGB stars. The contribution of metallic Fe to the wind driving mechanism is not completely understood yet, but as it can form at high temperatures, it may help driving the wind even at low mass-loss rates.

Höfner and Andersen (2007) came with another solution for the driving mechanism: they propose that winds of O-rich AGB stars are driven by small amounts of carbon grains. This

could only happen if not all the carbon is locked into CO as is generally expected for O-rich AGB stars. The direct detection of carbon grains in the spectra of O-rich AGB stars is unlikely to happen: the optical properties of amorphous carbon lead to featureless infrared (IR) spectra, whereas SiC, which has a pronounced feature around 11 μm, would not be produced enough to appear above amorphous carbon and the nearby silicate feature. Considering the relative opacities of SiC and silicates, this would require at least as much Si being bound in SiC as in silicates, which seems unlikely in an environment with C/O < 1.

1.2.5 Evolution along the AGB

In Section 1.2.2 we mentioned the evolution and change in stellar parameters occurring during the time a low- or intermediate-mass star spends on the AGB. Figure 1.6 shows this evolution for certain properties of an AGB star. From top to bottom the panel shows the effective temperature $T_{\rm eff}$, the luminosity normalised to the solar luminosity $L/L_{\odot}$, the period P in days, the mass-loss rate in units of $10^{-6}M_{\odot}$/yr ($\dot{M}_6$), and the total stellar mass M. The evolution in the beginning of the AGB phase continues without any abrupt changes. The effective temperature decreases, the luminosity and the period increase, the mass-loss rate is low and cannot be seen yet in the figure, and the stellar mass does not change. At about $6 \sim 7 \times 10^5$ year, the thermal pulses start. The He-shell flashes first cause an increase in luminosity followed by a luminosity dip. The luminosity then increases again until the next thermal pulse. The effective temperature reacts to the thermal pulses in the opposite way. At about the 5th thermal pulse, also abrupt changes in the mass-loss rate can be noticed from the figure. When the superwind phase starts and the star loses a significant fraction of its stellar mass, the period grows more rapidly than before. Very long periods exhibited by the dust-enshrouded AGB stars are a result of this.

To summarise: as AGB stars evolve, their luminosity, period, and mass-loss rate will increase, while their effective temperature decreases. At the end of the AGB phase, the star loses also a significant fraction of the mass in its stellar envelope.

1.2.6 OH/IR stars

OH/IR stars are oxygen-rich AGB stars at the end of the AGB evolution and go through the superwind phase. During this phase, they lose a significant fraction of the mass in their stellar envelopes. Because of this high mass-loss and the consequent dust formation in the outflow, the circumstellar material becomes optically thick. Due to this optically thick dust layer, the central star is no longer visible and the object can only be detected at longer wavelengths. Surveys searching for OH/IR stars therefore never search in the optical wavelengths, but they look in the infrared as well as at radio wavelengths.

OH/IR stars are not only AGB stars, they are also a subclass of the maser stars. Because of the OH maser at 1612 MHz, they can be clearly detected at radio wavelengths. The masering effect is a form of stimulated emission (see also Figure 1.7): photon-absorption by a molecule, results in an excitation of the molecule from the lower level l, to the upper

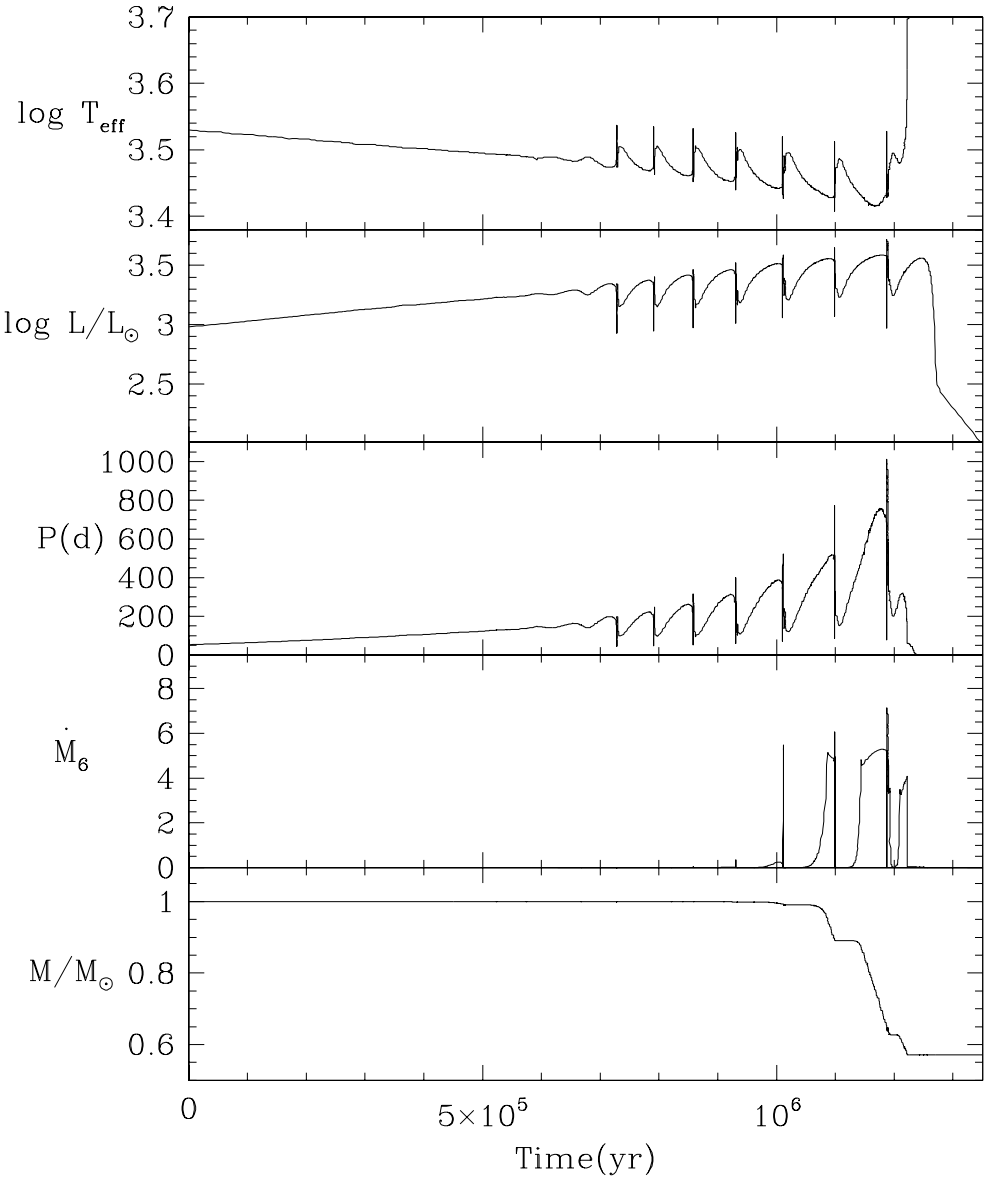

Figure 1.6: Various properties for a 1 $M_\odot$ AGB star with chemical composition $(Y, Z) = (0.25, 0.016)$ in function of time (Y is the He-fraction, Z is the fraction of all other elements except H and He). From top to bottom the panels show the effective temperature T_{eff}, the luminosity L, the period P, the mass-loss rate in units of 10^{-6} $M_\odot$/yr, and the total stellar mass M (taken from Lattanzio and Wood 2003; Vassiliadis and Wood 1993).

level u. When a similar photon meets an already excited molecule in level u, the passing of

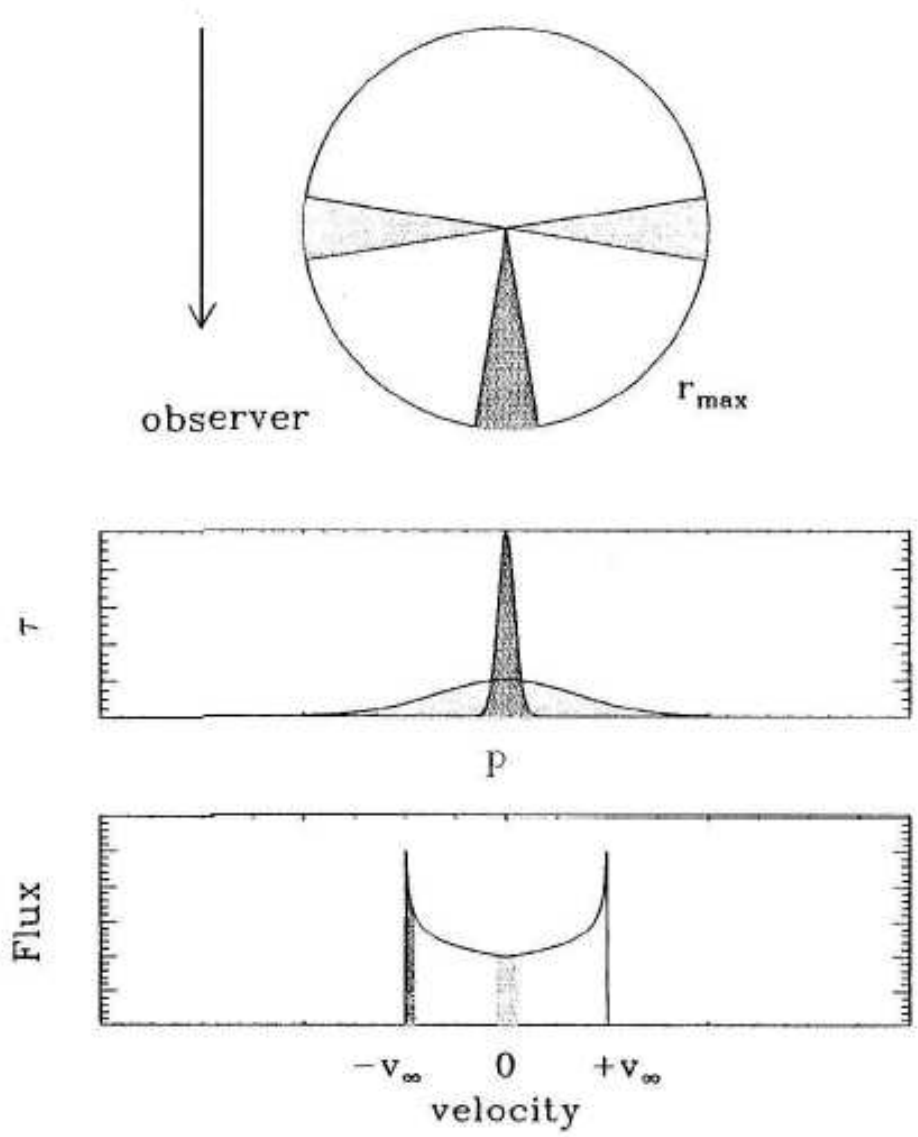

Figure 1.7: Velocity profile of an OH/IR star (taken from Lamers and Cassinelli 1999).

this photon triggers a de-excitation of the molecule from level *u* to level *l*, which is called stimulated emission of a photon with the same energy and direction as the one passing by. In a normal situation, there is a higher probability that photons are absorbed than created by stimulated emission. But in case of a population inversion, there is a higher probability for stimulated emission than absorption. Population inversion occurs when there are more

molecules in a higher rotational state than in a lower. When photons pass through a gas with population inversion, this results in an increase in intensity, rather than in a decrease caused by absorption.

The maximum masering occurs along a line of sight that has the highest number of molecules moving with the same velocity component to the observer. This is the case when the line of sight goes through the central star. The gas in front of the star moves with a constant Doppler velocity $-v$ to the observer. The gas almost behind the star moves with a constant Doppler velocity $+v$ away from the observer. This causes the characteristic double peaked profiles. The difference, ΔV between the velocities of the two peaks is an indicator of the initial mass of the star and $\Delta V/2$ is a good estimator of the gas expansion velocity ($v_{\rm exp}$) of the CSE (Lamers and Cassinelli 1999).

1.3 The Milky Way Galaxy

Figure 1.8[1] shows the Milky Way Galaxy (MWG) in the near-IR as observed in the 2MASS survey (see Chapter 7 for more information on this project). The MWG is a spiral galaxy and can in general be divided in four components: the disk, the bulge, the halo, and the centre. Often, the disk is again divided into two parts: the thin and thick disk.

Since we are part of our own MWG and we cannot (yet?) send satellites outside our MWG to observe it as a whole, it is very difficult to study the structure of our MWG. Nevertheless it is a very interesting galaxy to study as we are part of it and therefore have 3 dimensional information on it, which is very hard to obtain for other galaxies.

In this thesis, we will study stars located in the Galactic Bulge (GB) and close to the Galactic Centre (GC). Since the inner parts of our Milky Way are very crowded, they are an extremely interesting place to study, and provide us with a wealth of possible targets all more or less at the same (known) distance. On the other hand the crowdedness can make things difficult: when observing a specific target, it is not always easy to identify the object due to the crowdedness. Another difficulty is the heavy extinction in the inner regions. Luckily there are a few regions with less heavy extinction. These 3 windows were selected by Baade and are called *Sgr I*-window, *Sgr II*-window, and *NGC 6522*-window. The latter is the most famous one and is often refered to as *Baade's window*. Because of the lower extinction in these regions, they are often used to select targets and part of the objects that will be studied in Chapter 3 are also located in these regions. Because of the heavy extinction, it is easier to study the objects in these regions in the IR than at optical wavelengths, as extinction in the IR is significantly lower than in the optical.

In the centre of our galaxy a black hole, with a mass of 3×10^6 $M_\odot$, resides. The black hole coincides with the radio source SgrA*. Not only is SgrA* the position of the black hole,

[1] Atlas Image obtained as part of the Two Micron All Sky Survey (2MASS), a joint project of the University of Massachusetts and the Infrared Processing and Analysis Center/California Institute of Technology, funded by the National Aeronautics and Space Administration and the National Science Foundation.

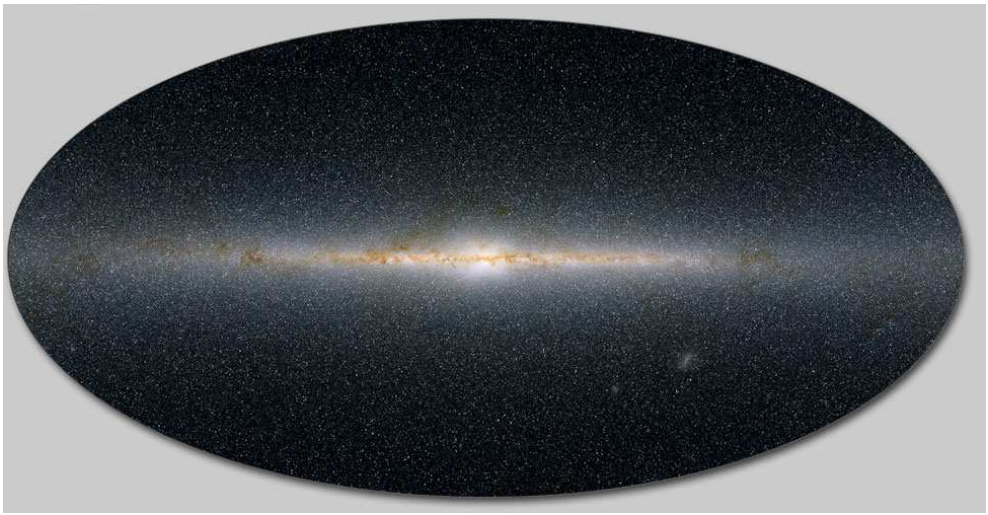

Figure 1.8: This panoramic view encompasses the entire sky as seen by Two Micron All-Sky Survey. The measured brightnesses of half a billion stars have been combined into colours representing three distinct wavelengths of infrared light: blue at 1.2 microns, green at 1.6 microns microns, and red at 2.2 microns.

it is also the dynamical centre of our galaxy. One of the studies confirming this is based on radial velocity measurements of M-giants (McGinn et al. 1989). Another study based on radial velocities of 18 OH/IR stars within 5 pc projected distance from SgrA* gives the same result (Habing and Olofsson 2003, based on Lindqvist et al. 1992a).

The inner region of the Galaxy has been extensively searched for OH/IR stars in the past two decades and it is believed that there are two different populations OH/IR stars in the GC. The first population is expected to be older. This population consists of OH/IR stars which have low expansion velocities, a larger spread in latitude, and a larger velocity dispersion than the second group, which is believed to be younger. Figure 1.9 also shows the position in longitudes of OH/IR stars in the inner regions of our MWG versus their radial velocity. In Chapter 2 we will study near-IR spectra of a sample of OH/IR stars in the Galactic Centre.

Figure 1.9 gives a nice indication on the sub-structures in the inner parts of the MWG ($-30^\circ < \ell < +30^\circ$). In this region, the Galactic Bulge (GB) is located. One of the substructures located in the GB could be a bar. A discussion on the GB is therefore inextricably bound up with a discussion on the bar. Since the last decade of the previous century, the debate on the GB and its bar is very vivid. Proof for the existence of such a bar comes e.g. from the COBE (Cosmic Background Explorer) satellite. Figure 1.10 shows that the contours of the near-IR emission around the GC are skewed to positive longitudes. Also the distribution of AGB stars observed with IRAS (Infrared Astronomical Satellite) shows an asymmetry consistent with the presence of a bar (Weinberg 1992a,b). All evidence taken together, it is extremely likely that there exists such a thing as a bar, but the accurate determination of the basic properties

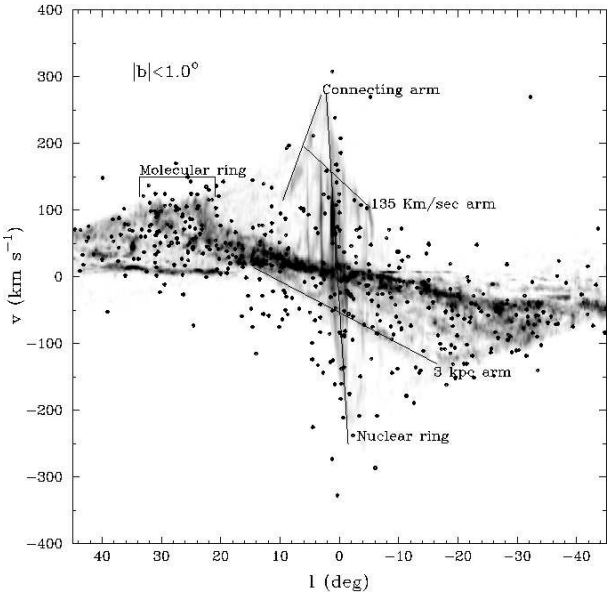

Figure 1.9: The dots are radial velocities of OH/IR stars as a function of galactic latitude. Underneath the dots is the distribution of velocities measured for the interstellar CO molecule. Straight lines indicate structures in the distribution of the CO gas (taken from Habing and Olofsson (2003), diagram courtesy of M. Messineo).

such as total mass, shape, angle between the major axis and the sun-centre line, age,... are not yet undoubtedly defined. Therefore it is still not clear whether one should draw a distinction between a triaxial central bulge and a bar component (Merrifield 2004). Sometimes the bulge is referred to as the bar (see e.g. Sevenster et al. 1999) and in other cases studies find a bar within the bulge (see e.g. López-Corredoira et al. 2007; Cabrera-Lavers et al. 2007). In this thesis we will adopt the formalism described by Sevenster (1999): we will use the term *Galactic Bulge* for the Galactic component seen in the general direction of $|\ell| \leq 10°$, we will use *bar* if we refer to the prolate or tri-axal component of the GB.

Bahcall and Soneira (1980) were the first to construct a model that aims at explaining the observed number counts in the galaxy. By studying the number counts of the galaxy, one obtains not only information on the kinds of stars, but also on the geometry and the structure in the galaxy. In such models, the galaxy is often divided in a few components such as the disk, halo, and bulge. Models simulating the number counts in the galaxy then simulate the density of stars within one of these components and afterwards bring things together. Another assumption often used in these models, is to assume an intrinsic luminosity function which is virtually independent of position. These luminosity functions can be obtained in two ways: or one assumes an empirical luminosity function derived from e.g. star counts in globular clusters or in the Solar Neighbourhood, or one assumes a theoretical luminosity function calculated from a set of evolutionary tracks together with suitable distributions of stellar masses, ages, and metallicities (Girardi et al. 2005). The first method was applied often in the past, but

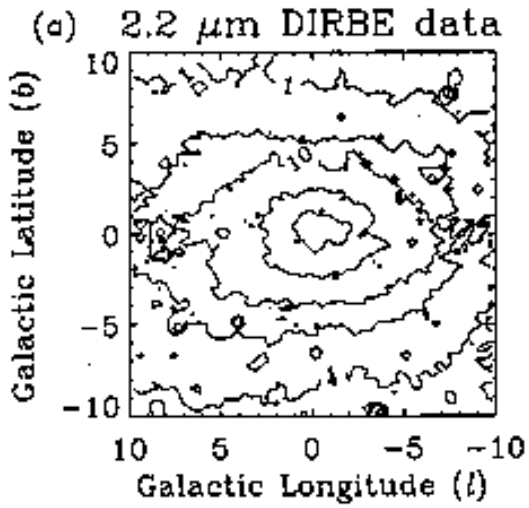

Figure 1.10: The contours of the distribution of near-IR emission at 2.2 μm around the Galactic Centre (taken from Dwek et al. 1995).

now most models use the second option. This option has significant advantages over the first method, such as that the luminosity function is more easily expressed as a function of other stellar parameters such as age and metallicity, while this is not possible in the first method.

In Chapter 7 we will study the characteristics of the GB in more detail. Using a galaxy model we will try to model observations of the GB and its bar. Not only will we discuss the parameters, also the star formation history and metallicity distribution will be discussed.

CHAPTER 2

Near-IR spectroscopy of OH/IR stars in the Galactic centre

This chapter is based on the paper:
Vanhollebeke, E., Blommaert, J.A.D.L., Schultheis, M., Aringer, B., and Lançon, A.: 2006, "Near-IR spectroscopy of OH/IR in the Galactic centre", *Astron. Astrophys.* **455**, 645-652

The inner region of our Galaxy has been extensively searched for OH/IR stars in the past two decades (see also Section 1.3). The studies of the GC region are severely hampered by extinction and also source confusion, especially in the visible wavelength range. Searches for OH/IR stars at radio wavelengths at the 1612 MHz OH maser line have therefore been very useful and also provided kinematic information on the detected stars. Lindqvist et al. (1992b) searched for OH/IR stars in six VLA primary beam fields and identified 134 OH/IR stars. Further searches, also using ATCA, were conducted by Sevenster et al. (1997), who found 145 new OH masering sources in the Bulge, and Sjouwerman et al. (1998), who discovered an additional 52 new OH/IR stars in the GC region. Figure 2.1(a) gives an overview of the OH/IR stars detected in the GC region.

Lindqvist et al. (1992a) studied the spatial and kinematic properties of their OH/IR sample and divided the stars into two groups based on their outflow velocities. The OH/IR stars with low expansion velocities ($v_{\rm exp} < 18.0$ km/s) have a larger spread in latitude and a larger velocity dispersion with respect to the Galactic rotation (see Figure 2.1(b)) than the group with higher expansion velocities (see Figure 2.1(c)). This was also found by Baud et al. (1981) for OH/IR stars in the Galactic disk. The low-expansion velocity stars are expected to be older objects with larger peculiar motions, whereas the other group may have a different formation history; it might be a later addition to the GC, possibly via a merger. The outflow velocity of the circumstellar shell is related to the luminosity of the star and to the properties

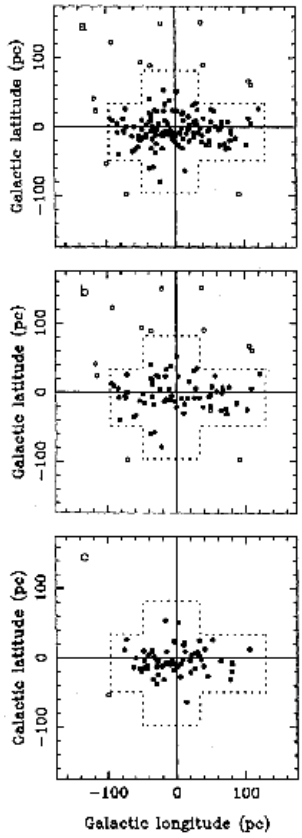

Figure 2.1: These figures shows the OH/IR stars detected by Lindqvist et al. (1992b) (filled circles), the dashed lines are the limits of this survey, and the open circles are stars detected by Habing et al. (1983). The top figure (a) shows all the OH/IR stars, the figure in the middle (b) shows only the stars with lower outflow velocities and the bottom figure (c) shows the OH/IR stars with the higher outflow velocities.

of the dust in the circumstellar shell (Habing et al. 1994; Elitzur et al. 2003).

Several groups have been searching for the infrared counterparts of the OH maser sources (Jones et al. 1994; Blommaert et al. 1998; Wood et al. 1998; Ortiz et al. 2002). It would be expected that the ‘older’ stars have lower luminosities than the high-expansion group. Blom-

maert et al. (1998) found that the high expansion velocity group contains higher luminosity stars but there is also a large overlap in the luminosity distributions of the 2 groups. Ortiz et al. (2002) also compared the measured luminosities using a larger number of stars and did not find any evidence of a distinction on the basis of luminosities between the 2 groups. The disadvantage of the latter study is that the luminosities were not corrected for variability and that the luminosities spread over a wider range. Nevertheless, it seems that the differences in luminosities between the 2 groups, if they exist, are not very big. If the luminosity is not sufficient for explaining the differences in expansion velocities then it is expected that differences in the gas-to-dust ratios and thus metallicities of the stars must exist. It was demonstrated by Wood et al. (1992) for OH/IR stars in the Large Magellanic Cloud and by Blommaert et al. (1993) for OH/IR stars in the outer Galaxy that the expansion velocities are low, even though the OH/IR stars have high luminosities. In both the LMC and in the outer Galaxy, it is expected that the stars indeed have low metallicities. The next logical step would be to investigate the metallicities of GC OH/IR stars.

In this chapter we discuss our attempt to apply the results of Schultheis et al. (2003) on medium-resolution near-IR spectra on a sample of GC OH/IR stars. We take a look at the influence of the water content on the atomic lines Na I and Ca I, discuss how periodicity can influence the water content and therefore also the near-IR spectrum, and we study a grid of dust models and show that hot dust also has an influence on the near-IR spectrum.

The sample, observations, and data-reduction are described in the next section. In Section 2.2, we explain our method of analysis and compare spectra we have in common with other authors. The problems one encounters analysing near-IR spectra of OH/IR stars will be discussed in Section 2.3, and finally in Section 2.4 we summarise and come to the conclusions.

2.1 Observations and data reduction

The sample consists of 70 OH/IR stars located in the GC region. Almost all stars were selected from Lindqvist et al. (1992b) and Sjouwerman et al. (1998). Our sample also includes the 15 OH/IR stars observed by Schultheis et al. (2003) so that we can compare our results and investigate the effect of the variability of this type of stars. We also selected the three "high-velocity" OH/IR stars that were detected in the direction of the GC (van Langevelde et al. 1992). As we wanted to apply the metallicity versus EW(Na), EW(Ca), and EW(CO) calibration used in Ramírez et al. (2000) and Frogel et al. (2001) to our sample, we also observed 11 stars from Ramírez et al. (1997, K-band spectra of 43 luminosity class III stars from K0 to M6) and Ramírez et al. (2000, K-band spectra of more than 110 M giants in the Galactic bulge (GB)). Finally, to investigate the effects of the variability of our long period variable stars (LPVs) on our analysis, we measured variable stars from Lançon and Wood (2000, spectra of cool, mostly variable, giant, and supergiant stars) (see Tables 2.9 to 2.11).

The near-IR spectra were obtained with the 3.58m NTT (ESO) at la Silla, Chile between June 28 - 30, 2003 using the red grism of the SOFI spectrograph. This resulted in spectra

from 1.53 μm up to 2.52 μm. Before the actual spectrum was obtained, the instrument was used in imaging mode to acquire the star in the slit. Several spectra were taken with the star in different places along the slit. Standard stars of spectral types O to G were observed as close as possible to the object stars' airmass in order to correct for telluric absorption features.

The data was reduced using the ESO-Munich Image Data Analysis System (MIDAS). The images were first corrected for cosmic ray hits. Several spectra of the same target along the slit were obtained and subtracted from each other to correct for the sky level. The images were flat-fielded using dome flats. A Gaussian fit perpendicular to the dispersion direction was used to subtract a one-dimensional spectrum out of the two-dimensional image: columns that fall within the FWHM of the Gaussian fit were added to the spectrum (3-4 columns on average). A correction for distortion along the slit was unnecessary. During the extraction process, a correction for bad pixels was made, they were left out of the spectrum, and no averaging was done around these pixels. The wavelength calibration was based on the spectrum of a Xenon lamp. This image was also flat-fielded using the dome flats and corrected for bad pixels in the same way as the other spectra. The wavelength calibration resulted in a dispersion of typically 10.13 Å/pixel and $\lambda/\Delta\lambda \approx 1000$.

The standard stars were reduced in the same way. Thereafter they were divided by the Kurucz-model that corresponds to each one's spectral type. The resulting curve was used to correct the objects for telluric lines and also to correct for the instrumental response function. Different curves for different airmasses were made in order to correct for the airmass. The dereddening law used is based on Cardelli et al. (1989), A_v values came from Schultheis et al. (1999). The resulting spectra are shown in Figures 2.15 to 2.22. More detailed figures for these spectra can be found in the electronic version of this manuscript at `http://www.ster.kuleuven.be/pub/index_en.html`.

2.2 Analysis

2.2.1 Equivalent line widths

The equivalent line widths of Na I, Ca I, and ^{12}CO(2,0) (see Tables 2.9 – 2.11) were obtained in exactly the same way as by Schultheis et al. (2003, see also Ramírez et al. (1997); Lançon and Wood (2000)). They were measured relative to the selected continuum bands using the Image Reduction and Analysis Facility (IRAF) (see Table 2.1 and Figure 2.2).

Ramírez et al. (1997) discuss how the equivalent line width measurements of Na I and Ca I in medium-resolution spectra contain contributions from other elements such as Sc, Ti, V, Si, and S. Thus, it turns out that a significant contribution of the Na I and Ca I features is due to other species. In the studied spectral region (1.53 – 2.52 μm), the CN molecule causes a noisy continuum (Origlia et al. 1993), introducing a pseudo-continuum opacity, which is clearly shown in the high-resolution spectrum of RX Boo (an M8 III star) in Wallace and Hinkle (1996). According to Ramírez et al. (1997), the continuum bands that were used to determine the EW(Ca) are affected by CN absorption for stars with $T_{eff} < 3000$ K. However, synthetic CN spectra based on hydrostatic MARCS models for giant stars (for a description

Table 2.1: Definition of band passes for continuum and features (Schultheis et al. 2003).

Feature	Band passes [μm]
Na I feature	2.204 – 2.211
Na I continuum #1	2.191 – 2.197
Na I continuum #2	2.213 – 2.217
Ca I feature	2.258 – 2.269
Ca I continuum #1	2.245 – 2.256
Ca I continuum #2	2.270 – 2.272
^{12}CO(2,0) feature band head	2.289 – 2.302
^{12}CO(2,0) continuum #1	2.242 – 2.258
^{12}CO(2,0) continuum #2	2.284 – 2.291
H_2O continuum	1.629 – 1.720
H_2O absorption wing 1	1.515 – 1.525
H_2O absorption wing 2	1.770 – 1.780

Table 2.2: Contribution of other species to the equivalent line-width measurement of Na I (based on Wallace and Hinkle 1996).

Na I feature	Na I continuum # 1	Na I continuum # 2
CN(0,2)	CN(0,2)	CN(0,2)
CN(1,3)	CN(1,3)	CN(1,3)
CN(2,4)	CN(2,4)	CN(2,4)
CN blend	Si	CN blend
V	Fe	
Na		
Fe		
Si		
Sc		

of such models see Aringer et al. (1997), in our case we assumed $\log(G\ [\mathrm{cm/s^2}]) = 0.0$, solar mass, and elemental abundances) show that CN is important in all cool objects below 4000 K, and even gets weaker below 3000 K.

The effective temperature has a strong impact on the Ca I and Na I features: as T_{eff} decreases, the equivalent widths of both features increase. Tables 2.2, 2.3, and 2.4 give an overview of what the respective Na I, Ca I, and ^{12}CO(2,0) lines in a medium-resolution spectrum are really made of. The tables are based on the high-resolution spectrum of RX Boo in Wallace and Hinkle (1996). For cooler oxygen–rich stars (Lançon and Wood 2000), such as OH/IR stars, H_2O absorption, instead of CN absorption, becomes very important (see Section 2.3.3).

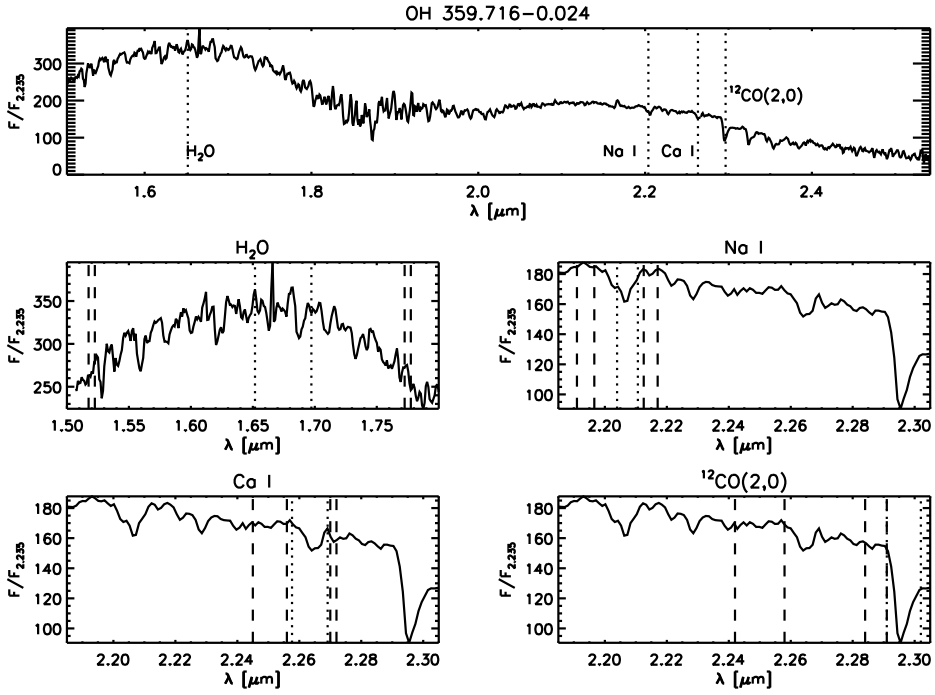

Figure 2.2: An overview of the chosen definition of band passes for continuum and features. The top figure shows the overall spectrum for a typical OH/IR stars. The dotted lines indicate the central positions of the features. The other 4 figures show for each line the selected passband for the feature (dotted lines) and the selected passband for the continuum (dashed lines). (For the ^{12}CO(2,0) the feature's first dotted line overlaps with the last dashed line from the continuum.)

2.2.2 Water absorption

The amount of water was obtained by measuring the curvature in the spectrum around 1.6 μm, as in Schultheis et al. (2003). The apparent bump around 1.6 μm is caused by strong and wide water-absorption bands around 1.4 and 1.9 μm. Formally, our measurements are equivalent widths of this bump relative to reference fluxes measured on either side of it in the wings of the water bands. As for the other equivalent line width measurements, its value is given in Å, but it takes negative values when water absorption is present (see Tables 2.9 – 2.11).

2.2.3 Comparison with previous work

We have 5 candidate Red Giant Branch (RGB) stars in common with Schultheis et al. (2003). These candidate RGB stars are probably genuine ones, since we see no significant difference between the Schultheis et al. (2003) observations of these stars and our own. Stars on the RGB are expected to show weak variations compared to OH/IR stars and Miras.

Table 2.3: Contribution of other species to the equivalent line-width measurement of Ca I (based on Wallace and Hinkle 1996).

Ca I feature	Ca I continuum # 1	Ca I continuum # 2
CN(0,2)	CN(0,2)	CN(2,4)
CN(1,3)	CN(1,3)	HF
CN(2,4)	CN(2,4)	S
CN blend	CN blend	
Si	Si	
Sc	Fe	
Ca	V	
Ti		
Fe		
Ni		

Table 2.4: Contribution of other species to the equivalent line-width measurement of ^{12}CO(2,0) (based on Wallace and Hinkle 1996).

^{12}CO(2,0) feature	^{12}CO(2,0) continuum #1	^{12}CO(2,0) continuum # 2
CN(0,2)	CN(0,2)	CN(0,2)
CN(1,3)	CN(2,4)	CN(1,3)
CN(2,4)	Si	CN(2,4)
Ti		CN blend
HF		Ti
CO(2,0)		HF

Schultheis et al. (2003) observed the stars with the same instrument (SOFI), using the same grism. This results in spectra with the same resolution as our spectra. The time difference between these observations is about 3 years. The spectra (normalised at 2.235 μm) are compared in Figure 2.3. Table 2.5 gives the mean values and standard deviations for the stars we have in common. The absolute average differences in equivalent line widths for these RGB stars are consistent with scatter due to formal errors ($\sim$ 1Å). One expects these errors to come from data-reduction issues and changing of observing conditions during the night. The absolute average differences are: 0.25 ± 0.17 Å for EW(Na), 0.72 ± 0.42 Å for EW(Ca), and 0.87 ± 0.82 Å for EW(CO) (see also Figure 2.4).

We have 8 late-type giants in common with Ramírez et al. (1997) and 6 red giants situated in the Bulge with Ramírez et al. (2000). A comparison was only made for EW(Na) and EW(Ca), since Ramírez et al. (1997) uses different continuum pass bands for obtaining EW(CO). Tables 2.6 and 2.7 give the mean values for the compared equivalent line widths. The absolute average differences with Ramírez et al. (1997) are: 0.39 ± 0.13 Å for EW(Na) and 1.29 ± 0.41 Å for EW(Ca). The absolute average differences with Ramírez et al. (2000) are 0.59 ± 0.23 Å for EW(Na) and 0.66 ± 0.35 Å for EW(Ca). The difference in EW(Na)

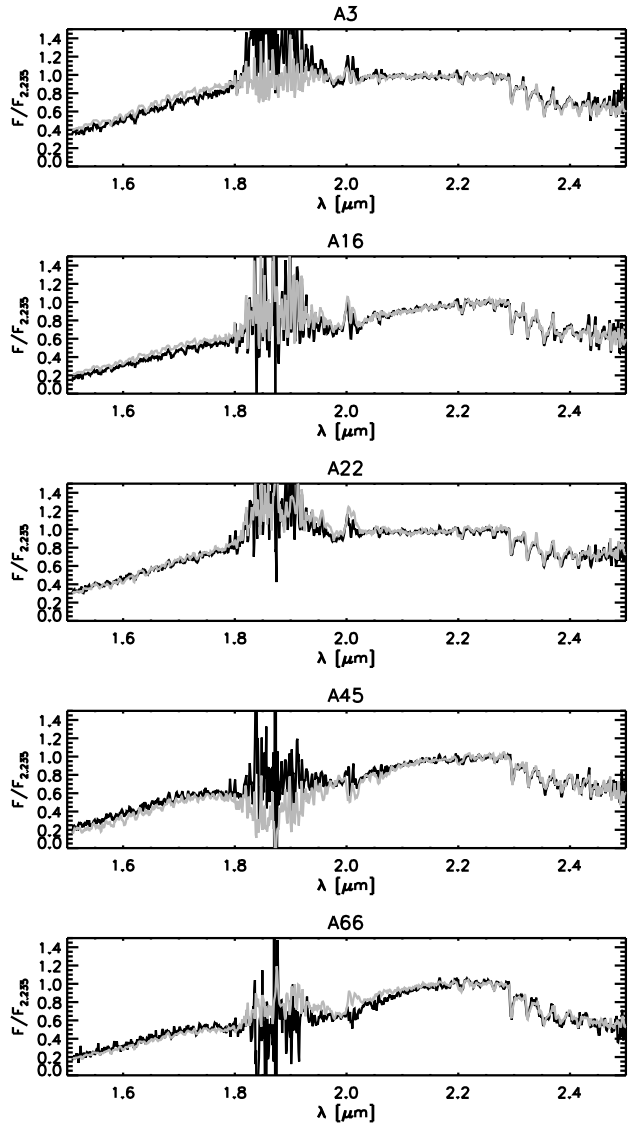

Figure 2.3: RGB stars in common with Schultheis et al. (2003); black line: this work, gray line: Schultheis et al. (2003). The features between 1.8 and 1.9 μm and around 2 μm are due to the atmosphere.

(Ramírez et al. 1997, 2000) and EW(Ca) (Ramírez et al. 2000) is again consistent with scatter due to formal errors. There is no obvious reason why the difference for EW(Ca) (Ramírez et al. 1997) is larger than $\sim$ 1Å (see also Figure 2.5), although we have to keep in mind that there is a difference in resolution between our spectra and the spectra of Ramírez et al. (1997,

Table 2.5: Mean values for the equivalent line widths for the stars in common with Schultheis et al. (2003).

	this work	Schultheis et al. (2003)
Na I	5.10 ± 0.74	5.21 ± 0.67
Ca I	2.52 ± 1.29	2.06 ± 0.74
^{12}CO(2,0)	19.95 ± 2.48	19.90 ± 1.69

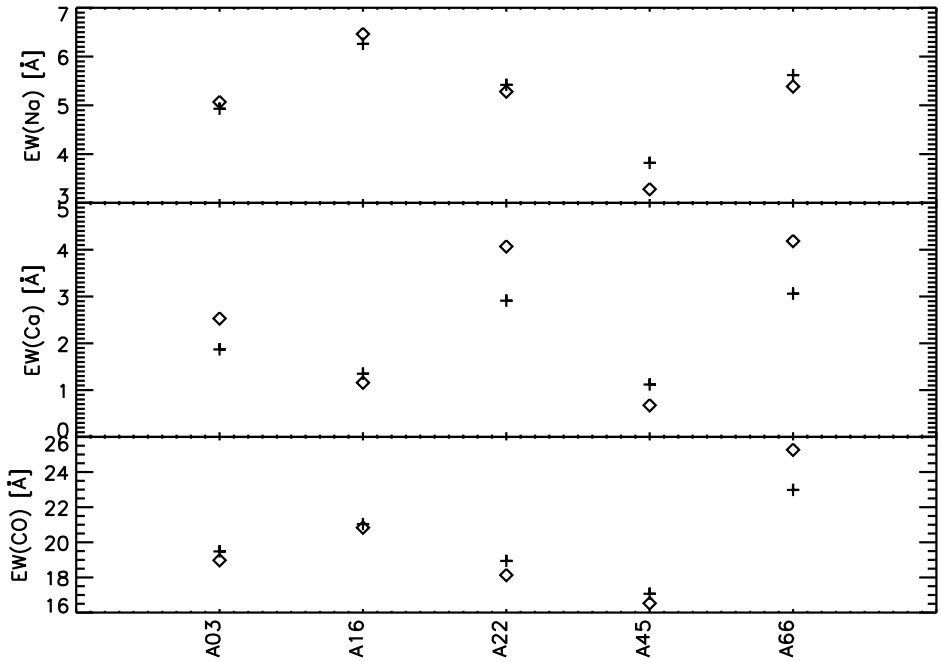

Figure 2.4: Equivalent line width measurements for the candidate RGB stars in common with Schultheis et al. (2003). The plus-signs are taken from Schultheis et al. (2003), the diamonds from this work.

2000), which can influence the difference between the measured equivalent line widths. The data from Ramírez et al. (2000) can be downloaded from the internet. After rebinning the data to our lower resolution, the following values could be measured: 3.95 ± 0.78 for the EW(Na) and 2.77 ± 0.47 for the EW(Ca), which resembles the values we found better (see Table 2.7). A similar test for Ramírez et al. (1997) could not be done.

We have 7 luminous cool stars in common with Lançon and Wood (2000). Three of these stars (WX Psc, AFGL 1686, and U Equ) are OH/IR stars (Lançon and Wood 2000), which (not situated in the GC) are used as a comparison for the equivalent line width measurements. The 4 other stars have periods in the range of 120 to 270 days. Some of the stars were ob-

Table 2.6: Mean values for the equivalent line widths for the stars in common with Ramírez et al. (1997).

	this work	Ramírez et al. (1997)
Na I	2.05 ± 0.62	2.39 ± 0.54
Ca I	1.64 ± 0.70	2.93 ± 0.82

Table 2.7: Mean values for the equivalent line widths for the stars in common with Ramírez et al. (2000).

	this work	Ramírez et al. (2000)	Ramírez et al. (2000) after rebining
Na I	3.55 ± 0.45	4.13 ± 0.54	3.95 ± 0.78
Ca I	2.62 ± 0.20	3.13 ± 0.48	2.77 ± 0.47

served several times by Lançon and Wood (2000). The differences in equivalent line widths between the measurements based on the available spectra of Lançon and Wood (2000) and our measurements are shown in Figure 2.6. The differences seen in this plot are large in comparison with the differences seen in Figures 2.4 and 2.5, especially for EW(CO), and cannot be explained by formal errors alone. The variability of the stars is responsible for the large variations in the equivalent line widths (see Section 2.3.4). Our measured equivalent line widths do fall within the range of equivalent line widths based on the spectra of Lançon and Wood (2000, see Figure 2.6). We can expect that the OH/IR stars that we have in common with Schultheis et al. (2003) will show similar variations in their equivalent line widths, as illustrated in Figure 2.7. The mean absolute differences for the OH/IR stars in common with Schultheis et al. (2003) concerning the equivalent line widths are: 1.56 ± 1.17 Å for EW(Na), 1.14 ± 1.16 Å for EW(Ca), 3.60 ± 2.47 Å for EW(CO) and 171.81 ± 193.03 Å for the water absorption. These variations are caused by the variability of these OH/IR stars, as will be explained in the following section.

Figure 2.8 gives an overview of the equivalent line widths for Na I, Ca I, and ^{12}CO(2,0) (see Section 2.2.1 and Table 2.1). The fourth histogram also gives the amount of water. Only the OH/IR stars are considered in this figure. Notice that the EW(Na), EW(Ca), EW(CO), and the EW(H_2O) are all in the same unit Å. The EW(H_2O) are all negative values, indicating water absorption in the spectrum around 1.6 μm, as can be seen from the spectra of the OH/IR stars in Figure 2.15. A negative value for EW(Ca) and EW(Na) indicates that the line could not been measured, since we do not expect these lines in emission. Figure 2.9 gives an example of this. It is especially clear for Ca I why the feature could not be measured: the second continuum band pass shows a very deep feature, which causes the flux measurement in the feature to be higher than in the continuum. This is also the case for the Na I feature, but here the first continuum band pass causes it (less clear than for the Ca I feature).

Fig. 2 in Ramírez et al. (2000) gives a 1 – 5 Å range for EW(Ca) and a 2 – 6 Å range for EW(Na) for a sample of red giants in the GB. Figure 2.8 shows that our ranges for the

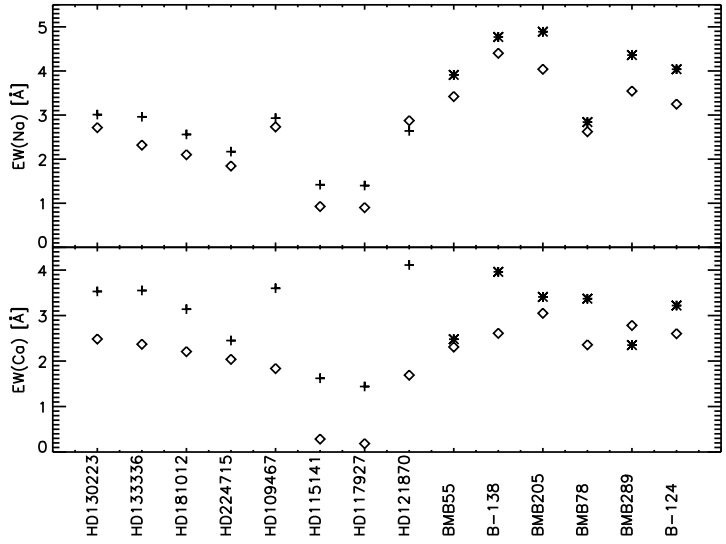

Figure 2.5: Equivalent line width measurements for the stars in common with Ramírez et al. (1997) and Ramírez et al. (2000). The plus-signs are taken from Ramírez et al. (1997), the stars are from Ramírez et al. (2000) and the diamonds are from this work.

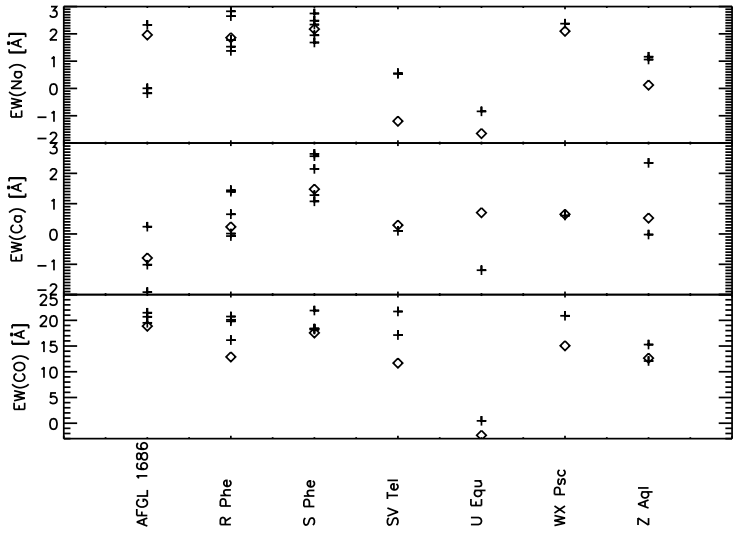

Figure 2.6: Variations in the equivalent widths for stars in common with Lançon and Wood (2000). The plus-signs indicate values taken from Lançon and Wood (2000), the diamonds those from this work.

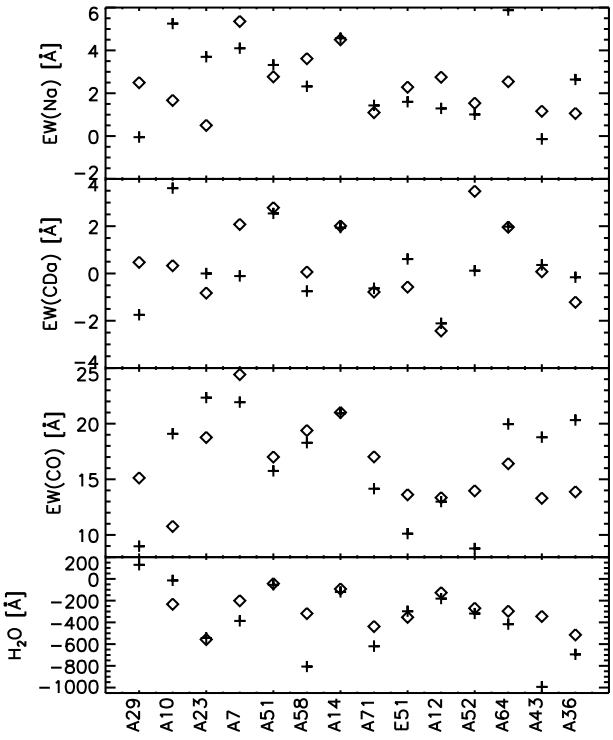

Figure 2.7: Equivalent line-width measurements for the OH/IR stars in common with Schultheis et al. (2003). The plus-signs indicate values taken from Schultheis et al. (2003), the diamonds those from this work.

equivalent widths for both Ca I and Na I are lower. Histograms for the equivalent line widths of Na I, Ca I, and ^{12}CO(2,0), and the water amount for the 15 OH/IR stars in Schultheis et al. (2003) are also shown in Figure 2.8 (dotted line). Their average equivalent widths are: 0.42 ± 1.56 Å for EW(Ca), 2.50 ± 1.90 Å for EW(Na), and 16.01 ± 5.16 Å for EW(CO). The equivalent widths for the OH/IR stars in this work are: 0.08 ± 1.88 Å for EW(Ca), 2.11 ± 1.27 Å for EW(Na), and 15.60 ± 4.69 Å for EW(CO). The largest difference is seen for EW(Ca); a lot of the OH/IR stars in this work and in Schultheis et al. (2003) have no measurable Ca I lines.

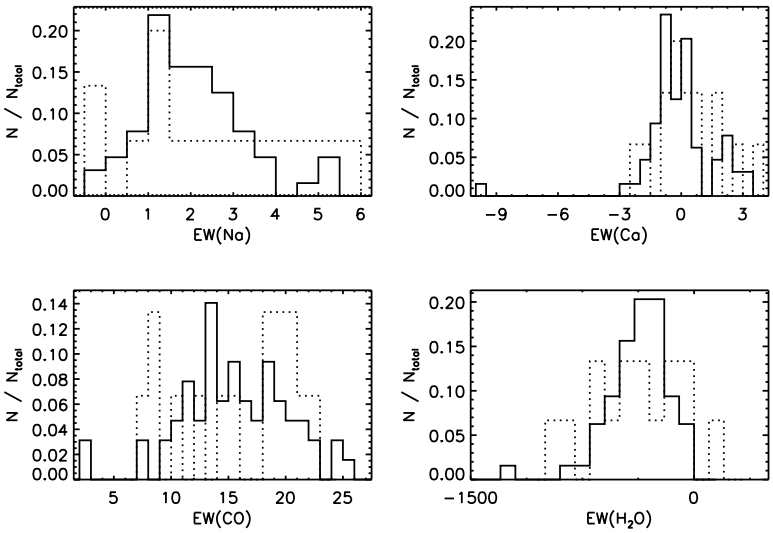

Figure 2.8: Histograms for EW(Ca), EW(Na), EW(CO) and the water absorption for the OH/IR stars from this work (full line) and the OH/IR stars from Schultheis et al. (2003) (dotted line). All x-axes are in the same unit Å.

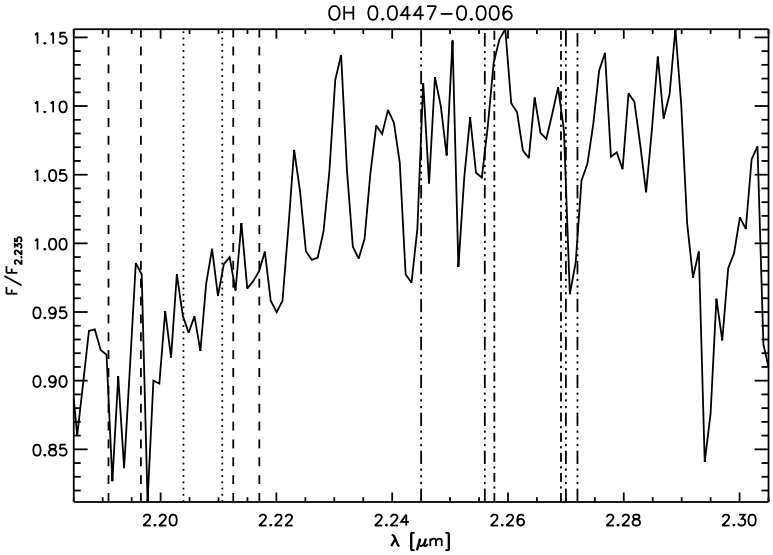

Figure 2.9: OH/IR star for which the Na I and Ca I lines could not be measured. The dotted lines indicate the Na I feature and the dashed lines the selected continuum points. The dashed-dotted lines indicate the Ca I feature with its corresponding continuum (dashed-triple-dotted).

2.3 Discussion

2.3.1 Metallicities of OH/IR stars in the GC

Schultheis et al. (2003) have investigated the metallicity distribution of 107 ISOGAL sources in the GB. The sample consists of different types of stars: non-variable giants, OH/IR stars, supergiants, and LPVs. The metallicity distribution is determined based on the equivalent line widths of Na I, Ca I, and ^{12}CO(2,0) (see Ramírez et al. 2000; Frogel et al. 2001; Schultheis et al. 2003), and the calibration of the relation is based on giants in globular clusters in the range $-1.8 < [Fe/H] < -0.1$. The mean [Fe/H] value in Schultheis et al. (2003) is consistent with previous chemical abundance studies of the GB (Schultheis et al. 2003). Apparently, variable stars, such as Miras and OH/IR stars, do not influence the peak in the metallicity distribution determined in Schultheis et al. (2003), although they might broaden the distribution. Applying their results to our sample of OH/IR stars could help to find a metallicity difference between the two separate groups of OH/IR stars in the GC as discussed in Section 1.2.6.

The equivalent line widths of Na I, Ca I, and ^{12}CO(2,0) are determined as described in Section 2.2.1. The values in Tables 2.9, 2.10, and 2.11 are given in Å. A positive value indicates absorption and a negative value indicates emission. One immediately notices all the negative values for EW(Ca). One does not expect the Ca I and the Na I lines to be in emission. Inspecting the spectra for these stars (Figures 2.15 to 2.18) shows that for several stars the Ca I lines seem to disappear in the continuum. This effect is also noticeable for Na I in some stars.

In the rest of this section we discuss the physical effects that can lead to the Ca I and sometimes the Na I to appear in emission.

2.3.2 Dust

OH/IR stars are AGB stars in their final phase on the AGB that are believed to be progenitors of Planetary Nebulae (e.g. Cohen et al. 2005; Habing 1996). These stars have high mass-loss rates between $\dot{M} = 10^{-6}$ $M_{\odot}/yr$ and 10^{-4} $M_{\odot}/yr$. It is likely that the dust formed around the star has an influence on the near-IR spectrum (Tej et al. 2003).

To study the effect of dust on the Na I and Ca I lines, the dust radiative transfer model of Groenewegen (1993) was used. In this model, the radiative transfer equation and the radiative equilibrium equation for the dust are solved simultaneously in spherical geometry (Groenewegen et al. 1994). For the dust properties we assume silicate dust (Volk and Kwok 1988) of radius $a = 0.02$ μm and a specific dust density of $\rho_{\rm d} = 2.0$ g/ cm^3. As the input model we used a blackbody with $T_{\rm eff} = 2500$ K and with the Ca I and Na I lines imposed upon it. A dust-to-gas ratio of $\Psi = 0.01$ and an outflow velocity of $v = 15$ km/s were assumed. For a grid of mass-loss and dust temperature the models indicate the influence of dust on these lines. Typical AGB mass-loss rates (between $\dot{M} = 10^{-7}$ $M_{\odot}/yr$ and 10^{-4} $M_{\odot}/yr$) and dust temperatures ($T_{dust} = 1500, 1000$ and 750 K) were used. The model with no mass-loss is used as a reference model.

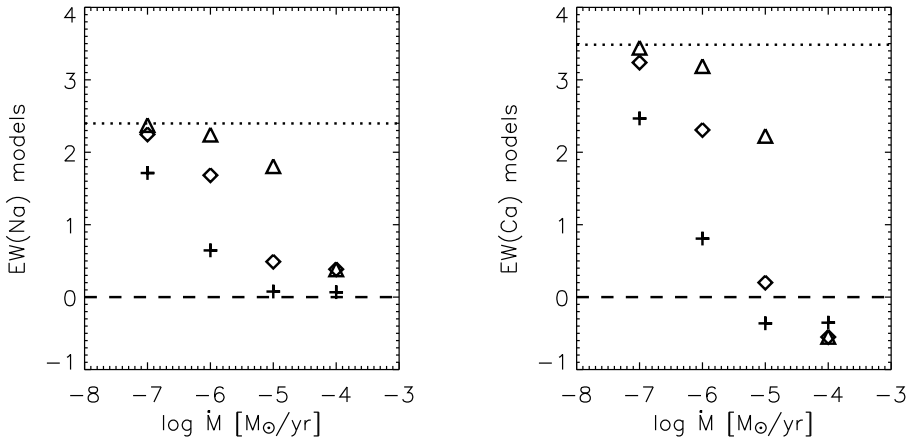

Figure 2.10: Equivalent line widths for the different models. The x-axis indicates the mass-loss rate, and the y-axis the equivalent line widths for Na I (left) and Ca I (right). The different symbols indicate the different dust temperatures. Crosses: T_{dust} = 1500 K, diamonds: T_{dust} = 1000 K, and triangles: T_{dust} = 750 K. The dotted line indicates the equivalent line width for the reference model. The line disappears when the equivalent width is below the dashed line.

Figure 2.10 shows the effect of the increasing dust amount on the equivalent line widths of Na I and Ca I. For both lines a similar trend can be seen in which the equivalent line widths decrease for increasing mass-loss rates. The effect is stronger for higher dust temperatures, except at the 10^{-4} $M_{\odot}/yr$ mass-loss rate where the Na I and Ca I lines become undetectable for the three dust temperatures. This effect is also stronger with increasing wavelength and affects the Ca I more than the Na I. Unfortunately, we do know neither the temperature of the dust, nor the mass-loss rate for our individual sources. We can only demonstrate here the possible influence of the dust on the measured near-infrared spectrum. Surprisingly, negative values for EW(Ca) were measured for these models. This is merely due to the chosen continuum: the change in the continuum's slope is so drastic that it causes negative equivalent line-width measurements.

2.3.3 Water content in OH/IR stars

Water absorption lines can influence the near-IR medium resolution spectra of AGB stars severely in a way which depends on the phase of the variable star as shown in Tej et al. (2003). The high-resolution spectrum of *o* Cet, a M type Mira, in Wallace and Hinkle (1996) shows that a lot of water lines are situated at wavelengths where the Ca I and Na I lines are observed. In the case of the Ca I line, the strong water lines are situated where the continuum of the line is determined. The water lines depress the continuum in a medium-resolution

spectrum and make the equivalent line-width measurements unreliable. When the depression of the continuum is strong enough, one can expect to start to see the Ca I line in apparent emission. In the case of the Na I line, the water lines affect both the continuum and the Na I line, so that one can expect to see the EW(Na) decrease because of a smaller contrast between the continuum and the line, similar to what is seen due to the influence of the dust on the spectrum, as discussed in the previous subsection.

These effects are reflected in Figure 2.11 where the EW(Ca) and the EW(Na) can be seen in comparison with our determination of the water absorption. We see that the RGB stars, with little water absorption, have higher EW(Ca) and the EW(Na) values than the LPVs and OH/IR stars. This effect seems stronger for Ca I where we basically have no more detections for EW(H_2O) below -300 Å. For the Na I line the decrease is more gradual with increasing water absorption. Of course the effect of dust and other factors (such as pulsation amplitude, T_{eff}) on the spectra is also included in these figures and cannot be distinguished from the effect that the water absorption has.

2.3.4 Variability

Figure 2.7 shows the differences in the measured absorption for water clearly for the stars we have in common with Schultheis et al. (2003). The water absorption is expected to be largely correlated with the phase for a given star: the most intense water features are seen at minimum light (Lançon and Wood 2000; Bessell et al. 1996; Tej et al. 2003).

Wood et al. (1998) determined periods for 80 GC OH/IR stars. We found *K*-band light curves for 41 out of the 50 stars in common with our sample. The lightcurves were extrapolated using the fundamental period and the first harmonic (Wood 2004) to determine the phase (= ϕ) when the star was observed in our campaign. The value of ϕ has been calculated in a non-traditional way, such that the maxiumum of the lightcurve is 0 and that the minimum is always at $\phi = 0.5$. The values of 0.25/0.75 were fixed when the lightcurve reaches $< K >$. The other values for ϕ were then interpolated between the fixed ones (see Figure 2.12).

Figure 2.13 shows the phase ϕ versus the equivalent line-width of water. The expected correlation can be seen in this figure, but not as clearly as anticipated. Figure 2.13 indicates that the water absorption is highest for all but one star for $\phi = 0.5$, which indicates the light minimum. For the other phases there is a large spread and no clear trend, which is expected as the individual stars have different parameters.

2.3.5 Expansion velocities

Lindqvist et al. (1992b) determined the expansion velocities v_{exp} for their sample of OH/IR stars close to the GC. As mentioned in Section 1.2.6, they divided the sample into two groups based on the expansion velocities. The first group with the lowest expansion velocities are kinematically different and show larger dispersions in their radial velocities.

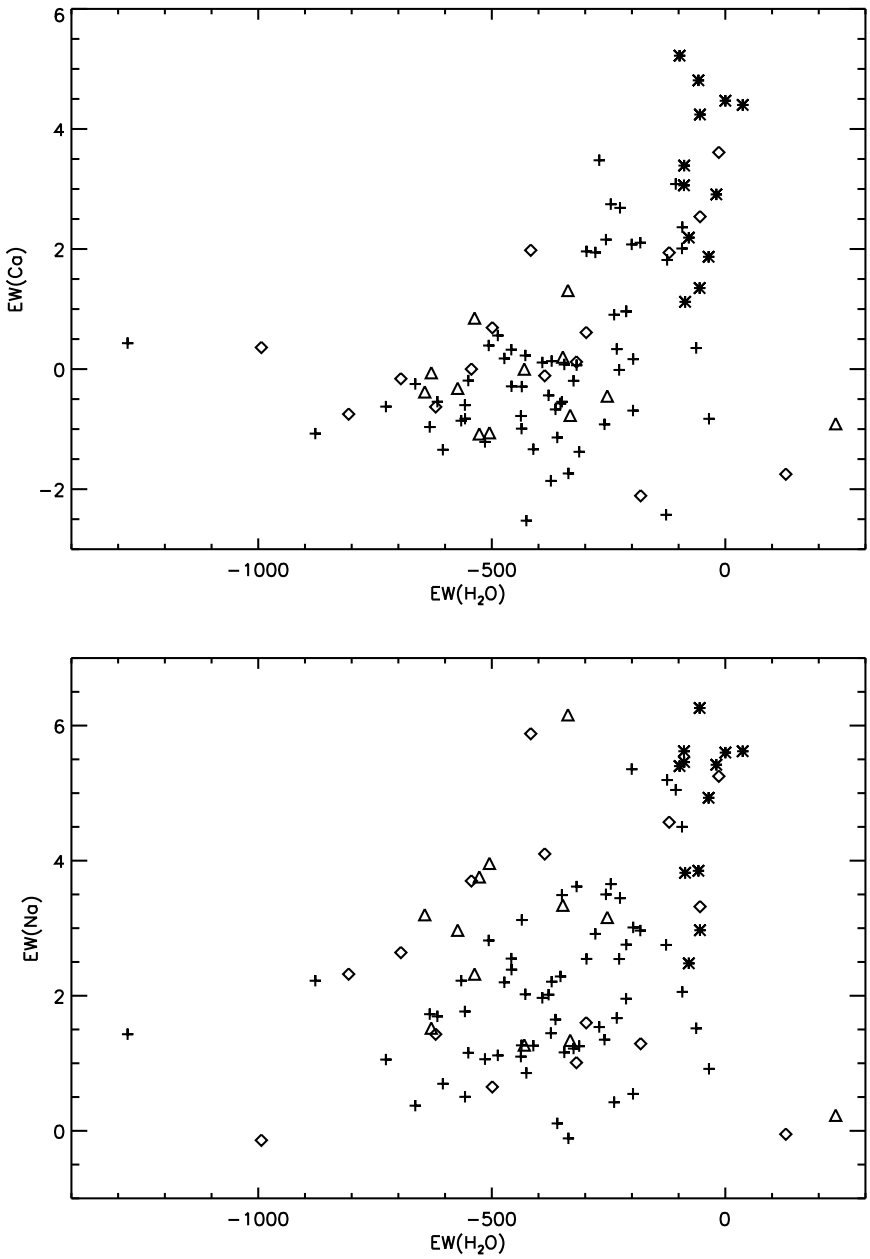

Figure 2.11: Upper panel: EW(Ca) vs EW(H_2O), lower panel: EW(Na) vs EW(H_2O). The OH/IR in this work are the crosses, RGB (Schultheis et al. 2003): stars, OH/IR (Schultheis et al. 2003): diamonds, LPV (Schultheis et al. 2003): triangles. All equivalent line widths are given in the same unit Å.

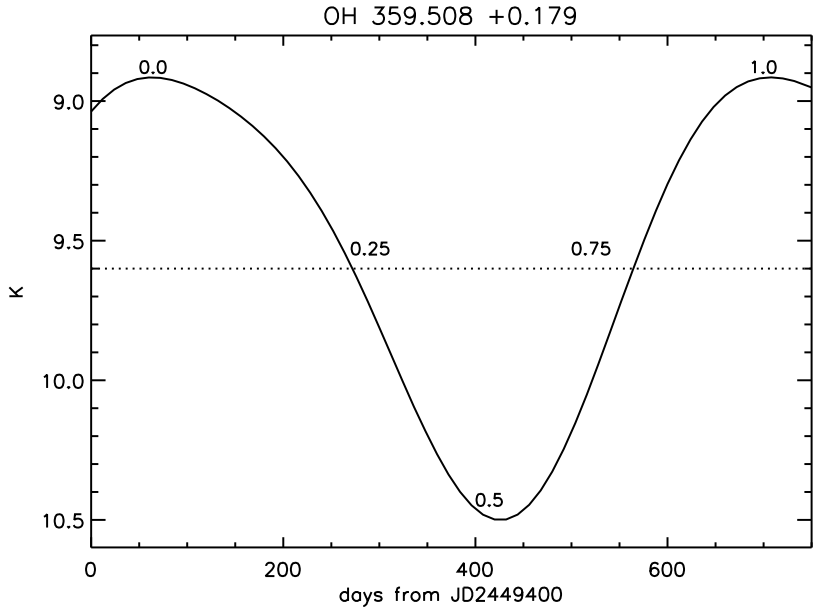

Figure 2.12: Determination of the phase ϕ. The dotted horizontal line gives $< K >$.

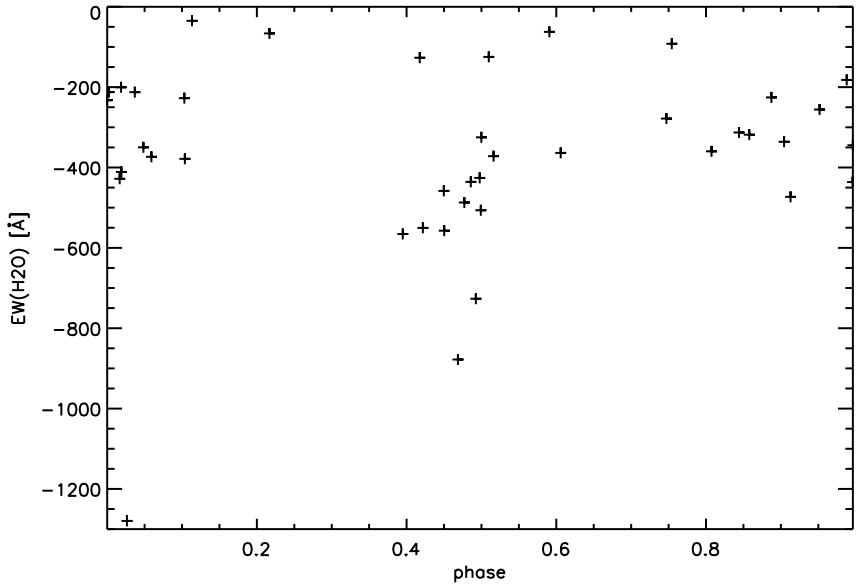

Figure 2.13: The phase at time of observation versus the equivalent line width of water absorption.

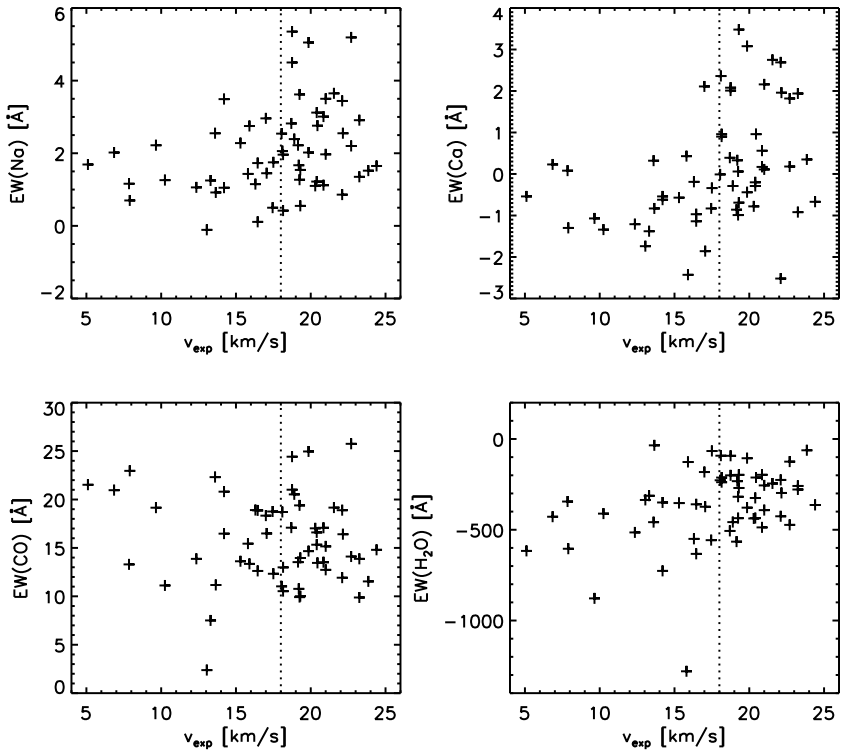

Figure 2.14: Comparison of the expansion velocities with the equivalent line widths of Na I, Ca I, ^{12}CO(2,0), and the water absorption. The dotted vertical line separates the 2 groups of OH/IR stars.

Table 2.8: Mean equivalent line width values for the two groups of OH/IR stars.

	v_{exp} < 18 km/s	v_{exp} > 18 km/s
Na I	1.57 ± 0.70	2.44 ± 1.02
Ca I	-0.65 ± 0.69	0.67 ± 1.17
^{12}CO(2,0)	15.73 ± 3.90	15.61 ± 3.44
H_2O	-452.90 ± 190.82	-294.97 ± 110.31

With our spectra we wanted to see whether we could find metallicity differences between the two kinematically different groups. As shown in the previous sections, this is not possible using the relationship based on the equivalent line widths of Na I, Ca I, and ^{12}CO(2,0) in non-variable stars with low mass-loss rates (see Ramírez et al. 2000; Frogel et al. 2001; Schultheis et al. 2003). We still wanted to investigate whether we find differences in the equivalent line widths of the individual lines for the two groups. Figure 2.14 shows the comparison between

the expansion velocities and the equivalent line widths of Na I, Ca I, ^{12}CO(2,0), and the water absorption around 1.6 μm, for our sample of OH/IR stars. Table 2.8 gives the mean values with standard deviation for the measured equivalent line widths and the water indication for the both groups.

Figure 2.14 and Table 2.8 seem to indicate that the OH/IR stars in the first group have smaller EW(Na) and a larger spread for the water absorption. Based on the numbers in Table 2.8, there is no difference between the EW(CO) for both groups. Concerning Ca I, the majority of the OH/IR stars in the first group have no measurable equivalent line widths. Since the water absorption has a larger spread for this group and because of the dependence seen in Figure 2.11, it is consistent that we measure negative EW(Ca) for the majority of these stars.

Decin (2000) indicates that the linestrength of H_2O increases with decreasing metallicity. This could explain why we see stronger water absorption for the OH/IR stars in the first group, provided these OH/IR stars are older and have lower metallicities than the stars in the second group, as suggested by kinematics and outflow velocities.

2.4 Conclusions

We obtained near-IR data (1.53 – 2.52 μm) with SOFI on the NTT for 70 OH/IR stars located in the GC. The spectra were analysed based on the equivalent line widths of Na I, Ca I, and ^{12}CO(2,0). The curvature of the spectrum around 1.6 μm indicates the amount of water. The equivalent line widths of Na I, Ca I, and ^{12}CO(2,0) were found to have low values in comparison to the GC static giant stars. For a large fraction of the OH/IR stars, we even found that Ca I lines could not be detected.

We discuss different elements which can influence the determination of the equivalent line widths in the near-infrared spectra. The OH/IR stars have a variable amount of water, which especially influences the Ca I lines. The water lines just beside the Ca I line depress the continuum, causing the Ca I lines to disappear in the spectrum. The effect is also noticeable for Na I but is not as strong.

We also discuss the effect of the circumstellar dust on the near-infrared spectrum. By using the radiative transfer model (Groenewegen 1993), it became clear that for the highest mass-loss rates the dust has the same effect on the Ca I and Na I lines as the water content: the lines become weaker and in the extreme case of mass-loss rates of the order of 10^{-4} $M_{\odot}/yr$ even disappear in the continuum and are no longer measurable. For the lower mass-loss rates ($\sim 10^{-6}$ $M_{\odot}/yr$), the decrease in the equivalent line widths depends strongly on the dust temperature. Since we do not know the exact dust temperature and the mass-loss rates of these OH/IR stars, we cannot distinguish between the possible effects that weaken the lines. The different effects discussed above prevent us from finding a clear distinction between the two groups of OH/IR stars.

Table 2.9: Log of the stars observed on 28/06/03.

Name	RA	Dec	References [a]	EW(Na) [Å]	EW(Ca) [Å]	EW(CO) [Å]	H_2O[Å]	P [b] [days]	v_{exp} [km/s]
OH 359.576 +0.091	17 44 57.80	-29 20 42.5	Li012, A29	2.50	0.47	15.13		672.0	18.6
OH 359.598 +0.000	17 44 39.71	-29 16 46.1	Li014, A10	1.67	0.33	10.77	-232.39	664.0	19.2
OH 359.669 -0.019	17 44 54.16	-29 13 44.9	Li020, A23	0.50	-0.83	18.76	-557.33	481.0	17.5
OH 359.675 +0.069	17 44 34.33	-29 10 38.6	Li021, A07, B98, S98	5.35	2.08	24.42	-200.35	698.0	18.8
OH 359.678 -0.024	17 44 56.83	-29 13 25.5	Li022, B98	3.65	2.75	19.16	-245.18		21.5
OH 359.681 -0.095	17 45 16.43	-29 15 37.6	Li023, A51, S98	2.76	2.78	17.01	-43.64	759.0	19.3
OH 359.711 -0.100	17 45 19.26	-29 14 01.1	Li025, A58, S98	3.62	0.06	19.39	-318.34	686.0	19.2
OH 359.748 +0.274	17 43 57.05	-29 00 28.4	Li030	-0.11	-1.74	2.38	-335.99	437.0	13.1
OH 359.755 +0.061	17 44 47.94	-29 06 49.9	Li031, A14, B98, S98	4.50	2.01	21.01	-92.73	0.0	18.8
OH 359.757 -0.136	17 45 34.41	-29 12 54.1	Sj002, A71, S98	1.10	-0.78	17.02	-437.67		20.3
OH 359.762 +0.120	17 44 34.96	-29 04 35.7	Li033, B98, E51, S98	2.28	-0.57	13.62	-352.97		15.3
OH 359.765 +0.082	17 44 44.43	-29 05 37.9	Li035, A12, S98	2.75	-2.43	13.35	-126.89	552.0	15.9
OH 359.768 -0.207	17 45 52.62	-29 14 30.4	Li036	1.27	-0.99	9.92	-436.23	602.0	19.2
OH 359.783 -0.392	17 46 38.12	-29 19 30.7	Li039	1.25	-1.38	7.51	-312.88	559.0	13.3
OH 359.797 -0.025	17 45 14.27	-29 07 20.8	Sj004, A52, S98	1.54	3.48	13.96	-269.95		19.3
OH 359.799 -0.090	17 45 29.50	-29 09 16.0	Li040, B98, S98	1.11	-0.51	15.97			18.1
OH 359.800 +0.165	17 44 30.11	-29 01 14.3	Li041	3.49	-0.54	16.47	-349.81	461.0	14.2
OH 359.803 -0.248	17 46 07.10	-29 13 56.1	Li043, S98	4.72	3.94	20.13	-25.58	803.0	18.5
OH 359.810 -0.070	17 45 26.35	-29 08 03.9	Li044, A64, B98, S98	2.55	1.96	16.41	-297.19		22.1
OH 359.825 -0.024	17 45 17.83	-29 05 53.3	Li047, B98, S98	0.37	-0.25	19.95	-663.81		
OH 359.837 +0.030	17 45 06.98	-29 03 34.9	Li048, A43, B98, S98	1.16	0.08	13.30	-344.67	402.0	7.8
OH 359.838 +0.053	17 45 01.70	-29 02 49.9	Sj011, A36	1.06	-1.21	13.87	-514.62		12.4
OH 359.889 +0.361	17 43 56.94	-28 50 30.8	Li054	2.54	-0.01	11.03	-227.34	389.0	18.1
OH 359.906 -0.041	17 45 33.17	-29 02 18.4	B98, S98	5.05	3.08	24.96	-106.08		19.8
OH 359.943 +0.260	17 44 28.17	-28 50 55.8	Li064, B98, S98	1.75	-0.34	12.33	-66.26	692.0	17.5
OH 0.001 +0.352	17 44 14.95	-28 45 06.0	Li076, S98	2.22	-1.07	19.15	-877.91	477.0	9.7
OH 0.019 +0.345	17 44 19.23	-28 44 21.8	Li079	1.52	0.35	11.54	-62.35	701.0	23.9
OH 0.138 -0.136	17 46 28.71	-28 53 19.5	Li094, S98	3.12	-0.29	16.60	-435.76	622.0	20.4
OH 0.173 +0.211	17 45 12.45	-28 40 44.4	Li096, S98	1.45	-1.86	16.49	-373.41	514.0	17.0
OH 0.200 +0.233	17 45 11.44	-28 38 43.2	Li101	1.43	0.43	15.44	-1279.67	825.0	15.8
OH 0.221 +0.168	17 45 29.02	-28 39 38.5	Li104	2.22	-0.86	13.53	-565.55	697.0	19.2
HD 130223	14 47 53.62	-32 14 49.5	R97	2.72	2.48	17.25	-11.74		
HD 133336	15 04 52.37	-31 16 44.7	R97	2.32	2.37	15.65	-11.83		
HD 181012	19 20 13.43	-36 13 39.8	R97	2.10	2.21	17.63	-17.89		
HD 224715	00 00 09.82	-35 57 36.8	R97	1.84	2.04	14.44	-33.38		
WX Psc	01 06 25.98	+12 35 53.0	L00	2.10	0.65	15.06	-290.88		

[a] Li: Lindqvist et al. (1992b), Sj: Sjouwerman et al. (1998) and Ortiz et al. (2002), B98: Blommaert et al. (1998), A: Schultheis et al. (2003), HV: van Langevelde et al. (1992), R97: Ramírez et al. (1997), R00: Ramírez et al. (2000), L00: Lançon and Wood (2000), and S98: Sjouwerman et al. (1998).

[b] Periods are taken from Wood et al. (1998).

Table 2.10: Log of the stars observed on 29/06/03.

Name	RA	Dec	References [a]	EW(Na) [Å]	EW(Ca) [Å]	EW(CO) [Å]	H_2O[Å]	P [b] [days]	v_{exp} [km/s]
OH 359.437 -0.051	17 44 28.30	-29 26 35.0	Li004	4.77	3.05	19.80	-45.15	0.0	15.3
OH 359.508 +0.179	17 43 44.74	-29 15 44.6	Li009	2.02	-0.44	14.67	-378.36	644.0	19.8
OH 359.513 +0.174	17 43 46.73	-29 15 38.4	Li010	1.26	-1.34	11.12	-411.05	461.0	10.2
OH 359.634 -0.195	17 45 30.45	-29 21 00.0	Li016	2.21	0.13	15.22	-371.80	501.0	0.0
OH 359.636 -0.108	17 45 10.39	-29 18 12.3	Li017	0.86	-2.52	11.92	-425.97	847.0	22.1
OH 359.640 -0.084	17 45 05.29	-29 17 13.4	Li018	2.55	0.32	22.31	-458.27	546.0	13.6
OH 359.684 -0.104	17 45 16.43	-29 15 37.6	Li024, S98	1.15	-0.19	18.91	-550.36	535.0	16.3
OH 359.716 -0.070	17 45 13.00	-29 12 54.0	Li026, S98	5.19	1.82	25.75	-124.72	691.0	22.7
OH 359.719 +0.025	17 44 51.25	-29 09 45.3	Li027	2.20	0.18	14.11	-473.12	669.0	22.7
OH 359.760 +0.072	17 44 45.96	-29 06 13.6	Li032	1.12	0.56	17.08	-487.08	676.0	20.9
OH 359.763 -0.042	17 45 13.07	-29 09 36.3	Li034, S98	1.05	-0.62	20.81	-726.67	453.0	14.2
OH 0.018 +0.156	17 45 03.30	-28 50 22.0	Li078, S98	2.02	0.23	20.96	-428.16	423.0	6.9
OH 0.036 -0.182	17 46 24.87	-29 00 01.4	Li080, S98	1.98	-1.61	7.64	-4085.92	660.0	18.8
OH 0.040 -0.056	17 45 56.08	-28 55 52.0	B98, S98	3.01	0.17	13.52	-197.38		20.8
OH 0.060 -0.018	17 45 50.07	-28 53 38.1	B98	0.55	-0.69	10.01	-197.71		19.3
OH 0.076 +0.146	17 45 13.91	-28 47 43.2	Li086, B98, S98	1.97	0.11	12.73	-391.78		21.0
OH 0.129 +0.103	17 45 31.45	-28 46 22.1	Li091, B98, S98	1.77	-0.60	21.15	-557.53		
OH 0.142 +0.026	17 45 51.33	-28 48 06.8	B98	1.35	-0.92	9.88	-258.59		23.2
OH 0.178 -0.055	17 46 13.85	-28 48 50.4	B98	1.73	-0.97	18.87	-632.77		16.5
OH 0.225 -0.055	17 46 22.11	-28 46 22.6	Li105, B98	0.11	-1.14	12.62	-359.80	521.0	16.5
OH 0.241 -0.014	17 46 14.96	-28 44 17.3	Li106	2.82	0.39	17.09	-506.51	535.0	18.7
OH 0.265 -0.078	17 46 33.12	-28 45 00.7	Li108	2.06	2.36	18.71	-92.13	595.0	18.1
OH 0.274 +0.086	17 45 56.08	-28 39 27.5	Li109	1.65	-0.67	14.80	-363.65	706.0	24.4
OH 0.307 -0.176	17 47 02.17	-28 45 55.8	Li110	1.22	-0.20	15.33	-324.90	657.0	20.4
OH 0.336 -0.027	17 46 31.30	-28 39 48.0	Li113	2.96	2.11	18.33	-182.05	514.0	17.0
HD 109467	12 35 04.30	-28 46 39.6	R97	2.73	1.84	17.68	-15.21		
HD 115141	13 15 49.54	-40 03 17.1	R97	0.93	0.29	7.28	-8.41		
HD 117927	13 34 15.34	-34 23 15.3	R97	0.90	0.19	6.03	-2.47		
HD 121870	13 58 53.01	-32 47 32.5	R97	2.87	1.69	17.03	-24.24		
AFGL 1686	14 11 17.61	-07 44 49.9	L00	1.96	-0.79	18.87	-528.16		
R Phe	23 56 27.57	-49 47 12.5	L00	1.86	0.23	12.89	-118.80		
S Phe	23 59 04.57	-56 34 32.3	L00	2.17	1.48	17.56	-15.30		
V Tel	18 56 17.94	-49 29 09.7	L00	-1.20	0.29	11.69	-481.43		
U Equ	20 57 16.28	+02 58 44.6	L00	-1.65	0.70	-2.35	-109.43		
Z Aql	20 15 11.04	-06 09 04.0	L00	0.12	0.53	12.65	-201.51		

[a] See Table 2.9.
[b] See Table 2.9.

Table 2.11: Log of the stars observed on 30/06/03.

Name	RA	Dec	References [a]	EW(Na) [Å]	EW(Ca) [Å]	EW(CO) [Å]	H_2O[Å]	P [b] [days]	v_{exp} [km/s]
OH 359.746 +0.134	17 44 29.42	-29 04 58.6	Li029, S98	0.70	-1.30	22.96	-604.71		7.9
OH 359.778 +0.010	17 45 03.20	-29 07 12.6	Li038, S98	3.50	2.16	15.16	-255.61	557.0	21.0
OH 359.814 -0.162	17 45 48.48	-29 10 45.2	Li045, S98	2.76	0.96	13.45	-212.24	554.0	20.5
OH 359.836 +0.119	17 44 45.97	-29 00 50.9	Sj009, HV	-1.31	1.01	14.06	-126.84		
OH 359.855 -0.078	17 45 34.79	-29 06 02.7	Li050	3.44	2.69	18.89	-225.50	617.0	22.1
OH 359.864 +0.056	17 45 04.71	-29 01 24.9	Sj013, A38, HV	0.09	0.57	22.89	-660.83		
OH 359.918 -0.055	17 45 38.46	-29 02 03.9	B98, S98	0.42	0.90	10.53	-238.09		18.1
OH 359.943 -0.055	17 44 28.20	-28 50 55.0	S98	2.49	1.66	14.73	31.60		
OH 0.017 +0.156	17 45 03.65	-28 50 27.7	S98	2.39	-0.29	20.53	-457.78		18.9
OH 0.037 -0.003	17 45 43.16	-28 54 21.8	S98	1.69	-0.54	21.52	-616.51		5.1
OH 0.335 -0.180	17 47 07.34	-28 44 28.3	HV, S98	3.33	1.65	17.06	-2.82		
OH 0.352 +0.175	17 45 46.57	-28 32 39.5	Li115	1.96	0.96	12.99	-212.56	661.0	18.1
OH 0.379 +0.159	17 45 54.18	-28 31 46.0	Li116	3.48	-0.37	2.75		985.0	15.3
OH 0.395 +0.008	17 46 31.48	-28 35 37.3	Li117	0.92	-0.83	11.17	-34.99	461.0	13.7
OH 0.447 -0.006	17 46 42.29	-28 33 26.1	Li120	-0.33	-9.57	14.46		445.0	13.1
OH 0.452 +0.046	17 46 30.70	-28 31 31.0	Li121	1.96	1.47	14.14	-36.33	339.0	10.2
OH 0.536 -0.130	17 47 24.02	-28 32 42.9	Li127	2.91	1.94	13.87	-278.26	669.0	23.2
	17 44 23.80	-29 08 55.3	A03	5.07	2.53	18.98	-10.57		
	17 44 48.60	-29 00 13.2	A16	6.46	1.16	20.84	-5.45		
	17 44 53.10	-28 59 46.5	A22	5.28	4.07	18.13	-6.80		
	17 45 09.80	-29 05 17.8	A45	3.28	0.68	16.53	-55.01		
	17 45 27.50	-29 04 39.9	A66	5.39	4.18	25.26	-58.05		
BMB 55	18 03 08.16	-29 57 47.4	R00	3.42	2.31	19.45	-90.37		
B-138	18 03 46.00	-29 59 12.1	R00	4.40	2.61	21.97	-48.03		
BMB 205	18 03 54.85	-30 04 19.2	R00	4.04	3.05	21.95	-57.11		
BMB 78	18 03 15.54	-29 51 09.0	R00	2.62	2.36	18.30	-28.21		
BMB 289	18 04 22.72	-29 54 50.6	R00	3.54	2.78	22.39	-111.15		
B-124	18 04 43.73	-30 05 15.3	R00	3.25	2.60	19.47	-33.46		

[a] See Table 2.9.
[b] See Table 2.9.

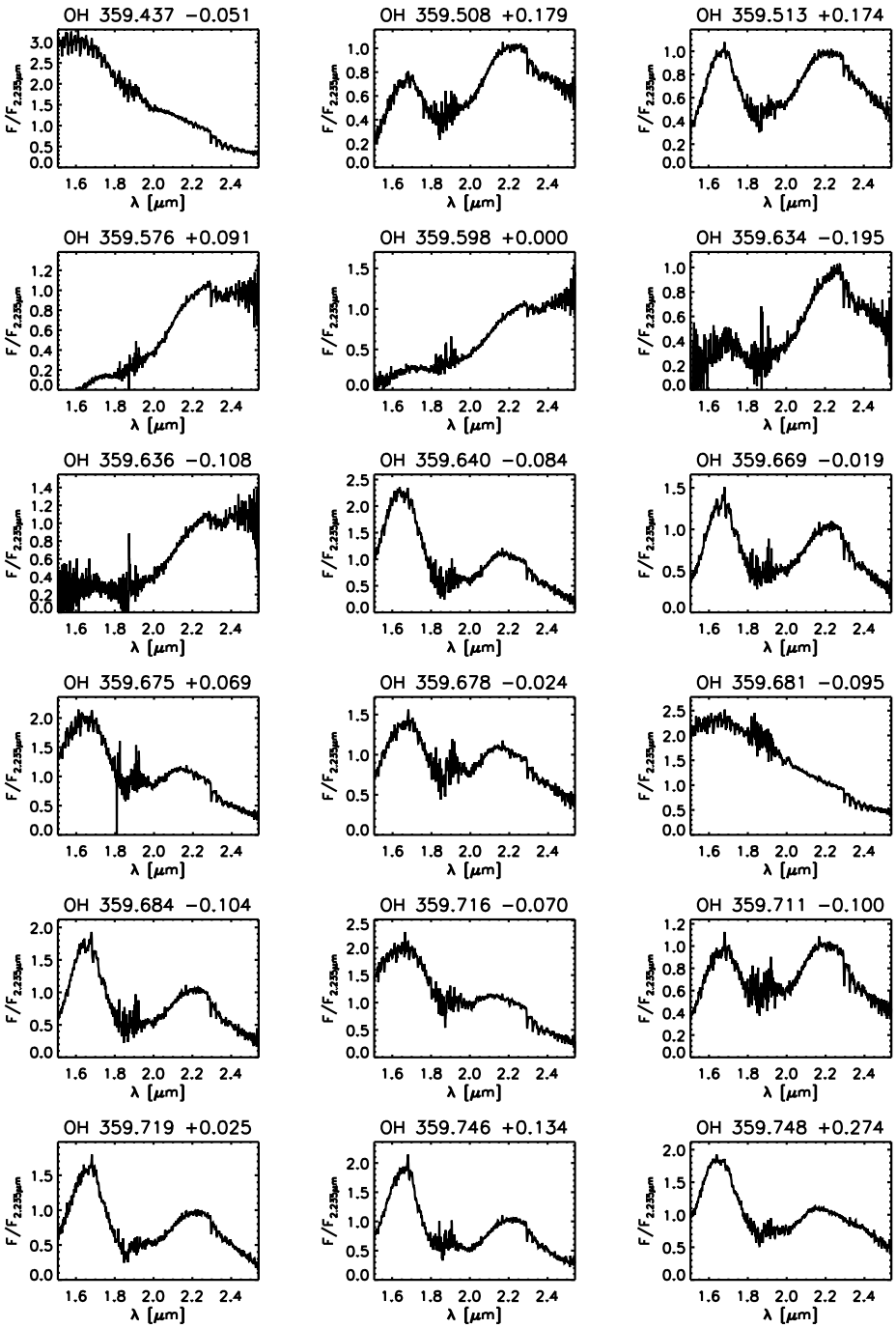

Figure 2.15: OH/IR stars. OH 359.437-0.051 is possibly a mismatch.

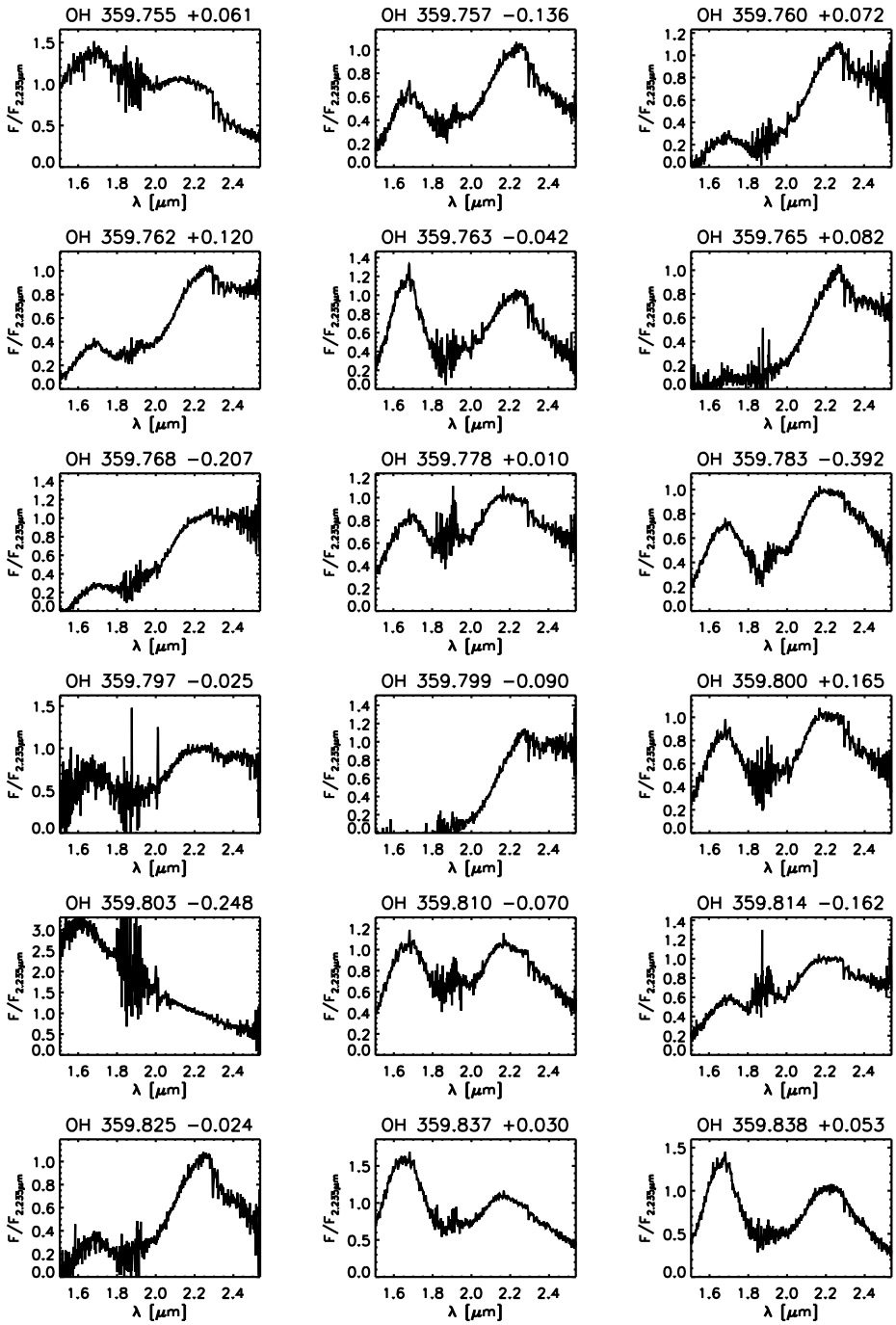

Figure 2.16: OH/IR stars - continued. OH 359.803-0.248 is possibly a mismatch.

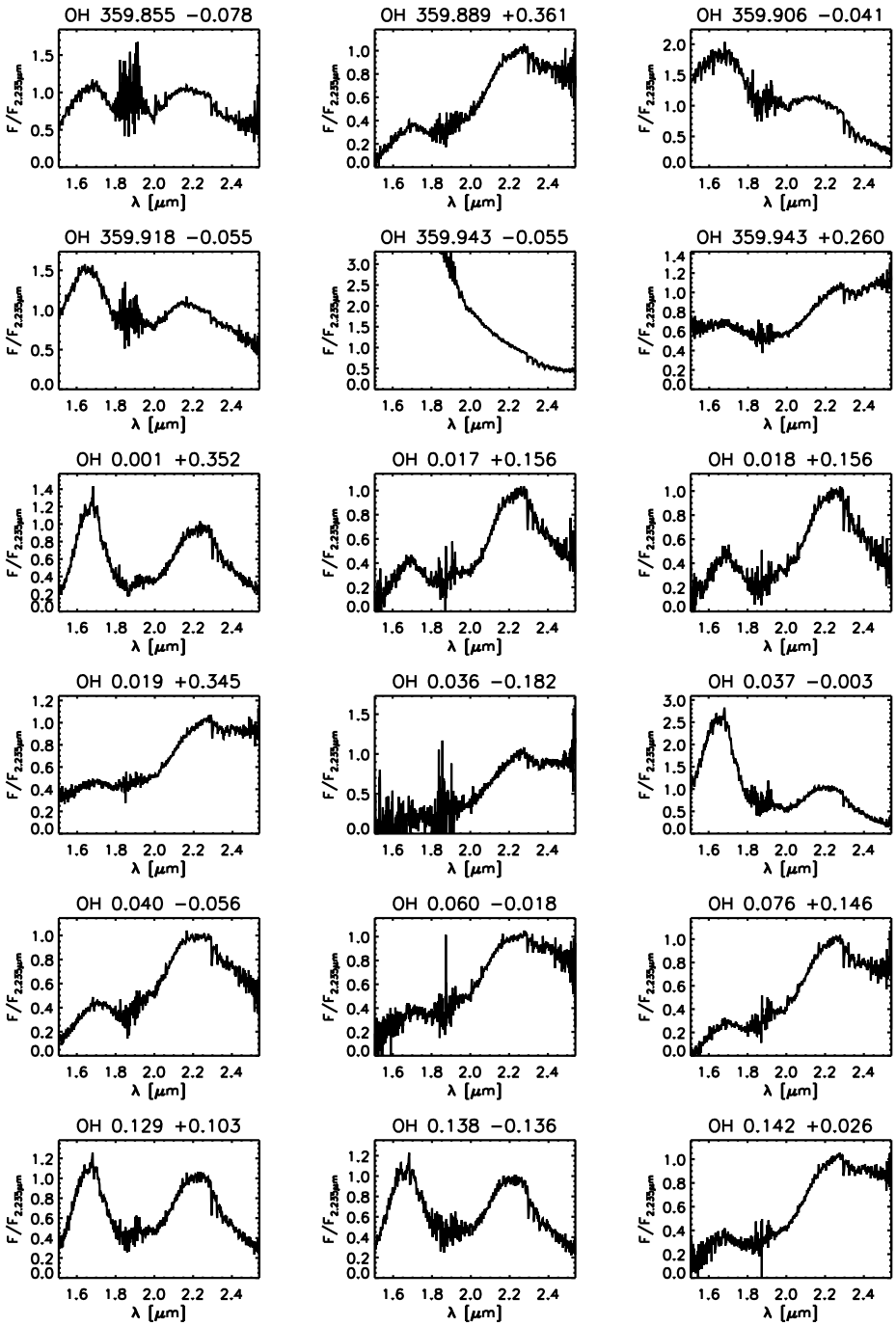

Figure 2.17: OH/IR stars - continued. OH 359.943-0.055 is possibly a mismatch.

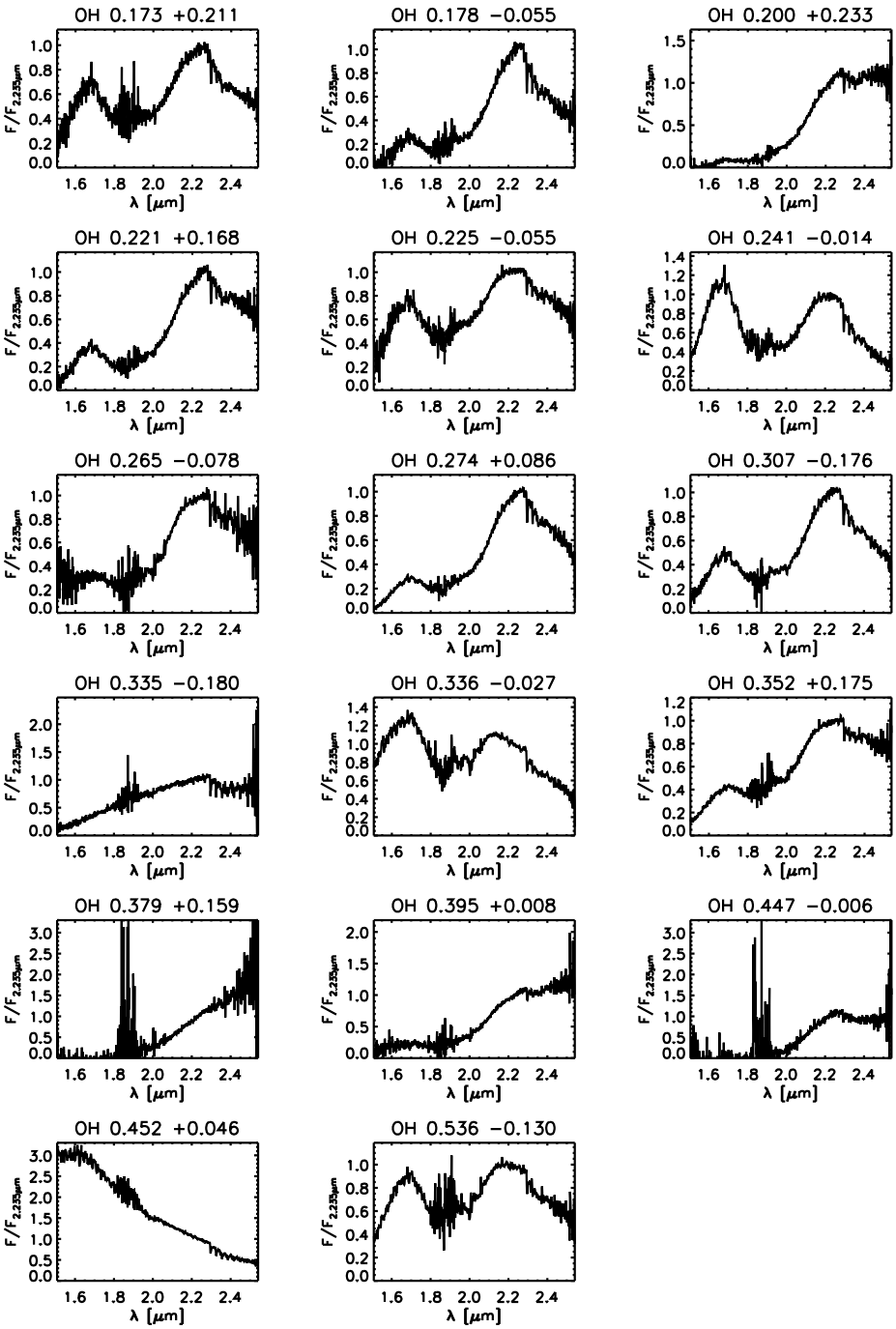

Figure 2.18: OH/IR stars - continued. OH 0.452+0.046 is possibly a mismatch.

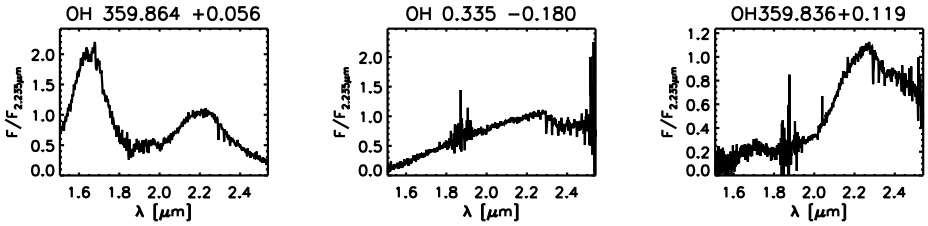

Figure 2.19: High-velocity OH/IR stars (van Langevelde et al. 1992).

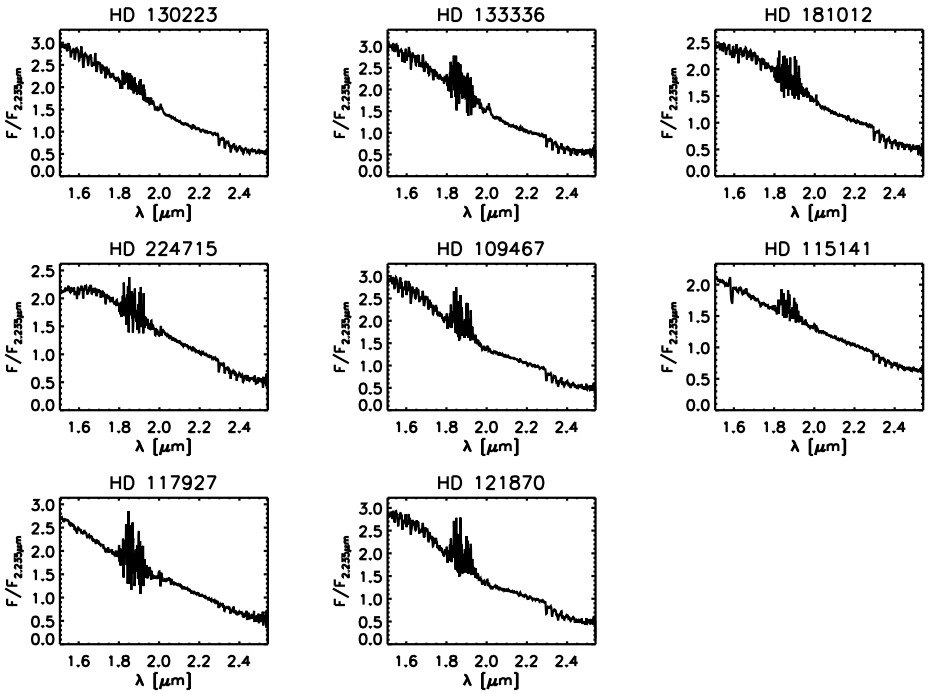

Figure 2.20: Stars in common with Ramírez et al. (1997).

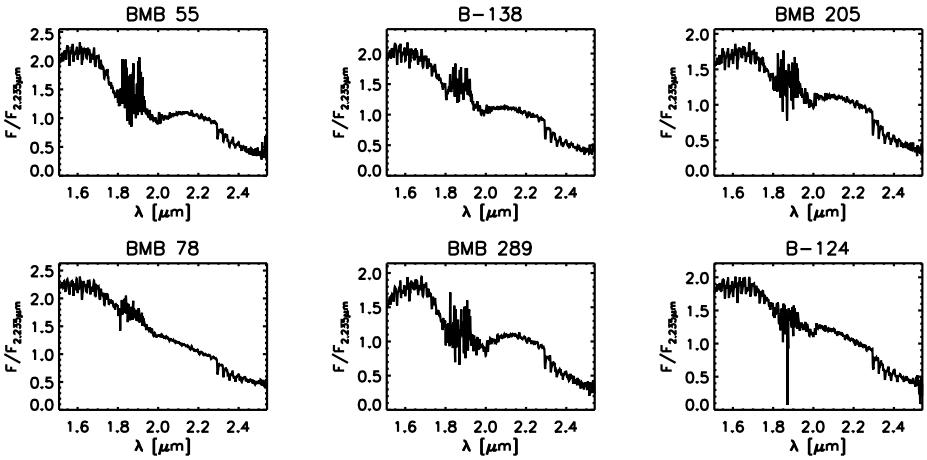

Figure 2.21: Stars in common with Ramírez et al. (2000).

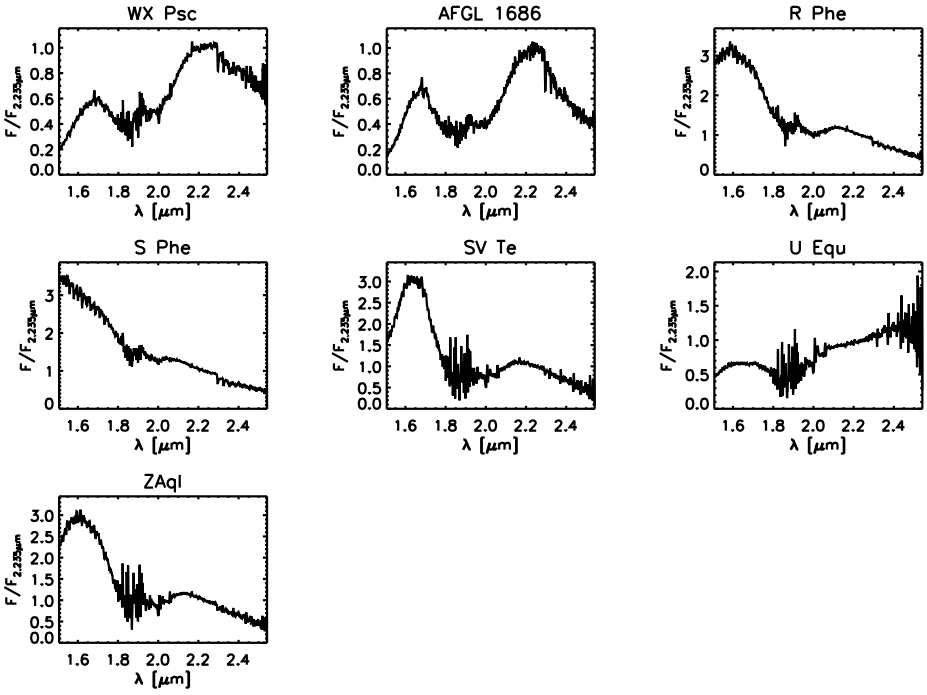

Figure 2.22: Stars in common with Lançon and Wood (2000).

CHAPTER 3

Spitzer-IRS observations of a sample of Galactic Bulge AGB stars

This chapter uses data gathered with the Spitzer Space Telescope in Cycle I, program 3167: "The dust sequence along the AGB".
PI : J.A.D.L. Blommaert, Co-I's: J. Cami, M.A.T. Groenewegen, H.J. Habing, F. Markwick-Kemper, A. Omont, M. Schultheis, A.G.G.M. Tielens, E. Vanhollebeke, L.B.F.M. Waters, and P.R. Wood.

Low-mass stars are known to lose a significant amount of mass during the AGB phase. During this phase, the AGB stars create a circumstellar envelope (CSE), in which dust can be formed. The oxygen-rich dust condensation sequence as described in Section 1.2.4 has been proposed to explain the dust formation process around oxygen-rich AGB stars (see also Tielens 1990; Tielens et al. 1997). These condensation sequences are based on condensation sequences developed in thermodynamic equilibrium in order to explain the dust condensation in the solar neighbourhood (see e.g. Tielens et al. 1997; Speck et al. 2000, and references therein).

Since IRAS and ISO it became possible to study the dust around AGB stars in the infrared (IR) with satellites. Most studies which aim at evaluating the dust around oxygen-rich AGB stars, analysed AGB stars in the solar neighbourhood (see e.g. Cami 2002). These samples are inhomogeneous in terms of initial mass and also their current age on the AGB is unknown. These samples are therefore not ideal to evaluate the oxygen-rich dust condensation sequence. With the high sensitivity of Spitzer-IRS, it is now possible to obtain good quality IR spectroscopic observations of AGB stars located further away. Using Spitzer-IRS it is therefore easier to create a homogeneous sample. Lebzelter et al. (2006) obtained Spitzer-IRS observations of AGB stars in 47 Tuc to study the oxygen-rich dust condensation sequence. AGB stars in such a globular cluster are believed to originate from the same population. Such

samples are therefore homogeneous in terms of initial masses and age. Also AGB stars in the Galactic Bulge (GB) are believed to originate from the same population (Groenewegen and Blommaert 2005; Blommaert et al. 2006). Moreover for many AGB stars in the GB, an estimate of the mass-loss rate is available. Based on the mass-loss rate, an idea on the current age of the object on the AGB can be obtained (see Section 1.2.5). Another advantage of studying AGB stars in the GB is the number of objects. There are much more AGB stars located in the GB than in e.g. a globular cluster such as 47 Tuc. Therefore a larger sample can be selected. The AGB stars in the GB are also located at about the same distance, which makes that one can directly compare the spectra.

In the following chapters (Chapters 3 to 6) we will study a sample of AGB stars selected in the GB to get a better understanding of the oxygen-rich dust condensation sequence along the AGB. This chapter will focus on the presentation and analysis of the observations obtained with the Spitzer Space Telescope.

3.1 Introduction to the Spitzer Space Telescope

The Spitzer Space Telescope (aka Spitzer or SST and formerly known as SIRTF - Space InfraRed Telescope Facility) is the fourth and final element in NASA's family of Great Observatories. The Spitzer Space Telescope, was launched on August 25th, 2003 from Cape Canaveral, Florida. A Delta 7920H rocket brought Spitzer in a earth-trailing heliocentric orbit. This kind of orbit has several advantages, e.g. it prolongates the cooled lifetime of Spitzer and the visibility is less constrained than it would have been, when an near-Earth orbit was chosen. Trailing the Earth in a heliocentric orbit, Spitzer drifts away from us at the rate of $\sim$ 0.12 AU/year. This drift will eventually cause needs for a different communication strategy. Another disadvantage comes from the lack of protection, Spitzer is outside the protection area of the Earth's magnetosphere, against solar proton storms and other Galactic cosmic ray flux.

The in-orbit check-out showed that the pointing performance of Spitzer is better than expected. The star tracker has proven to be very accurate, it can be used to directly point the telescope to better than 1". Once the telescope pointing has settled, it is stable to within 0.03" for times up to 600 s. Figure 3.1 shows the Operational Pointing Zone (OPZ). It is the area defined by two limiting hard pointing constraints: the angle between the boresight and the direction of the sun may never be less than 82.5° nor exceed 120°. Also bright objects, such as the Earth are avoided because they would degrade the quality of the observation due to direct exposure of stray light, but this is not a strict constraint.

Spitzer consists of five basic elements: the Cryogenic Telescope Assembly (CTA), the spacecraft and the three science instruments. The overall layout of the flight configuration is shown in Figure 3.2. The observatory is approximately 4.5 m high, has a diameter of 2.1 m, and a mass of $\sim$ 900 kg.

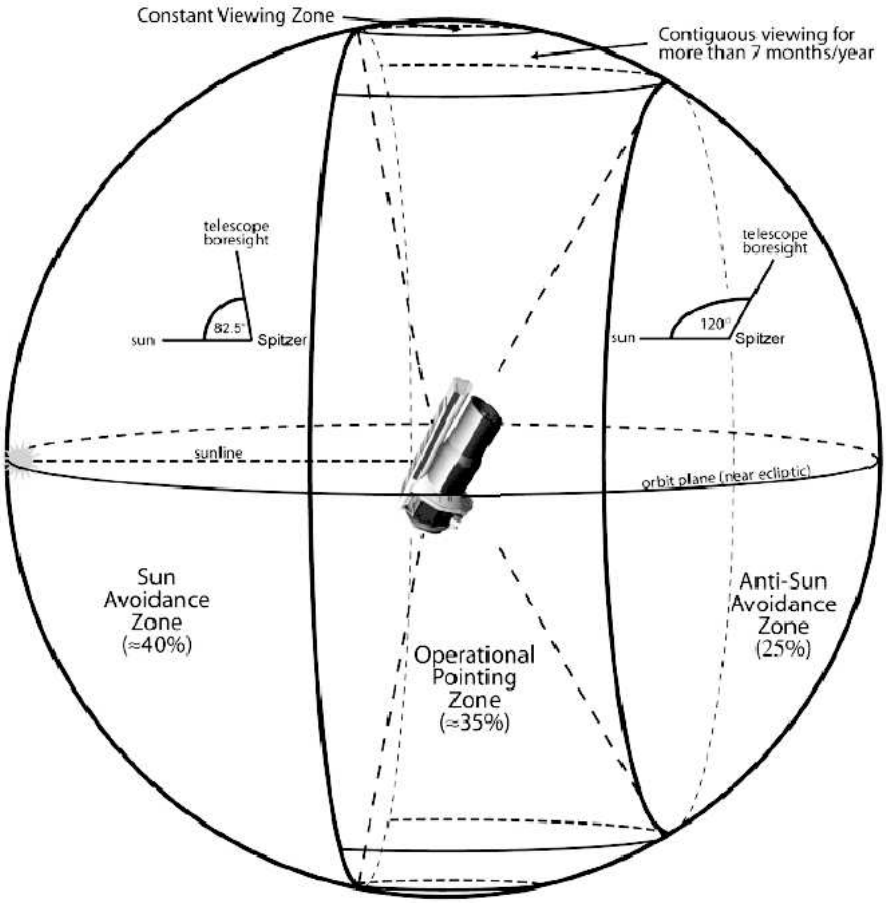

Figure 3.1: The main geometric observing constraints form an area called the Operational Pointing Zone (OPZ) (taken from the Spitzer Observer's Manual SOM, see also `http://ssc.spitzer.caltech.edu/documents/som/`).

3.1.1 Cryogenic Telescope Assembly

Spitzer's instruments are all observing in the IR. Therefore, they need to be cooled: the thermal emission from the optics needs to be negligible compared to the natural zodiacal background. All the parts that need to be cooled are gathered in the Cryogenic Telescope Assembly (CTA). The CTA is cooled by a combination of superfluid liquid helium, helium boil-off gas and radiative cooling. The helium bath temperature is kept at 1.24 K, the telescope temperature can be ≤ 6 K and the outer shell temperature is approximately 34 K. The missions minimum lifetime requirement was set at 2.7 yr. At this moment, the post launch lifetime is expected to be 5.3 yr and 4.0 yr in the "worst case scenario".

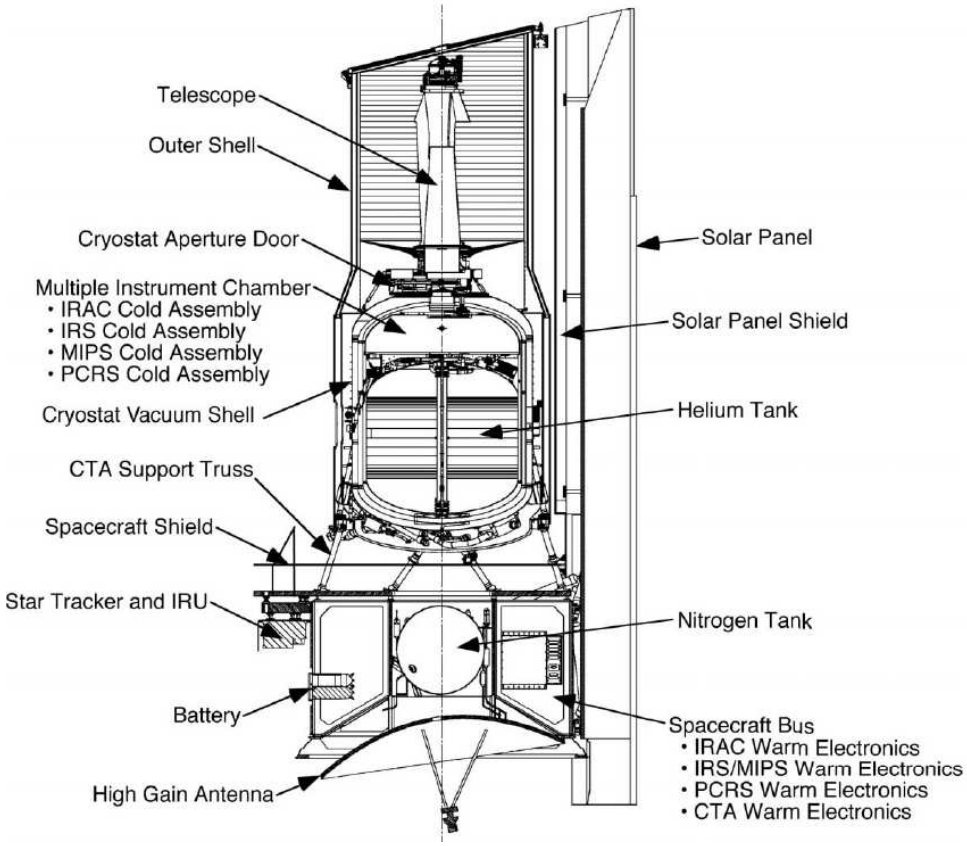

Figure 3.2: Cutaway view of the Spitzer flight hardware (taken from Werner et al. 2004).

Up until August 2003 all satellites that need to be cooled in space, encountered a *cool launch*, i.e. the telescope was already cooled prior to launch and had to be kept cool during the launch and in orbit. Keeping a satellite cool during launch requires huge amounts of cooling fluids: it is a commonly know fact that launching a Delta rocket coincides with loads of freed energy and thus heating. Spitzer, on the other hand, had a *warm launch*. The telescope was at ambient temperature at the time of launch and reached over 45 days after launch its lowest operating temperature. The warm launch was chosen over the cool launch, because in the warm launch scenario, the telescope is less heavy as less cooling fluids are needed.

3.1.2 The Spacecraft

The Spitzer spacecraft itself, handles all the basic operations: the observatory's power generation, pointing and momentum control, data processing and storage, and telecommunication functions. This part of Spitzer contains also the warm electronics of the scientific instruments.

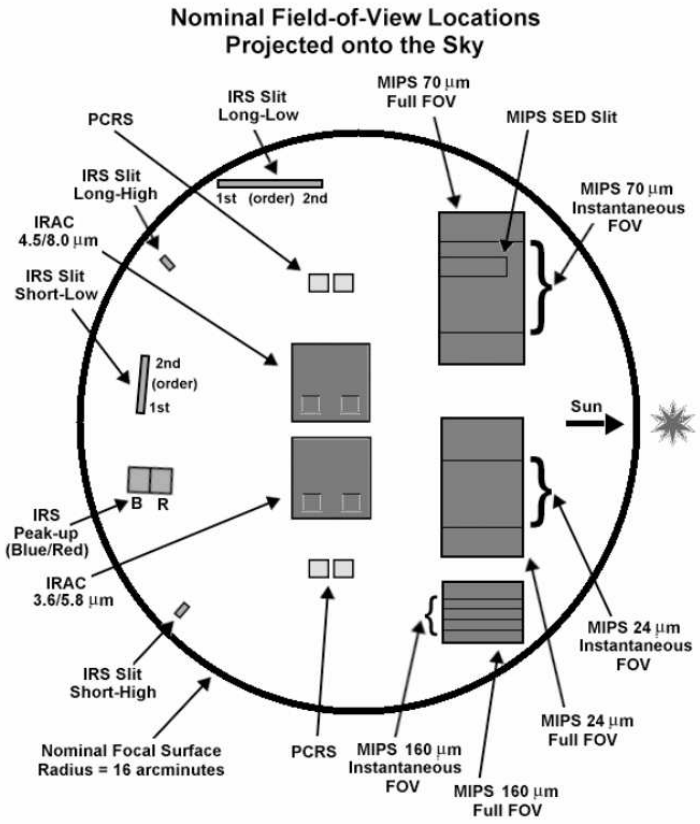

Figure 3.3: Spitzer focal plane layout as seen looking down from the telescope aperture. The +Z direction points towards the sun (taken from the SOM).

3.1.3 Instruments on board Spitzer

The Spitzer Space Telescope has three infrared instruments on board: the Infrared Array Camera (IRAC), the Infrared Spectrograph (IRS) and the Multiband Imaging Photometer for Spitzer (MIPS). Figure 3.3 shows the instrument payload. Not only the 3 instruments are shown, also the locations of the two pointing calibration reference sensor (PCRS) arrays and the two point sources that were used for ground-based focus checks and focal plane mapping. Spitzer can only use one instrument at the same time.

In this thesis we will only make use of observations obtained with the Infrared Spectrograph. Therefore only a short introduction to this instrument will be given. For more information about the other two instruments, we refer the interested reader to Werner et al. (2004) and the Spitzer web site: `http://ssc.spitzer.caltech.edu/`.

Table 3.1: Overview on the wavelength sensitivities of the different Spitzer-IRS arrays.

module	Wavelength range [μm]	Bonus order [μm]
SL2	5.2 – 7.7	7.3 – 7.7
SL1	7.4 – 14.5	
LL2	14.0 – 21.3	19.4 – 21.7
LL1	19.5 – 38.0	

Infrared Spectrograph – IRS

The infrared Spectrograph on board Spitzer provides the astronomical community with low and medium resolution spectroscopy. IRS is divided into four modules. The *Short-Low module* (SL) is sensitive in the wavelength range from 5.2 to 14.5 μm and has a resolution of $\sim$ 60 – 127. The *Short-High module* (SH) is the medium resolution counterpart of the SL module and has a wavelength range from 9.9 to 19.6 μm with a resolution of $\sim$ 600. The *Long-Low module* (LL) is sensitive to the longer wavelengths: 14.0 – 38.0 μm with a resolution of $\sim$ 57 – 126. The last module is the *Long-High module* (LH) which is sensitive in the wavelength range 18.7 – 37.2 μm and has a resolution of $\sim$ 600.

Concerning the SL and LL modules, each of this module is again divided into two sub-arrays. Table 3.1 gives an overview on the wavelength ranges. This table also shows that both SL2 and LL2 have a *bonus order*. This part of the array contains additional information in the wavelength range overlapping the two sub-arrays in each module. This bonus order is very useful when one needs to merge the different parts of the spectrum into one.

Apart from these 4 modules there are also two small imaging sub-arrays, the *peak-up arrays*, in the Short-Low (SL) module. These peak-up arrays allow objects to be placed accurately into any of the IRS entrance slits and can additionally provide images of sources for photometric or structural information. If the peak-up arrays cannot be used to aquire the star in the slit, one can also use the Pointing Calibration Reference Sensor (PCRS). In general the PCRS is used to periodically calibrate the telescope-to-star tracker. PCRS operates in the visual wavelength range (5050 – 5950 Å).

3.2 Scientific goal and sample selection

Over the past years several studies were performed to get a better understanding of the oxygen-rich dust condensation sequence. Especially after IRAS and ISO scientists were able to study the dust formation process around AGB stars in function of their mass-loss rate in the infrared. Among the major drawbacks of these studies are the inhomogeneous samples. Because of the inhomogeneities in the samples the age on the AGB is unknown as well as the initial mass of the star and no clear correlations could be found between the evolution on the AGB and the observed dust properties. Because of the high sensitivity of Spitzer-IRS with respect to IRAS and ISO, obtaining good quality infrared spectroscopy on AGB stars is

not restricted anymore to the solar neighbourhood or very bright objects located further away.

To overcome the problem of an inhomogeneous sample, AGB stars located in the GB and detected by the ISOGAL survey (Omont et al. 2003) can be used. ISOGAL, the second largest survey program performed with the ISO satellite (Kessler et al. 2003), is a detailed mid-infrared imaging survey of the inner galaxy (Omont et al. 2003). It provides a point source catalogue in 5 wavelength bands and includes near-infrared (I, J, and K_s DENIS observations, Epchtein et al. 1999), 7, and 15 μm photometry. This survey covered about 16 square degrees in the inner galaxy. About 10^5 sources were detected which are mostly AGB stars, red giants and Young Stellar Objects (YSOs). The survey is complete for sources which are brighter than 9 magnitudes at 7 μm and 8 magnitudes at 15 μm (Omont et al. 1999).

Ojha et al. (2003) studied the ISOGAL sources in the "intermediate" galactic bulge ($|\ell| < 2^\circ$ and $|b| \sim 1^\circ - 4^\circ$). They combined the ISOGAL-DENIS Point Source Catalogue with 2MASS J, H, and K_S-photometry and MSX (mid-IR) in order to determine the nature of the point sources. They conclude that almost all ISOGAL sources detected both at 7 and 15 μm on the line of sight of the bulge are AGB stars or stars at the tip of the RGB. Prior to ISOGAL, it was already known that the $(K - [12])_0$ colour, with [12] the IRAS flux at 12 μm, is a good mass-loss indicator (Ojha et al. 2003, and references therein). Ojha et al. (2003) showed that also $(K_s - [15])_0$ correlates with the mass-loss rate $\dot{M}$, nevertheless with a slightly different calibration than if one uses $(K - [12])_0$. Also Blommaert et al. (2006) confirm the use of this colour as a mass-loss indicator by analysing mid-IR (ISOCAM-CVF) spectra of a sample of GB AGB stars.

Stars in these "intermediate" GB fields are also believed to belong to the bulge stellar population which only shows a small range in masses. These giants have evolved from a population of stars of about 1.5 $-$ 2 $M_\odot$ (Groenewegen and Blommaert 2005; Blommaert et al. 2006). As $(K_s - [15])_0$ can be used as a mass-loss indicator and since the ISOGAL sample is complete in terms of magnitudes (to 8 mag at 15 μm), the ISOGAL sample is also complete for the lowest mass-loss rates (about 10^{-8} $M_\odot$ yr^{-1}, Blommaert et al. 2006). Therefore, AGB stars from the GB which are detected in the ISOGAL sample cover the full range of mass-loss rates, starting from the onset of (dust) mass-loss up to the mass-loss rates of 10^{-4} $M_\odot$/yr associated with the so-called superwind phase in OH/IR type AGB stars.

In Chapter 7 we study the stellar populations in the GB using a galaxy model. In this study, no intermediate age population could be revealed. This does not immediately prove that there is no such population: the method described in Chapter 7, using 2MASS and OGLE data, is unable to reveal this population. Therefore we will continue this work under the assumption (based on Groenewegen and Blommaert 2005) that the selected AGB stars originate from an intermediate age population and form a homogeneous sample.

With all the stars in these "intermediate" bulge fields originating from about 1.5 $M_\odot$ stars, the main difference between these objects is their age on the AGB. A Colour-Magnitude Diagram (CMD) for these stars, as the one presented in Figure 3.4, effectively corresponds to the evolutionary track on the AGB for a 1.5 $M_\odot$ star, characterised by varying luminosities and mass-loss rates. These fields therefore offer unique opportunities to study the evolution

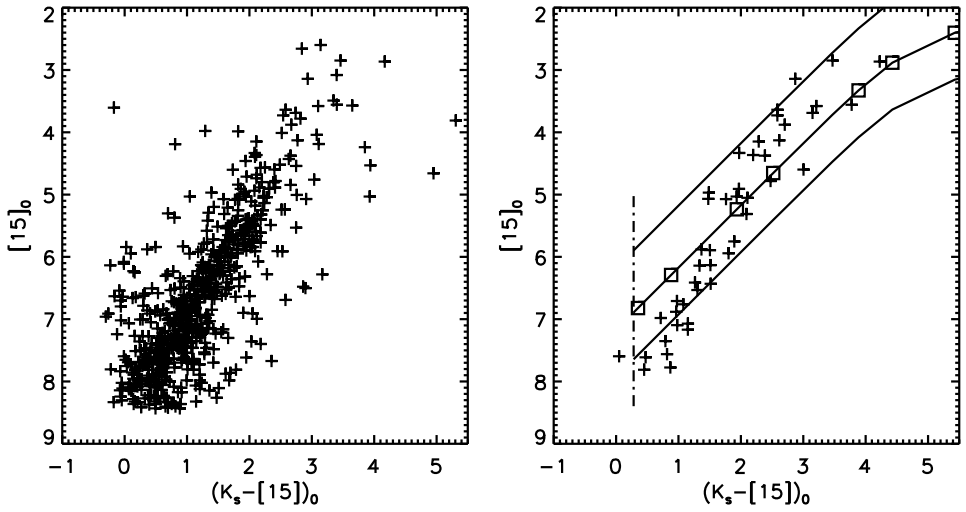

Figure 3.4: $[15]_0/(K_s - [15])_0$ colour-magnitude diagrams. The left figure shows all sources detected in our selected ISOGAL fields (see also Figure 3.5). A linear sequence of increasing redder colours (and thus mass-loss rates) for brighter 15 μm fluxes can be seen. The right figure shows the sources we have selected for this project, illustrating the fact that we have a representative sample which covers the sequence of increasing mass-loss rate. The overplotted curves represent 2 000, 4 000, and 10 000 $L_\odot$ giant tracks with increasing mass-loss rate (using a mixture of amorphous silicate and aluminum oxide dust, Blommaert et al. 2006). The mass-loss rates range from 10^{-9} to $3{\times}10^{-6}$ $M_\odot$ / yr. The squares on the 4000 $L_\odot$ track indicate the following mass-loss rates: 10^{-9}, 10^{-8}, 5×10^{-8}, 10^{-7}, 5×10^{-7}, 10^{-6} and 3×10^{-6} $M_\odot$ / yr. The dot-dashed line represents a track of increasing luminosity without mass-loss. The selected OH/IR stars have no corresponding 2MASS counterparts and are therefore not shown in this CMD.

of 1.5 $M_\odot$ stars and their circumstellar material as they evolve on the AGB. For all the above mentioned reasons, AGB stars in the GB detected with ISOGAL are ideal to create a homogeneous sample in order to study the oxygen-rich dust condensation sequence along the AGB.

The left panel in Figure 3.4 shows a $(K_s - [15])_0$ versus $[15]_0$ CMD for all the objects in the selected ISOGAL fields (c32, c35, ogle, NGC 6522, see Figure 3.5). ISO/SWS studies of nearby AGB stars have revealed the presence of at least 5 distinct components in the wavelength range 8 – 27 μm, and several more features at wavelengths longer than 30 μm (for an overview see Blommaert et al. 2005). Judging from the variations in the dust composition of these spectra and their range in mass-loss rates, we selected $\sim$ 15 sources per logarithmic bin in mass-loss rate (using $(K_s - [15])_0$ as a mass-loss rate indicator) to fully sample the dust variations in a statistically significant way. We included sources with $(K_s - [15])_0$ values close to zero to ensure that we can trace the dust at the onset of mass-loss. From the Bulge fields in the ISOGAL sample, we selected 47 sources. We also included OH/IR stars, which

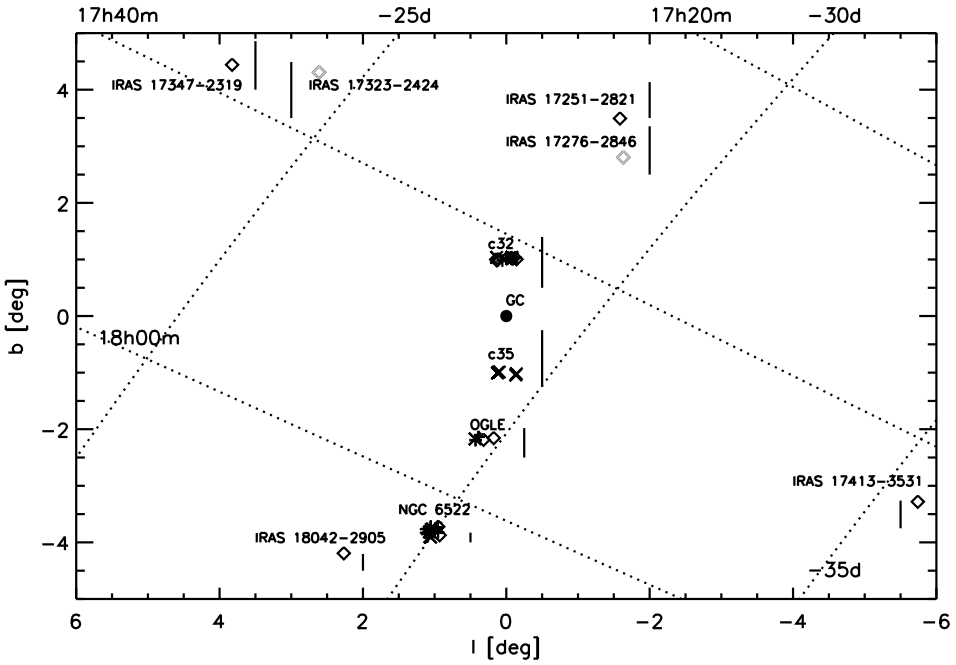

Figure 3.5: Position of the objects in the sample with respect to the GC. The dotted lines indicate different Ra and Dec values. The diamonds are Mira variables, the crosses are semi-regular variables and the plus-signs are small-amplitude variables (as defined later in Chapter 4). The name of the fields c32, c35, OGLE, and NGC 6522 refer to the fields in the ISOGAL survey from which most of the objects were selected (see also Blommaert et al. 2006). The length of the vertical lines close to each (group of) object(s) indicates the relative extinction values.

represent the highest mass-loss rates on the AGB. As the superwind phase is extremely short (less than 10 000 years) OH/IR stars are rare in the ISOGAL bulge sample and we therefore have included 6 IRAS detected OH/IR stars to enlarge our sample on the high mass-loss rate end. These objects were selected from the same latitude range as our ISOGAL sources and have similar luminosities as our Mira sources and are thus expected to belong to the same population. Hence, we cover ~ 4 orders of magnitude in mass-loss rate (10^{-8} – 10^{-4} $M_{\odot}$/yr) and have a final sample of 53 sources. The resulting list of selected sources is presented in Table 3.2. The sources are also shown in the right panel of Figure 3.4. Figure 3.5 shows how these sources are distributed with respect to the GC.

Table 3.2: Observed bulge stars with ISOGAL or IRAS name. The [7] and [15] magnitudes are taken from the ISOGAL catalogue and have uncertainties of typically 0.15 mag (Schuller et al. 2003). The 2MASS J, H and K_s magnitudes have uncertainties in the order of 0.03 mag, also included is the Spitzer-IRS observing date. In the two last column we give A_K values derived for each object and the reference (see Section 3.4).
S99: Schultheis et al. (1999), S04: Sumi (2004), M06: Marshall et al. (2006).

Number	Star	Ra [J2000]	Dec [J2000]	J [mag]	H [mag]	K_s [mag]	[7] [mag]	[15] [mag]	Observation date	A_K [mag]	Ref
1	IRAS 17251-2821	17:28:18.50	-28:23:55.8						21/03/2005	0.368	M06
2	IRAS 17276-2846	17:30:48.31	-28:49:01.9						24/04/2003	0.495	M06
3	IRAS 17323-2424	17:35:26.00	-24:26:32.0						15/04/2005	0.574	M06
4	IRAS 17347-2319	17:37:46.28	-23:20:52.8						24/04/2003	0.498	M06
5	J174117.5-282957	17:41:17.50	-28:29:57.5	9.702	7.872	6.996	5.36	4.42	20/04/2005	0.571	S99
6	J174122.7-283146	17:41:22.70	-28:31:47.0				3.47	1.54	20/04/2005	0.602	S99
7	J174123.6-282723	17:41:23.56	-28:27:24.2	10.715	8.993	8.245	7.57	6.98	20/04/2005	0.518	S99
8	J174126.6-282702	17:41:26.60	-28:27:02.2	11.557	9.285	7.895	5.44	3.83	20/04/2005	0.518	S99
9	J174127.3-282851	17:41:27.26	-28:28:52.1	10.008	8.306	7.304	5.78	4.40	20/04/2005	0.507	S99
10	J174127.9-282816	17:41:27.88	-28:28:17.1	9.569	7.828	7.016	6.30	5.24	20/04/2005	0.507	S99
11	J174128.5-282733	17:41:28.51	-28:27:33.8	9.580	7.968	7.107	6.41	5.34	20/04/2005	0.507	S99
12	J174130.2-282801	17:41:30.15	-28:28:01.3	11.353	9.662	8.880	7.77	7.44	20/04/2005	0.507	S99
13	J174134.6-282431	17:41:34.60	-28:24:31.4	10.902	9.137	8.163	5.97	4.87	20/04/2005	0.507	S99
14	J174139.5-282428	17:41:39.48	-28:24:28.2	9.528	7.801	6.874	5.34	4.00	20/04/2005	0.507	S99
15	J174140.0-282521	17:41:39.94	-28:25:21.2	9.630	7.977	7.143	6.09	4.15	20/04/2005	0.497	S99
16	J174155.3-281638	17:41:55.27	-28:16:38.7	9.610	7.739	6.785	5.61	3.91	20/04/2005	0.528	S99
17	J174157.6-282237	17:41:57.53	-28:22:37.7	9.852	8.272	7.438	6.74	5.18	20/04/2005	0.476	S99
18	J174158.8-281849	17:41:58.73	-28:18:49.2	10.160	8.415	7.348	5.57	3.85	20/04/2005	0.507	S99
19	J174203.7-281729	17:42:03.69	-28:17:29.9	10.262	8.501	7.398	5.38	3.96	20/04/2005	0.518	S99
20	J174206.9-281832	17:42:06.86	-28:18:32.4	9.641	7.893	6.878	4.82	3.12	20/04/2005	0.550	S99
21	IRAS 17413-3531	17:44:43.45	-35:32:34.3						27/03/2004	0.283	M06
22	J174917.0-293502	17:49:16.96	-29:35:02.7	10.869	9.157	8.199	7.40	6.49	20/04/2005	0.602	S99
23	J174924.1-293522	17:49:23.99	-29:35:22.2	10.466	9.030	8.417	7.55	7.33	20/04/2005	0.539	S99
24	J174943.7-292154	17:49:43.65	-29:21:54.5	10.810	8.889	7.970	6.97	6.23	20/04/2005	0.624	S99
25	J174948.1-292104	17:49:48.05	-29:21:04.8	11.401	9.520	8.560	7.75	7.11	20/04/2005	0.550	S99
26	J174951.7-292108	17:49:51.65	-29:21:08.7	10.829	9.043	8.116	7.39	6.24	20/04/2005	0.581	S99

Table 3.2: continued.

Number	Star	Ra [J2000]	Dec [J2000]	J [mag]	H [mag]	K_s [mag]	[7] [mag]	[15] [mag]	Observation date	A_K [mag]	Ref
27	J175432.0-295326	17:54:31.94	-29:53:26.5	8.906	7.623	6.957	6.00	4.49	20/04/2005	0.302	S04
28	J175456.8-294157	17:54:56.80	-29:41:57.4	8.827	7.438	6.757	5.81	4.48	20/04/2005	0.302	S04
29	J175459.0-294701	17:54:58.98	-29:47:01.4	10.422	8.530	7.287	4.88	2.98	20/04/2005	0.302	S04
30	J175511.9-294027	17:55:11.90	-29:40:27.8	10.422	9.254	8.841	8.17	7.89	20/04/2005	0.302	S04
31	J175515.4-294122	17:55:15.41	-29:41:22.8	10.005	8.770	8.271	7.79	7.21	20/04/2005	0.302	S04
32	J175517.0-294131	17:55:16.97	-29:41:31.9	9.371	8.339	7.839	7.65	7.71	20/04/2005	0.302	S04
33	J175521.7-293912	17:55:21.70	-29:39:13.0				8.56		20/04/2005	0.302	S04
34	J180234.8-295958	18:02:34.78	-29:59:58.9	8.177	6.894	6.146	4.66	3.22	15/04/2005	0.127	S99
35	J180238.8-295954	18:02:38.72	-29:59:54.6	9.411	8.327	7.780	7.31	5.83	15/04/2005	0.111	S99
36	J180248.9-295430	18:02:48.90	-29:54:31.0	9.574	8.485	7.969	7.62	6.61	07/09/2005	0.155	S99
37	J180249.5-295853	18:02:49.44	-29:58:53.4	9.932	8.953	8.512	8.15	7.64	07/09/2005	0.180	S99
38	J180259.6-300254	18:02:59.51	-30:02:54.3	9.070	7.880	7.391	6.79	4.86	15/04/2005	0.106	S99
39	J180301.6-300001	18:03:01.60	-30:00:01.1	9.773	8.661	8.219	7.94	7.69	07/09/2005	0.106	S99
40	J180304.8-295258	18:03:04.80	-29:52:59.3	9.888	8.792	8.395	8.02	7.89	07/09/2005	0.063	S99
41	J180305.3-295515	18:03:05.25	-29:55:15.9	8.714	7.620	7.098	6.49	5.11	15/04/2005	0.090	S99
42	J180305.4-295527	18:03:05.33	-29:55:27.8	9.293	8.243	7.810	7.54	6.49	07/09/2005	0.090	S99
43	J180308.2-295747	18:03:08.11	-29:57:48.0	9.470	8.360	7.777	7.16	6.21	07/09/2005	0.106	S99
44	J180308.6-300526	18:03:08.52	-30:05:26.5	8.077	7.064	6.437	5.85	4.41	15/04/2005	0.095	S99
45	J180308.7-295220	18:03:08.69	-29:52:20.4	9.492	8.417	7.878	7.40	6.02	15/04/2005	0.063	S99
46	J180311.5-295747	18:03:11.47	-29:57:47.2	9.353	8.200	7.535	6.53	5.39	15/04/2005	0.106	S99
47	J180313.9-295621	18:03:13.88	-29:56:20.9	9.407	8.398	7.978	7.70	6.96	07/09/2005	0.085	S99
48	J180316.1-295538	18:03:15.99	-29:55:38.3	9.752	8.744	8.276	7.90	7.43	07/09/2005	0.063	S99
49	J180323.9-295410	18:03:23.84	-29:54:10.7	9.536	8.543	8.082	7.59	6.51	07/09/2005	0.063	S99
50	J180328.4-295545	18:03:28.36	-29:55:45.4	8.999	7.879	7.291	6.74	5.13	15/04/2005	0.085	S99
51	J180333.3-295911	18:03:33.26	-29:59:11.5	9.832	8.795	8.357	8.06	7.15	07/09/2005	0.106	S99
52	J180334.1-295958	18:03:34.07	-29:59:58.8	8.658	7.520	6.967	6.50	5.15	15/04/2005	0.099	S99
53	IRAS 18042-2905	18:07:24.40	-29:04:48.0						20/04/2005	0.172	M06

3.3 Observations and data reduction

3.3.1 Observations

The observations of our sample were obtained using the Spitzer Space Telescope's (SST) InfraRed Spectrograph (IRS) (Houck et al. 2004). They were part of a GO-1 (General Observers) proposal and were performed in April and September 2005 (see also Table 3.2). Three stars of our selected sample appeared to be in the ROC database (Reserved Observations Catalogue) and were observed in 2003/2004 as part of a DDT (Director's Discretionary Time) program, principal investigator (PI) was F. Markwick-Kemper (see Table 3.2).

The targets were observed with Spitzer-IRS in low resolution mode over the entire wavelength range (5.2 – 38.0 μm). The resolution for the short wavelength range (SL mode: 5.2 –14.5 μm) and long wavelength range (LL mode: 14.0 – 38.0 μm) ranges between 60 – 125. For each target, we selected 3 observing cycles in each module in order to have a more reliable background subtraction and cosmic ray hit removal (see next section).

3.3.2 Data reduction

The data reduction has been started on the pipeline level of Basic Calibrated Data (BCD) S12.4.0. Detailed information about the processes performed in the pipeline can be found in the IRS Data Handbook (2006) and the Spitzer Space Telescope Observer's Manual (SOM 2005). The additional reduction steps have been performed using SMART (Spectroscopic Modelling Analysis and Reduction Tool, Higdon et al. 2004) unless mentioned otherwise.

The GB is a very crowded region with a highly structured and varying background, especially at lower latitudes ($|b| \lesssim 3^\circ$). This can cause problems when one wants to locate a target. Because of the high background levels, the peak-up for most of our targets has been done using the Pointing Control Reference Sensor (PCRS) in stead of the recommended IRS peak up (for field NGC 6522 and the OH/IR stars selected from the ISOGAL catalogue the IRS peak up could be used). Using the reconstructed pointing keywords in the BCD fits headers, we visualised the field of view at the time the observations were made in order to make sure that the slit was positioned correctly with respect to the target. This showed that the pointing was successful for all observations.

Figure 3.6 shows an IRAC 8 μm-band image for J174117.5-282957 taken from the GLIMPSE-II survey (a legacy program with the Spitzer Space Telescope, using the IRAC instrument, see Benjamin et al. 2003). The star itself is located at the top of the figure inside the thick red square. The rectangles also shown in this figure are the different slits overlaid for this object. The smallest ones are from the SL module and the largest ones are the LL module. The yellow rectangles are order 2 (SL2 and LL2) and the red rectangles are order 1 (SL1 and LL1). Not only does this figure illustrate the successful pointing for this object, but it also gives a hint on the crowdedness in these spatial regions. Especially for the LL module, the probability to observe additional stars is very large.

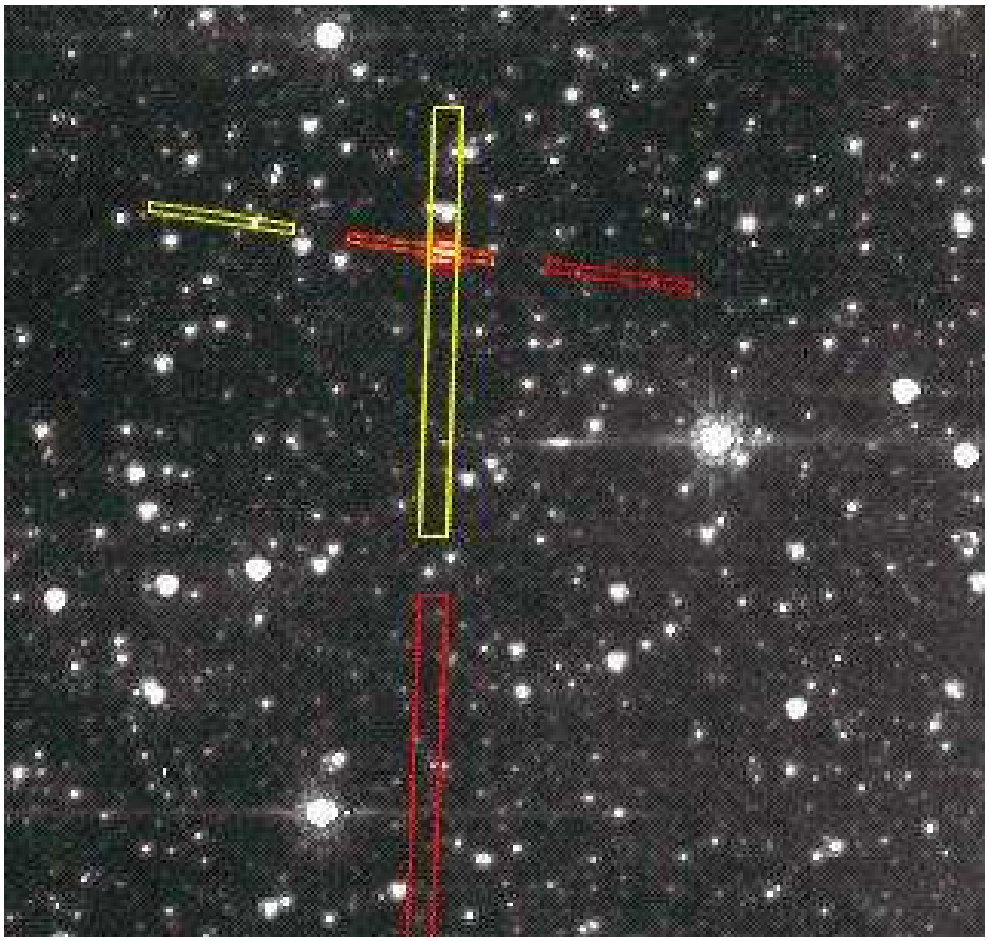

Figure 3.6: IRAC 8 μm-band image for J174117.5-282957 (inside the thick red square) from the GLIMPSE-II survey (Benjamin et al. 2003). Overlaid are the different slit positions for the two nods for the SL module (thin rectangles) and the first nod for the LL module (largest rectangles). The red rectangles originate from the 1st orders (SL1 and LL1) and the yellow rectangles from the 2nd order SL2 and LL2).

When observations are made with Spitzer-IRS, the object is always observed twice within one cycle (the amount of cycles is chosen by the observer). In the short time span between the two observations within one cycle, Spitzer nods and therefore the second observation gives the object in a different position on the slit. Infrared observers typically use these nods to correct for the background.
If Spitzer-IRS is used with the low resolution modules, there is also another possibility to correct for the background. In Section 3.1.3 the layout of Spitzer-IRS has been explained. The instrument has four modules of which we only used two: the short and long low resolution modules (SL and LL modules). Each of these two low resolution modules can be split

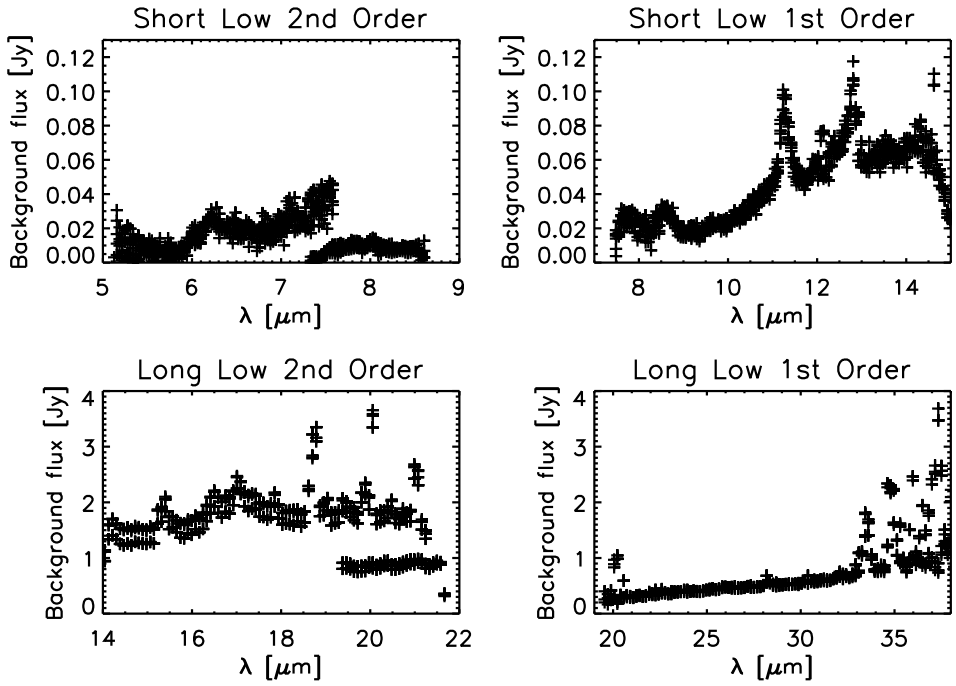

Figure 3.7: Background fluxes for the different nods and cycles used to correct J174127.9-282816 for the background. The jumps seen in the 2nd order of SL and LL module originate from the S12.0.4 pipeline calibration and are in the objects corrected for using standard star observations.

into two sub-arrays or orders: the first and the second order. When observations are made with one of these low resolution modules e.g. in the second order, the first order of the same module also gathers light because Spitzer has no shutters. The light detected in the first order when observing in the second order comes from the vicinity of the object. This additional light gathered in the first order, can then be used to background subtract observations made in the first order. This is also true the other way around: if one observes a target with the first order, the second order also gathers light from the vicinity of the object, which can then be used to background subtract observations made with the second order.
Since the background in the GB can vary significantly within a very small area, the first option using the different nod positions is to be preferred over the second one: the background spectrum obtained in the first method is closer to the target itself and therefore more reliable. We always applied the first method unless it was not possible because of crowding, in that case we applied the second method (see Section 3.3.3 for an discussion on the background residuals in the spectra).

Figure 3.7 shows the typical shape of the background fluxes. The upper two panels illustrate the background levels for the two orders in the SL module, the bottom two panels

for the two orders in the LL module. The most pronounced features seen in the background are polycyclic aromatic hydrocarbon (PAH) features and can be seen around 6.2, 7.7, 8.6, 11.3, and 12.7 μm (Peeters et al. 2004). Besides these well-known features, Van Kerckhoven et al. (2000) identified an additional emission plateau between 15 and 20 μm originating from PAH molecules using ISO-SWS data of a sample of compact H II regions, YSOs, and evolved stars. They show that although the overall shape of this plateau is very similar in all sources, the detailed profiles vary from source to source.
Figure 3.7 also shows that there is a fairly large spread in the background flux at each wavelength, indicative of small-scale variations in the shape and intensity of the background. This is more pronounced in the LL module observations than the SL observations. The consequences of these variations for the data reduction process will be discussed at great length in Section 3.3.3. Finally, note that the flux values in Figure 3.7 should not be taken at face value when comparing SL and LL observations since both slits have different widths.

The next step in the data reduction process is cleaning the images for bad pixels. This has been done using the IDL routine "irsclean_mask". Bad pixels were defined by the bad pixel mask that comes with the BCD data, the rogue masks for each campaign, and the interactive routine within "irsclean_mask" to search for additional bad pixels. For all observations within one cycle, the same bad pixel mask was used.

The spectra were extracted using the column extraction method in the SMART package. At this stage all parts of the spectra obtained with the LL module, were also corrected for fringes using IRSFRINGE. After the extraction, the different nods and cycles were combined into one spectrum for each module using 3-σ clipping. In this way cosmic ray hits that were not corrected for using the "irsclean_mask" routine, were left out of the spectrum. Also concerning background residuals, this method improves the spectrum at longer wavelengths.

All the reduction steps described above were also performed on 3 standard stars: HR 6348, HD173511, and HD166780 which were then used to flux calibrate the spectra. For most of the stars, this resulted in spectra for each order and module that continuously overlapped. For stars with a less reliable background subtraction, the different modules show rather big discontinuities. The two orders in the SL module overlapped nicely, therefore the orders of the LL module were multiplied with a constant to form a continuous spectrum with the SL orders.

3.3.3 Remaining artifacts

Figure 3.7 already illustrated the variation in the background levels that can be found, Figure 3.8 shows this in more detail for J174951.7-292108 in the second order of the LL module. This figure shows two background regions across the slit, parallel to the object in the slit. Black is the pixel row 7 pixels left of the object, grey the pixel row 18 pixels to the right of the target. One pixel in the LL module is about 5.1" (one pixel in the SL module is about 1.8"). These regions give an idea on the varying background levels in function of the distance to the object. This figure clearly illustrates that although all features are present at the different positions across the slit, the intensities can vary significantly (to about 20% in the S III line at 18.7 μm and 10% in the PAH features around 17 μm).

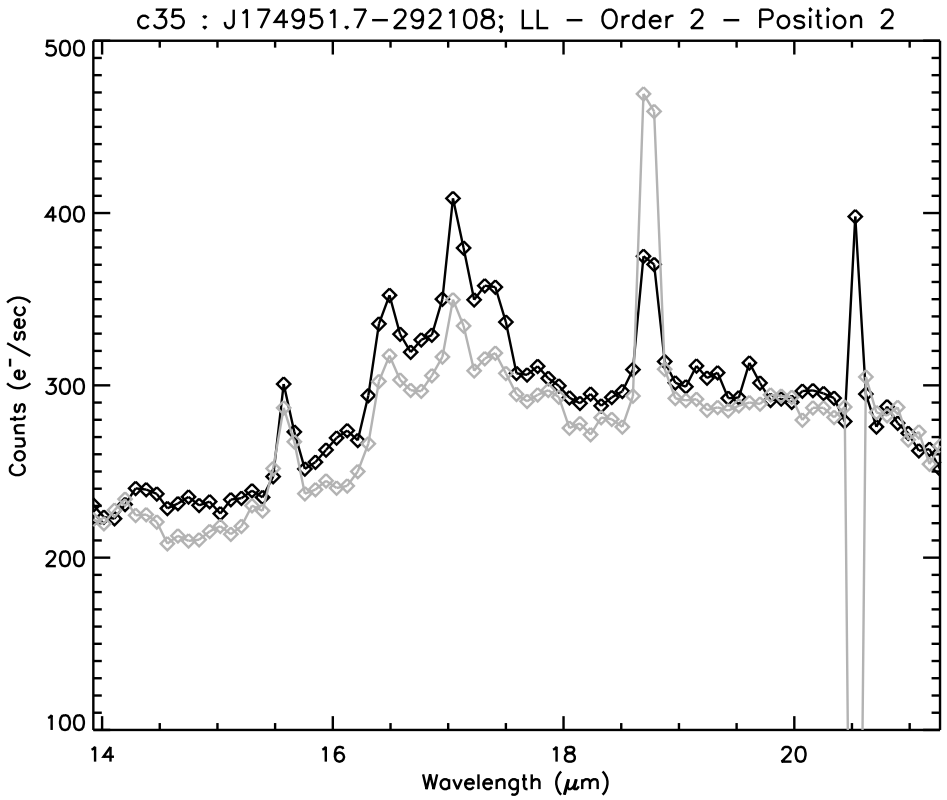

Figure 3.8: Variation in the background. The two lines represent a pixel row parallel to the object. Black: 7 pixels to the left of the object, grey: 18 pixels to the right of the object.

The background emission is very strong in the longer wavelength region and also increases with wavelength. For most of the objects the background emission at these longest wavelengths is equally strong or even stronger than the flux of the object itself. Especially for these objects, uncertainties of 10 to 20% in the background levels result in much larger uncertainties in the final dust spectra. Figure 3.9 shows the difference in the obtained spectrum that can occur due to the variation in the background. The black line shows the spectrum when using the background shown in Figure 3.8 as the black line, the grey line shows the spectrum obtained when using the background shown as the grey line in Figure 3.8. The differences between the two obtained spectra in Figure 3.9 can be understood based on the differences seen for the two background regions shown in Figure 3.8.

Figures 3.15 to 3.17 show the spectra after extinction correction (see Section 3.4). Inspection of these spectra, reveals that there still remain some difficulties with the data. First, we still see some residual effects of the non-perfect background subtraction in our spectra. Since the background emission increases with wavelength, the effect of background residuals are

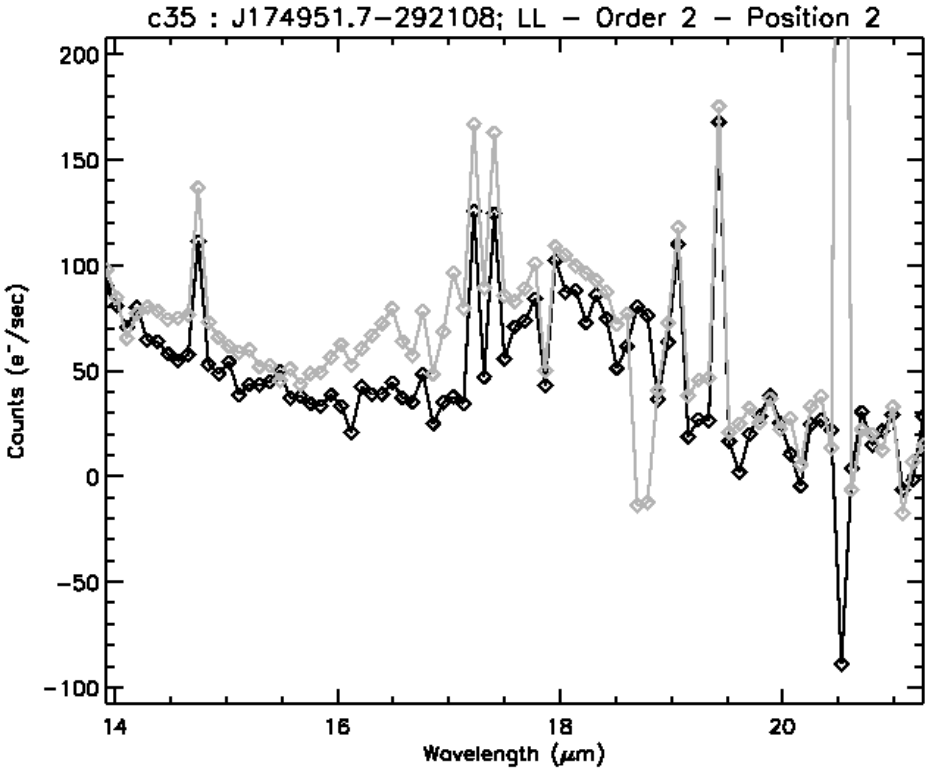

Figure 3.9: Variation in the obtained spectrum due to using the two different background regions shown in Figure 3.8. The spectrum in black is created using the background 7 pixels to the left of the object, the grey line shows the spectrum created using the background 18 pixels to the right of the object.

larger at longer wavelengths. For the stars with number 7, 10, 11, 12, 13, 14, 21, 22, 23, 24, 25, 26, 35, 36, 43, or 49 we expect larger residuals from the background subtraction as we had to use the second method, using the different order, for the background subtraction (see e.g. the bump around 17 μm in star number 12 in Figure 3.15). Especially J174948.1-292104 (number 25) had severe residuals in the longer wavelength regions due to the background extraction, and therefore the longer wavelengths are neglected for this object in any further analysis. The very pronounced features at 18.7 μm and 33.5 μm, seen in some spectra, are artifacts caused by a forbidden line from SIII, also the feature at 34.8 μm is linked with a forbidden line from SIII and originates from the non-perfect background subtraction.

Also for J175511.9-294027 (number 30) the longer wavelength region is not shown in Figure 3.15. This star was too weak to enable us to recover any useful information from the Spitzer-IRS LL band images.

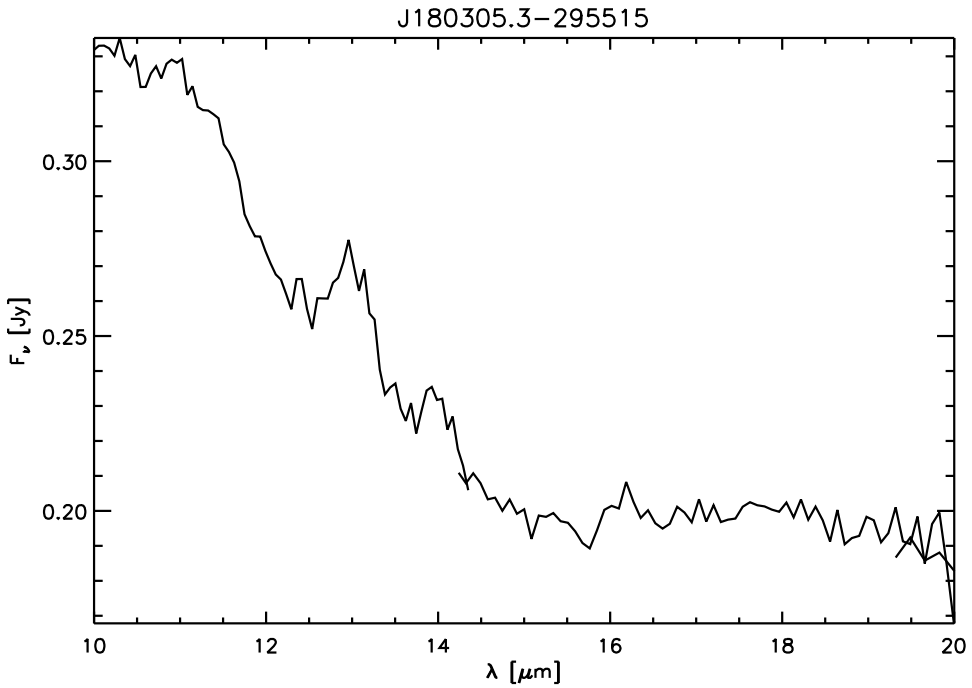

Figure 3.10: Example on the 14 μm teardrop, an artefact seen in many spectra.

Many spectra also show a bump around 14 μm at the end of the SL1 band. An example of this is given in Figure 3.10. The feature seen at 14 μm is an artefact and is referred to as the "14 μm teardrop". It is believed to originate from scattered light (for more information we refer to the Spitzer Science Center web site at
`http://ssc.spitzer.caltech.edu/irs/calib/teardrop`).

The IRSFRINGE routine was not successful with all of our OH/IR star spectra. Figure 3.17 shows that most stars still suffer from fringes at the beginning of their LL band (around 21 μm.)

3.4 Extinction correction

This homogeneous sample of AGB stars located in the GB has been selected to study the dust along the AGB (see Section 3.2). Although the location of our objects in the bulge has many advantages, such as the AGB stars originating from the same population and the almost identical distance to these objects, there is also a disadvantage inherent to the location of our sample: extinction. There are not only many stars present in the inner regions of our galaxy, there is also a large amount of dust. This dust, located in the interstellar medium (ISM) alters the shape of the observed spectra, most notably around 10 and 20 μmwhere strong silicate

bands are present. Since we want to study the dust around our target stars and not the interstellar dust, it is crucial to properly correct our spectra for interstellar extinction.

3.4.1 Dereddening law

There exist several dereddening laws in the literature that can be used to correct for extinction. Before ISO there were e.g. the extinction laws derived by Draine (1989, who combined independent studies based on reddening of stars and hydrogen line ratios from H II regions), Cardelli et al. (1989, using parametrised extinction data for the ultraviolet, and various sources for the optical and near-IR), and O'Donnell (1994, which is an update on Cardelli et al. 1989).
Based on ISO-SWS observations Lutz et al. (1996) showed that the extinction law in the direction of the GC does not show the deep minimum in the 4 – 8 μm region as is seen in e.g. Draine (1989) using graphite-silicate mixes. Therefore Lutz et al. (1996) conclude that there must be an additional contributor to the extinction. They also state that as most of the extinction to the GC arises in the foreground ISM rather than locally, it is likely that the new extinction curve they derived is more widely applicable than only for the GC.
Based on near-IR and Spitzer IRAC data, Indebetouw et al. (2005) derive an extinction law from 1.25 to 8.0 μm. The derived extinction law is consistent with Lutz et al. (1996) and as Indebetouw et al. (2005) derived very similar extinction laws for two very different directions in the Galactic plane, they suggest that their relative extinction values A_λ/A_K may be generally applicable.
Chiar and Tielens (2006) constructed two interstellar extinction curves from 1.25 to 27 μm using ISO-SWS measurements towards four heavily extincted galactic WC-type Wolf-Rayet stars. Because of the good agreement between Indebetouw et al. (2005) and Lutz et al. (1996), Chiar and Tielens (2006) combined the two extinction curves to represent the continuum extinction. Longwards of 8 μm, Chiar and Tielens (2006) constructed individual extinction curves for the local ISM and the GC as there is more silicate per unit of visual extinction towards the GC compared to the local ISM (these extinction curves are shown in Figure 3.11). Recently Román-Zúñiga et al. (2007) confirm that the extinction law in the 3 – 8 μm region towards the dense molecular cloud Barnard 59 is more or less flat. Nevertheless they find some differences with Chiar and Tielens (2006). Although these differences are modest, this could indicate that the extinction law in the near- and mid-IR may vary slightly as a function of environment.

To correct our spectra for interstellar extinction, we will use the extinction curves of Chiar and Tielens (2006). The difference between these two extinction curves longwards of 8 μm, is the intensity in the silicate profiles at 10 and 18 μm (see Figure 3.11). The silicate profile in the extinction curve for the GC (based on ISO-SWS observations of GCS3: Galactic Centre Source 3 in the direction of the quintuplet cluster) is more pronounced than in the extinction curve for the local ISM (based on ISO-SWS observations of WR 98a). Using the three dimensional extinction maps of Marshall et al. (2006) one can estimate from which distance the extinction originates. Their maps show a small increase in A_K at distances from 4 to 8 kpc in the direction towards our targets, in contrast to the extinction map in the direction to GCS3. This increase in extinction around 8 kpc is larger for the objects in fields c32 and c35, than

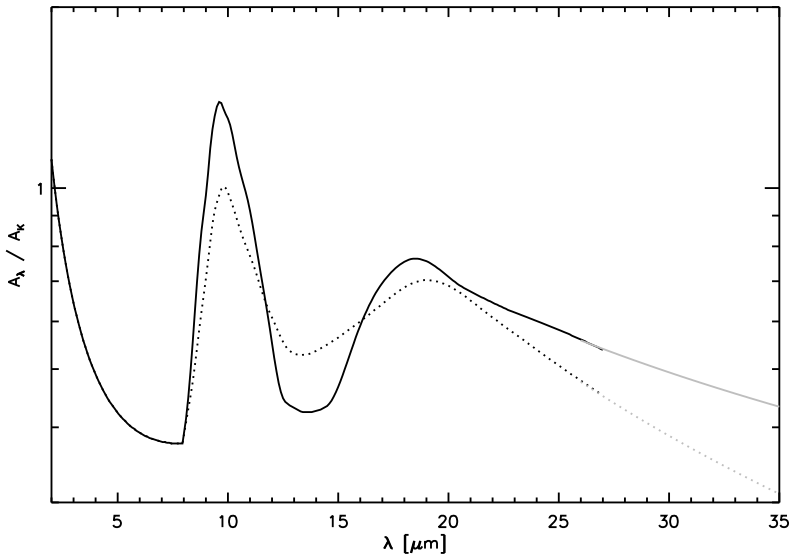

Figure 3.11: A_λ/A_K extinction curves derived in Chiar and Tielens (2006). The full line gives the GC extinction curve, the dotted line the local. The grey lines at the longest wavelengths indicate how the curves were extrapolated.

for the objects in the fields further away from the GC, like e.g. NGC 6522, but still small in comparison to the increase in extinction towards the quintuplet. Since most of the extinction therefore seems to originate from the local interstellar medium rather than from the vicinity of the GC for all fields, we used the local extinction curve from Chiar and Tielens (2006).

After applying the local extinction correction to the observed spectra, we verified that no clear extinction residuals are present in the spectra. For these purposes, we used stars without any sign of circumstellar dust (the naked stars, see Section 3.6.1). Figure 3.12 shows the spectrum of J175517.0-294131 (object number 32) in the ogle field after applying the extinction correction. From comparison with a model spectrum shown in the same figure, no obvious residuals can be discerned, and the local extinction curve of Chiar and Tielens (2006) seems appropriate for this field. The same conclusion holds for all naked stars in the ogle and NGC 6522 fields.

However, when performing a similar inspection for naked stars in the c32 and c35 fields, we noticed that there are some residuals which peak around 9.7 μm. Figure 3.13 illustrates this for J174924.1-293522 (object number 23) in field c35: when comparing the spectrum of this object to the aforementioned naked star spectrum from the ogle field, there is a clear absorption band which is reminiscent of the interstellar silicate absorption band. While this may indicate that we have used too low a value for A_K, we also note that when using the Chiar and Tielens (2006) curve for the GC rather than for local extinction, this absorption band disappears entirely, strongly suggesting that for these fields we should use the GC ex-

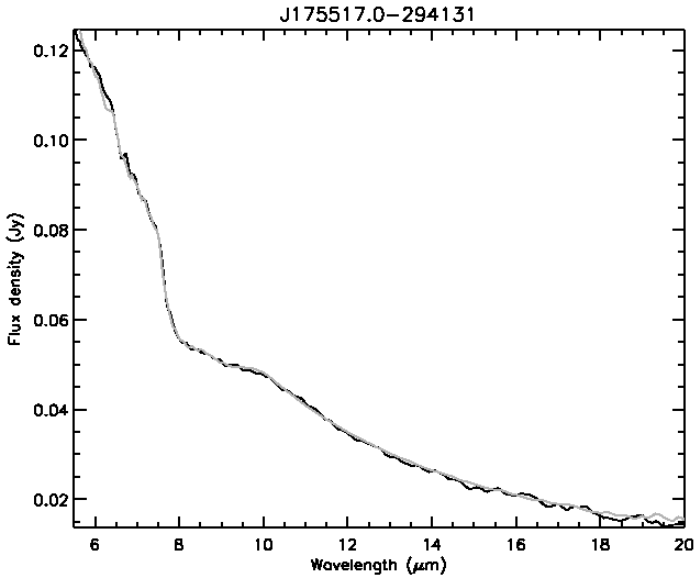

Figure 3.12: Model (grey line) for J175517.0-294131 (object number 32, black line).

tinction curve rather than the local extinction curve. Again, this holds for all naked stars in the c32 and c35 fields.

This result is surprising in view of the extinction maps from Marshall et al. (2006) which clearly show that most of the extinction arises from the local interstellar medium. However, we should note that the c32 and c35 fields are the closest to the GC (see Figure 3.5) and therefore it is not unreasonable that at least part of the extinction bears some resemblance to the GC extinction curves. Most likely, the "perfect" extinction curve to use for our targets in these fields is some combination of the local and GC curves since at least part of the extinction to these fields must be due to the local interstellar medium.

In view of these results, we therefore applied the GC extinction curve for the stars in the c32 and c35 fields, and the local extinction curve for objects in other fields.

Since the extinction curves derived in Chiar and Tielens (2006) only have data points from 1.25 μm to 27.0 μm, we extended the curves till 35 μm by fitting a straight line longwards of 21.0 μm in the log-log plane of A_λ/A_K vs λ, using the same slope as the extinction curve from 21.0 to 27.0 μm. This is indicated in Figure 3.11 by the grey lines.

3.4.2 Extinction values

Several extinction maps exist to determine A_V values based on the position of a target in the Galactic Bulge (see e.g. Schlegel et al. 1998; Schultheis et al. 1999; Sumi 2004; Marshall

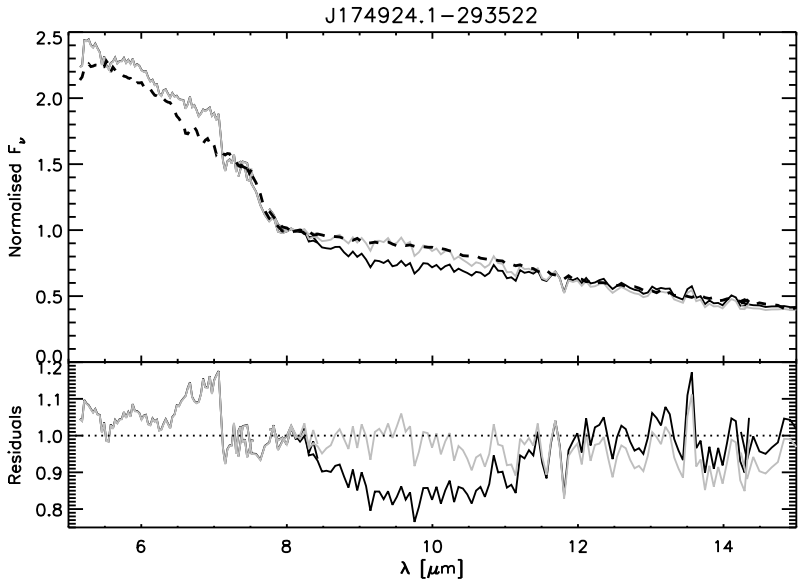

Figure 3.13: Effect of the used extinction curve for a star with no signs of circumstellar dust in field c35. Upper panel: the full black line gives the spectrum for J174924.1-293522 using the Chiar and Tielens (2006) local extinction curve, the grey line gives the spectrum for the same object using the Galactic Centre curve. The dashed black line is the spectrum for J175517.0-294131, an object in the ogle field. The spectra in this panel are normalised to the fluxes at 8 μm. In the lower panel we divided the spectrum of J174924.1-293522 by the spectrum of J175517.0-294131. The black line gives the residuals using the local extinction curve, the grey line using the GC extinction curve.

et al. 2006). The extinction maps derived by Marshall et al. (2006) are consistent with the extinction map of Schultheis et al. (1999) if one accounts for the different A_K/A_V values used. The map of Schultheis et al. (1999) is more dense in the region of our targets and therefore we will use Schultheis et al. (1999) whenever possible (some targets fall outside the latitude range of the map). Schultheis et al. (1999) use $A_{K_S}/A_V = 0.089$ (Glass 1999) to convert their extinction map in A_{K_S} to the published A_V values. Chiar and Tielens (2006) normalised their extinction curves to the K-band and therefore we will calculate the extinction in K from Schultheis et al. (1999) using $A_{K_S}/A_V = 0.089$ and $A_K = 0.95A_{K_S}$ (Dutra et al. 2003).
For the targets with RA around 17:55:00 we could not use the extinction maps of Schultheis et al. (1999). Since the closest point in the extinction maps of Marshall et al. (2006) is a few arcminutes away and these targets are located in fields 4 and 39 from the OGLE-II survey, we used the extinction values from Sumi (2004). These two fields have extinction values A_V of 2.59 and 2.62 (Sumi 2004), therefore $A_V = 2.60$ has been chosen for the stars located in this area. Using the results of Marshall et al. (2006), extinction values around $A_V = 2.17$ are found. Especially in the mid-IR the difference between this value and the one derived from Sumi (2004) is small. To derive A_K values $A_K/A_V = 0.116$ (Cardelli et al. 1989; O'Donnell

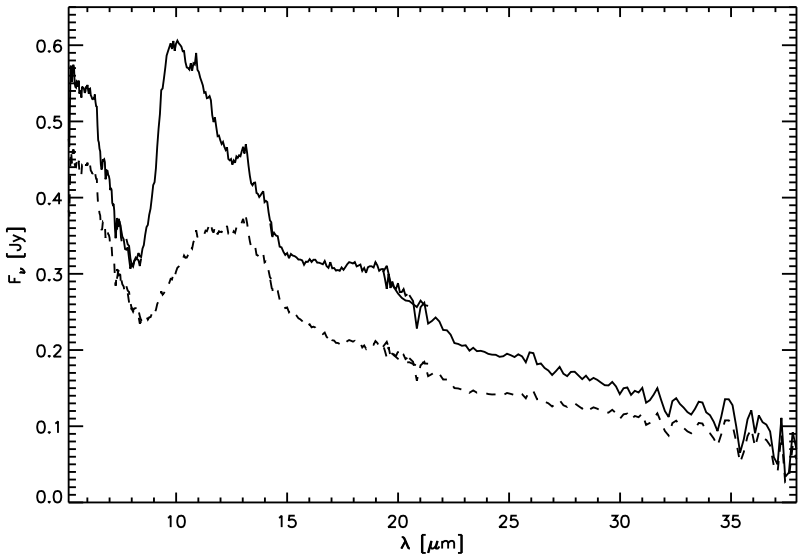

Figure 3.14: Effect of the extinction correction for J174117.5-282957. The dashed line is the spectrum not corrected for extinction, the full line gives the spectrum after extinction correction.

1994) has been used. One should remind that these A_K/A_V values are valid for a standard extinction curve with $R_V = 3.1$. The use of an anomalous extinction curve, as claimed by Sumi (2004) and as explored in Chapter 7, would just slightly change this ratio.
For the remaining OH/IR sources selected from the IRAS catalogue, Schultheis et al. (1999) nor Sumi (2004) could be used. Therefore the extinction has been derived based on Marshall et al. (2006). Since these objects are located further away from the galactic plane (see Figure 3.5), the extinction values are smaller and therefore also the error made based on applying a lower resolution extinction map as Marshall et al. (2006) is likely to be small.

Figure 3.14 gives an example of the effect of the extinction correction for J174117.5-282957. The dotted line is the spectrum before the extinction correction, the full line gives the spectrum after the extinction correction.

Additionally the used extinction law has it effects on the A_{15} value and therefore also on $(K_s - [15])_0$. Based on the extinction curve for the local extinction we found that $A_{15}/A_K = 0.585$, if we assume the GC extinction curve than $A_{15}/A_K = 0.484$. These values are used to correct the ISOGAL [15] observations for extinction based on the derived A_K values.

Table 3.2 lists in the last two columns the chosen A_K and the reference. This resulted in the spectra shown in Figures 3.15 – 3.17. The numbers in the figures correspond to the numbers in Table 3.2.

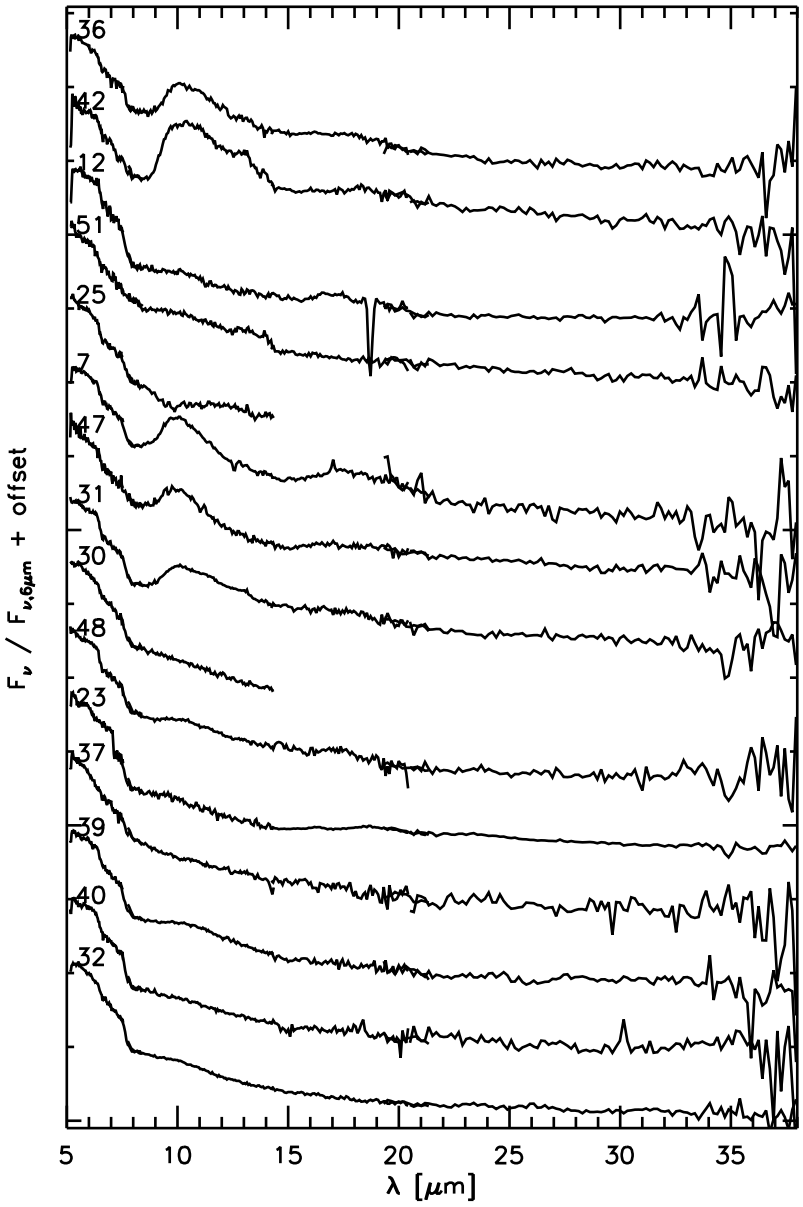

Figure 3.15: IRS spectra after extinction correction for stars with the lowest $(K_s - [15])_0$ value. The $(K_s - [15])_0$ colour increases from bottom to top.

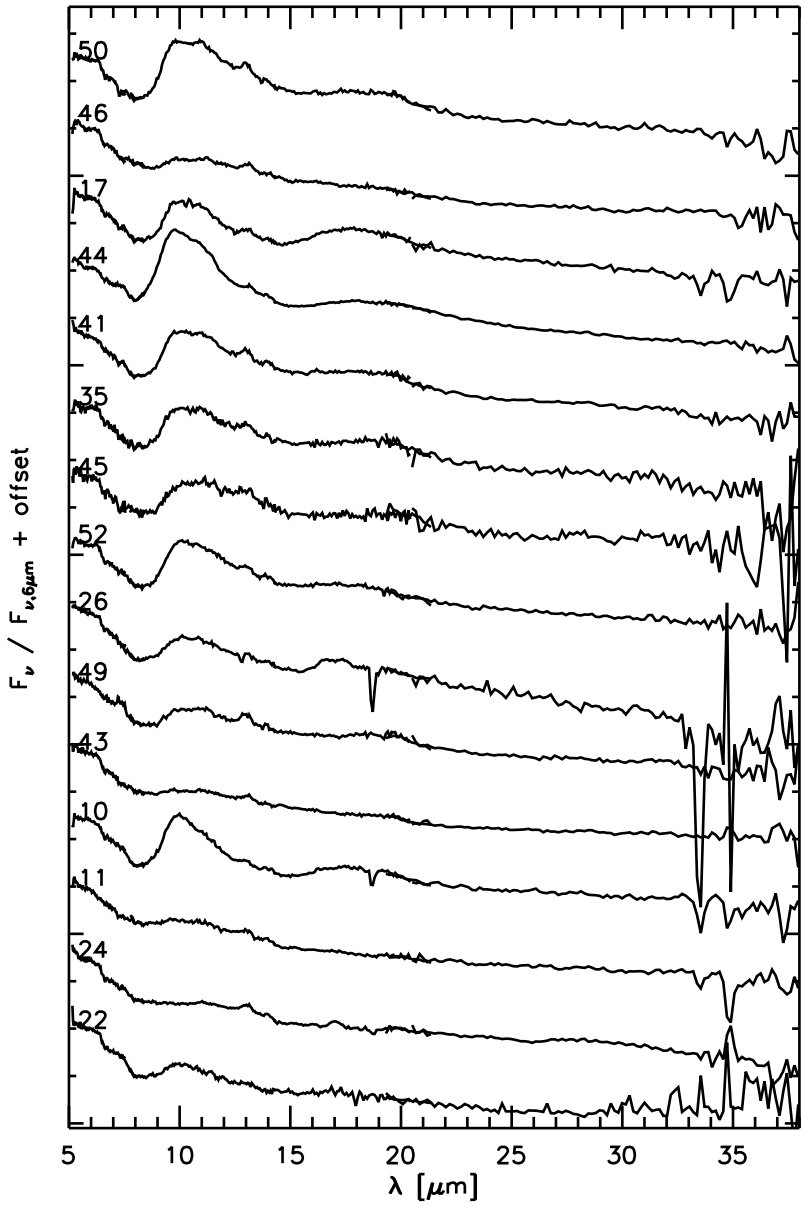

Figure 3.16: IRS spectra after extinction correction for stars with higher $(K_s - [15])_0$ values. The $(K_s - [15])_0$ colour increases from bottom to top.

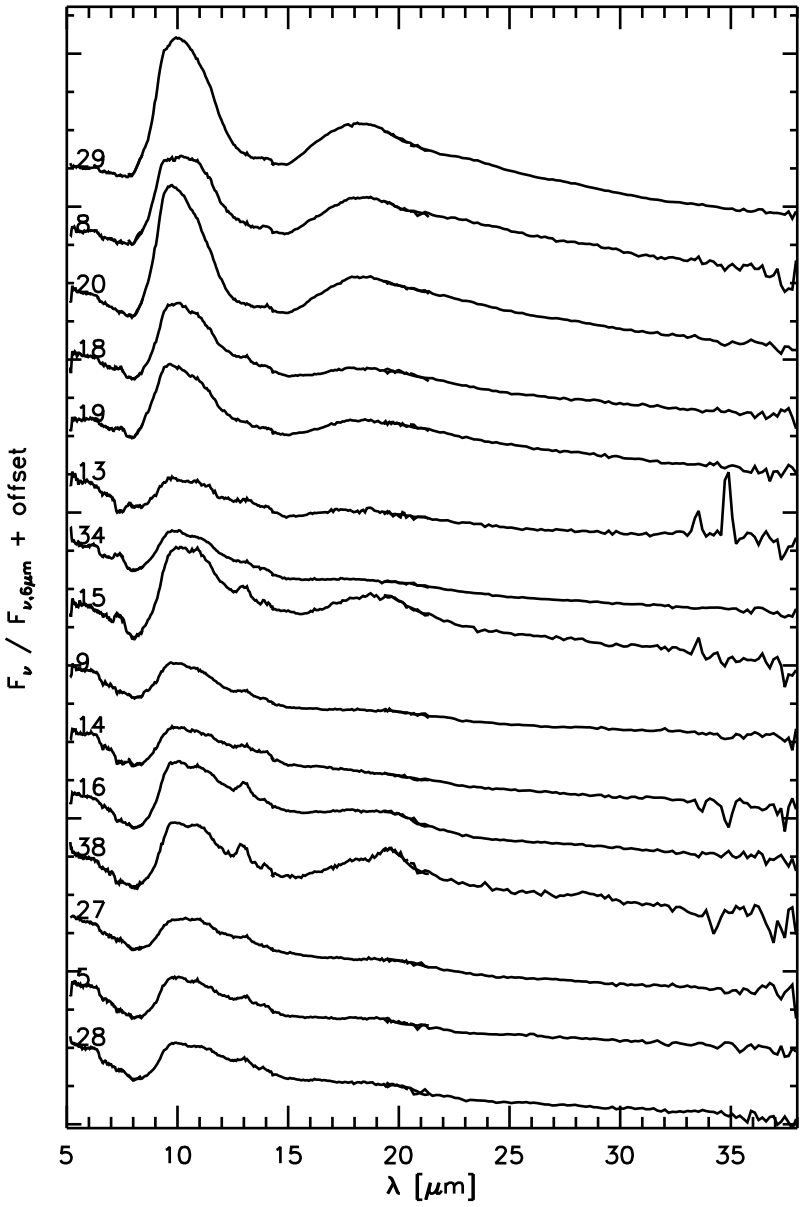

Figure 3.17: IRS spectra after extinction correction for stars with the highest $(K_s - [15])_0$ values, except the OH/IR stars. The $(K_s - [15])_0$ colour increases from bottom to top.

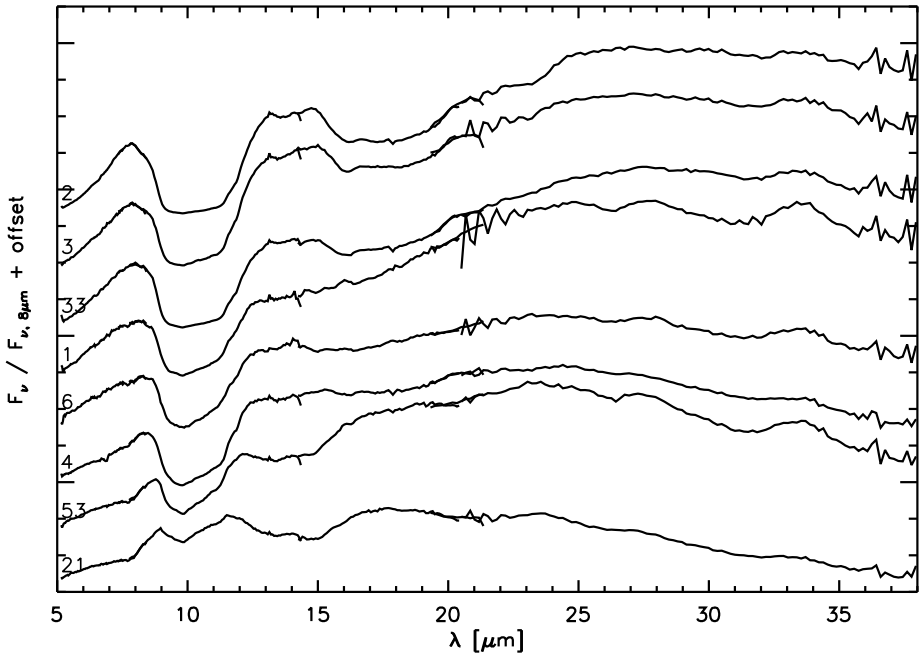

Figure 3.18: IRS spectra after extinction correction for the OH/IR stars, ordered from bottom to top with increasing depth of the 10 μm silicate feature.

3.5 Stellar photosphere

Up to 8 – 9 μm the spectra of our stars are dominated by the emission from the stellar photosphere or the warm molecular layers around the star (see e.g. Tsuji et al. 1997). Figure 3.19 shows the stellar spectra up to 10 μm together with template spectra (see Cami 2002) for different molecular species that can be identified in the spectra. The spectra of the OH/IR stars are not included as their optically thick circumstellar shells completely obscure the stellar radiation. The shortest wavelengths of the IRS spectrometer covers certain ro-vibrational bands from H_2O, SiO, SO_2 and CO_2 which are commonly seen in the infrared spectra of O-rich AGB stars. At the resolution of our IRS spectra detailed line profiles are smeared out, but the molecular bands are often strong enough to leave a noticeable footprint in the spectra of our target stars.

Water has a strong opacity over almost the entire wavelength range and can produce significant continuum-like distortions to the spectrum. At high enough column densities, this results in a very opaque layer of water vapour, the main effect of which is to lower the colour temperature of the continuum flux in the infrared (Cami 2002). The presence of significant amounts of water vapour in the mid-infrared spectra can most easily be ascertained by the fairly strong jump in flux around 6.5 μm, but water vapour still has significant opacity

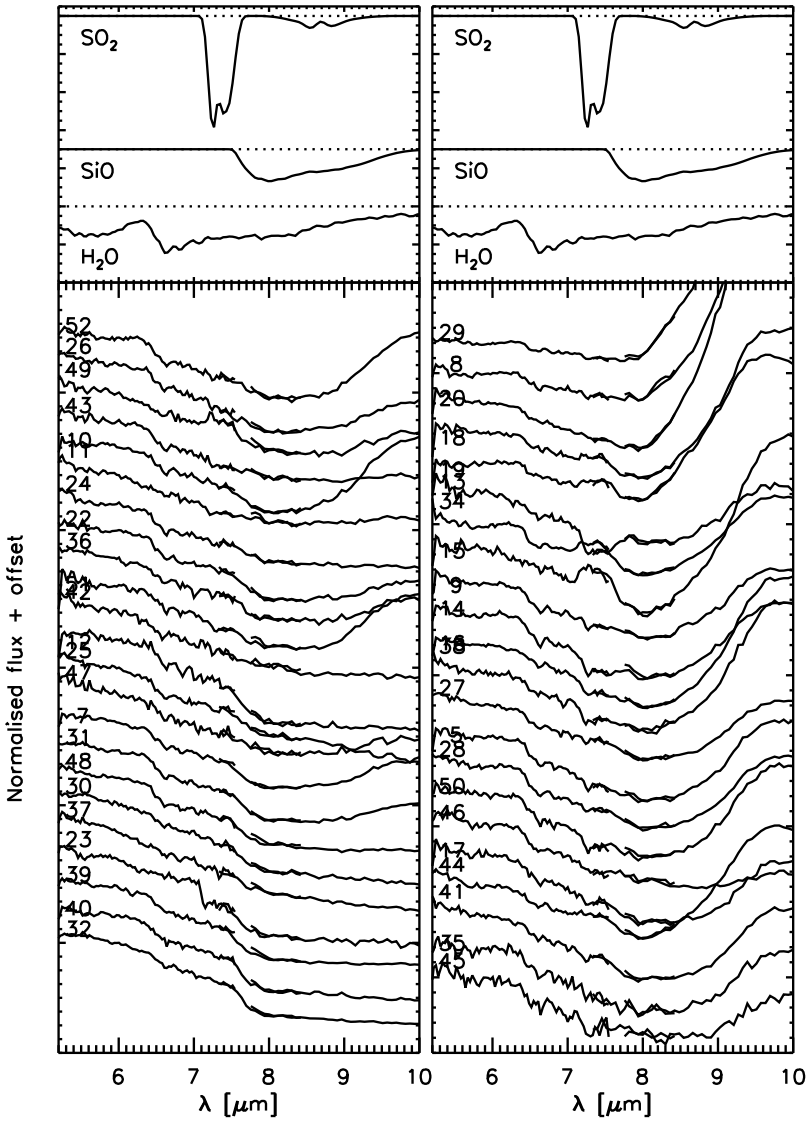

Figure 3.19: The 5 – 10 μm part of the spectra, showing the molecular features. The spectra are ordered with increasing $(K_s - [15])_0$ colour from bottom to top and left to right and are normalised at 6 μm. Template spectra for SO_2, SiO, and water are shown for comparison (see Section 3.5). Following parameters were used to create these templates: a temperature of 1 500 K and a column density of 10^{20} cm^{-2} for water and SiO and a temperature of 500 K and a column density of 10^{18} cm^{-2} for SO_2.

at longer wavelengths too. Almost all the spectra show this jump in flux at about 6.5 μm, indicating the presence of a water layer, which may lower the colour temperature of the continuum flux of these objects.

SiO is after CO (which has no clear features in the wavelength range shown in Figure 3.19, only some absorption in the beginning of the Spitzer-IRS wavelength range) and H_2O one of the most abundant molecules in the atmospheres of AGB stars and is formed in all cooler oxygen-rich stars. Model spectra show that significant amounts of SiO are formed in stellar atmospheres with effective temperatures of $\sim$ 4000 K and less (Aringer 2000). SiO is also a primary constituent for oxygen-rich dust and can be considered a prerequisite for mass loss (Lebzelter et al. 2001, and references therein). The fundamental vibrational mode has its band head around 7.5 μm; at high temperatures and column densities however, the red wing of this band extends to typically 10 – 12 μm and can therefore significantly alter the profile of the 10 μm dust feature. Figure 3.19 reveals that almost every object shows clear signs for SiO absorption, which is important to remember when evaluating the dust around these objects.

The SO_2 ν_3 stretch band is situated at 7.3 μm and can appear in absorption or emission but is not present in all oxygen-rich AGB stars. The discovery of this band in ISO-SWS spectra in some oxygen-rich AGB stars is described in Yamamura et al. (1999). Time-series of T Cep show that the SO_2 band is not constant over the pulsation cycle. The drop in opacity at the band centre is characteristic for this band profile which is sometimes seen in absorption and sometimes in emission (Cami 2002; Van Malderen 2003). Figure 3.19 shows that there are indications for this SO_2 band in some spectra of our sample.

Also CO_2 is often observed in Miras and semi-regulars at its fundamental bending mode around 15 μm. The first report on CO_2 emission at 14.98 μm from M giants was given in Ryde et al. (1997) and has been confirmed by Justtanont et al. (1998). Justtanont et al. (1998) detected strong emission lines at 13.87, 14.97, and 16.18 μm in the ISO-SWS spectra of oxygen-rich AGB stars. The lines were only found in the spectra of Miras and semi-regular variables when they also showed a 13 μm feature. Given the low resolution of our spectra and the uncertainties at the longest wavelengths, we find no irrefutable evidence for the presence of CO_2 features in our spectra.

3.6 Circumstellar dust shell

To study the dust properties of our sample, the stellar contribution and the possible contribution from the molecular layers known to surround these objects need to be subtracted from the observed spectrum corrected for extinction. How this is done is explained in the following subsection. Once the dust spectra have been created (Section 3.6.2), the dust contribution will be analysed in a few different ways (Sections 3.6.3 to 3.6.6) to see whether there is a relation between the mass-loss rates, the amount of dust, and the dust composition (Section 3.7).

The analysis of the dust around the OH/IR stars in the sample is very different from the analysis of the other objects in this sample because the OH/IR stars have an optically thick

dust shell. Therefore, the OH/IR stars are not considered in this chapter, but will be discussed separately in Chapter 5.

3.6.1 Naked stars

The so-called "naked stars" have no dust contribution, hence reveal best how the radiation from the central star and a possible molecular gas layer looks like. These "stellar spectra" can then be used as templates to remove the stellar emission from other spectra showing a clear infrared excess caused by the circumstellar dust. Because of their importance as templates, a careful selection of naked stars is necessary, which is described in this subsection.

The Spitzer-IRS spectra of AGB stars without dust show a continuum spectrum with some additional molecular bands (see Section 3.5). The main absorption features in the wavelength range until about 11 μm are H_2O, SiO, and SO_2 (in some cases SO_2 can also appear in emission, see e.g. Figure 3.19). The Spitzer-IRS spectra of the naked stars can often be fitted using a black body, except for the molecular bands present in the wavelength region between 7 and 11 μm. Figure 3.15 shows that J175517.0-294131 (object number 32) is a very good example of this. This spectrum is also shown in the upper panel of Figure 3.20 (black line). We fitted a black body to this spectrum (grey line) on the wavelength region from 5 to 7 μm and from 11 to 20 μm, which illustrates the similarities between the star with no dust contribution and a black body. The temperature of the black body is 2430 K. The lower panel shows the spectrum divided by the black body. The main feature in this normalised spectrum is the absorption feature around 8 μm. Based on Figure 3.19, this feature can be identified as SiO. Also water is present in this spectrum and can be seen by the jump in flux at 6.5 μm.

In Section 3.6.3 the typical shape of the expected dust features for this sample of stars will be described (see also Figure 3.32). Based on the shape of these dust features, the spectra shown in Figures 3.15 to 3.17 were searched for obvious dust features. The objects for which no clear dust features can be found are selected as candidate naked stars. For these objects, we fitted a black body to the spectrum as described in the previous paragraph. The spectra of the candidate naked stars were then divided by the fitted black body to create normalised spectra (similar to what is shown in Figure 3.20). These normalised spectra have again been searched for residuals resembling the shape of the expected dust features. When no dust features are found, the object is labelled as a naked star. Using this method, 10 naked stars are selected. These objects with their fitted black body overlaid are shown in Figure 3.21.

Figure 3.21 shows an unexpected large spread in colour temperatures of the naked stars. These temperatures range from about 1360 K to 3000 K. The effective temperatures for the objects in this sample are situated between 2500 and 3500 K (see Chapter 4). For all but four naked stars we find temperatures significantly lower than these values based on the fit with the black body. Cami (2002) showed that this could be due to the presence of a molecular water layer: Fig. A.21 in Cami (2002) shows optical depth profiles of water vapour, one at 500 K and another at 2500 K. These figures show that if a water layer is present around our objects and if the column density of the water is high enough, it will lower the colour temperature of the continuum flux even if the layer is not optically thick. Figure 3.19 showed that most of

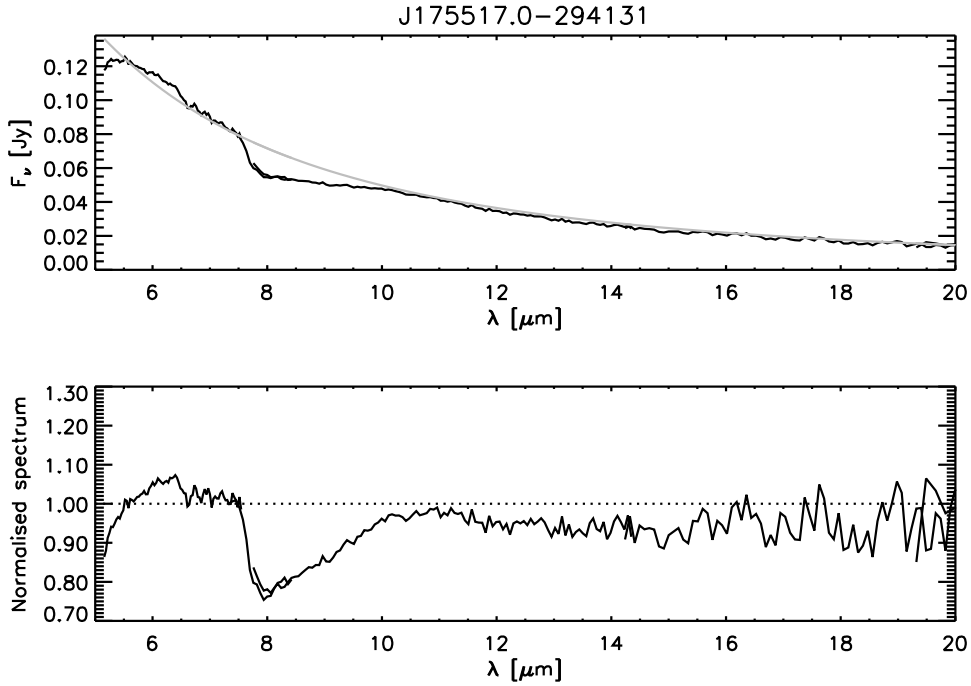

Figure 3.20: The upper panel shows the observed spectrum, corrected for extinction, of J175517.0-294131 (black line). The grey line is a fitted black body of 2470 K. The lower panel shows the observed spectrum divided by the black body.

the objects in our sample exhibit a jump around 6.5 μm due to water absorption. This may explain why the colour temperatures for the naked stars show such a large spread.

Table 3.3 shows the objects arranged for increasing $(K_s - [15])_0$. The naked stars are also listed in this table. Figure 3.22 shows the CMD for our objects, in which the naked stars are indicated by diamonds and the other objects by crosses. We expect based on our sample selection method that the naked stars are the bluest objects in $(K_s - [15])_0$ as these objects are expected to have the lowest mass-loss rates. Inspecting Table 3.3 and Figure 3.22 reveals that there are objects with a dust contribution which have a smaller $(K_s - [15])_0$ value than the reddest naked stars. On top of that, there exists a large spread in $(K_s - [15])_0$ values for the naked stars: from -0.01 to 1.16 mag. This surprisingly large range in $(K_s - [15])_0$ for the naked stars seems to correspond to the large spread we find in IR colour temperatures (Figure 3.21) for these objects. Indeed, if we calculate the spread in $(K_s - [15])_0$ we would find by using black body curves with the colour temperatures derived from the fit, we would find a spread of about 1.9 magnitudes. Since the colour temperature variations are likely the consequence of different water absorption and/or emission characteristics, we thus find that the presence of water around these objects causes a fairly large spread in $(K_s - [15])_0$.

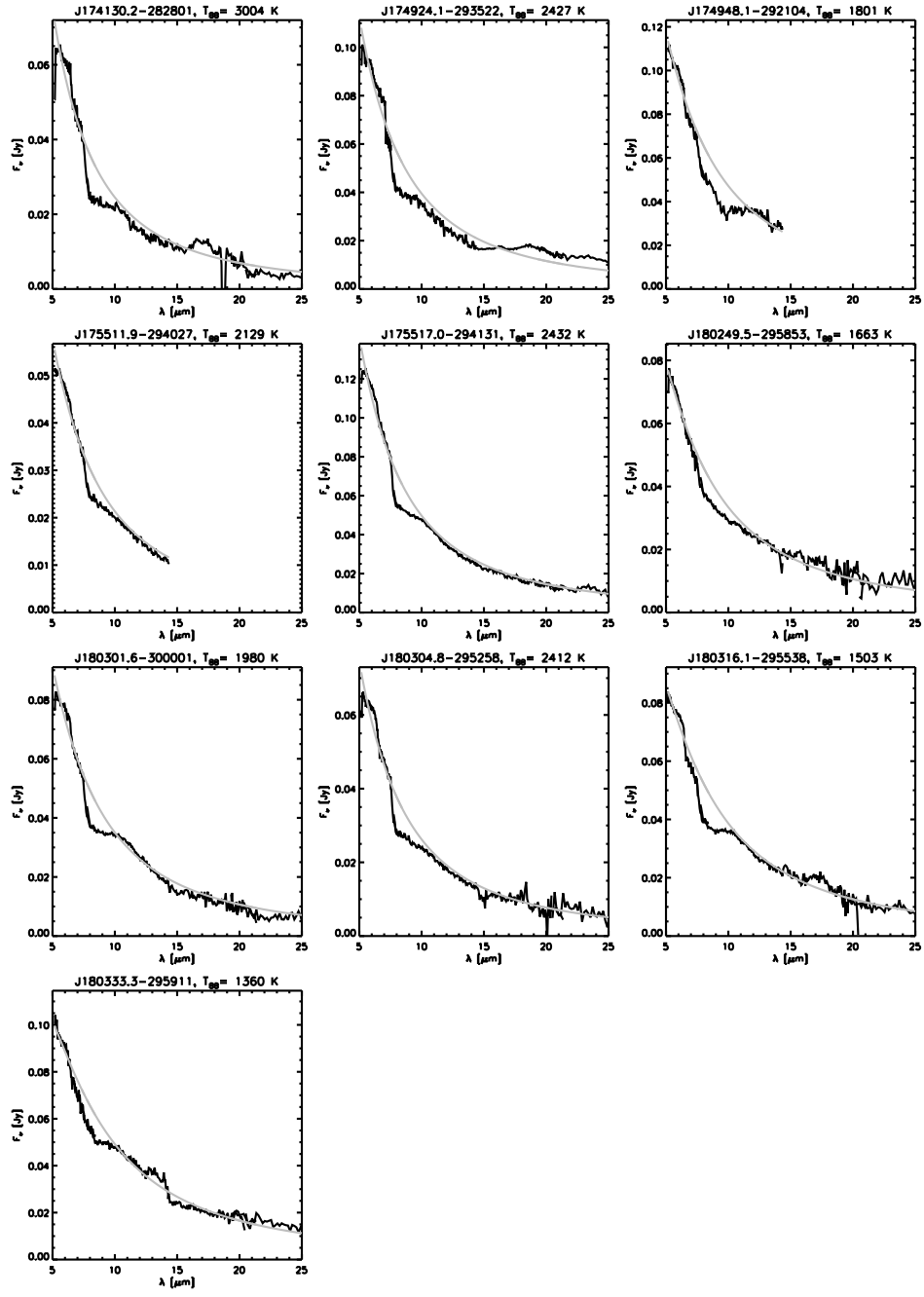

Figure 3.21: Spectra for the naked stars with the fitted black body in grey.

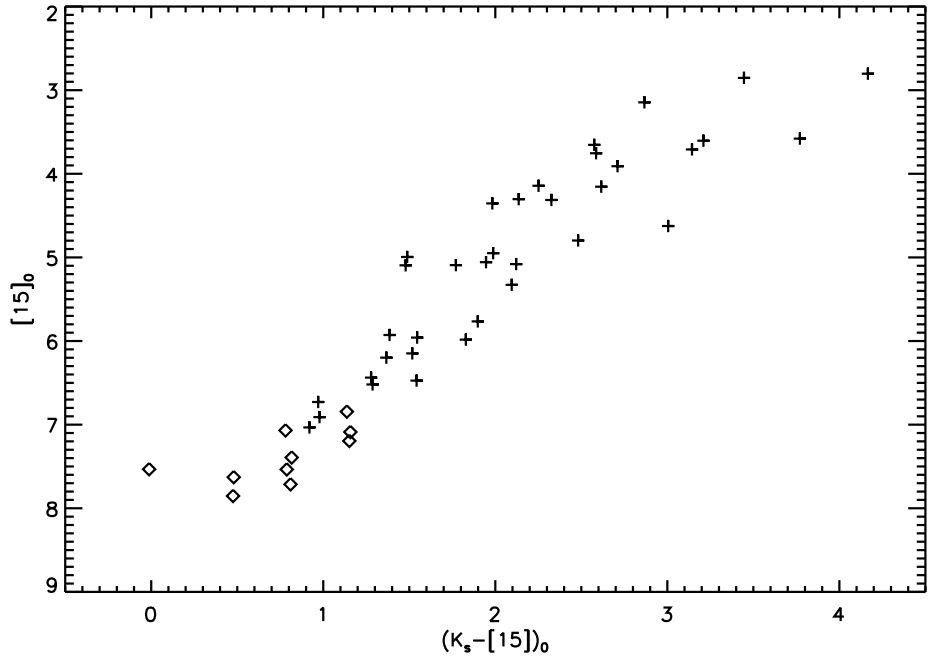

Figure 3.22: $(K_s - [15])_0$ vs $[15]_0$ CMD for the objects in our sample. The diamonds represent the naked stars, the crosses indicate the objects which show signs of a dust contribution.

In this subsection, we selected 10 objects which show no sign of circumstellar dust contribution, the naked stars. These objects will be used in the following subsection to remove the emission from the central star and a possible molecular layer to create dust spectra for objects that do show a circumstellar dust contribution. Based on the analysis of these naked stars, we must conclude that $(K_s - [15])_0$ cannot be used alone to decide whether an object is a naked star or not. There exists a large spread in $(K_s - [15])_0$ of about 1.17 mag for the naked stars and additionally there were objects found with a dust contribution which have bluer colours than the reddest naked stars. This indicates that $(K_s - [15])_0$ is not a perfect mass-loss indicator at the onset of dust formation.

3.6.2 Dust spectra

3.6.2.1 Creation of the dust spectra

We will now discuss the methods used to derive the dust spectra. A dominant feature in the stellar spectra is the SiO absorption, which extends to about 11 μm (see Figure 3.19). It is important to be able to correct properly for this broad feature as it overlaps with the 10 μm complex, caused by circumstellar dust. Most objects in this sample show a clear SiO ab-

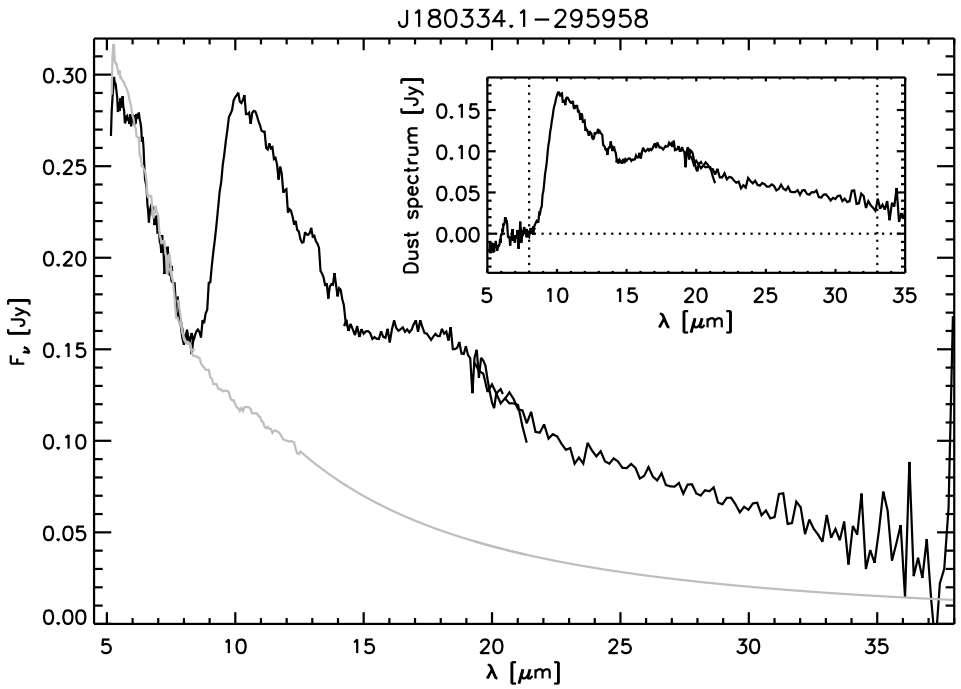

Figure 3.23: Example on the method used to obtain the dust spectra for objects with an SiO absorption band. The star in black is J180334.1-295958. The template star, in grey, is J180249.5-295853. The inset shows the resulting dust spectrum for this star.

sorption feature (see Figure 3.19). For these objects one of the naked stars is used to remove the emission originating from the central star and a possible molecular layer to obtain a dust spectrum. This method is illustrated in Figure 3.23. For each object with an SiO absorption band, we selected the naked star with the SiO band that resembles best the SiO absorption profile from the target. In most cases the slope of the template then also resembled the slope of the object for which we want to obtain a dust spectrum. In order not to add additional noise to the dust spectra, the template stars have been smoothed to remove the noise and keep the information on the molecular bands. Figure 3.15 showed that it was not always possible to reduce the data from the LL images (see also Section 3.3.3), therefore only the smoothed short wavelength range (5.2 – 14.5 μm) is used which is then completed with a black body curve. The temperature of the used black body is the temperature derived in Section 3.6.1 (see also Figure 3.21). The grey line in Figure 3.23 shows the template created in this way used to remove the emission from the central star for this object. The inset shows the resulting dust spectrum. The dotted horizontal line in the inset is the zero flux level and the two dotted vertical lines indicate the area which will be used to estimate the amount of dust (see Section 3.6.4).

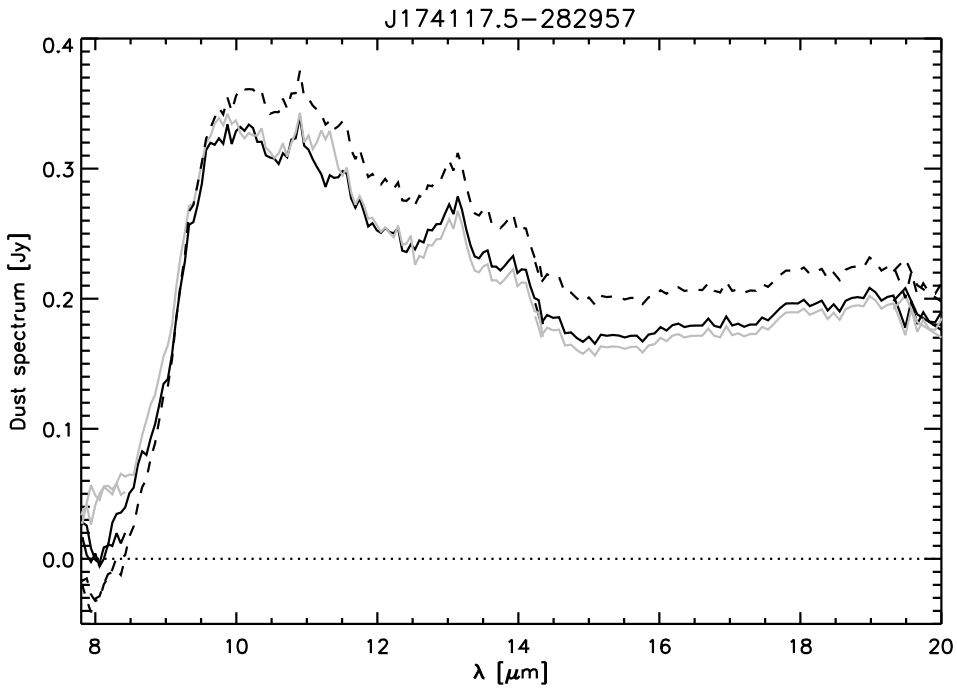

Figure 3.24: Dust spectrum for J174117.5-282957. The full black line shows the dust spectrum when using a template with a similar SiO band as the object. The grey line shows the dust spectrum when a template is used with a too deep SiO band, and the dashed black line gives the dust spectrum when a black body curve is used.

The method described above was not able to remove the entire SiO absorption band for three of our stars (objects number 34, 41, and 49). To overcome this issue, we normalised the naked stars by their fitted blackbodies and used the colour temperature of the object (determined based on the blue wavelength region) to create a new template. The templates created in this way resembled better the slope of the blue wavelength region as well as the depth of the SiO absorption feature.

If the SiO absorption in the estimated stellar spectrum is over- or underestimated, it will affect the estimate of the dust contribution as well as the shape of the 10 μm complex. This is illustrated in Figure 3.24 for J174117.5-282957 (object number 5), which exhibits an SiO absorption band (see Figures 3.17 and 3.19). The full black line in Figure 3.24 shows the dust spectrum when the SiO band is corrected for using the method described above. The grey line shows the dust spectrum when the SiO band is corrected too much for (using a template with a stronger SiO profile than what is seen in the target). The dashed black line shows the dust spectrum when the SiO band is not corrected for (using a black body curve as template). Especially when the SiO band is not corrected for, the shape of the dust spectrum changes significantly. But also when the SiO band is overestimated, the shape of the 10 μm complex

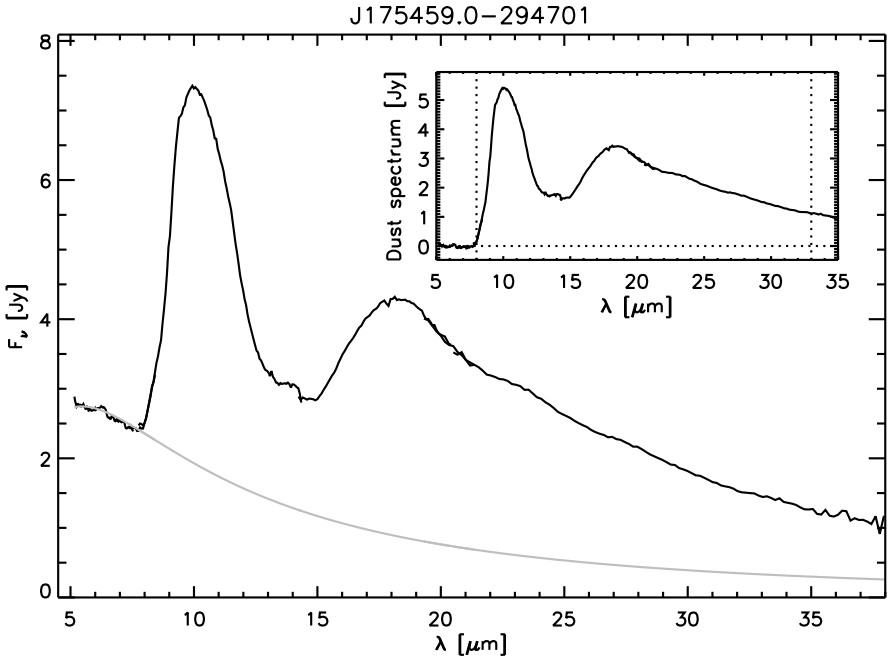

Figure 3.25: Example illustrating the method used to create the dust spectrum for objects with no clear SiO absorption bands.

changes: the peak position of the complex is shifted to the blue in comparison with the full black line.

The objects which show no sign of a clear SiO absorption feature are easier to correct for the emission from the central star and a possible molecular layer. In this case, the emission from the central star can be represented by a black body fitted to the wavelength region from 5 to 8 μm. The dust spectrum is then obtained by subtracting this black body from the observed spectrum. Figure 3.25 illustrates this method for J175459.0-294701. In this figure the spectrum is shown (in black) with a fitted black body in grey. The inset shows the resulting dust spectrum. The dust spectra for all the objects which were not labelled as naked stars and which are no OH/IR stars are shown in Figures 3.29 to 3.31.

3.6.2.2 Uncertainties in the dust spectra

Before we can address the differences seen between the dust spectra, we need to obtain an idea on the uncertainties in the dust spectra. Uncertainties in the dust spectra are caused by several factors: the uncertainties of the original spectra and the fit to subtract the emission from the central star.

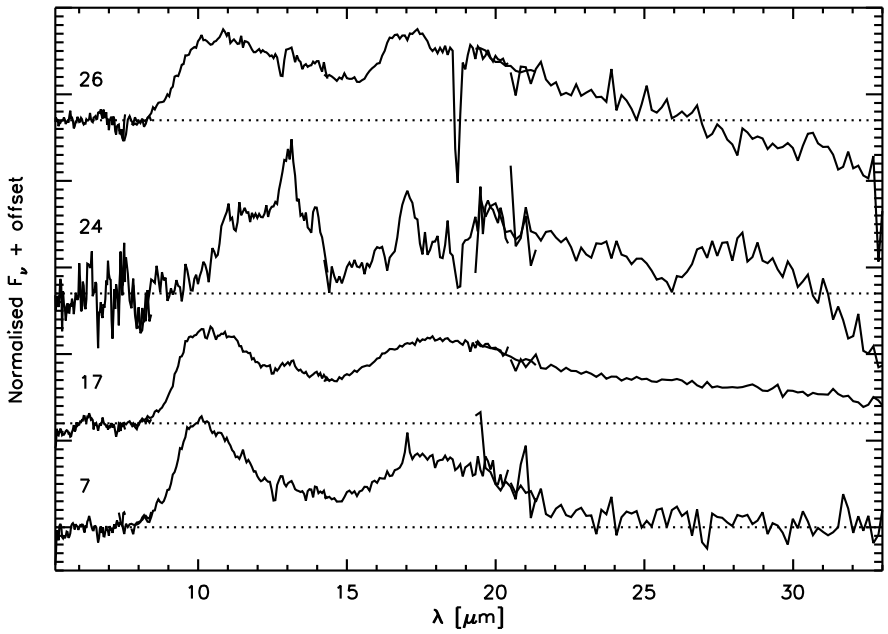

Figure 3.26: Dust spectra for the objects showing the clearest background residuals. The spectra are normalised at 11 μm.

Background residuals

The original spectra and therefore also the obtained dust spectra contain residuals from a non-perfect background subtraction (see Section 3.3.3). Any residuals at wavelengths longer than 33 μm will be ignored, as this region will not be used in the analysis.

Figure 3.26 shows the dust spectra for the objects with the most apparent background residuals. Object 24 shows very severe residuals longwards of 14 μm, originating from PAH emission. This part of the spectrum is therefore unreliable. The same is true for object 26. The dust spectrum beyond 14 μm shows similar characteristics as the dust spectrum of object 24. The longer wavelength range of this object is also unreliable. These two objects also show very clearly the forbidden S III line at 18.7 μm.

Smaller background residuals can be seen in objects 7 and 17. Object number 7 shows a residual absorption feature just before 13 μm and a sharp peaked emission feature around 17 μm, which are artefacts. The overall shape of the dust spectrum does not seem to be contaminated by PAH emission residuals (a typical profile for such a background residual can be seen in Figure 3.8 as well as in objects 24 and 26 in Figure 3.26). Object number 17 shows an artefact just before 10.5 μm, as well as the absorption feature just before 13 μm already seen in the dust spectrum of object number 7. Also for this object the residuals do not seem to alter the overall shape of the dust spectrum.

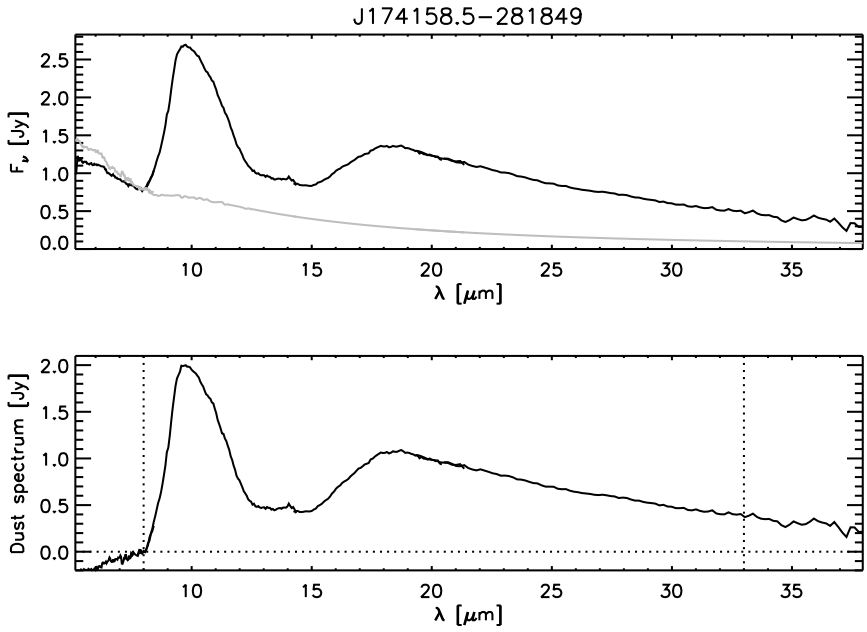

Figure 3.27: The creation of the dust spectrum for J174158.5-281849, using template star J180333.3-295911. The top panel shows the spectrum in black with the template star in grey. The bottom panel shows the resulting dust spectrum.

To estimate the influence of a non-perfect background subtraction in this area, the pixel variations across the slit around 18.7 μm are studied. The 18.7 μm line is about 2 pixels on the slit. For each star we derived the variation in background flux around this forbidden line and averaged this over all nods and cycles observed for each object. The derived percentages are given in Table 3.3. The listed numbers give an idea on the variation of the background: the larger the number, the larger the possibility of background residuals in the spectra. Also the amount of dust plays a key role in this. For objects with a larger amount of dust, variations in the background have a smaller influence than for objects with a small dust contribution. Therefore these percentages need to be considered relative to the amount of dust.

Residuals of the emission from the central star

The fifth column in Table 3.3 indicates for which objects the removal of the emission originating from the central star was not fully satisfactory. We already discussed the effect of the SiO absorption in Section 3.6.2.1. In the remainder of this subsection we will discuss the possible residuals of emission from the central star in more detail and show how these can be recognised.

In Section 3.6.1 we mentioned that due to the large opacity of water over the entire wavelength range (see also Fig. A.21 in Cami 2002), water can suppress the continuum flux of the object and hence be a cause of errors when subtracting the emission from the central star.

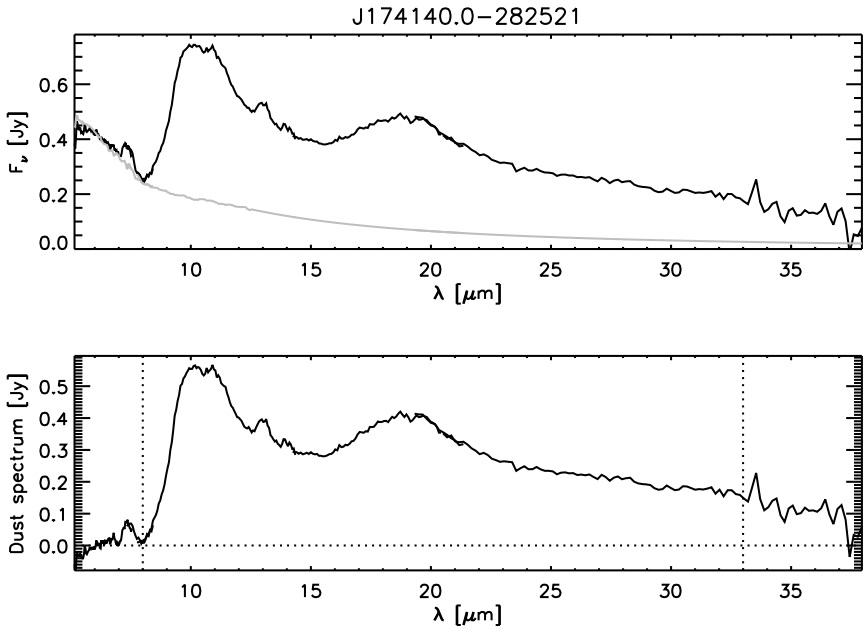

Figure 3.28: The creation of the dust spectrum for J174140.0-282521, using template star J180249.5-295853. The top panel shows the spectrum in black with the template star in grey. The bottom panel shows the resulting dust spectrum.

Because water has no features in the studied wavelength range that look similar to the dust features we will discuss, we cannot accidently attribute a water residual to a dust component. An example of this is given in Figure 3.27. For two of the objects with the reddest $(K_s - [15])_0$ colour, the water absorption changes the slope of the spectrum: it becomes more flat and the used templates do not fit anymore. Because these objects (J174158.8-281849 and J174203.7-281729, numbers 18 and 19) have large dust contributions however, the relative effect is small and we expect that this will not have a severe impact on our analysis.

The last molecule also shown in Figure 3.19 is SO_2. Some objects show SO_2 in emission (see e.g J174140.0-282521, number 15, in Figures 3.19 and 3.28) while the templates chosen to remove the emission from the central star only show SO_2 in absorption. Figure 3.28 shows object J174140.0-282521 for which a dust spectrum is created using a template star (J180249.5-295853). Because the template stars exhibit no SO_2 emission, the dust spectrum still shows an SO_2 emission feature (see lower panel Figure 3.28). Also for objects with no clear water or SiO absorption for which we used a black body to remove the emission from the central star, SO_2 residuals can be found in the dust spectra (see e.g. the dust spectrum of J174134.6-282431, object number 13 in Figure 3.31). As we will not use the dust spectra shortwards of 8 μm in further analysis (and the SO_2 feature has its band between 7.1 and 7.8 μm), this is not an important issue and has no effect on the analysis.

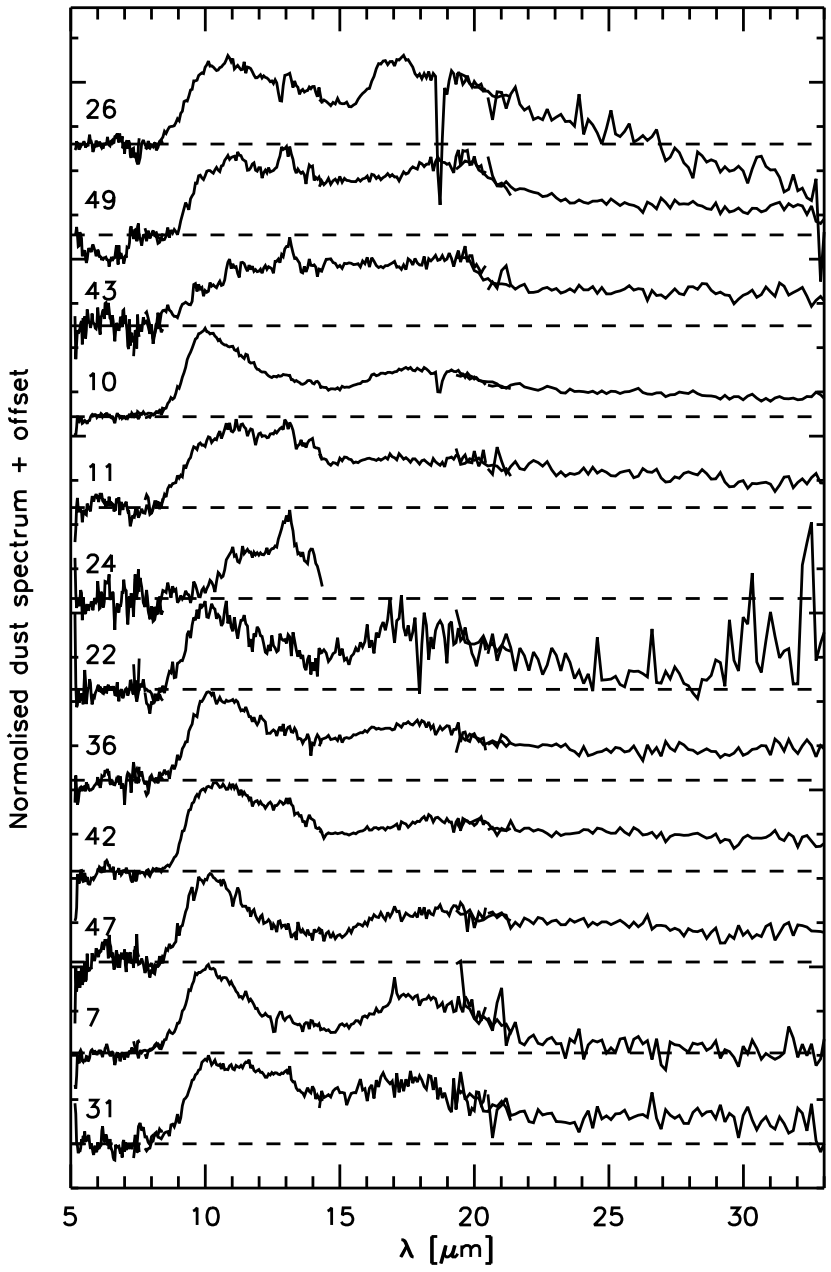

Figure 3.29: Dust spectra, the horizontal dashed lines indicate the zero-flux level. The $(K_s - [15])_0$ colour increases from bottom to top. The spectra are normalised to their maximum flux.

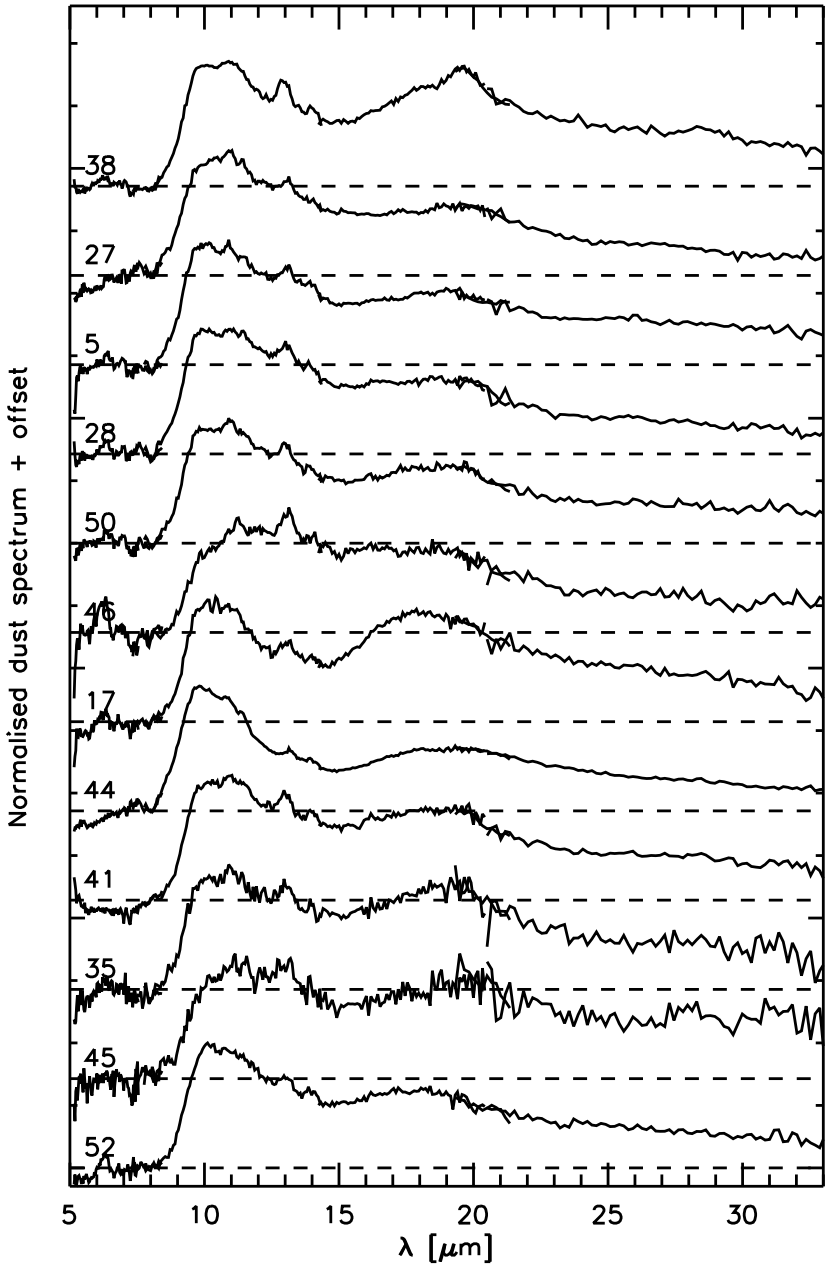

Figure 3.30: Dust spectra continued.

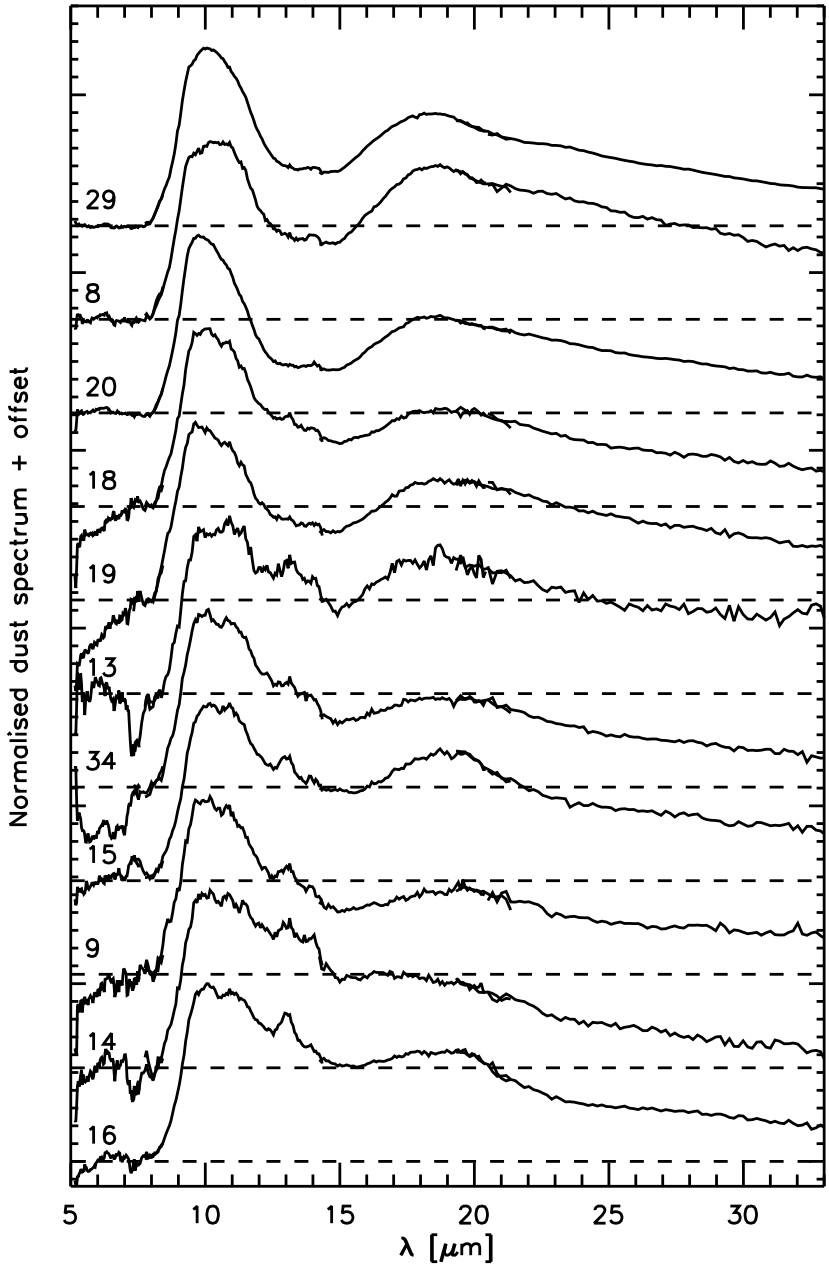

Figure 3.31: Dust spectra continued.

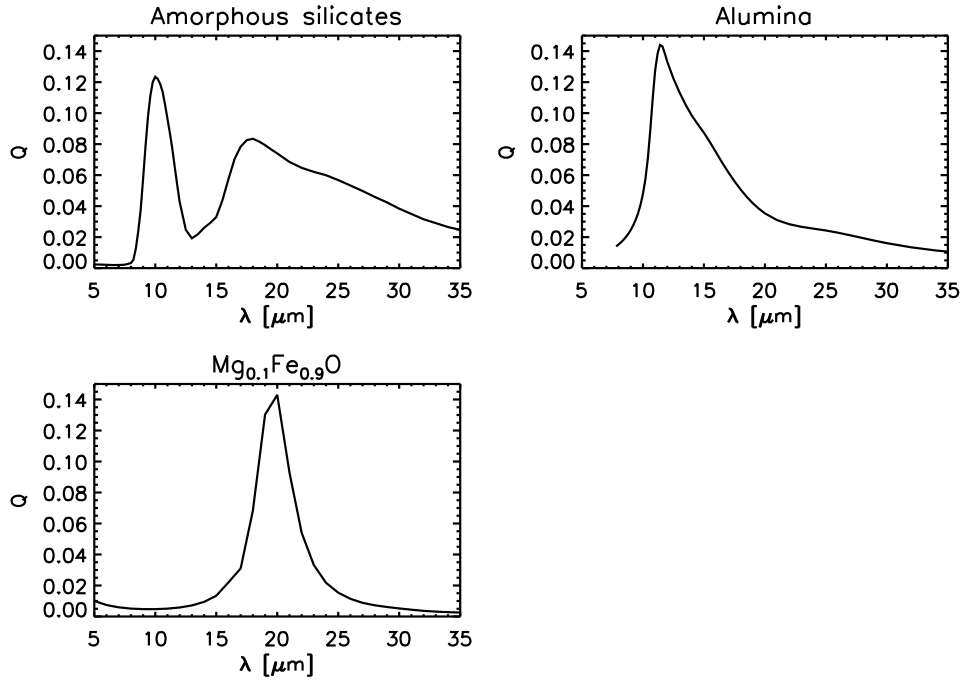

Figure 3.32: Efficiencies Q for different types of dust.

3.6.3 Dust features

In this section we describe the different dust species that can be easily detected in our sample of dust spectra, i.e. without need for radiative transfer modelling. Table 3.3 gives an overview on the detected features for each spectrum. Figure 3.32 shows the efficiencies Q of some dust species described in this section. This parameter indicates how well a dust species absorbs/emits at a certain wavelength and is here only mentioned for illustrative purposes.

3.6.3.1 Amorphous silicates

One of the most common features in oxygen-rich dust spectra are the broad features around 10 and 18 μm which originate from amorphous silicates. Figure 3.32 shows in the upper left panel the wavelength-dependent efficiencies Q for amorphous silicates. These features were first detected by Woolf and Ney (1969) and are very typical for oxygen-rich AGB stars. Also in this sample amorphous silicates can be very clearly seen, especially for the dust spectra shown in Figures 3.30 and 3.31.

The efficiencies Q for amorphous silicate have been compared with all the dust spectra. Based on this comparison, an inventory is made which lists the stars showing amorphous silicates (see Table 3.3).

3.6.3.2 Amorphous aluminum oxide grains

Another feature often seen in oxygen-rich dust spectra is a broad feature that peaks at ~ 11 μm, which is different from the amorphous silicate feature. This feature has already been detected in Mira variables observed with the Infrared Astronomical Satellite's Low Resolution Spectrometer (IRAS–LRS) by Little-Marenin and Little (1990), who propose crystalline olivine to be the carrier of this feature. Cami (2002) shows, based on ISO-SWS spectra, that this feature peaks at 11.1 μm, while crystalline olivines peak at slightly longer wavelengths (11.3 μm). Begemann et al. (1997) and Miyata et al. (2000) relate the 11 μm feature to amorphous aluminum oxide grains (alumina, Al_2O_3).

The upper right panel in Figure 3.32 shows the wavelength-dependent efficiencies for alumina. This shows that not only the peak position of alumina is different than for amorphous silicates, but also the shape of the 10 μm complex is different. Alumina shows a much broader profile and has a less steep slope at the red wing than the efficiencies of amorphous silicates show. Also for alumina we made an inventory of the objects that show this feature (see Table 3.3).

3.6.3.3 The 13 μm feature

Another feature which is clearly seen many spectra, but not in all of them, is the 13 μm feature. Vardya et al. (1986) discovered this feature when they studied IRAS-LRS spectra of about 20 Miras. They attributed the feature to "some sort of silicate". The feature was later associated with oxygen-rich AGB stars (Sloan and Price 1995). In the recent literature, many species have been proposed to be the carrier of the 13 μm feature. The 3 main candidates are corundum (crystalline Al_2O_3), spinel ($MgAl_2O_4$), and silicon dioxide (SiO_2) (see DePew et al. 2006, and references therein).

Because the carrier of the 13 μm feature is still rather unclear, we do not show efficiencies for this feature, but it can be easily spotted in many objects. Object J174140.0-282521 (number 15) shows a nice example of a 13 μm feature in its dust spectrum (see Figure 3.31).

3.6.3.4 The 19.5 micron feature

The 19.5 μm feature (sometimes also called the 19.8 μm feature) is a broad, but sharply peaked feature. Little-Marenin and Little (1990) and Goebel et al. (1994) already detected it in IRAS-LRS spectra. Cami (2002) proposed that the feature could be attributed to Mg-Fe-oxides ($Mg_{1-x}Fe_xO$) based on ISO-SWS observations of a sample of oxygen-rich AGB stars. Also Posch et al. (2002), Van Malderen (2003), and Heras and Hony (2005) prefer $Mg_{0.1}Fe_{0.9}O$ to explain the 19.5 μm feature seen in the ISO-SWS spectra they studied.

The emissivities for this feature are shown in the lower panel in Figure 3.32. This sharply peaked feature is clearly seen in only one object: J180259.6-300254, number 38 and possibly in J180308.2-295747 and J180323.9-295410 (numbers 43 and 49). Because the feature is lo-

Table 3.3: Analysis of the dust spectra. For each object this table gives the $(K_s - [15])_0$ colour, an estimate of the background residuals and an overview on the features seen in the dust spectra in Figures 3.15 to 3.17. The objects are ordered with increasing $(K_s - [15])_0$ colour. –/✓indicates the absence/presence of emission from the central star and the different features. The naked stars are also listed in this table.

	Number & Star	$(K_s - [15])_0$	estimate background residuals [%]	residual emission central star	alumina	amorphous silicates	13 μm feature	19.5 μm feature
32	J175517.0-294131	-0.01	10.99	naked star				
40	J180304.8-295258	0.48	12.73	naked star				
39	J180301.6-300001	0.48	16.31	naked star				
23	J174924.1-293522	0.78	13.47	naked star				
37	J180249.5-295853	0.79	9.24	naked star				
30	J175511.9-294027	0.81	16.31	naked star				
48	J180316.1-295538	0.82	9.49	naked star				
31	J175515.4-294122	0.92	9.59	–	✓	✓	✓	–
7	J174123.6-282723	0.97	40.02	–	–	✓	✓	–
47	J180313.9-295621	0.98	7.53	–	–	✓	–	–
25	J174948.1-292104	1.14	34.67	naked star				
12	J174130.2-282801	1.15	41.70	naked star				
51	J180333.3-295911	1.16	8.26	naked star				
42	J180305.4-295527	1.28	7.36	–	✓	✓	✓	–
36	J180248.9-295430	1.29	6.83	–	–	✓	–	–
22	J174917.0-293502	1.37	10.46	–	–	✓	–	–
24	J174943.7-292154	1.39	14.62	–	✓	–	✓	–
11	J174128.5-282733	1.48	42.63	–	✓	–	✓	–
10	J174127.9-282816	1.49	30.65	–	–	✓	✓	–
43	J180308.2-295747	1.52	6.90	–	✓	–	✓	✓
49	J180323.9-295410	1.54	7.42	✓	✓	✓	✓	✓
26	J174951.7-292108	1.55	30.17	–	✓	✓	–	–
52	J180334.1-295958	1.77	6.62	–	✓	✓	✓	–
45	J180308.7-295220	1.83	6.88	–	✓	✓	✓	–
35	J180238.8-295954	1.90	8.76	–	✓	✓	✓	–
41	J180305.3-295515	1.95	6.61	✓	✓	✓	✓	–
44	J180308.6-300526	1.98	8.95	✓	–	✓	✓	–
17	J174157.6-282237	1.99	44.23	–	–	✓	✓	–
46	J180311.5-295747	2.10	9.44	✓	✓	–	✓	–
50	J180328.4-295545	2.12	9.52	–	✓	✓	✓	–
28	J175456.8-294157	2.14	7.75	–	✓	✓	✓	–
5	J174117.5-282957	2.25	25.32	–	✓	✓	✓	–
27	J175432.0-295326	2.33	7.84	✓	✓	✓	✓	–
38	J180259.6-300254	2.48	7.37	✓	✓	✓	✓	✓
16	J174155.3-281638	2.57	21.03	–	✓	✓	✓	–
14	J174139.5-282428	2.59	45.31	✓	✓	✓	✓	–
9	J174127.3-282851	2.62	25.47	✓	–	✓	✓	–
15	J174140.0-282521	2.71	37.71	✓	✓	✓	✓	–
34	J180234.8-295958	2.87	8.13	✓	–	✓	✓	–
13	J174134.6-282431	3.00	44.13	✓	✓	✓	✓	–
19	J174203.7-281729	3.14	21.52	✓	–	✓	–	–
18	J174158.8-281849	3.21	24.82	✓	–	✓	✓	–
20	J174206.9-281832	3.45	19.49	–	–	✓	–	–
8	J174126.6-282702	3.77	40.87	–	–	✓	–	–
29	J175459.0-294701	4.17	9.74	–	–	✓	–	–

cated on top of the 18 μm amorphous silicate band, its presence is not always easy to discern.

3.6.3.5 Crystalline silicates

Crystalline silicates produce sharp features around 11, 16, 19, 23, 28 and 32 μm in the wavelength range of Spitzer-IRS and can be detected in the OH/IR stars (see e.g. the bumps at

Table 3.4: The dust characteristics. The normalised dust luminosity and its estimated uncertainty are derived. This table also gives the relative amount of alumina with respect to amorphous silicate and a 1-σ error and the silicate emission index as described by Sloan and Price (1995) using the method to create dust spectra described in Blommaert et al. (2006) The typical error on this SE index is about 1 (see text).

	Number & Star	normalised dust luminosity	$\sigma_{\rm ndl}$	alumina / (alumina + silicate)	$\sigma_{\rm al}$	SE index
5	J174117.5-282957	0.553	0.022	0.240	0.010	5
7	J174123.6-282723	0.349	0.167	0.128	0.009	7
8	J174126.6-282702	0.735	0.020	0.177	0.005	6
9	J174127.3-282851	0.474	0.016	0.175	0.004	5
10	J174127.9-282816	0.592	0.052	0.151	0.011	7
11	J174128.5-282733	0.396	0.048	0.420	0.010	3
13	J174134.6-282431	0.582	0.054	0.260	0.009	5
14	J174139.5-282428	0.501	0.033	0.254	0.010	4
15	J174140.0-282521	0.779	0.040	0.234	0.007	5
16	J174155.3-281638	0.716	0.015	0.251	0.010	5
17	J174157.6-282237	0.609	0.084	0.237	0.014	5
18	J174158.8-281849	0.632	0.015	0.143	0.004	6
19	J174203.7-281729	0.648	0.014	0.117	0.010	6
20	J174206.9-281832	0.759	0.007	0.054	0.004	8
22	J174917.0-293502	0.267	0.030	0.189	0.015	5
24	J174943.7-292154	0.050	0.005	1.000	0.033	1
26	J174951.7-292108	0.330	0.087	0.352	0.015	4
27	J175432.0-295326	0.479	0.007	0.290	0.007	4
28	J175456.8-294157	0.519	0.008	0.286	0.012	4
29	J175459.0-294701	0.724	0.001	0.122	0.003	7
31	J175515.4-294122	0.316	0.052	0.323	0.019	4
34	J180234.8-295958	0.495	0.004	0.207	0.006	5
35	J180238.8-295954	0.545	0.030	0.320	0.015	4
36	J180248.9-295430	0.430	0.034	0.276	0.021	5
38	J180259.6-300254	0.755	0.015	0.268	0.011	5
41	J180305.3-295515	0.586	0.011	0.321	0.017	4
42	J180305.4-295527	0.564	0.016	0.293	0.019	4
43	J180308.2-295747	0.305	0.018	0.652	0.019	2
44	J180308.6-300526	0.563	0.006	0.139	0.004	6
45	J180308.7-295220	0.560	0.028	0.474	0.022	3
46	J180311.5-295747	0.452	0.018	0.585	0.037	2
47	J180313.9-295621	0.426	0.051	0.137	0.011	8
49	J180323.9-295410	0.433	0.035	0.519	0.039	3
50	J180328.4-295545	0.594	0.018	0.285	0.011	4
52	J180334.1-295958	0.594	0.014	0.299	0.018	5

longer wavelengths in Figure 3.18, see also Chapter 5).

3.6.4 Dust luminosity

The amount of dust varies significantly between the different dust spectra shown in Figures 3.29 to 3.31. Assuming that the properties of the dust shells are identical except for the mass-loss rate, the flux received from the dust shell will be larger for an object with a larger amount of dust. Therefore, the integrated area under the dust spectrum, the integrated spectral flux density, can be used to quantify the amount of dust. We will call this value the dust luminosity. In most targets, the dust emission begins from 8 μm onwards and most spectra become very noisy beyond 33 μm (see also Section 3.3.3). Therefore the wavelength range used to calculate the dust luminosity is the interval between 8 and 33 μm (see insets Figures 3.23 and 3.25).

The dust luminosity provides a mass-loss estimator, which should be compared with the $(K_s - [15])_0$ parameter we introduced and discussed earlier. Before confronting both parameters,we point out a certain number of effects which may affect the accuracy of the dust luminosity as introduced above as a mass-loss tracer.
The first uncertainty comes from the spectra themselves. Due to the crowdedness, we could not always use all pixels in the slit belonging to the object as they were also affected by another close by object. Therefore, the spectra are not absolutely flux calibrated. In order to overcome this uncertainty, we calculated the integrated spectral flux density in the same wavelength range as for the dust luminosity (from 8 to 33 μm) for the original spectra and used it to normalise the dust luminosity. The calculated normalised dust luminosities are listed in Table 3.4.
Also the background residuals influence the normalised dust luminosity. Based on the electron counts in the images around the Si III line at 18.7 μm, we estimated the relative variance of the background (see Section 3.6.2.2 and Table 3.3), which can be used to estimate the effects of background residuals. If the background subtraction can e.g. be 10% off, than also the area under the spectra is about 10% off, both for the area under the dust spectrum as the area under the original spectrum. As these two values are divided to account for the possible offset in absolute flux calibration, error propagation is used to estimate the errors on the normalised dust luminosity by:

$$\sigma_{\mathrm{ndl}} = \sqrt{\left(\frac{\sigma_{\mathrm{bg}}}{b}\right)^2 + \left(\frac{a}{b^2}\sigma_{\mathrm{bg}}\right)^2}, \tag{3.1}$$

with σ_{ndl} the estimated uncertainty on the normalised dust luminosity, a = the integrated flux density of the dust emission, b = the integrated flux density of the dust and central star emission, and σ_{bg} the estimated uncertainties on the background. The derived values are listed in Table 3.4.

Figure 3.33 shows the $(K_s - [15])_0$ colour versus the normalised dust luminosity. The size of the symbols indicate the error-bars on the parameters. We will adopt this formalism (unless mentioned otherwise) throughout the entire chapter.

Based on the calculations in Vassiliadis and Wood (1993), Lattanzio and Wood (2003) showed that as the star evolves on the AGB and the mass-loss rate increases, also the pulsation period and the amplitude increase (i.e. Mira variables have larger amplitudes than

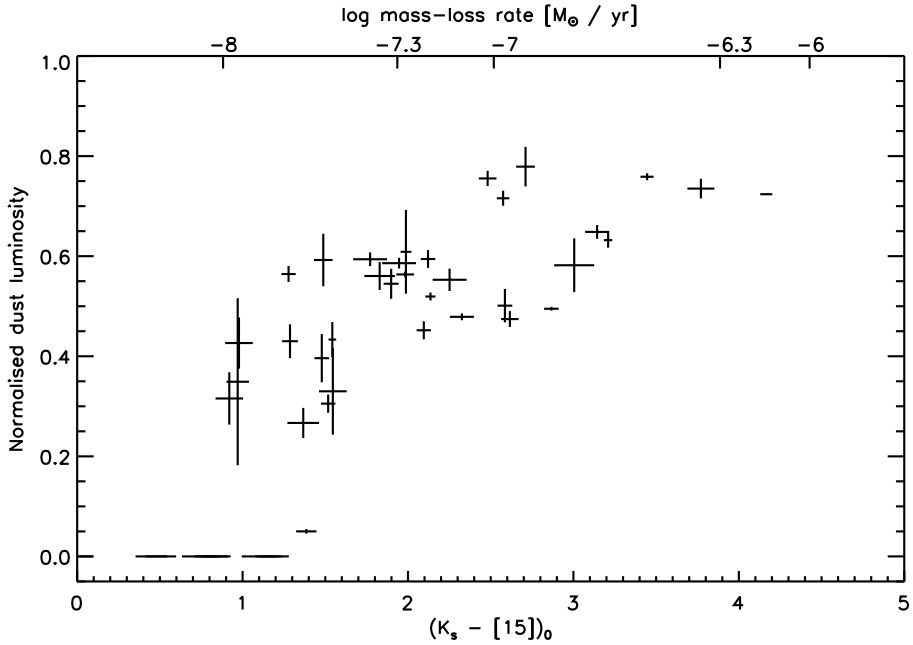

Figure 3.33: $(K_s - [15])_0$ colour used to select the sample versus the normalised dust luminosity. The error bars on $(K_s - [15])_0$ only indicate the photometric uncertainties. The error bars on the normalised dust luminosity are derived based on the values in Table 3.3 and are also listed in Table 3.4. The axis at the top of the figure indicates the different mass-loss rates as already shown in Figure 3.4.

semi-regular variables which are believed to be less evolved, see also Section 1.2.3). One has to keep in mind, however, that these objects do not have a constant position in the HR diagram and may alter between semi-regular and Mira variables (Speck et al. 2000, and references therein). Therefore the evolutionary sequence is not that straightforward.
The observations of the 2MASS K_s and the ISOGAL [15] magnitude have not been obtained simultaneously. Especially for the redder objects which have larger amplitudes, there can be a large shift in $(K_s - [15])_0$ due to the variability: a Mira variable e.g. can have an amplitude of about 1 mag in K. The uncertainties on $(K_s - [15])_0$ shown in Figure 3.33 are based on the photometric uncertainties listed in the 2MASS database for K_s and in the ISOGAL database for [15]. These uncertainties are therefore especially for the redder objects, an underestimate of the actual uncertainties as we did not account for variability. The error due to variability for the bluest sources is negligible.

The uncertainties on the normalised dust luminosity plotted in Figure 3.33 are derived based on the estimated variance in the background around the forbidden Si III line, see Eq. (3.1). As is to be expected, the variance in the background levels has a smaller influence on the objects with a larger dust contribution, which is illustrated in Figure 3.33.

Normalised dust luminosities for naked stars have not been calculated as these objects have per definition a zero dust contribution. In order to complete Figure 3.33 for the bluest colours, the $(K_s - [15])_0$ colour for the naked stars is added. For the reddest sources, the normalised dust luminosity reaches till $\sim$ 0.8. For the objects shown in this figure, a normalised dust luminosity of 1 cannot be reached. As long as the dust shell is optically thin, we always see the contribution of the central star. For the OH/IR stars on the other hand, the dust shell is optically thick, and the central star is hidden from the observer. These objects would therefore have a dust contribution of 1. We cannot show the OH/IR stars in this diagram: due to the large dust contribution, these objects were not detected in K_s and the objects selected from the IRAS catalogue were also not observed with ISOGAL.

Notwithstanding the estimated uncertainties, Figure 3.33 confirms that an increasing trend between $(K_s - [15])_0$ and the normalised dust luminosity occurs. From the uncertainties on both parameters, it is not surprising that this trend is not a clear one-to-one relation: there is a very large spread in normalised dust luminosity for objects with comparable $(K_s - [15])_0$ values as well as there is a very large spread in $(K_s - [15])_0$ colour for objects with comparable amounts of dust. For $(K_s - [15])_0 \sim 1$ e.g. we see objects with no signs of dust (the naked stars) as well as objects with a normalised dust luminosity of the order of 0.4. For objects with the same normalised dust luminosity there can be a colour difference of 2. All this indicates that $(K_s - [15])_0$ can be used at first as a mass-loss rate indicator, to obtain an initial idea, but independent methods are needed to derive good estimates for the mass-loss rates of the bluest objects. Such independent methods could come from detailed radiative transfer modelling, which is beyond the scope of this chapter.

3.6.5 Alumina and amorphous silicates

Alumina and amorphous silicates are the main contributors to the dust spectra in this sample of stars. In terms of the oxygen-rich dust condensation sequence, alumina is to be formed before amorphous silicates. To gain more information on the composition of the dust spectra in terms of amorphous silicates and alumina, the 10 μm complexes of the dust spectra were decomposed in function of the shape of alumina and amorphous silicates as shown in Figure 3.32. We fitted the dust spectrum from 8.5 to 12 μm with these efficiencies multiplied with a black body to estimate the relative contribution of alumina to amorphous silicates. We did not fit the dust spectra longward of 12 μm as many objects have a 13 μm feature which is not represented by this method. The temperature for alumina has been put at 1700 K (based on the condensation temperature of alumina, see Section 1.2.4), while the temperature for amorphous silicates has been chosen at 1000 K. Above this temperature (the glass temperature) silicates are formed as crystalline silicates (Tielens et al. 1997) which are not observed in AGB stars with optically thin dust shells, while amorphous silicates are one of the main contributors to the majority of the 10 μm complexes observed in this sample.

Figure 3.34 shows the 10 μm complexes of 4 objects (full black lines). Each panel also shows the efficiencies Q multiplied with a black body (dotted line represents alumina, dashed line amorphous silicates). The thick grey line shows the resulting fit. Two columns in Ta-

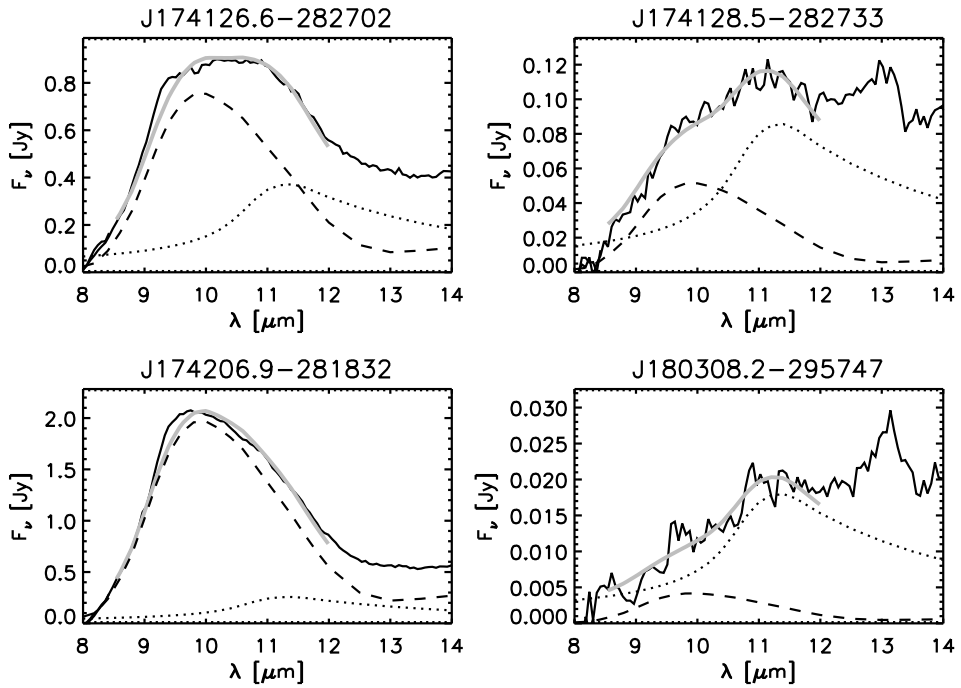

Figure 3.34: Dust spectrum for J174126.6-282702, J174128.5-282733, J174206.9-281832, and J180308.2-295747 in the wavelength range 8 – 14 μm. Shown underneath are the efficiencies Q for for alumina (dotted line) and amorphous silicate (dashed line) multiplied with a black body of respectively 1700 and 1000 K. The thick grey line gives the resulting fit.

ble 3.4 list the relative abundance of alumina to the total amount of alumina and amorphous silicate and a 1-σ error on the derived ratio.

Figure 3.35 shows the abundance of alumina relative to the amount of amorphous silicates (as listed in Table 3.4) in function of $(K_s - [15])_0$. The majority of our objects has a relative abundance of alumina with respect to amorphous silicates between 0.1 and 0.4. There is only one object with no indications of amorphous silicate and an additional five objects have slightly higher relative amounts for alumina than 0.4. There is also no object without alumina based on this method.

In our fit we only included two dust species (alumina and amorphous silicates). Including elements such as e.g. gehlenite (see Figure 1.5) would alter the relative amounts derived here as gehlenite has about the same profile as amorphous silicates in the 10 μm region. We expect that if we would have included also gehlenite, the importance of amorphous silicates would be lower, but no higher amount of alumina would be found.

In contrast to our results, Blommaert et al. (2006) found a majority of alumina-dust spec-

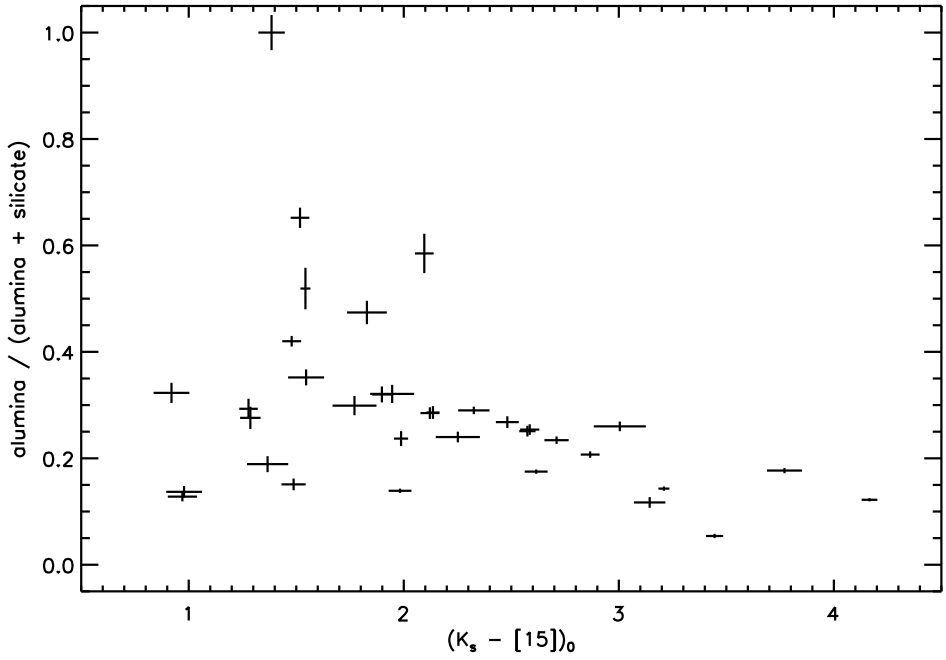

Figure 3.35: The relative abundance of alumina to amorphous silicates in function of the $(K_s - [15])_0$ colour.

tra for their sample of GB AGB stars. The sample studied in Blommaert et al. (2006) is however not as equally distributed over $(K_s - [15])_0$ as ours: relatively more blue objects were selected there which have a higher probability of exhibiting an alumina dominated dust spectrum. Nevertheless for the 6 sources we have in common, Blommaert et al. (2006) predict for all but one a much higher amount of alumina. J174943.7-292154 (object number 24) is the only object that can be fitted by only alumina in our sample and this is also found by Blommaert et al. (2006). In Section 3.4, we discussed the effect of the extinction law on the data and found that especially for the objects closest to the GC an additional correction for interstellar silicates is needed, using the Chiar and Tielens (2006) GC extinction curve. The majority of the objects in Blommaert et al. (2006) is located in fields c32 and c35, for which this extra correction was needed and which is not included in Cardelli et al. (1989) used by Blommaert et al. (2006) to correct their spectra for interstellar extinction. This alters the shape of the 10 μm complex in favour of the shape of alumina and therefore may explain why according to Blommaert et al. (2006) the sources are dominated by alumina-rich dust.

Dijkstra et al. (2005) studied the 10 μm feature of a sample of M-type stars in the LMC. Their analysis revealed that the objects with the lowest mass-loss rates show a dust composition that can be attributed to alumina and amorphous silicates, while the objects with the highest mass-loss rates are dominated by amorphous silicates. Heras and Hony (2005) stud-

ied a sample of oxygen-rich AGB stars with optically thin dust envelopes, with the lowest mass-loss rates in the order of 10^{-7} $M_{\odot}$/yr. They found that none of the objects can be modelled solely by alumina. Also Speck et al. (2000) found on a sample of AGB stars located in the solar neighbourhood that the broad feature seen in oxygen-rich dust spectra of these objects often assigned to alumina, cannot solely be attributed to alumina. The feature appears to be due to a combination of alumina and silicates such as e.g. amorphous olivine. The majority of objects in our sample can also not be explained with alumina alone, amorphous silicates are needed to model the shape of the 10 μm complex. In contrast to Speck et al. (2000), Dijkstra et al. (2005), and Heras and Hony (2005) we have found one object which shows a 10 μm complex attributed to only alumina.

Based on the oxygen-rich dust condensation sequence and our method to select this sample, we expected to find more objects with a large alumina content. One possible explanation for this discrepancy is the Al/Si-ratio content in our sample. Rich et al. (2007) show, based on high-resolution near-IR spectroscopy of 17 M giants in the inner GB, that the bulge is enriched in α-elements (see also Ballero et al. 2007; Fulbright et al. 2007; Rich and Origlia 2005). As Si is an α-element, while Al is not, it might be that objects in the GB have a higher intrinsic Si/Al ratio than what is seen for objects in the solar neighbourhood and therefore have a higher chance of forming silicates than alumina.

Although there is clearly no one-to-one relation between $(K_s - [15])_0$ and the relative amount of alumina and amorphous silicate, there exists a trend of decreasing relative amount of alumina with respect to amorphous silicates for objects with redder $(K_s - [15])_0$ colours. For the bluest objects on the other hand, there exists a very large scatter with respect to dust composition and we therefore cannot predict the relative amount of alumina with respect to amorphous silicates based on $(K_s - [15])_0$. A possible explanation for this large scatter in dust composition for the bluest objects could come from aspherical mass loss (Heras and Hony 2005, and references therein). If there are clumps of higher density in the CSE, amorphous silicates could already be formed in these regions, although we may not have expected their presence based on the integrated mass-loss rate.

3.6.6 Silicate Emission index

Little-Marenin and Little (1990) observed IRAS-LRS spectra of oxygen-rich Mira variables and classified their spectra based on the emission features around 10 μm into 7 groups. Also Sloan and Price (1995) derived a classification scheme for oxygen-rich AGB stars based on IRAS-LRS observations, consisting of 8 groups, the so-called silicate emission (SE) index (see their Figure 3). The smaller the SE index of an object, the broader the 10 μm complex. Based on the oxygen-rich dust condensation sequence, the AGB stars are supposed to move through these SE classes. The very broad 10 μm complex indicates alumina dust. While moving through the classes, the feature becomes narrower and the peak position shifts towards shorter wavelengths. This indicates that the amount of silicate increases with respect to the amount of alumina. Stars in group 8 have a dust spectrum that is dominated by emission from amorphous silicates. This SE index provides another approach to quantify dust spectra which we here apply to the data we have obtained.

Sloan and Price (1995) used a method to derive the dust spectra which is different from the method explained in Section 3.6.2.1. To model the central star, Sloan and Price (1995) used an Engelke function and modified it using IRAS-LRS observations of five bright naked giants. This modification of the Engelke function is needed to model also the strong SiO band around 8 μm. To be able to compare our results with the results of Sloan and Price (1995), we calculated additional dust spectra for our targets using the method described in Blommaert et al. (2006). Their method is very similar to the method described in Sloan and Price (1995). Blommaert et al. (2006) also adapted an Engelke function, but instead of using naked stars to model the SiO profile, they used the absorption profile of the SiO band from MARCS theoretical modelling for a 3500 K M giant and scaled the feature to get the same absorption maximum as Sloan and Price (1995).

To derive the SE index, the fluxes at 10, 11, and 12 μm were obtained from the dust spectra. Sloan and Price (1995) found that the flux ratios follow a power law:

$$F_{10}/F_{12} = 1.32(F_{10}/F_{11})^{1.77},$$

with F_{10}, F_{11}, and F_{12} respectively the flux in the dust spectrum at 10, 11, and 12 μm. The silicate emission index (SE) is then derived using the ratio of the flux at 11 and 12 μm:

$$\mathrm{SE} = 10(F_{11}/F_{12}) - 7.5.$$

This ratio classifies the objects into the 8 different groups (see Fig. 2 in Sloan and Price 1995). The value is truncated and not rounded.

The dashed line in Figure 3.36 shows the power law derived by Sloan and Price (1995). The diamonds are the flux ratios derived from the dust spectra created in this chapter. This figure indicates that our data are very well represented by this power law. There are only two objects that could be considered as outliers: J174917.0-293502 and J180313.9-295621 (resp. numbers 22 and 47). These two stars are among the objects with the bluest $(K_s - [15])_0$ colours (see Figure 3.29 and Table 3.4) and therefore the subtraction of the central star in order to obtain a dust spectrum has a larger influence on the final dust spectrum than for stars with redder $(K_s - [15])_0$ colours. This could explain why these stars seem to be outliers. The majority of the objects in Sloan and Price (1995) have an F_{10}/F_{11} ratio between 0.6 and 1.4 and an F_{10}/F_{12} ratio between 0.5 and 2. The majority of this sample of stars has an F_{10}/F_{11} ratio between 0.5 and 1.5 and an F_{10}/F_{12} ratio between 0.5 and 2.5, which is very similar to Sloan and Price (1995).

The plus-signs in Figure 3.36 represent the flux ratios derived using the method in Blommaert et al. (2006). These flux ratios are very similar to the flux ratios based on the dust spectra derived in Section 3.6.2.1 (diamonds). This is to be expected as the method described in Sloan and Price (1995) traces the shape of the 10 μm complex. The shape of the 10 μm complex can be altered by the method used to create the dust spectra (see also Section 3.6.2) and therefore the differences between the flux ratios using the two methods indicate the uncertainty on the classification method described in Sloan and Price (1995). Because the flux ratios between our method and the method described in Blommaert et al. (2006) are very similar and because we want to derive SE indices in the same way as Sloan and Price (1995), we

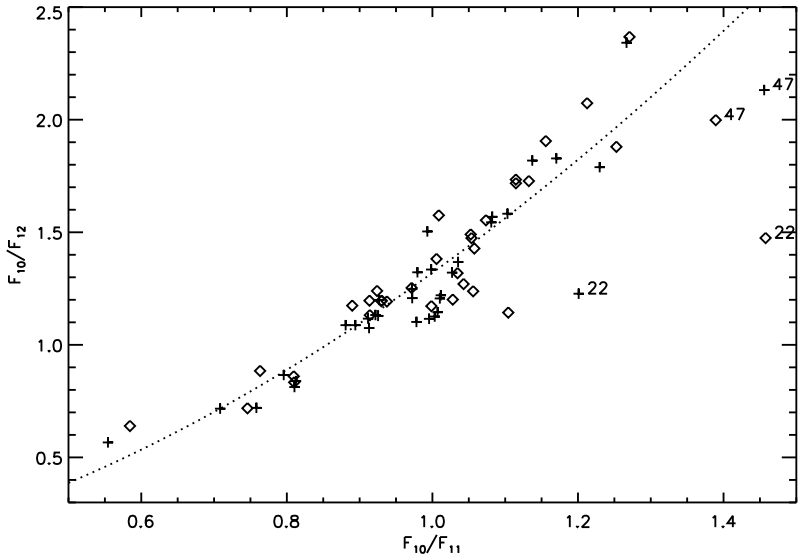

Figure 3.36: F_{10}/F_{11} vs. F_{10}/F_{12}. The dotted line indicates the power law from Sloan and Price (1995). The plus-signs originate from the dust spectra created in the same way as Blommaert et al. (2006). The diamonds represent the dust spectra created in Section 3.6.2.1.

will continue the analysis of the SE index with the dust spectra created in this section based on the method of Blommaert et al. (2006). The resulting SE indices are given in Table 3.4. If we would have used the dust spectra created in Section 3.6.2.1 the difference between the derived SE indices is of the order of 1. Therefore we assume a typical error of 1 on the SE indices induced by the creation of dust spectra.

Figure 3.37 shows the distribution of SE indices. At least one object is found for each SE index; the majority of our objects have an SE index of 4 or 5. There is no obvious reason based on a visual inspection of the dust spectra to why the objects are clustered at SE indices 4 and 5. Based on the decomposition of our objects in alumina and amorphous silicates in the previous section, we already noted that we have very few objects dominated by alumina rich dust. The majority of our dust spectra had a relative abundance of alumina to amorphous silicates between 0.1 and 0.4. This is also reflected in the SE indices as the majority of our objects are situated in classes 4 and 5. The shape of the 10 μm complex for objects in these classes are determined by a mixture of alumina and amorphous silicate dust.

Based on the definition of the SE index and the method used to derive the relative abundance of alumina with respect to amorphous silicates, we expect to find a clear decreasing trend between these two parameters. Figure 3.38 shows the relative amount of alumina with respect to the amorphous silicates in function of the SE index: the expected trend can be clearly seen. This shows that these two parameters trace the same aspect about the 10 μm

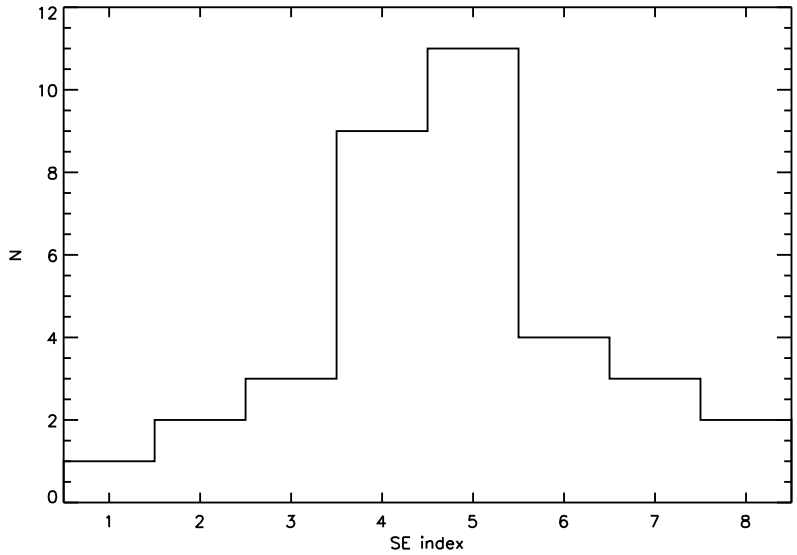

Figure 3.37: Histogram showing the distribution of SE indices.

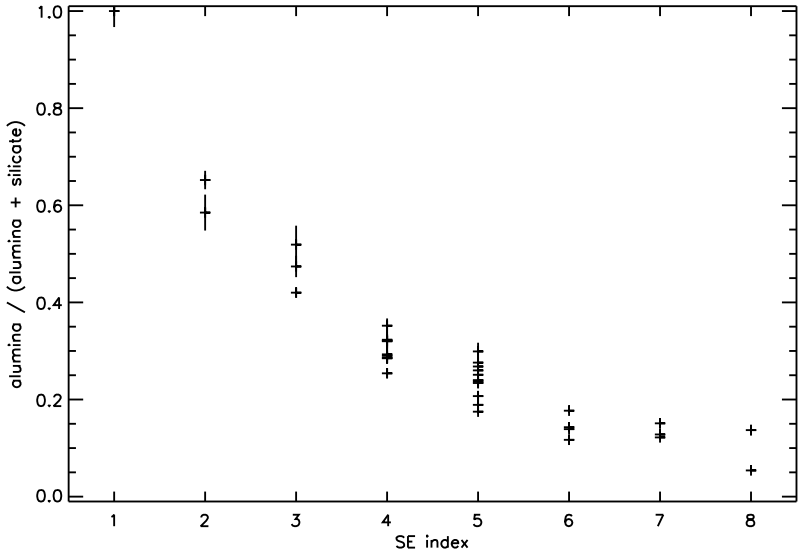

Figure 3.38: The relative amount of alumina to amorphous silicates in function of the SE index.

complex: the shape which is dependent on the composition of the dust. Also the small spread in the relative abundance of alumina within one SE index is expected because the SE index is a discrete parameter while the relative abundance of alumina is defined as a non-discrete parameter. We also have to keep in mind that the error on the SE index (which is not shown in this diagram) is about 1 index.

3.7 Discussion

As an AGB star moves up the mass-loss sequence as shown in Figure 3.4, it creates a circumstellar dust shell. Based on the oxygen-rich dust condensation sequence, the first dust species to form is alumina. When the AGB star belongs to the reddest objects in $(K_s - [15])_0$, the dust spectrum of the star will be dominated by amorphous silicate emission (see also Sections 1.2.4 and 3.6.3.1). Since the stars in our sample are selected based on their $(K_s - [15])_0$ colour, which is believed to be a mass-loss indicator (Ojha et al. 2003), the stars are observed in different stages of the evolution on the AGB. Therefore we expect to see different phases of the oxygen-rich dust condensation sequence in the spectra because the freeze-out occurred at a different steps in the condensation sequence (see also Section 3.2).

In this section we will discuss all the derived parameters based on the obtained dust spectra in function of each other and the oxygen-rich dust condensation sequence.

3.7.1 Qualitative interpretation of the dust spectra in function of the mass-loss rate indicator

As can be seen from Figure 3.15 the stars with the bluest $(K_s - [15])_0$ colours show hardly any dust. We also noted that there are already objects which show a small dust contribution but which have bluer colours than the reddest naked star. This indicates that $(K_s - [15])_0$ can have a large spread for objects with about the same mass-loss rate, at least for the lowest mass-loss rates.

Table 3.3 revealed that the bluest object in our sample exhibiting a dust contribution, not only shows signs of alumina but also the 9.7 and 18 μm emission bands of amorphous silicates can be detected. There are only 4 objects in our sample which show no clear signs for amorphous silicate dust. Table 3.3 also shows that most of these objects are situated in the first half of the given sequence arranged for increasing $(K_s - [15])_0$, but these objects do not have the bluest $(K_s - [15])_0$ colours.
Most of the objects which show no clear evidence for alumina dust have the reddest colours and are therefore expected to have the largest mass-loss rates. There are also some of the bluest stars that show no signs of alumina. Based on the oxygen-rich dust condensation sequence, this is quite unexpected. Because of the freeze-out, the bluest objects with the lowest mass-loss rates are expected to be dominated by alumina rich dust, rather than amorphous silicate dust.

To illustrate the differences (and similarities) in the dust spectra with respect to increasing $(K_s - [15])_0$, we selected 8 stars equally spread over the $(K_s - [15])_0$ sequence throughout this sample. The stars selected (with their numbers given between parenthesis) are J175515.4-294122 (31), J174917.0-293502 (22), J180323.9-295410 (49), J180305.3-295515 (41), J175456.8-294157 (28), J174139.5-282428 (14), J174203.7-281729 (19), and J175459.0-294701 (29). For these stars the dust spectra are shown in Figure 3.39 with in addition the wavelength-dependent efficiencies for the different dust components shown in Figure 3.32. This figure is merely an illustration of the possible presence of certain dust components and does not have the intention to actually fit the shown dust spectra. The chosen emissivities are compact alumina, amorphous silicate, and $Mg_{0.1}Fe_{0,9}O$. As the carrier of the 13 μm feature is still uncertain (see Section 3.6.3.3), we do not show emissivities for a possible carrier of this feature.

J175515.4-294122 is the first object shown in Figure 3.39. It is the object with the bluest $(K_s - [15])_0$ colour showing a dust contribution. The blue side of the 10 μm complex coincides with the efficiencies for amorphous silicates as well is there an 18 μm emission band present in the dust spectrum. The amorphous silicates alone cannot explain the entire 10 μm complex. The slope of the red wing of the emissivity of compact alumina is very similar to the slope of the red flank of the 10 μm complex, suggesting that this feature could also be partially attributed to alumina. This object also shows a clear 13 μm feature.
The next star in Figure 3.39 is J174917.0-293502. The dust spectrum resembles the emissivity for amorphous silicate and there does not seem to be any other feature present.
J180323.9-295410 shows a dust spectrum dominated by alumina dust and also a 13 μm feature is present. Additional flux at shorter wavelengths than the emissivities for alumina can be found in this object. Since there is also indication for an amorphous silicate band at 18 μm, the additional flux seen in this dust spectrum could be due to amorphous silicate. This object also exhibits a 19.5 μm feature.
The following three stars in the figure (J180305.3-295515, J175456.8-294157, and J174139.5-282428) are very similar. For these objects, the slope of the red wing of the 10 μm complex resembles the slope of alumina, while the slope of the blue wing resembles the slope of amorphous silicates. For these objects, we also see a clear emission bump around 18 μm, which originates from amorphous silicates. This suggest that these stars contain both alumina and amorphous silicates. These three objects also show a clear 13 μm feature.
The shape of the dust spectrum for the last two stars (J174203.7-281729 and J175459.0-294701) resembles the shape of the dust spectrum of J174917.0-29350. These two stars are dominated by amorphous silicate and show no sign for any other dust feature in their spectra.

Based on this analysis and the results given in Table 3.3 we see no obvious trend between the dust composition and the general shape of the dust spectra with respect to the $(K_s - [15])_0$ colour of the object, especially not for the bluest objects. This lack of a trend between $(K_s - [15])_0$ and the dust composition is unexpected.

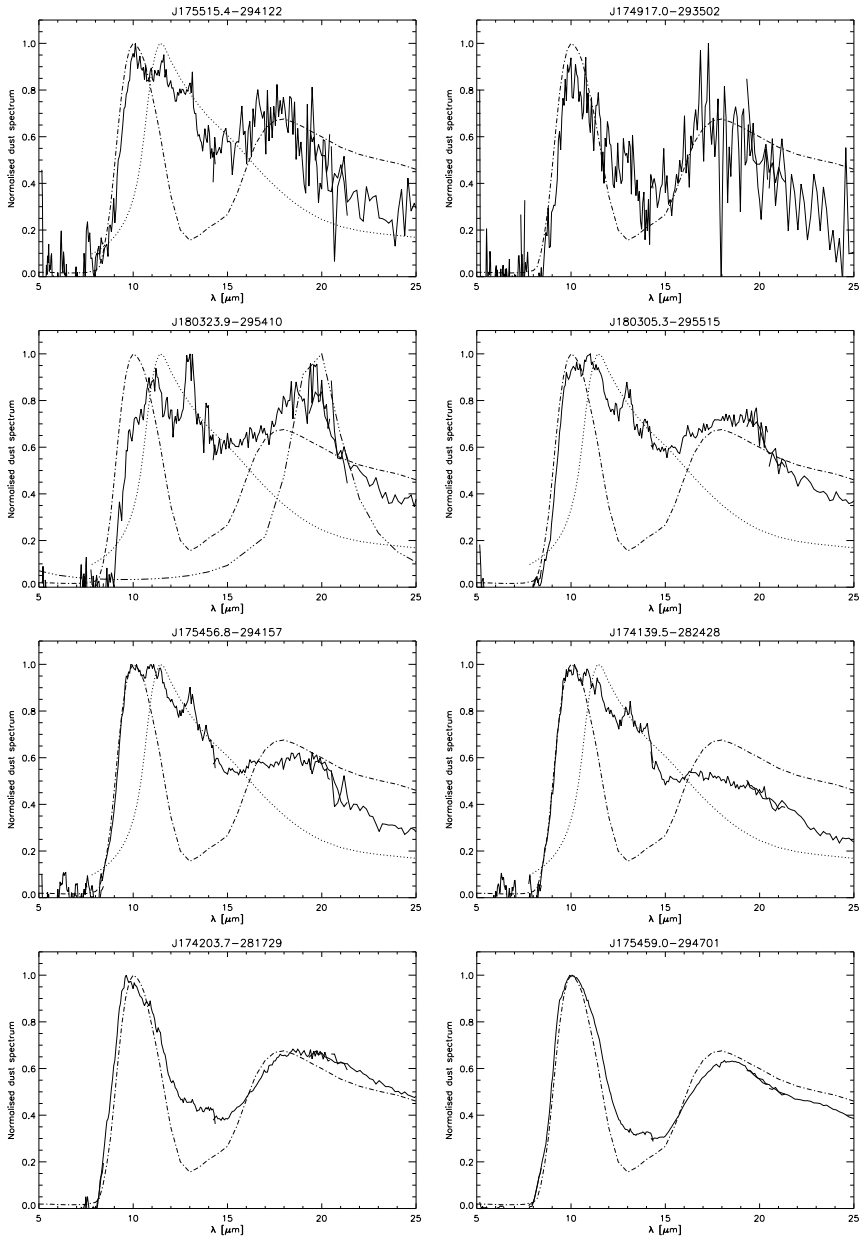

Figure 3.39: Normalised dust spectra for 8 AGB stars. The $K_{s,0} - [15]$ colour increases from left to right and top to bottom. Overplotted are the emissivities for compact alumina (dotted line), amorphous silicate (dash-dotted line), and $Mg_{0.1}Fe_{0.9}O$ (dashed-triple dotted line).

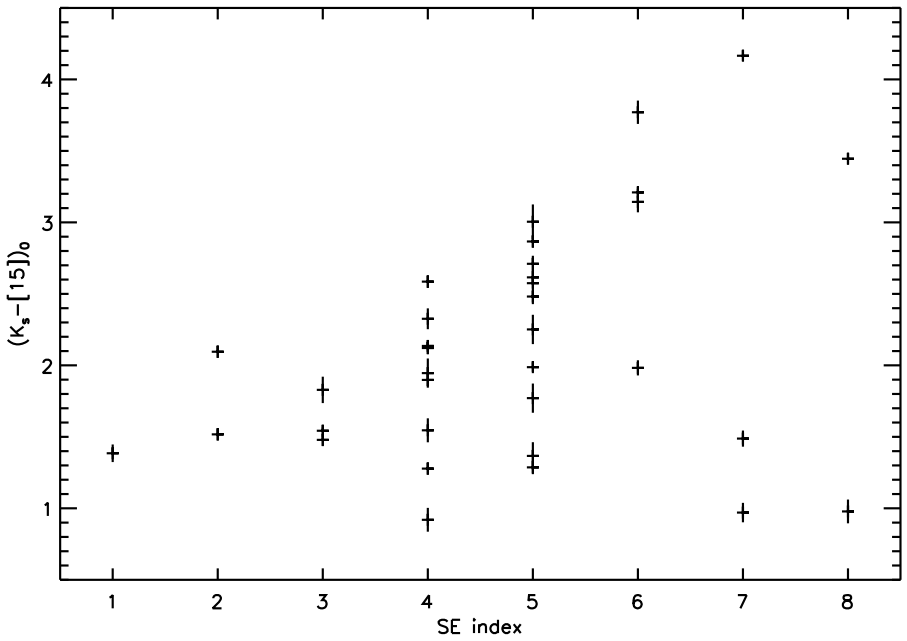

Figure 3.40: Silicate Emission index versus $(K_s - [15])_0$.

3.7.2 The shape of the 10 μm complex in function of the mass-loss rate

We investigated the shape of the 10 μm complex in two ways in the previous sections. We decomposed the 10 μm complex in function of the efficiencies of alumina and amorphous silicates and derived a relative abundance of alumina with respect to the amorphous silicates. Using the method described in Sloan and Price (1995) we also grouped our dust spectra in terms of the shape of their 10 μm complexes based on their fluxes at 10, 11, and 12 μm.

Since the SE indices trace the shape of the 10 μm complex and since based on the oxygen-rich dust condensation sequence it is expected that the 10 μm complex becomes less broad as the object evolves, it can be expected that AGB stars move through these 8 different SE indices. Figure 3.40 shows the $(K_s - [15])_0$ colour in function of the SE index. This diagram seems to suggest an increasing trend between $(K_s - [15])_0$ and the SE index as there are no data points located in the upper left corner of the scatter plot. But the spread on this possible increasing trend is very large and can be about 2 magnitudes, or larger, in $(K_s - [15])_0$ within one index (see e.g. the higher SE indices). What can be deduced from this figure is that for an object with a certain $(K_s - [15])_0$ colour, it must have a certain SE index or higher. For example, if an object has an $(K_s - [15])_0$ colour of about 3, than it must have an SE index of 5 or higher. For $(K_s - [15])_0$ colours bluer than about 1.5 every SE index is possible. This again shows that based only on the $(K_s - [15])_0$ it is impossible, especially for the bluest objects, to predict the shape of the 10 μm complex or the dust composition of the CSE.

Table 3.5: Relative numbers of dust spectra exhibiting a 13 μm feature within one SE index.

SE index	1	2	3	4	5	6	7	8
Objects with 13 μm feature [%]	100	100	100	87.5	81.2	50.0	66.7	0

Figure 3.38 suggests that the SE index classifies the objects based on their shape in a reliable way. This does not explain why we find the majority of our objects in SE indices 4 and 5 or equivalent with a relative abundance of alumina to amorphous silicates of between 0.1 and 0.4. Based on the oxygen-rich dust condensation sequence, it is expected that as the mass-loss rate increases, and therefore also the particle densities in the outflow, the amount of alumina gradually decreases as other elements form from the Al-rich condensation sequence (see Figure 1.5). This decreasing trend for alumina does clearly not scale linearly with increasing mass-loss.

Based on the analysis of the SE indices as well as the decomposition of the 10 μm complexes in terms of amorphous silicates and alumina, we conclude that the formation of amorphous silicates must already occur for fairly low mass-loss rates. Alumina seems to be a dust component present in the dust spectra of even the stars with the reddest $(K_s - [15])_0$ colours or the highest mass-loss rates, but there are no red objects with relatively high amounts of alumina.

3.7.3 Appearance of the 13 and 19.5 μm features

Hron et al. (1997) showed that the carrier of the 13 μm feature is very sensitive to the physical conditions in the dust shell: the feature only appears in a narrow range of effective temperature and optical depth of the dust shell. Therefore the feature does not appear in all the targets of the samples of Little-Marenin and Little (1990) and Sloan and Price (1995). This is also seen in this sample.

Table 3.3, arranged for increasing $(K_s - [15])_0$ colour, shows for which objects we detect a 13 μm feature. Almost all objects in our sample show a 13 μm feature although it is not always present for the bluest and the reddest objects. If Tables 3.3 and 3.4 are compared as well as the dust spectra with respect to their SE index, this reveals that all the objects with an SE index of 3 or smaller have a 13 μm feature. For the objects with the higher SE indices, there are fewer objects exhibiting a 13 μm feature. This is summarised in Table 3.5: for each SE index we give the percentage of objects exhibiting a 13 μm feature. From this table it appears that the 13 μm feature is always present for the objects with relative high abundances of alumina or a small SE index, while this is not necessarily the case for the objects which are dominated by amorphous silicates. If we can interpret the SE indices in terms of an evolutionary sequence, than the 13 μm feature occurs to be one of the first dust species formed and it disappears again for objects which are dominated by amorphous silicates. This feature is also not seen in the OH/IR stars which are believed to be at the end of their evolution on the AGB.

There are only three objects in this sample for which a 19.5 μm feature is detected. This is in contrast to the AGB stars discussed in Cami (2002) for which this feature is seen in almost every object. Concerning the presence of the 19.5 μm feature, we have to keep in mind that this feature is located in the wavelength regions which show the largest background residuals. This may explain why we did not clearly detect the feature in some of our spectra. Nevertheless the difference between our sample and the sample studied in Cami (2002) is very large with respect to the 19.5 μm feature. This suggests that the difference between these two samples may be intrinsic to the location of the objects: the sample of Cami (2002) is located in the solar neighbourhood, while our sample is selected using AGB stars located in the GB, which have a subsolar metallicity (see Chapter 7).

Sloan et al. (2003) studied ISO-SWS spectra of objects with an oxygen-rich dust shell available in the ISO archive. Based on this study, they found a correlation between the presence of the 13 and the 19.5 μm feature. Based on the objects in our sample, a correlation between the 13 and the 19.5 μm feature cannot be found. Table 3.3 only shows that if we detect a 19.5 μm feature, also a 13 μm feature is detected, the presence of a 19.5 μm feature if there is a 13 μm feature present cannot be confirmed using this sample.

3.7.4 The effect of a thermal pulse on the dust composition

AGB stars are known to go through luminosity dips during the TP-AGB phase (see also Section 1.2.2). Vassiliadis and Wood (1993) calculated evolutionary models for stars with initial masses in the range $0.89 \leq M_*/M_\odot \leq 5.0$ from the main-sequence phase up to the end of the AGB. These models show that thermal pulses occur about every 10^5 year for a star with an initial mass of 1.5 $M_\odot$, a He-mass fraction Y of 0.25 and metallicity Z of 0.008 (see Fig. 5 in Vassiliadis and Wood 1993). They state that the behaviour of stars with this abundance is also typical for stars with other abundances and therefore we will use the results of this model to look into the effect of thermal pulses. For the low-mass stars, Vassiliadis and Wood (1993) found that following each thermal pulse, there is a brief ($\sim$ 500 yr) pulse of surface luminosity followed by a substantial luminosity dip which lasts for $\sim$ 20% – 30% of the flash cycle. In our case for a star of $\sim$ 1.5 $M_\odot$, this means that the star spends about $(2-3) \times 10^4$ years in this luminosity dip. After this, the luminosity rises again to a value which increases slowly with time until the next thermal pulse occurs and the entire cycle starts over again.

In order to test if the bluest objects with a dust contribution and a clear amorphous silicate dominated dust spectrum are caused by a thermal pulse, we can make a rough calculation which will give us an estimate of the time needed before the grains reach the region were we observe the amorphous silicates. If this timescale is short (i.e. a few hundred years) this means that the we see the dust that is formed very recently, if this timescale is long (i.e. a few thousand years), this could mean that we still see dust that is formed a long time ago in evolutionary terms. In case of the latter, this would suggest that even if the mass-loss rate is smaller due to the thermal pulse, we can still see the dust from when the object had a higher mass-loss rate at the end of the previous thermal cycle. The luminosity L_* of a star is given by:

$$L_* = 4\pi R_*^2 \sigma T_{\rm eff}{}^4, \tag{3.2}$$

with R_* the radius of the star and σ the Stefan-Boltzmann constant. If the grains have a radius a, a temperature T_g, are at a distance R_g, and if we assume that the grains behave like a black body, then the energy absorbed by the grains per second is given by $L_* \frac{\pi a^2}{4\pi R_g^2}$. The energy re-radiated by the grains per second is then given by $4\pi a^2 \sigma T_g^4$. In equilibrium the later two equations must be equal:

$$\begin{aligned} L_* \frac{\pi a^2}{4\pi R_g^2} &= 4\pi a^2 \sigma T_g^4, \text{ and} \\ L_* &= 16\sigma\pi R_g^2 T_g^4. \end{aligned} \tag{3.3}$$

Eqs. (3.2) and (3.3) must also be equal and we find that

$$\begin{aligned} R_*^2 {\mathrm{T_{eff}}}^4 &= 4R_g^2 T_g^2, \text{ or} \\ R_g &= \frac{R_*}{2}\left(\frac{\mathrm{T_{eff}}}{T_g}\right)^2. \end{aligned}$$

If we assume the object has a $\mathrm{T_{eff}}$ of 3000 K and the dust observed is about 300 K, than the radius of the location of the grains is given by $\mathrm{R_g} = \mathrm{R_*}/2\left(\frac{3000}{300}\right)^2 \mathrm{R_*} = 50\mathrm{R_*}$. A typical radius for an AGB star is about 350 solar radii or $\mathrm{R_*} \approx 350 \times 7 \times 10^{10}$cm $\approx 2.45 \times 10^{13}$cm, thus $\mathrm{R_g} \approx 1.225 \times 10^{15}$cm. If we assume a very slow wind of about 5 km/s, than the time needed for the particles to reach the area were the dust has a temperature of about 300 K is given by $t = \frac{\mathrm{R_g}}{v_{\mathrm{wind}}} = \frac{1.225\times10^{15}}{5\times10^5}$ s$= 2.45 \times 10^9$ s which is about 78 years. 78 years is a very short time scale, which means that we observe the dust as it is formed, and that we do not see older dust as this has already moved away too far and is now too cool to detect in the Spitzer-IRS wavelength region. Therefore these objects must be really creating amorphous silicate at the time being and the anomalies observed cannot be attributed to the effects of thermal pulses.

3.8 Summary and conclusions

We obtained for a sample of GB AGB stars Spitzer-IRS spectroscopy. The AGB stars are selected based on their $(K_s - [15])_0$ colour to represent the mass-loss sequence along the AGB. In order to create dust spectra, objects with no signs of dust contribution, the naked stars, were selected. A fairly large spread of about 1.17 mag in $(K_s - [15])_0$ was found for objects with no signs of dust contribution. A colour temperature difference between the naked stars, probably induced by the presence of a water layer, is able to explain the observed spread. The naked stars were then used to create dust spectra for the other targets.

For each dust spectrum we investigated if the spectrum contains alumina, amorphous silicates, and a 13 μm feature. We also searched the spectra for the presence of the 19.5 μm $Mg_{0.1}Fe_{0.9}O$ feature, but it can only be detected in three objects. The 13 μm feature can be seen in the majority of the dust spectra, but it is detected in a smaller percentage of objects with the reddest $(K_s - [15])_0$ colours. Crystalline silicate features are only seen in the OH/IR stars (see also Chapter 5).

Using these dust spectra, the normalised dust luminosity has been calculated. We showed that this parameter shows an increasing correlation with $(K_s - [15])_0$.
Using the efficiencies of alumina and amorphous silicate, we decomposed the 10 μm complex of the dust spectra in terms of relative abundances of alumina with respect to amorphous silicates. This revealed that the majority of our objects have a relative abundance of alumina between 0.1 and 0.4. We only found one object which is fitted solely by amorphous alumina. Also the silicate emission (SE) index has been derived. The majority of our objects have an SE index of 4 or 5, which is consistent with the found relative abundance of alumina to amorphous silicates.

Based on the analysis in this chapter, we found no clear relation between $(K_s - [15])_0$, a mass-loss rate indicator, and the dust composition of the objects with respect to the oxygen-rich dust condensation sequence, especially for the bluest objects. Independent mass-loss estimates for these objects (coming from e.g. detailed radiative transfer modelling) will therefore most likely alter the order in which the spectra were arranged in the different figures. Nevertheless even if the spectra are arranged in a slightly different order, we still do not expect to find a very clear relation between the mass-loss rate and the oxygen-rich dust condensation sequence. Which indicates that the dust formed around oxygen-rich AGB stars does not necessarily occur under the circumstances of thermodynamic equilibrium under which the oxygen-rich dust condensation sequence is developed.
Another effect that may have an important role in this is the metallicity. If the objects have a different metallicity, the sample may not be as homogeneous as we anticipated. This will be discussed in Chapters 4 and 6.

Acknowledgements. This work is based on observations made with the Spitzer Space Telescope, which is operated by the Jet Propulsion Laboratory, California Institute of Technology under a contract with NASA. The IRS was a collaborative venture between Cornell University and Ball Aerospace Corporation funded by NASA through the Jet Propulsion Laboratory and Ames Research Center. SMART was developed by the IRS Team at Cornell University and is available through the Spitzer Science Center at Caltech. This publication makes use of data products from the Two Micron All Sky Survey, which is a joint project of the University of Massachusetts and the Infrared Processing and Analysis Center/California Institute of Technology, funded by the National Aeronautics and Space Administration and the National Science Foundation.

CHAPTER 4

Ground-based observations of a sample of Galactic Bulge AGB stars

This chapter is based on the paper:
Vanhollebeke, E., Wood, P.R., and Blommaert, J.A.D.L. : 2007, "Ground based observations of a sample of Galactic Bulge AGB stars", Astron. Astrophys., to be submitted

The inner regions of our Milky Way Galaxy are an ideal environment to study different stellar populations, amongst which are AGB stars. There are several advantages of studying AGB stars in the Galactic Bulge (GB), besides their large numbers. Groenewegen and Blommaert (2005) showed that the Mira population in the GB originates from stars with initial masses from 1.5 – 2 $M_{\odot}$. In addition, these AGB stars have a similar distance which makes it possible to compare the stars directly. The differences seen between these AGB stars must then originate from different evolutionary stages. In Chapter 3 we selected a sample of AGB stars in the GB to study the dust formation process along the AGB using Spitzer-IRS observations. We obtained additional ground-based data for this sample of stars, which will be discussed in this chapter.

The observations and data reduction are discussed in Section 4.1. An overview on the spectral features in this sample is given in Section 4.2. Section 4.3 shows the characteristics for this sample of AGB stars and explains how we can obtain that information from our data. In Section 4.4 we discuss the derived parameters and look for correlations. Finally in Section 4.5, we summarise and come to the conclusions.

Table 4.1: Overview of the grisms used to obtain the near-IR spectroscopy.

Grism	Wavelength range μm	Dispersion Å/pixel
J	0.99 – 1.32	13.76
H	1.50 – 1.81	15.89
K	1.98 – 2.47	21.50

4.1 Observations and data reduction

We have obtained ground-based observations of the Spitzer targets given in Chapter 3. Information on the targets (e.g. Ra, Dec, 2MASS and ISOGAL magnitudes) can be found in Table 3.2. The numbers identifying the targets and given in Tables 4.6 – 4.9 are the numbers given to the objects in Chapter 3. Figure 3.5 shows the position of the stars in the (l, b) plane with respect to the Galactic Centre (GC).

4.1.1 Optical spectroscopy

Optical spectroscopy has been obtained using the Double-Beam Spectrograph (DBS) mounted on the Nasmyth focus of the Australian National University 2.3-m telescope (sometimes also called the Advanced Technology Telescope) at Siding Spring Observatory (Australia). More information on the instrument can be found in Rodgers et al. (1988). Standard IRAF reduction routines were used for the data reduction. After additional extinction correction (see Section 4.1.3), this resulted in medium-resolution spectra from 0.6 – 0.95 μm with a dispersion of $\sim$ 4.1 Å/pixel, shown in Figures 4.17 – 4.19.

4.1.2 Near-IR observations

Using the Cryogenic Array Spectrometer and Imager (CASPIR), also mounted on the Australian National University 2.3-m telescope, we obtained near-IR observations for our sample. CASPIR (McGregor, P. and Hart, J. and Hoadley, D., and Bloxham, G. 1994) uses a Santa Barbara Research Center 256x256 InSb detector array to provide direct imaging and spectroscopic capabilities in the 1 – 5 μm wavelength range.

4.1.2.1 Near-IR spectroscopy

To obtain the near-IR spectroscopy on our targets, CASPIR was used with the long-slit *J*, *H*, and *K* grisms (see Table 4.1). The reduction process consist of standard routines involving background subtraction, flat-fielding, correction for the spectral response function and telluric lines. This resulted in low-resolution spectra for the *J*, *H*, and *K*–band. The near-IR spectra were corrected for extinction (see Section 4.1.3) and are shown in Figures 4.20 – 4.22.

4.1.2.2 Near-IR photometry

Near-IR images have been obtained with the *J*, *H*, *K*, and *nbL* filters. *nbL* is a narrow-band *L* filter centred at 3.59 μm (see Wood et al. 1998). The first steps of the data reduction process included bias subtraction and flat fielding. After this, the program DoPHOT (Schechter et al. 1993) has been used to extract the objects from the images. DoPHOT is an extraction program which uses PSF fitting to obtain the required photometry. This results in good relative photometry within one image, even in non-photometric conditions. Absolute photometry for the reference stars for each field were derived using standard star observations during the photometric nights. Each image from a non-photometric night has then been scaled to the photometry of an image from a photometric night. Figures 4.23 to 4.26 show the resulting *K*–band light-curves and Table 4.8 gives mean *J*, *H*, *K*, and *nbL* magnitudes.

4.1.3 Extinction correction

Correction of spectra for reddening and photometry for extinction is necessary, although the stars were selected in fields with relatively low extinction values for the inner galaxy (see Chapter 3). O'Donnell (1994), which is an updated version of Cardelli et al. (1989), has been used to correct the spectroscopy for extinction. The derived extinction values for these targets are discussed in Chapter 3 and the A_K values are given in Table 3.2. O'Donnell (1994) requires A_V values to correct the spectroscopy for extinction. Therefore $A_K/A_V = 0.116$ (consistent with the combined Cardelli et al. (1989) and O'Donnell (1994) extinction law) has been used to convert the A_K values given in Table 3.2 to A_V values needed to correct the optical and near-IR spectroscopy in this paper for extinction. Table 4.6 list the A_V values used and the horizontal lines in Figure 3.5 show the relative amount of extinction for each (group of) object(s). Table 4.7 also lists the mean values of $(J-K)_0$ and M_{K_0} assuming a distance to the objects of 8.5 kpc, which results in a distance modulus of 14.647.

4.2 Identification of spectral features

Molecular bands are the dominant source of opacity in stars of spectral type M (see also Section 1.2.2.2). Lançon and Wood (2000) present a library of 0.5 – 2.5 μm spectra of cool, mostly variable, giant and supergiant stars. The spectra in their library are a clear example on how molecular bands dominate the optical and near-IR part of the spectrum. In the optical part of the spectrum, these molecules are mainly TiO and also some VO bands. At longer wavelengths the dominant molecules are CO and H_2O, but OH and CN absorption also occurs (see also Houdashelt et al. 2000). In addition to molecular bands some atomic lines play an important role in the study of this sample of AGB stars. The molecular and atomic features in the spectra are described in detail in the next two subsections.

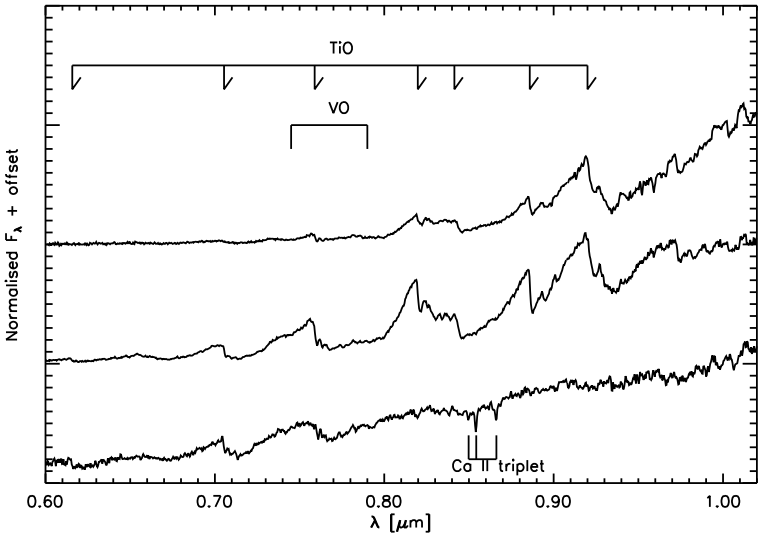

Figure 4.1: Identification of some of the stronger TiO band heads and VO features in the optical spectra. The spectrum at the bottom is J174924.1-293522 an M4.5-type star, the middle spectrum is J180248.9-295430 an M7 and the spectrum at the top is J174139.5-282428 a late M-type AGB star (M10) (based on Lançon and Wood 2000). Note that the slope of the continuum at wavelengths longer than $\sim 0.96\,\mu$m is suspect due to contamination of the blue flux calibrators by second order light.

4.2.1 Molecular bands

TiO is the dominant molecule in the optical spectra of this sample of O-rich AGB stars. Identifications of TiO can be found in Lançon and Wood (2000, and references therein). The TiO bands indicated in Figure 4.1 can be easily detected in almost all spectra in Figures 4.17 – 4.19. For some spectra, the lack of flux in the blue is an indication of a late-M type. Figure 4.2 shows the location of four more TiO bands in the *J*–band near-IR spectroscopy.

Absorption bands of VO are an indicator of a late M type (see e.g. Brett 1990; Couch et al. 2003), and together with H_2O absorption bands, they are expected to appear only in spectral types M5 and later (Houdashelt et al. 2000).

Figure 4.3 shows the major band-heads of ^{12}CO ($\Delta\nu = 3$) and ^{13}CO ($\Delta\nu = 3$) visible in the *H*–band. The band-heads of ^{12}CO are clearly visible. The band-heads of ^{13}CO are not so clear, but small suppressions at the indicated wavelength positions can be noticed. The most studied CO bands in the near-IR spectra of cool AGB stars are the ^{12}CO $\Delta\nu = 2$ bands, starting at 2.29 μm. Figure 4.4 indicates their wavelength positions. These bands can be clearly seen in almost all the *K*–band spectra shown in Figures 4.20 – 4.22. The ^{13}CO $\Delta\nu = 2$ bands are also indicated on Figure 4.4. As expected, they are much weaker than the ^{12}CO bands.

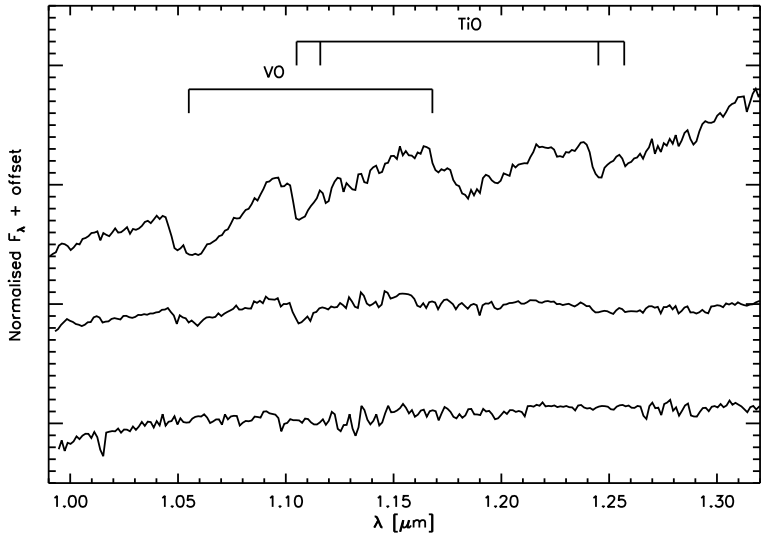

Figure 4.2: Molecular band identification of the *J*–band spectra (based on Joyce et al. 1998; Lançon and Wood 2000). The spectra are from the same stars as in Figure 4.1.

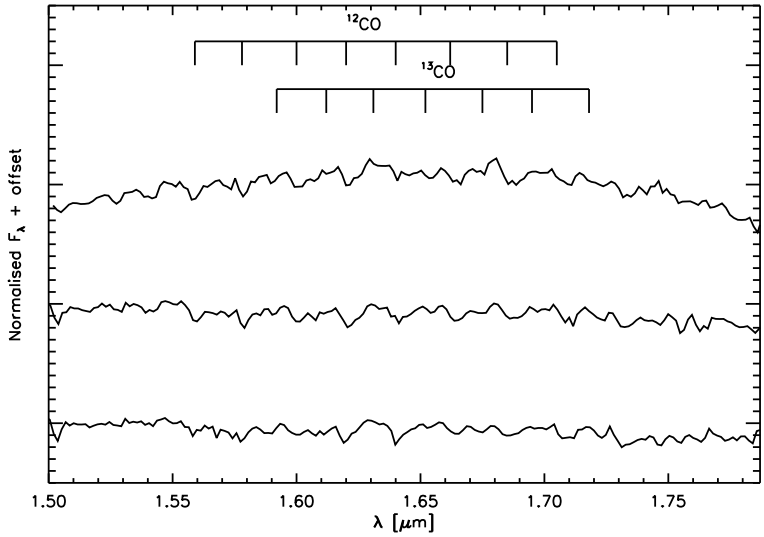

Figure 4.3: Molecular band identification of the *H*–band spectra (based on Origlia et al. 1993; Lançon and Wood 2000). The spectra are from the same stars as in Figure 4.1.

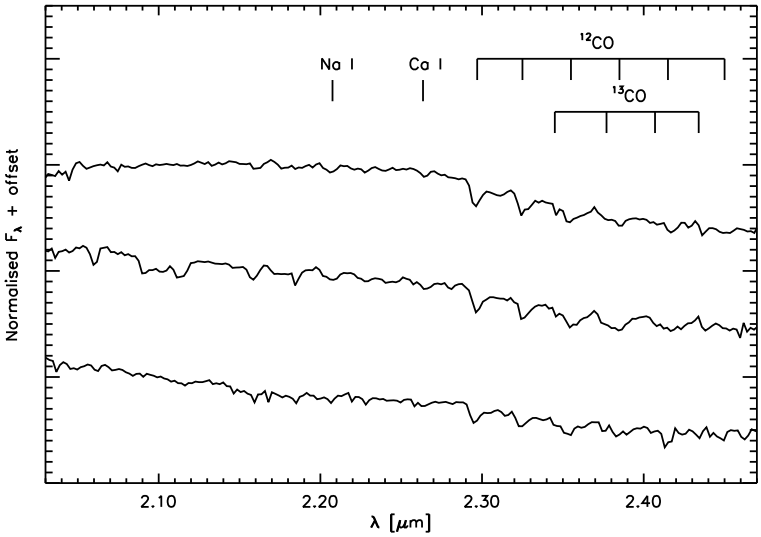

Figure 4.4: Molecular band and line identification of the *K*–band spectra (based on Lançon and Wood 2000; Ramírez et al. 2000). The spectra are from the same stars as in Figure 4.1.

The curvature of some of the *H*–band spectra is caused by two strong and wide water-absorption bands around 1.4 and 1.9 μm at both ends of the *H*–band (see e.g. top spectrum in Figure 4.3, as well as many examples in Figures 4.20 – 4.22). The H_2O band depths and shapes are very sensitive to the precise structure of the outer layers of the atmospheres (Tej et al. 2003) and are also expected to be largely correlated with the variability of the star (Bessell et al. 1996; Lançon and Wood 2000; Tej et al. 2003).

In O-rich stars, CN is relatively rare, since most of the carbon is used to form CO. The line strengths of the CN molecule are much stronger than e.g. those of CO(6,3) and this could compensate for the much lower abundance of CN (Origlia et al. 1993). Nevertheless from $\lambda > 1.5$ μm the effect of CN is to produce an apparently noisy continuum: this effect decreases at short wavelengths. Therefore CN is an important source of pseudo-continuum opacity but it does not produce narrow features in the *H* atmospheric window (Origlia et al. 1993). For a description of the importance of CN lines in the near-IR spectra of cool giants, we refer the reader to Chapter 2 (Section 2.2.1).

4.2.2 Atomic lines

Although the spectra of M giants are dominated by molecular bands, some atomic lines can be of interest. The Ca II triplet (8498, 8542, and 8662 Å) can be seen in stars of early M spectral type (see Figure 4.1), but it disappears when TiO absorption takes over for later types

Table 4.2: Definition of band passes to determine the equivalent line width of the Ca II triplet (wavelength given in Å).

Feature	Blue continuum band	Red continuum band
8494.00 – 8542.00	8477.75 – 8485.25	8523.50 – 8528.50
8537.00 – 8547.00	8523.50 – 8528.50	8566.00 – 8586.00
8657.50 – 8666.50	8632.00 – 8644.00	8702.50 – 8717.50

Table 4.3: Equivalent width measurements for the stars which show a Ca II triplet.

Number	Name	Date	$Ca_{8498\ Å}$	$Ca_{8542\ Å}$	$Ca_{8662\ Å}$	$\sum$Ca
23	J174924.1-293522	10/10/04	0.57	2.39	1.83	4.79
		18/03/05	0.93	2.33	1.75	5.01
		20/05/05	0.61	2.37	1.70	4.68
		27/07/05	0.94	2.46	1.30	4.70
30	J175511.9-294027	10/10/04	0.19	1.55	1.43	3.17
		18/03/05	0.41	1.42	1.39	3.22
		20/05/05	0.07	0.44	0.62	1.13
		28/07/05	0.31	1.22	1.05	2.58
32	J175517.0-294131	09/10/04	0.40	1.49	1.45	3.34
		10/10/04	0.28	1.30	1.60	3.18
		18/03/05	0.35	1.11	1.34	2.80
		28/07/05	0.42	1.44	1.32	3.18
37	J180249.5-295853	18/03/05	0.16	0.38	0.65	1.19
		27/07/05	0.10	0.70	0.75	1.55
39	J180301.6-300001	18/03/05	0.52	1.27	1.45	3.24
		27/07/05	0.08	0.66	0.74	1.48
40	J180304.8-295258	18/03/05	0.24	0.76	1.23	2.23
		27/07/05	0.18	0.56	0.88	1.62

which is typical for most LPV spectra (Lançon and Wood 2000). Indicated on Figure 4.4 are the Na I and Ca I lines, which can be used to estimate the metallicity (see e.g. Ramírez et al. 2000, see also Section 4.4.3).

4.3 Analysis

4.3.1 Equivalent line width measurements

As already mentioned, the presence of the Ca II triplet in the optical spectrum indicates that the spectrum belongs to an early M type star. Therefore the equivalent line widths for the Ca II triplet have been measured. Table 4.2 gives an overview of the bands selected to measure the equivalent line width and Table 4.3 gives the resulting values for the objects which were visually identified to show the Ca II triplet. The spread in equivalent line widths between different

observations, gives an indication on the accuracy of the obtained equivalent line widths, as this spread is related to the wavelength calibration of the low-resolution spectroscopy. To obtain one value for the equivalent line width of the Ca II triplet, the 3 measurements were summed:

$$\sum \mathrm{Ca} = \mathrm{EW}(\mathrm{Ca}_{8498\ \text{Å}}) + \mathrm{EW}(\mathrm{Ca}_{8542\ \text{Å}}) + \mathrm{EW}(\mathrm{Ca}_{8661\ \text{Å}}).$$

The equivalent line widths of Na I, Ca I, and ^{12}CO(2,0) have been measured in exactly the same way as Schultheis et al. (2003) (see also Chapter 2). The resulting equivalent line widths are given in Table 4.7. These equivalent widths are used below to estimate metal abundances.

The curvature of the *H*–band spectrum has been measured in order to have an estimate of the water absorption. Again we refer to Schultheis et al. (2003) and Chapter 2 for a description of the method used. These values are also listed in Table 4.7. Note that the definition of water absorption used in this method leads to negative values.

4.3.2 Spectral classification

For a sample of 97 very bright M-giant stars in the Solar neighbourhood, Fluks et al. (1994) derived effective temperatures and constructed a mathematical spectral classification criterium. This criterium was used to classify the stars in our sample into the Case spectral classification scheme.

The method to derive the Case spectral classification is based on 3 strong TiO absorption bands in the optical wavelength range (0.706 – 0.724 μm, 0.770 – 0.807 μm, and 0.829 – 0.857 μm). Based on these absorption bands, 3 spectral parameters are defined:

$$\begin{aligned}
S_{1/2,Sp} &= \frac{\int_{0.706}^{0.724} F(\lambda)_{Sp}\mathrm{d}\lambda}{\int_{0.770}^{0.807} F(\lambda)_{Sp}\mathrm{d}\lambda}, \\
S_{1/3,Sp} &= \frac{\int_{0.706}^{0.724} F(\lambda)_{Sp}\mathrm{d}\lambda}{\int_{0.829}^{0.857} F(\lambda)_{Sp}\mathrm{d}\lambda}, \text{ and} \\
S_{2/3,Sp} &= \frac{\int_{0.770}^{0.807} F(\lambda)_{Sp}\mathrm{d}\lambda}{\int_{0.829}^{0.857} F(\lambda)_{Sp}\mathrm{d}\lambda}.
\end{aligned}$$

These 3 spectral parameters are used to determine the spectral classification. Table 4.6 displays the values for the 3 spectral parameters and the resulting M spectral types when they could be determined. The first band could not always be measured due to lack of signal for the very red sources and for these objects only one value based on the second and third band can be derived.

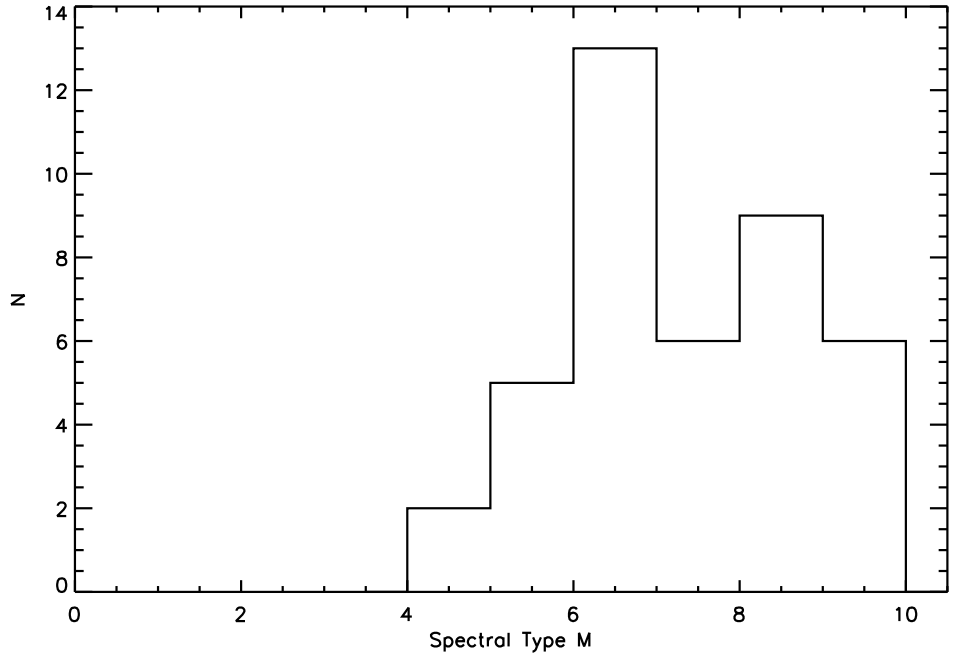

Figure 4.5: Distribution of M spectral types, derived using Fluks et al. (1994).

As can be seen from Table 4.6, the 3 spectral parameters do not give exactly the same spectral classification. To obtain one spectral classification for each observation, the 3 spectral parameters were averaged and the sample standard deviation has been calculated (which is only possible when at least two spectral parameters have been successfully determined), which can be treated as the lower limit to the errors on the determination of the spectral type. The typical uncertainty on the derived spectral type is of the order of 0.4. One can also notice differences between observations on different dates for the same object. These differences in spectral type are caused by the variability of the stars.

Figure 4.5 shows the distribution of spectral subtypes M for this sample. We find that all objects have spectral types between M4 and M10, the majority of the objects have a spectral type later than M6.

Glass et al. (1999) studied the stars detected with ISOGAL in Baade's Windows and showed that most of the detected objects are late M-type giants on the AGB with spectral types later than M3 – M4. Figure 4.5 shows the same sort of distribution, which was to be expected as this sample has been selected based on ISOGAL (see Section 3.2).

4.3.3 Effective temperatures

Based on Fluks et al. (1994), one can derive effective temperatures from the spectral classification derived using the 3 spectral parameters (see Section 4.3.2). Table 4.6 lists the values found. Based on the typical error in the determination of the subtype, we derive an error for the effective temperatures of about 100 K.

4.3.4 Period analysis

The near-IR photometric observations to monitor light-curves were performed during 8 observing runs of a few days each. The spacing of the *K*-band data shown in Figures 4.23 – 4.26 shows this clearly. The plotted error bars on each observation result from the DoPHOT extraction algorithm (see also Section 4.1.2.2). For each cluster of observations corresponding to one observing run (typically two or three days), we derived an error on the *K*-band data based on the spread between the data-points. For the whole dataset of one star, we define an overall error to be the maximum of (a) the median of the individual DoPHOT errors, and (b) the median of the errors derived for the observations obtained within 2 or 3 days. When this overall error is larger than the standard deviation of the observed magnitudes about the magnitude mean, we did not look for a period in the data and assumed that the variability could not be detected. In all other cases, where the overall measurement error was smaller than the apparent variation, an attempt was made to derive a period using a Levenberg-Marquardt minimisation procedure (see Chapter 15.5 in Press et al. 1992) to fit a sinusoidal curve to the data. The period to start the minimisation procedure from has been derived by an eye-fit. Periods longer than 800 days were rejected as we have only observations over a time span of about 820 days. The stars for which we could not find a period in this manner are still considered to be variable. In this way, we divided our sample into three categories based on the *K*-band photometry: the stars for which we could not detect any variability, the stars that do show signs for variability but for which we could not derive a period, and the stars for which we derived a period. The found full amplitudes a_K are in the range of 0.42 – 2.46 mag. Stars with full amplitudes in *K* larger than 0.4 magnitudes are referred to herein as Mira variables since Mira variables have amplitudes of this size (see Feast et al. 1982, for the *K* amplitude distribution of Mira variables). For the objects in which variability could be detected but no period could be found, we also determined an estimate of the *K*-band amplitude based on the *K*-band light-curves.

Figures 4.23 – 4.26 show the *K*-band light-curves. When possible we used the periods derived from the *K* light-curves to fit the *J*, *H*, and *nbL*–band data and thereby derived mean values for these bands. When no period was available, an average value was used. Table 4.8 gives an overview of the periods found, the resulting mean magnitudes, and the *K*-band full amplitude. The last column indicates whether we could detect variability based on the standard deviation and the error on the data.

Table 4.4: Different types of pulsation.

Pulsation type	Selection criteria
small-amplitude variable	no variability could be detected in the *K* band, variability could be detected in the *I*-band
semi-regular variable	variability could be detected in the *K*-band but no period could be derived, or amplitude derived from *I*-band photometry is smaller than 0.9 mag
Mira variable	*K*-band amplitude larger than 0.4 mag or *I*-band amplitude larger than 0.9 mag

4.3.5 Cross-correlation with OGLE-II

Based on the catalogue of OGLE-II variable objects presented by Wozniak et al. (2002), a cross-correlation has been performed between the stars in this sample and the OGLE-II catalogue. Table 4.9 lists the stars in this sample for which a counter part could be found in the OGLE-II database.

The same minimisation procedure described in Section 4.3.4 has been used to derive periods in the OGLE-II *I*-band data. In this case the value to start the minimisation procedure has not been derived by an eye-fit as this was not obvious for most of the stars. Instead, the Phase Dispersion Minimisation (pdm) method has been used to obtain an initial guess. The Levenberg-Marquardt minimisation procedure was used to find the best fitting period. Since the OGLE *I*-band light-curves have many observations, we could look for additional periods in the data after prewhitening with the period(s) already determined. An additional period has been accepted if the resulting variance decreased significantly (i.e. by more than 20% of the remaining variance). The resulting periods are listed in Table 4.9 and the light-curves are shown in Figures 4.27 and 4.28.

For the 23 stars with OGLE *I*-band photometry, we detected a period in 5 objects for which we could not detect variability in the *K*-band. Additionally, we derived a period from the *I*-band photometry for 10 stars which we labelled as variable based on the *K*-band photometry but for which we could not find a *K*-band period. For 6 stars a period could not be assigned using the *I*-band photometry, but the photometry does show signs of variability. For the remaining 2 stars we had already found a period using the *K*-band photometry. For these two large amplitude variables, the period from the near-IR photometry and the main period (first period labelled in Table 4.9) agree within 5%.

All the 23 *I* light-curves show signs of variability. Objects with a full amplitude in the *I*-band larger than 0.9 are labelled Mira variables (Groenewegen and Blommaert 2005, and references therein). Stars of smaller amplitude for which we were able to determine a period, we will refer to as semi-regular variables. The remaining stars, including the stars for which no variability could be detected in the *K*-band, we will refer to as small-amplitude variables. Table 4.4 gives an overview on the different pulsation types assigned to the objects in this chapter.

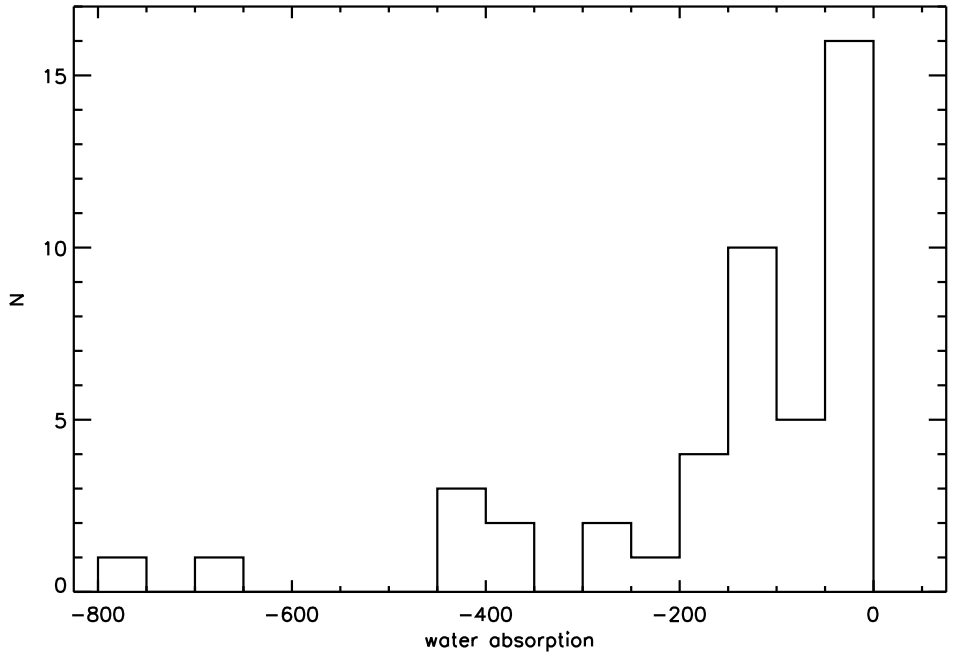

Figure 4.6: Histogram showing the distribution of the equivalent line widths of the water absorption (in Å).

4.4 Discussion

4.4.1 Ca II triplet

When an AGB star evolves to higher luminosities and cooler effective temperatures, the TiO bands become stronger and dominate the opacity in the optical part of the spectrum. The Ca II triplet disappears as the TiO absorption increases (see Section 4.2.2). There are only 3 objects for which clearly in all observations the Ca II triplet is present: J174924.1-293522, J175511.9-294027, and J175517.0-294131. For 3 other objects some spectra showed the triplet while others did not. These objects are J180249.5-295853, J180301.6-300001, and J180304.8-295258. The measured equivalent line widths are shown in Table 4.3. These 6 objects are the 6 bluest objects in $(K_s - [15])_0$ in the sample. The first three objects have a spectral type between M4.8 and M5.6. The 3 objects for which the detection was not clear in all observations have spectral types between M5.6 and M6.1.

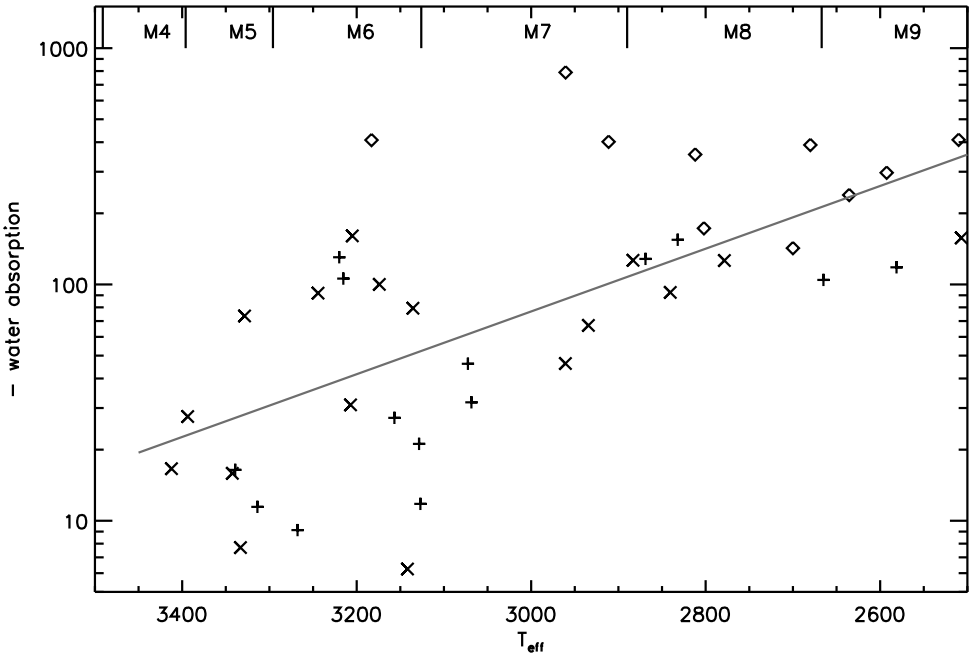

Figure 4.7: T_{eff} (in K) plotted against − (water absorption) (in Å) on a logarithmic scale. The gray line indicates the best fit, which gives a Pearson statistic of 0.40. The spectral subtype is indicated at the top of the figure. The diamonds represent Mira variables, the plus signs are the semi-regulars, and the crosses are small-amplitude variables.

4.4.2 Water absorption

Figure 4.6 shows the distribution of the water absorption. Most of the stars have a water absorption between 0 and -200 Å. The spectra of stars in this range are not badly contaminated by the water (see also Figure 2.11).

Figure 4.7 shows the water absorption plotted against the effective temperature. The best exponential fit is given by $\log(-\text{water absorption}) = (5.87 \pm 0.75) + (-0.0013 \pm 0.0002)\, T_{eff}$ and has a rather low Pearson goodness of fit statistic of 0.40. This figure clearly indicates that as the AGB star evolves to lower T_{eff}, the water layers become more prominent and therefore also have a larger effect on the near-IR spectrum.

It is also apparent that the large amplitude stars (Mira variables) have strong water absorption over a wide T_{eff} range. This is also seen in Figure 4.8 which shows the water absorption in function of the *K*-band amplitude for the objects for which a period could be derived or variability could be detected based on the *K*-band photometry.

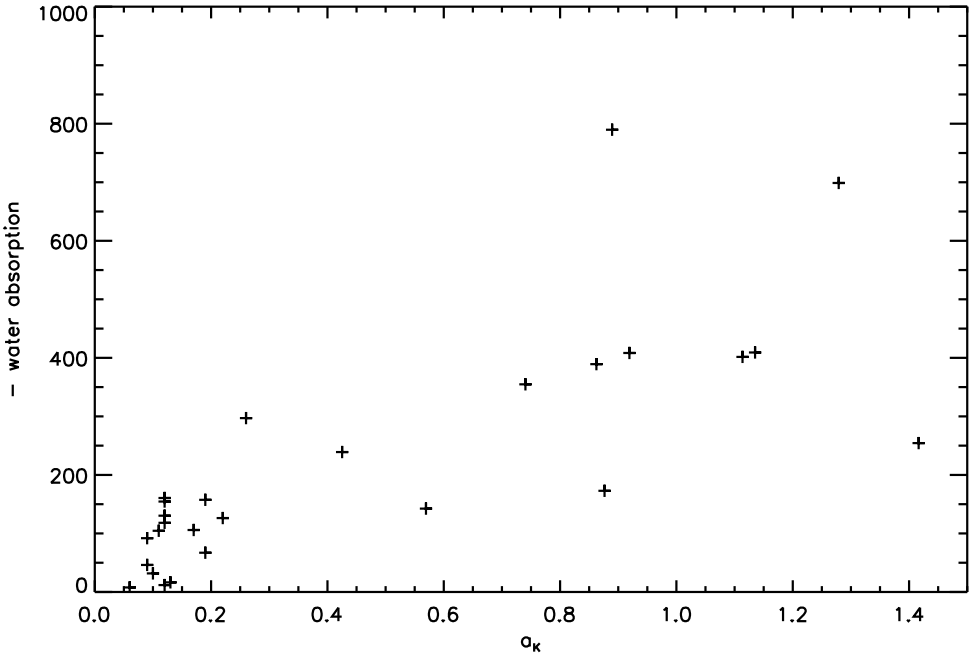

Figure 4.8: The *K*-band full amplitude for the objects in which a period could be found or variability could be detected versus the water absorption (in Å).

4.4.3 Metallicity

Frogel et al. (2001) (see also Ramírez et al. 2000) determined two empirical relationships between the equivalent line widths of Na I, Ca I, and ^{12}CO(2,0) and [Fe/H] for globular cluster red giants. Using their method, they were able to reproduce the abundance scale of Harris (1996) with an accuracy of about ±0.10 dex over the range $-1.8 \leq$ [Fe/H] ≤ 0.0.

The first empirical relation includes only the equivalent line width measurements and is given by:

$$\begin{aligned} \text{[Fe/H]} \;=\; & -1.811 + 0.389\,\text{EW(Na)} - 0.047\,\text{EW(Na)}^2 \\ & -0.030\,\text{EW(Ca)} + 0.024\,\text{EW(Ca)}^2 \\ & +0.043\,\text{EW(CO)} - 0.001\,\text{EW(CO)}^2. \end{aligned} \tag{4.1}$$

The second empirical relation uses not only the equivalent line width measurements but also $(J-K)_0$ and M_{K_0}:

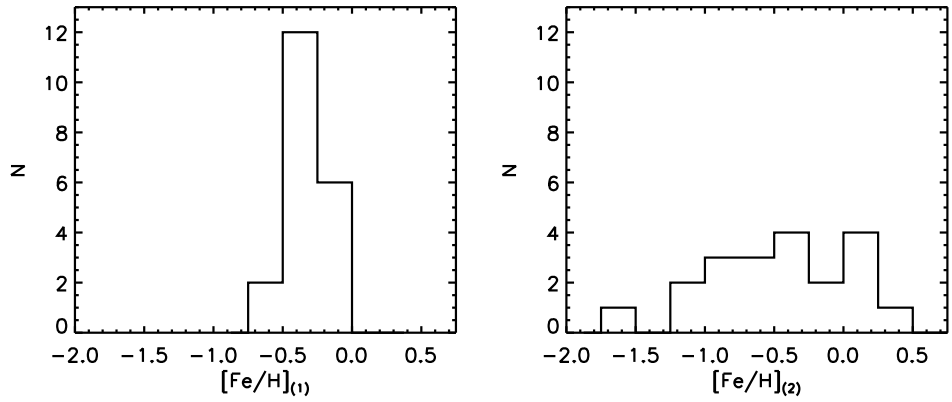

Figure 4.9: Metallicity distribution for objects with a water absorption larger than −200 Å. The left panel is based on eq. (4.1), the right panel on eq. (4.2).

Table 4.5: The metallicity distribution for objects with a water absorption larger than −200 Å.

[Fe/H]	Mean	Variance (σ)
eq. (4.1)	-0.34	0.18
eq. (4.2)	-0.45	0.53

$$\begin{aligned}[\mathrm{Fe/H}] \;=\; & 1.097 + 0.130\ \mathrm{EW(Na)} + 0.016\ \mathrm{EW(Na)}^2 \\ & +0.058\ \mathrm{EW(Ca)} - 0.004\ \mathrm{EW(Ca)}^2 \\ & +0.028\ \mathrm{EW(CO)} \\ & +5.240\ (\mathrm{J-K})_0 - 2.313\ (\mathrm{J-K})_0^2 \\ & +1.812\ \mathrm{M}_{\mathrm{K}_0} + 0.147\ \mathrm{M}_{\mathrm{K}_0}^2 .\end{aligned} \tag{4.2}$$

Figure 4.9 shows on the left the histogram for the metallicity using eq. (4.1) and on the right the metallicity using eq. (4.2). It was not possible to measure the equivalent line widths of Na I or Ca I in all stars, so they are not all included in the histograms. In addition, strong water absorption will tend to reduce the equivalent line widths and lead to anomalously low derived metallicities. Therefore, the histograms were made using only stars with a water absorption weaker than −200 Å.

Table 4.5 gives a summary of the mean and variance of the metallicity distributions. Because of the uncertainties of extinction and reddening of the objects, our preferred metallicity is the first value in the table, −0.34 with a standard deviation σ of 0.18. The error on the

mean is then given by $\sigma/\sqrt{N} = 0.05$. Finally, we note that we showed in Chapter 2 that the spectral resolution can influence the derived abundances. If the spectral resolution is lower than the resolution of the spectroscopy used to derive the relation between equivalent width and [Fe/H], the derived metallicity may be shifted to lower values by 5 to 10%. This is a small effect (< 0.05 dex).

Ramírez et al. (2000) prefer eq. (4.2) to derive the metallicity for their sample of bulge stars. Eq. (4.1) is supposed to be less sensitive to [Fe/H] for higher metallicities as the equivalent line width of ^{12}CO(2,0) reaches a platform for higher metallicities. Also because eq. (4.2) includes $(J-K)_0$ and M_{K_0} it is believed to be more reliable at higher metallicities. In our case eq. (4.2) is less reliable than eq. (4.1). In Section 4.4.5 we will show that many of the $(J-K)_0$ colours of the objects in our sample are influenced by the dust contribution. Therefore $(J-K)_0$ is not the intrinsic $(J-K)_0$ of the central star.

Rich and Origlia (2005) studied 14 M giants in Baade's Window ($\ell = -3.93°, b = 1.02°$) using high resolution near-IR spectroscopy and derived detailed abundances. They showed that the bulge M giants are α-enhanced in comparison to a sample of M giants in the solar neighbourhood. They found [Fe/H] in the range −0.4 and +0.0 dex for their giant late-type stars in the GB, with an average of <[Fe/H]>= -0.19 ± 0.020 and a 1σ dispersion of 0.080 ± 0.015. The derived iron composition of these M giants is similar to those of the K giants. More recently, Rich et al. (2007) studied 17 M giants in the inner Galactic Bulge ($\ell = 0°, b = -1°$) using high-resolution, near-IR spectroscopy and find a mean [Fe/H] abundance of -0.22 ± 0.03, with a 1σ dispersion of 0.14 ± 0.024. They conclude that the derived iron abundance and composition of this inner bulge sample is indistinguishable from that of Rich and Origlia (2005). Our mean results are consistent within the error bars with the slightly sub solar metallicity distributions of both Rich and Origlia (2005) and Rich et al. (2007), especially our preferred distribution in the left panel of Figure 4.9.

4.4.4 Variability

The variability of AGB stars is mainly caused by pulsation, although there is some evidence for variations caused by episodic ejections of dust shells or orbiting dust clouds (Habing and Olofsson 2003). Also helium shell flashes can lead to longer-term variability.

A lot of work has been done to study Period-Luminosity (PL) relations of variable red giants (see e.g. Feast et al. 1989; Hughes and Wood 1990; Wood 2000; Groenewegen 2004; Ita et al. 2004; Groenewegen and Blommaert 2005; Fraser et al. 2005). Studies on these PL-relations indicate at least five sequences A to E (and sequence B can be divided into two close, parallel sequences) (for a review see Lattanzio and Wood 2003). Since sequence E contains mainly the binary RGB stars, we are only interested in sequences A, B, C, and D. Sequences A, B, and the lower part of C are mainly populated by semi-regular variables which pulsate in different modes. Mira variables are located on sequence C and have one pulsation mode, the fundamental radial mode. The origin of stars on sequence D is still a mystery, but they are known to be multi periodic, having one period on sequence D and another lying on sequence A, B, or (occasionally) C (Wood et al. 2004).

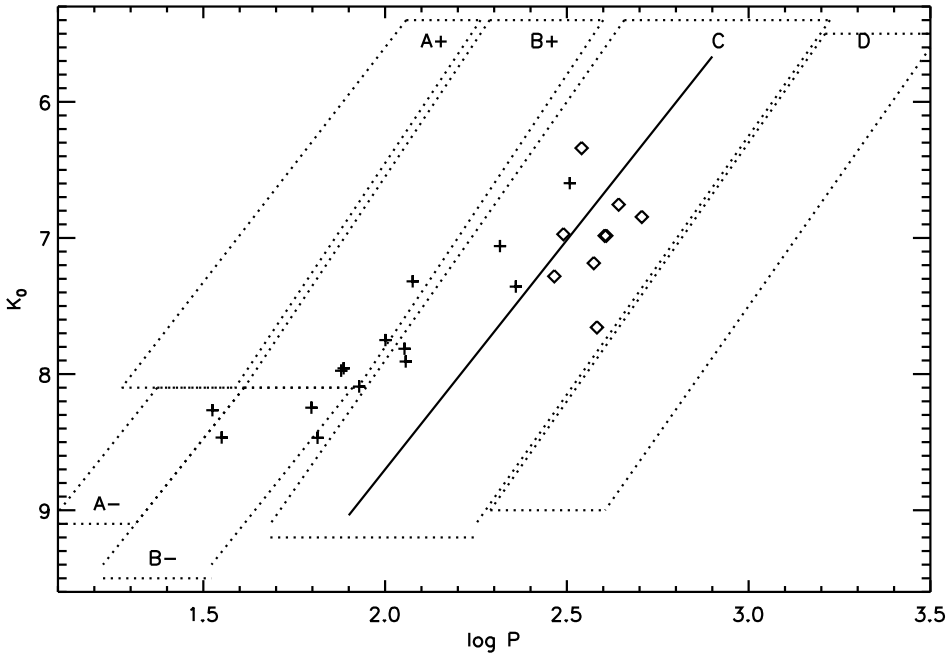

Figure 4.10: Period-luminosity diagram. Diamonds represent Mira variables (full *K* amplitude greater than 0.4 mag or full *I* amplitude greater than 0.9) with *J*-*K* < 2 and plus-signs are semi-regular variables. The boxes (dotted lines) indicate the different sequences and the full line is the PL-relation for Mira variables (based on Ita et al. 2004; Groenewegen and Blommaert 2005).

In Figure 4.10 we show the Period-Luminosity diagram for this sample of stars. Stars with $(J-K)_0 > 2$ are too much affected by their circumstellar extinction and are therefore left out in this diagram (see also Groenewegen 2004). The dotted lines indicate the different sequences as defined by Ita et al. (2004) and the full line indicates the Period-Luminosity relation for Mira's (based on Groenewegen and Blommaert 2005). We find that the Mira variables (diamonds) lie on the upper part of sequence C while the semi-regular variables lies on sequences A–, B–, B+ and C. This is consistent with other studies (Lattanzio and Wood 2003).

4.4.5 The (K,$J-K$) diagram and extinction

The (K,$J-K$) diagram for the stars in this study is shown in Figure 4.11. The solid circles are the observed values without dereddening. Clearly, many of the stars suffer from heavy extinction. After dereddening (open circles), Figure 4.11 shows that there is still a large scat-

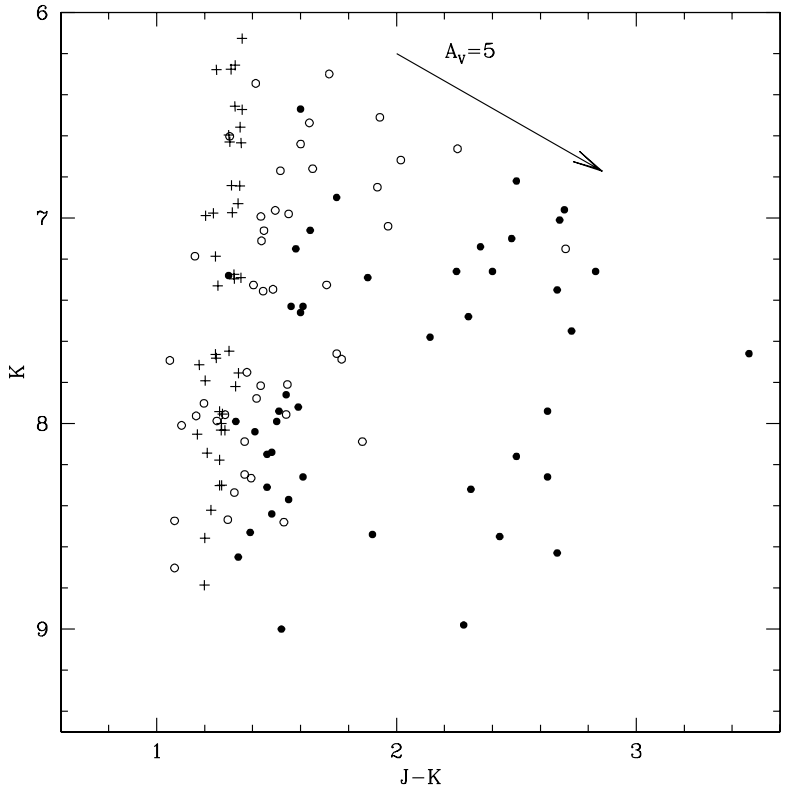

Figure 4.11: The (K,$J-K$) diagram for the stars in this study. Solid circles are the observed values, and open circles are the dereddened values obtained using the extinction values listed in Table 3.2. The crosses are the dereddened values obtained assuming the intrinsic $J-K$ value obtained from the spectral type. The arrow shows the effect of 5 magnitudes of visual extinction.

ter in $J-K$ (about 1 mag). The extinction in the GB is known to vary within small regions (Udalski 2003). Clearly, the adopted extinction values do not take into account the variation of extinction on fine scales on the sky as the extinction maps used to derive the extinction values (see Chapter 3) are not given at such fine scale (of about 1.5 mag in A_V).

Since we have spectral types and T_{eff} values for many of the stars, we can use theoretical models to estimate the intrinsic $J-K$ from the known T_{eff}. Then we can estimate E($J-K$)

by subtracting the intrinsic $J-K$ from the observed $J-K$. Here we have used the theoretical $J-K$ and T_{eff} values for pulsating red giants given by Bessell et al. (1989) to derive the intrinsic $J-K$ colour. The corresponding A_V and A_K values were derived from the extinction laws described earlier, and the A_V values are given in Table 4.6. Note that extinction derived here is both interstellar and circumstellar. However, stars with thick circumstellar shells do not have extinctions derived by this method as they were optically too faint for a spectral type to be derived.

The dereddened objects are shown in Figure 4.11 as crosses. The stars fall on a tight sequence with a small slope to cooler temperatures at higher luminosities, as expected. The open circles are the dereddened $J-K$ values using extinction values derived in Chapter 3. Objects with $K > 7.5$ show similar $J-K$ colours based on the two methods. These objects have a still relatively small dust contribution, so the derived extinction based on the intrinsic $J-K$ colour is similar to the interstellar extinction. For brighter objects, the circumstellar extinction becomes also important and for these objects, the differences between the two methods is much larger. Looking at the different estimates for the extinction, and the reddening vector, it can be seen that the intrinsic estimates of the K magnitude of the stars should be accurate to 0.1 to 0.2 magnitudes.

4.4.6 Mass-loss rate indications

Our sample of stars has been selected based on $(K_s-[15])_0$ vs $[15]_0$ CMD (see Chapter 3). Figure 4.12 shows this CMD. Stars with large $(K_s-[15])_0$ are expected to have large mass-loss rates.

The location of the stars in our sample nicely illustrates the association of large amplitude pulsation with high mass-loss rates. The small-amplitude variables are located at the lower part of the sequence. Most stars in the middle are semi-regular variables. The Mira variables are located on the upper half of the sequence where the mass-loss rates are higher. The Mira variables with the reddest $(J-K)_0$ are located at the top of the sequence where the mass-loss rates are highest. Note that the 4 IRAS sources with large pulsation amplitudes are not shown in the plot as they do not have an ISOGAL [15] magnitude.

Figure 4.13 shows the mass-loss indicator $(K_s-[15])_0$ as a function of the derived periods. This figure illustrates that the star becomes redder and has a higher mass-loss rate as the period of the object increases. The grey line in the figure is the best linear fit and is given by: $(K_s-[15])_0 = (0.70\pm0.17) + (0.006\pm0.001)\mathrm{P}$. The fit has a Pearson statistic of 0.89.

The association of high mass-loss rate with pulsation amplitude is shown in Figure 4.14. For the small amplitude pulsators ($a_K < 0.4$ mag), $(K_s-[15])_0$ ranges from small to intermediate values. Once large-amplitude ($a_K > 0.4$ mag) fundamental mode pulsation starts, we see that $(K_s-[15])_0$ (the mass-loss rate) increases strongly with period. The grey line shows the best fit to the data with the following coefficients: $K_{s,0}-[15] = (0.52\pm0.34)+(2.38\pm0.35)a_K$ and has a Pearson statistic of 0.78 (the errors in the coefficients are 1-σ errors).

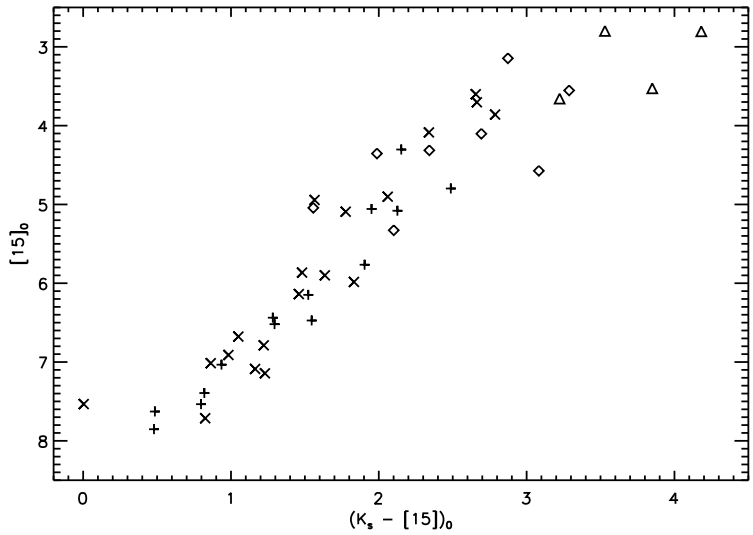

Figure 4.12: $(K_s - [15])_0$ vs $[15]_0$ CMD. The plus-signs and diamonds are the same symbols as in Figure 4.10, the triangles are Mira variables with $(J - K)_0 > 2$, and crosses are small amplitude variables.

A similar analysis can be performed using the derived amplitudes in the *I*-band. Figure 4.15 shows these amplitudes for the main period versus the $(K_s - [15])_0$ colour. Stars with an amplitude > 0.9 mag are Mira variables (see Section 4.3.4). Figure 4.15 shows that the stars with the smallest amplitudes correlate with $(K_s - [15])_0$. A linear fit to these data points gives $(K_s - [15])_0 = (0.58 \pm 0.22) + (5.17 \pm 1.19)a_I$ and has a Pearson statistic of 0.74.

Figures 4.7 and 4.8 in Section 4.4.2 indicated that as the stars evolve and their effective temperature decreases, the amount of water absorption increases. This suggests that $(K_s - [15])_0$ should correlate with the amount of water absorption in the photosphere. Figure 4.16 shows this effect.

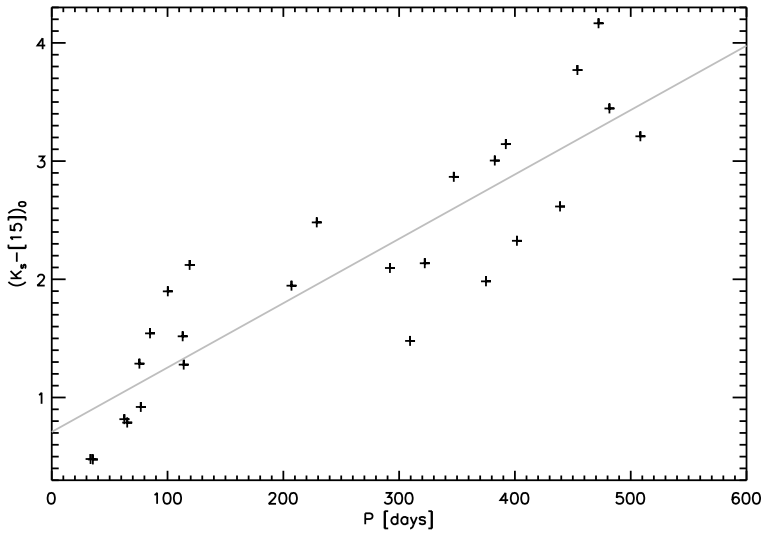

Figure 4.13: $(K_s - [15])_0$ in function of the derived periods. The grey line shows the best linear fit to the data and has a Pearson statistic of 0.89.

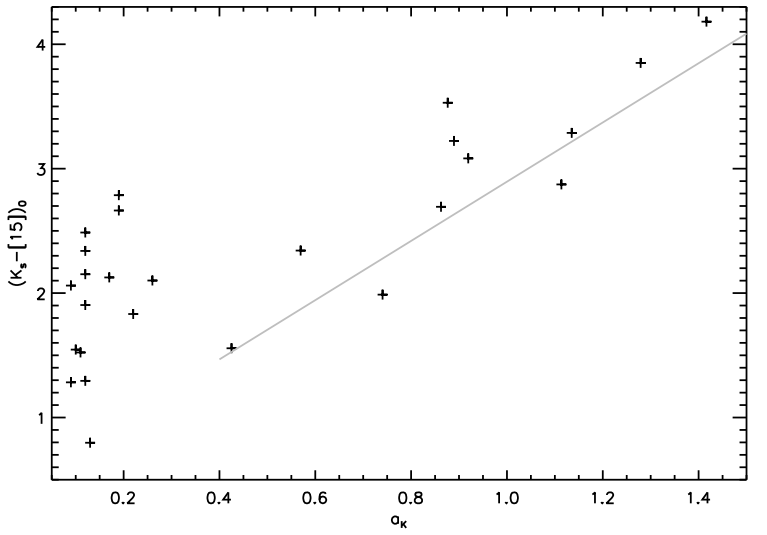

Figure 4.14: The amplitude in the K-band vs $(K_s - [15])_0$. The grey line shows the best linear fit to the Mira variables and has a Pearson statistic of 0.78.

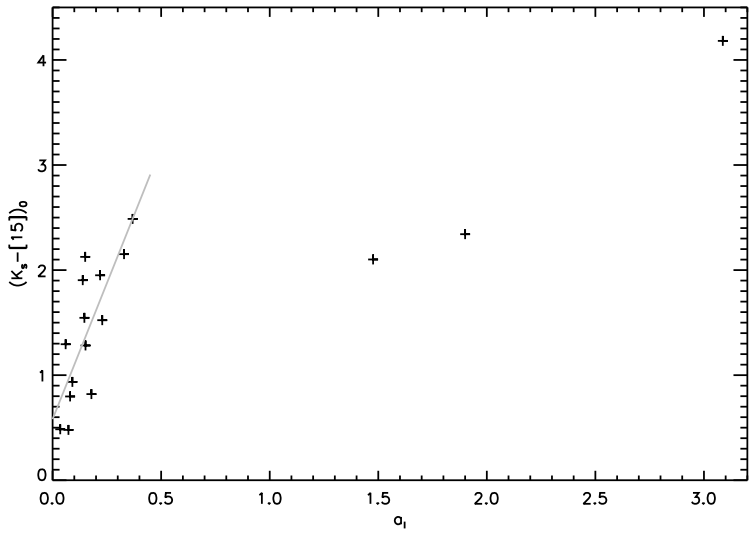

Figure 4.15: $(K_s - [15])_0$ in function of the main amplitude in the *I*-band. The grey line shows the best linear fit to the stars excluding the Mira variables which have an *I*-band amplitude > 0.9 mag.

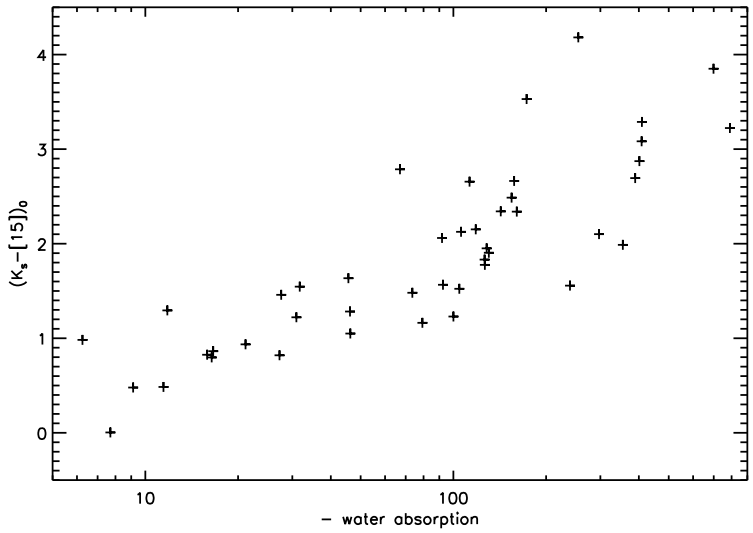

Figure 4.16: $K_{s,0} - [15]$ in function of the water absorption (in Å).

4.5 Summary and conclusions

We have used ground-based spectroscopy and photometry to study a sample of Galactic Bulge AGB stars selected in Chapter 3 for spectroscopic observation with the Spitzer Space Telescope. From the optical spectroscopy, we derived a spectral M subtype, effective temperature, and the equivalent line widths of the Ca-triplet. From the near-IR spectroscopy, we derived the equivalent line widths for Na I, Ca I, and ^{12}CO(2,0) and used these to derive an estimate of the metallicity. The metallicity distribution we derived is consistent with the results of Rich and Origlia (2005) and Rich et al. (2007), who obtained metallicities for Galactic Bulge red giants using high dispersion spectroscopy.

Using near-IR photometry obtained over a 900 day interval, we divided our sample in three groups: small amplitude variables, semi-regular variables of intermediate amplitude, and Mira variable with K amplitudes greater than 0.4 mag. We derived periods where possible from one or both of two sources: the K photometry and OGLE-II I photometry. The PL-relation shows that the Mira variables are located on the upper part of sequence C while the semi-regular variables are located on sequences C, A–, B–, and B+. No objects were found on sequence D.

Using $K_{s,0} - [15]$ as a mass-loss rate indicator, we showed that there is a clear relation between the period and amplitude of pulsation variability and the mass-loss rate. The amount of water absorption in the near-IR spectra also increases with the pulsation amplitude and the $K_{s,0} - [15]$ colour.

Table 4.6: Optical spectroscopy. The numbers in the first column refer to the numbering given in Table 3.2. This table lists the A_V values derived in Chapter 3 as used for the extinction correction and the A_V values derived in this work based on the intrinsic $J-K$ colour of the objects. The latter is the sum of the estimated interstellar and circumstellar extinction. Also given in this table are the 3 spectral parameters used to derive the M spectral subtype as well as the effective temperature (±100 K).

Number	Name	A_V [mag] chapter 3	A_V [mag] this chapter	Observation date	$Sp_{1/2}$ M type	$Sp_{1/3}$ M type	$Sp_{2/3}$ M type	M Sp Case	Standard deviation	T_{eff} [K]
1	IRAS 17251-2821	3.17								
2	IRAS 17276-2846	4.27								
3	IRAS 17323-2424	4.95								
4	IRAS 17347-2319	4.29								
5	J174117.5-282957	4.92	7.18	09/10/04	5.4	6.1	7.4	6.3	1.0	3248
				15/03/05	5.8	6.8	8.9	7.2	1.6	3090
				20/05/05	5.8	6.7	8.3	6.9	1.2	3140
				27/07/05	4.3	5.6	6.7	5.5	1.2	3342
6	J174122.7-283146	5.19								
7	J174123.6-282723	4.47	5.88	09/10/04	–	9.3	6.8	8.1	1.7	2875
				15/03/05	6.5	6.8	7.0	6.8	0.2	3166
				20/05/05	–	9.2	7.9	8.6	0.9	2764
				27/07/05	–	7.9	6.8	7.4	0.8	3038
8	J174126.6-282702	4.47								
9	J174127.3-282851	4.37	6.137	15/03/05	–	–	–	–	–	–
				20/05/05	–	–	8.9	8.9	–	2680
10	J174127.9-282816	4.37	5.97	15/03/05	8.9	8.1	7.5	8.2	0.7	2853
				20/05/05	–	8.5	8.1	8.3	0.3	2828
11	J174128.5-282733	4.37	5.56	15/03/05	–	–	9.4	9.4	–	2597
				21/05/05	–	9.9	8.0	9.0	1.3	2674
12	J174130.2-282801	4.37	5.94	09/10/04	6.3	6.4	6.3	6.3	0.0	3239
				20/05/05	6.9	7.0	7.3	7.1	0.2	3109
13	J174134.6-282431	4.37	7.27	15/03/05	5.9	6.6	7.8	6.8	1.0	3164
				21/05/05	3.9	5.8	8.2	6.0	2.1	3296
				27/07/05	6.2	6.9	8.3	7.2	1.1	3089
14	J174139.5-282428	4.37	7.73	15/03/05	–	–	10.0	10.0	–	2507
				21/05/05	–	–	–	–	–	–
15	J174140.0-282521	4.28	5.52	09/10/04	–	–	8.0	8.0	–	2881
				15/03/05	–	8.4	7.9	8.2	0.4	2855
				21/05/05	6.9	7.2	7.6	7.2	0.3	3067
16	J174155.3-281638	4.56		09/10/04	–	–	–	–	–	–
				15/03/05	–	–	–	–	–	–
				21/05/05	–	–	–	–	–	–
17	J174157.6-282237	4.10	5.28	09/10/04	5.9	6.1	6.4	6.1	0.2	3270
				15/03/05	5.8	6.2	6.6	6.2	0.4	3262
				21/05/05	5.8	6.4	7.1	6.4	0.7	3224

Table 4.6: continued.

Number	Name	A_V (Chapter 3) [mag] chapter 3	A_V [mag] this chapter	Observation date	$Sp_{1/2}$ M type	$Sp_{1/3}$ M type	$Sp_{2/3}$ M type	M Sp Case	Standard deviation	T_{eff} [K]
				27/07/05	6.2	6.5	6.6	6.4	0.2	3221
18	J174158.8-281849	4.37	7.67	09/10/04	–	–	9.9	9.9	–	2510
				15/03/05	–	–	–	–	–	–
				21/05/05	–	–	–	–	–	–
19	J174203.7-281729	4.47	8.34	09/10/04	8.4	9.7	9.9	9.3	0.8	2613
				15/03/05	4.1	5.8	7.7	5.9	1.8	3308
				21/05/05	–	–	–	–	–	–
20	J174206.9-281832	4.74	8.77	09/10/04	5.2	6.4	8.9	6.8	1.9	3154
				15/03/05	–	–	8.9	8.9	–	2699
				20/05/05	–	–	9.7	9.7	–	2553
21	IRAS 17413-3531	2.44								
22	J174917.0-293502	5.19	7.31	10/10/04	4.9	5.6	6.3	5.6	0.7	3337
				18/03/05	4.2	5.5	6.5	5.4	1.1	3355
				21/05/05	1.6	4.1	6.3	4.0	2.4	3489
23	J174924.1-293522	4.65	4.26	10/10/04	5.0	4.9	4.9	4.9	0.0	3402
				18/03/05	3.5	3.7	4.5	3.9	0.5	3501
				20/05/05	4.8	5.1	5.3	5.1	0.3	3387
				27/07/05	5.5	5.4	5.2	5.4	0.1	3359
24	J174943.7-292154	5.38	8.32	09/10/04	2.7	4.7	6.3	4.6	1.8	3437
				20/05/05	–	–	–	–	–	–
				27/07/05	3.9	6.1	9.4	6.4	2.7	3220
25	J174948.1-292104	4.74	8.30	10/10/04	–	–	–	–	–	–
				27/07/05	6.8	6.5	6.3	6.5	0.3	3207
26	J174951.7-292108	5.01								
27	J175432.0-295326	2.60	3.16	09/10/04	–	–	–	–	–	–
				15/03/05	–	–	9.4	9.4	–	2596
				20/05/05	–	–	–	–	–	–
				27/07/05	6.6	8.6	10.0	8.4	1.7	2804
				28/07/05	–	–	–	–	–	–
28	J175456.8-294157	2.60	2.32	09/10/04	–	–	9.4	9.4	–	2595
				5/03/05	–	–	9.5	9.5	–	2584
				0/05/05	–	–	9.7	9.7	–	2543
				28/07/05	–	–	9.4	9.4	–	2603
29	J175459.0-294701	2.60		15/03/05	–	–	–	–	–	–
				20/05/05	–	–	–	–	–	–
				28/07/05	–	–	–	–	–	–
30	J175511.9-294027	2.60	1.87	10/10/04	5.9	5.6	5.0	5.5	0.4	3346
				18/03/05	5.8	5.5	5.0	5.4	0.4	3352
				20/05/05	5.8	5.6	5.2	5.6	0.3	3339
				28/07/05	5.9	5.7	5.3	5.6	0.3	3333
31	J175515.4-294122	2.60	1.99	09/10/04	–	–	7.6	7.6	–	2980

Table 4.6: continued.

Number	Name	A_V (Chapter 3) [mag] chapter 3	A_V [mag] this chapter	Observation date	$Sp_{1/2}$ M type	$Sp_{1/3}$ M type	$Sp_{2/3}$ M type	M Sp Case	Standard deviation	T_{eff} [K]
				15/03/05	5.8	6.0	6.3	6.0	0.2	3291
				20/05/05	6.6	6.7	6.8	6.7	0.1	3178
				28/07/05	–	–	7.3	7.3	–	3065
32	J175517.0-294131	2.60	1.74	09/10/04	6.6	5.9	5.2	5.9	0.7	3304
				10/10/04	5.9	5.6	5.1	5.6	0.4	3339
				18/03/05	5.5	5.3	5.0	5.3	0.3	3367
				20/05/05	6.1	5.9	5.4	5.8	0.3	3314
				28/07/05	5.8	5.6	5.2	5.5	0.3	3342
33	J175521.7-293912	2.60								
34	J180234.8-295958	1.09	1.70	10/10/04	–	9.5	8.5	9.0	0.8	2666
				18/03/05	5.4	6.5	8.7	6.9	1.7	3150
				20/05/05	6.7	8.4	9.7	8.2	1.5	2839
				27/07/05	6.8	7.6	8.3	7.6	0.8	2990
35	J180238.8-295954	0.96	1.72	18/03/05	5.8	6.3	6.8	6.3	0.5	3241
				20/05/05	6.0	6.7	7.6	6.8	0.8	3163
				27/07/05	5.7	6.2	6.8	6.2	0.6	3256
36	J180248.9-295430	1.34	1.23	18/03/05	8.0	7.0	6.7	7.3	0.7	3066
				20/05/05	8.1	7.1	6.7	7.3	0.7	3061
				27/07/05	7.1	6.7	6.2	6.7	0.4	3184
				18/09/05	6.4	6.6	6.7	6.6	0.2	3197
37	J180249.5-295853	1.55	0.81	18/03/05	5.4	5.5	5.6	5.5	0.1	3342
				20/05/05	5.7	5.7	5.6	5.6	0.1	3332
				27/07/05	5.6	5.5	5.2	5.4	0.2	3352
				18/09/05	5.4	5.6	5.9	5.6	0.3	3331
38	J180259.6-300254	0.91	1.62	18/03/05	–	8.1	6.9	7.5	0.9	3001
				20/05/05	–	9.8	8.3	9.0	1.0	2663
39	J180301.6-300001	0.91	1.98	18/03/05	4.2	5.1	5.5	4.9	0.6	3403
				21/05/05	5.5	5.7	5.9	5.7	0.2	3324
				27/07/05	6.5	6.3	6.1	6.3	0.2	3240
				18/09/05	5.8	6.0	6.3	6.0	0.2	3288
40	J180304.8-295258	0.55	0.95	18/03/05	6.1	6.0	6.0	6.0	0.0	3290
				21/05/05	6.4	6.2	6.1	6.2	0.1	3256
				27/07/05	6.5	6.2	5.9	6.2	0.3	3259
				18/09/05	6.0	6.2	6.3	6.2	0.1	3266
41	J180305.3-295515	0.77	1.55	18/03/05	–	8.7	7.5	8.1	0.9	2869
				21/05/05	8.4	8.1	7.8	8.1	0.3	2869
42	J180305.4-295527	0.77	0.32	18/03/05	7.9	6.8	6.3	7.0	0.8	3119
				21/05/05	8.8	7.1	6.4	7.4	1.2	3023
				27/07/05	–	7.3	6.3	6.8	0.7	3159
				18/09/05	8.6	7.4	6.8	7.6	0.9	2989
43	J180308.2-295747	0.91	1.45	09/10/04	–	–	9.2	9.2	–	2633

Table 4.6: continued.

Number	Name	A_V (Chapter 3) [mag] chapter 3	A_V [mag] this chapter	Observation date	$Sp_{1/2}$ M type	$Sp_{1/3}$ M type	$Sp_{2/3}$ M type	M Sp Case	Standard deviation	T_{eff} [K]
				18/03/05	–	–	9.4	9.4	–	2606
				21/05/05	–	–	9.3	9.3	–	2610
				27/07/05	–	–	8.2	8.2	–	2841
				18/09/05	–	9.4	9.0	9.2	0.2	2635
44	J180308.6-300526	0.82	-0.14	09/10/04	–	–	–	–	–	–
				18/03/05	–	8.0	7.1	7.6	0.6	2995
				21/05/05	–	–	9.2	9.2	–	2629
45	J180308.7-295220	0.55	1.06	09/10/04	–	–	8.4	8.4	–	2795
				21/05/05	–	9.3	7.9	8.6	1.0	2762
46	J180311.5-295747	0.91	1.22	09/10/04	–	–	9.3	9.3	–	2612
				21/05/05	–	–	9.6	9.6	–	2573
47	J180313.9-295621	0.73	0.86	09/10/04	8.6	6.8	5.9	7.1	1.4	3106
				21/05/05	7.7	6.6	5.9	6.8	0.9	3167
				27/07/05	8.1	6.6	5.7	6.8	1.2	3157
				18/09/05	8.1	6.7	6.0	6.9	1.0	3137
48	J180316.1-295538	0.55	1.16	09/10/04	6.4	6.4	6.4	6.4	0.0	3222
				21/05/05	7.8	7.0	6.6	7.1	0.6	3096
				27/07/05	8.1	6.9	6.5	7.2	0.8	3083
				18/09/05	6.2	6.4	6.6	6.4	0.2	3226
49	J180323.9-295410	0.55	1.03	10/10/04	–	7.6	6.6	7.1	0.7	3109
				21/05/05	–	8.5	6.7	7.6	1.3	2989
				27/07/05	–	8.1	6.4	7.3	1.2	3058
				18/09/05	–	7.6	6.5	7.0	0.8	3118
50	J180328.4-295545	0.73	2.13	10/10/04	5.2	5.8	6.7	5.9	0.8	3306
				21/05/05	6.0	6.6	7.4	6.7	0.7	3181
				27/07/05	6.5	6.8	7.1	6.8	0.3	3159
51	J180333.3-295911	0.91	1.22	10/10/04	–	7.2	6.1	6.6	0.8	3186
				21/05/05	–	7.2	6.2	6.7	0.7	3176
				27/07/05	–	8.0	6.3	7.2	1.3	3088
				18/09/05	–	7.8	6.5	7.1	0.9	3092
52	J180334.1-295958	0.85	1.91	10/10/04	–	8.4	7.6	8.0	0.6	2890
				21/05/05	–	9.0	7.8	8.4	0.9	2802
				22/05/05	7.0	7.4	7.6	7.3	0.3	3050
				27/07/05	–	8.9	8.0	8.4	0.6	2791
53	IRAS 18042-2905	1.48								

Table 4.7: Near-IR spectroscopy. This table gives the equivalent line width measurements of Na I, Ca I, and ^{12}CO(2,0), as well as the amount of water absorption based on the curvature of the *H*-band spectrum. We also give the dereddened $J-K$ and M_K values. The numbering of the objects in this table refers to the numbering given in Table 3.2.

Number	Name	Observation date	EW(Na) [Å]	EW(Ca) [Å]	EW(CO) [Å]	EW(H_2O) [Å]	$(J-K)_0$ [mag]	M_{K_0} [mag]
5	J174117.5-282957	14/03/05	4.81	4.01	23.05	-160.59	1.93	-8.22
7	J174123.6-282723	25/07/05	–	–	23.28	-46.28	1.77	-6.92
8	J174126.6-282702	14/03/05	–	–	20.63	-698.74	2.96	-7.27
9	J174127.3-282851	14/03/05	1.44	1.04	15.34	-389.22	2.02	-7.85
10	J174127.9-282816	14/03/05	4.22	4.12	21.29	-92.51	1.87	-8.14
11	J174128.5-282733	14/03/05	4.88	5.12	15.97	-239.09	1.79	-8.05
12	J174130.2-282801	14/05/06	4.52	5.39	21.31	-100.03	1.79	-6.27
13	J174134.6-282431	25/07/05	–	–	24.11	-408.32	2.05	-6.99
14	J174139.5-282428	14/03/05	3.20	2.80	20.17	-157.46	1.97	-8.28
15	J174140.0-282521	14/03/05	2.89	3.69	16.97	-67.09	1.81	-8.00
16	J174155.3-281638	14/03/05	6.65	3.17	21.65	-112.84	2.11	-8.39
17	J174157.6-282237	25/07/05	–	6.03	22.92	-91.87	1.77	-7.69
18	J174158.8-281849	14/03/05	–	–	13.37	-409.20	2.12	-7.81
19	J174203.7-281729	14/03/05	–	0.96	15.69	-789.76	2.16	-7.77
20	J174206.9-281832	14/03/05	2.58	2.31	17.59	-172.86	2.02	-8.32
22	J174917.0-293502	25/07/05	4.14	2.73	23.86	-27.61	1.85	-7.05
23	J174924.1-293522	25/07/05	3.82	4.94	18.70	-16.61	1.32	-6.77
24	J174943.7-292154	25/07/05	5.74	3.96	22.11	-73.57	2.00	-7.30
25	J174948.1-292104	25/07/05	–	–	15.72	-30.93	2.10	-6.64
26	J174951.7-292108	25/07/05	–	–	23.36	-45.62	1.93	-7.11
27	J175432.0-295326	14/03/05	4.71	2.88	23.21	-142.45	1.54	-7.99
		25/07/05	2.59	1.51	21.93	-354.52	1.54	-7.99
28	J175456.8-294157	14/03/05	4.73	3.16	24.08	-118.20	1.66	-8.19
		25/07/05	4.19	3.26	20.60	-85.27	1.66	-8.19
29	J175459.0-294701	25/07/05	3.13	–	21.99	-254.38	2.73	-7.66
30	J175511.9-294027	25/07/05	2.49	5.01	18.15	-15.87	1.17	-6.11
31	J175515.4-294122	25/07/05	–	–	23.08	-21.15	1.33	-6.68
32	J175517.0-294131	25/07/05	9.06	–	20.52	-7.70	1.12	-7.11
34	J180234.8-295958	25/07/05	3.30	2.73	24.33	-401.63	1.86	-8.63
35	J180238.8-295954	25/07/05	3.75	3.98	20.18	-130.33	1.48	-6.98
36	J180248.9-295430	20/09/05	–	3.76	26.66	-11.79	1.39	-6.83
		24/07/05	4.40	4.49	20.21	-15.87	1.39	-6.83
37	J180249.5-295853	20/09/05	–	6.52	23.39	-16.42	1.18	-6.32
		24/07/05	1.49	3.91	16.30	-15.70	1.18	-6.32
38	J180259.6-300254	14/05/06	2.82	3.10	21.70	-154.52	1.54	-7.36
39	J180301.6-300001	20/09/05	–	6.92	26.67	-11.45	1.41	-6.53
		24/07/05	3.83	5.66	21.09	-10.23	1.41	-6.53
40	J180304.8-295258	21/09/05	–	3.75	23.46	-9.13	1.41	-6.32

Table 4.7: continued.

Number	Name	Observation date	EW(Na) [Å]	EW(Ca) [Å]	EW(CO) [Å]	EW(H_2O) [Å]	$(J-K)_0$ [mag]	M_{K_0} [mag]
		24/07/05	3.07	7.91	20.77	-12.21	1.41	-6.32
41	J180305.3-295515	14/05/06	3.38	3.79	21.14	-128.22	1.49	-7.64
42	J180305.4-295527	21/09/05	–	5.41	21.80	-46.17	1.36	-6.93
		24/07/05	–	–	19.35	-25.52	1.36	-6.93
43	J180308.2-295747	21/09/05	5.93	5.18	16.38	-104.54	1.55	-6.98
		24/07/05	2.27	4.27	21.30	-65.51	1.55	-6.98
44	J180308.6-300526	14/05/06	1.41	2.85	18.12	-354.76	1.51	-8.31
45	J180308.7-295220	14/05/06	5.12	3.96	21.47	-126.26	1.53	-6.83
46	J180311.5-295747	14/05/06	2.93	2.60	21.66	-297.03	1.68	-7.22
47	J180313.9-295621	21/09/05	–	4.60	26.61	-6.25	1.31	-6.75
		24/07/05	–	–	10.81	-23.63	1.31	-6.75
48	J180316.1-295538	21/09/05	–	–	25.29	-27.26	1.39	-6.43
		24/07/05	3.15	0.63	23.74	-19.91	1.39	-6.43
49	J180323.9-295410	21/09/05	–	5.92	21.71	-31.71	1.37	-6.63
		24/07/05	2.98	2.64	19.01	-41.08	1.37	-6.63
50	J180328.4-295545	25/07/05	3.19	5.16	26.31	-105.89	1.59	-7.44
51	J180333.3-295911	21/09/05	–	3.38	16.80	-79.32	1.33	-6.40
		24/07/05	2.38	2.88	18.19	-92.09	1.33	-6.40
52	J180334.1-295958	25/07/05	4.54	5.03	24.08	-126.51	1.56	-7.78

Table 4.8: Near-IR photometry. Based on the near-IR photometry we give for each object the period (when it could be derived) and the mean magnitudes in the *J*, *H*, *K*, and *nbL*-band. Also the full amplitude in *K* is given. The last column indicates if variability could be detected in the *K*-band. The numbering of the objects in this table refers to the numbering given Table 3.2.

Number	Name	Period [days]	$< J >$ [mag]	$< H >$ [mag]	$< K >$ [mag]	$< nbL >$ [mag]	a_K [mag]	variability detected
1	IRAS 17251-2821	–	–	–	14.47	8.11	0.90	yes
4	IRAS 17347-2319	355.42	–	13.78	11.09	7.02	0.46	yes
5	J174117.5-282957	–	9.58	7.71	7.10	6.30	0.12	yes
6	J174122.7-283146	593.72	–	–	11.56	6.80	2.46	yes
7	J174123.6-282723	–	10.63	9.09	8.32	7.82	–	no
8	J174126.6-282702	453.97	11.13	9.06	7.66	6.15	1.28	yes
9	J174127.3-282851	438.95	9.66	7.98	7.26	6.49	0.86	yes
10	J174127.9-282816	–	9.49	7.78	7.14	6.50	–	no
11	J174128.5-282733	309.46	9.78	8.23	7.48	6.63	0.42	yes
12	J174130.2-282801	–	11.26	9.58	8.98	8.36	–	no
13	J174134.6-282431	382.59	10.66	9.03	8.16	7.25	0.92	yes
14	J174139.5-282428	–	9.58	7.85	7.04	6.26	0.19	yes
15	J174140.0-282521	–	9.51	7.85	7.26	6.55	0.19	yes
16	J174155.3-281638	–	9.32	7.78	6.82	6.02	–	no
17	J174157.6-282237	–	9.72	8.24	7.58	7.02	0.09	yes
18	J174158.8-281849	508.33	10.02	8.17	7.35	6.21	1.14	yes
19	J174203.7-281729	392.12	10.28	8.54	7.55	6.41	0.88	yes
20	J174206.9-281832	481.61	10.09	8.34	7.26	6.02	0.88	yes
21	IRAS 17413-3531	624.10	–	12.85	10.09	–	2.20	yes
22	J174917.0-293502	–	10.98	9.23	8.55	7.98	–	no
23	J174924.1-293522	–	10.44	9.06	8.54	8.19	–	no
24	J174943.7-292154	–	10.57	8.74	7.94	7.15	–	no
25	J174948.1-292104	–	11.30	9.47	8.63	7.96	–	no
26	J174951.7-292108	–	10.89	9.03	8.26	7.59	–	no
27	J175432.0-295326	401.74	9.17	7.98	7.29	6.56	0.56	yes
28	J175456.8-294157	–	8.65	7.53	6.90	6.36	0.12	yes
29	J175459.0-294701	472.19	9.66	7.77	6.96	5.54	1.42	yes
30	J175511.9-294027	–	10.52	9.28	9.00	8.76	–	no
31	J175515.4-294122	–	9.87	8.78	8.26	7.85	–	no
32	J175517.0-294131	–	9.49	8.28	7.99	7.67	0.06	yes
34	J180234.8-295958	347.18	8.07	6.96	6.47	–	1.12	yes
35	J180238.8-295954	–	9.40	8.37	7.86	7.41	0.12	yes
36	J180248.9-295430	–	9.61	8.48	8.13	–	0.12	yes
37	J180249.5-295853	–	9.99	8.89	8.65	8.60	0.13	yes
38	J180259.6-300254	–	9.06	7.91	7.46	7.04	0.12	yes
39	J180301.6-300001	–	9.92	8.65	8.37	–	–	no
40	J180304.8-295258	–	9.92	8.76	8.53	8.23	–	no
41	J180305.3-295515	–	8.73	7.58	7.15	6.68	–	no
42	J180305.4-295527	–	9.32	8.20	8.00	7.58	0.09	yes
43	J180308.2-295747	–	9.51	8.33	7.92	7.44	0.11	yes
44	J180308.6-300526	374.99	8.58	7.52	7.28	6.23	0.74	yes
45	J180308.7-295220	–	9.45	8.38	7.94	8.23	0.22	yes
46	J180311.5-295747	–	9.03	7.99	7.39	6.73	0.26	yes
47	J180313.9-295621	–	9.45	8.33	8.04	7.93	–	no
48	J180316.1-295538	–	9.77	8.61	8.31	8.05	–	no
49	J180323.9-295410	–	9.61	8.50	8.15	7.82	0.10	yes
50	J180328.4-295545	–	9.02	7.85	7.40	6.83	0.17	yes
51	J180333.3-295911	–	9.92	8.81	8.44	2.10	–	no
52	J180334.1-295958	–	8.70	7.60	7.06	6.65	–	no
53	IRAS 18042-2905	594.40	–	–	10.87	–	1.56	yes

Table 4.9: OGLE counterparts for the targets in this sample. For each object for which we could find a counterpart in the OGLE-II survey, we list its OGLE name and the derived periods based on the *I*-band photometry, as well as the full *I*-band amplitude of the dominant period. The numbering of the objects in this table refers to the numbering given in Table 3.2.

Number	Name	OGLE name	Periods [days]					A_I
22	J174917.0-293502	bul_sc44_7783	–	–	–	–	–	–
23	J174924.1-293522	bul_sc44_7808	–	–	–	–	–	–
27	J175432.0-295326	bul_sc4_2833	405.86	772.74	139.68	–	–	1.90
28	J175456.8-294157	bul_sc4_5023	322.11	402.16	184.91	–	–	0.33
29	J175459.0-294701	bul_sc4_4215	497.80	116.71	–	–	–	3.09
30	J175511.9-294027	bul_sc39_3998	–	–	–	–	–	–
31	J175515.4-294122	bul_sc39_3882	76.90	341.94	–	–	–	0.09
32	J175517.0-294131	bul_sc39_3885	–	–	–	–	–	–
35	J180238.8-295954	bul_sc1_2026	100.20	495.10	833.61	377.25	113.69	0.14
36	J180248.9-295430	bul_sc1_2478	75.69	727.27	82.34	–	–	0.06
37	J180249.5-295853	bul_sc1_2131	65.18	459.89	183.89	–	–	0.08
38	J180259.6-300254	bul_sc1_1872	228.87	308.53	128.94	–	–	0.37
39	J180301.6-300001	bul_sc1_2050	33.49	–	–	–	–	0.04
40	J180304.8-295258	bul_sc45_1501	35.52	341.68	–	–	–	0.07
41	J180305.3-295515	bul_sc45_1426	207.02	549.53	112.57	–	–	0.22
42	J180305.4-295527	bul_sc45_1385	113.94	443.64	259.32	–	–	0.15
43	J180308.2-295747	bul_sc45_1312	113.04	–	–	–	–	0.23
45	J180308.7-295220	bul_sc45_1539	–	–	–	–	–	–
46	J180311.5-295747	bul_sc45_1316	292.04	–	–	–	–	1.48
47	J180313.9-295621	bul_sc45_1355	–	–	–	–	–	–
48	J180316.1-295538	bul_sc45_1390	62.69	41.27	150.39	–	–	0.18
49	J180323.9-295410	bul_sc45_1477	84.86	214.49	–	–	–	0.15
50	J180328.4-295545	bul_sc45_1401	119.09	432.42	–	–	–	0.15

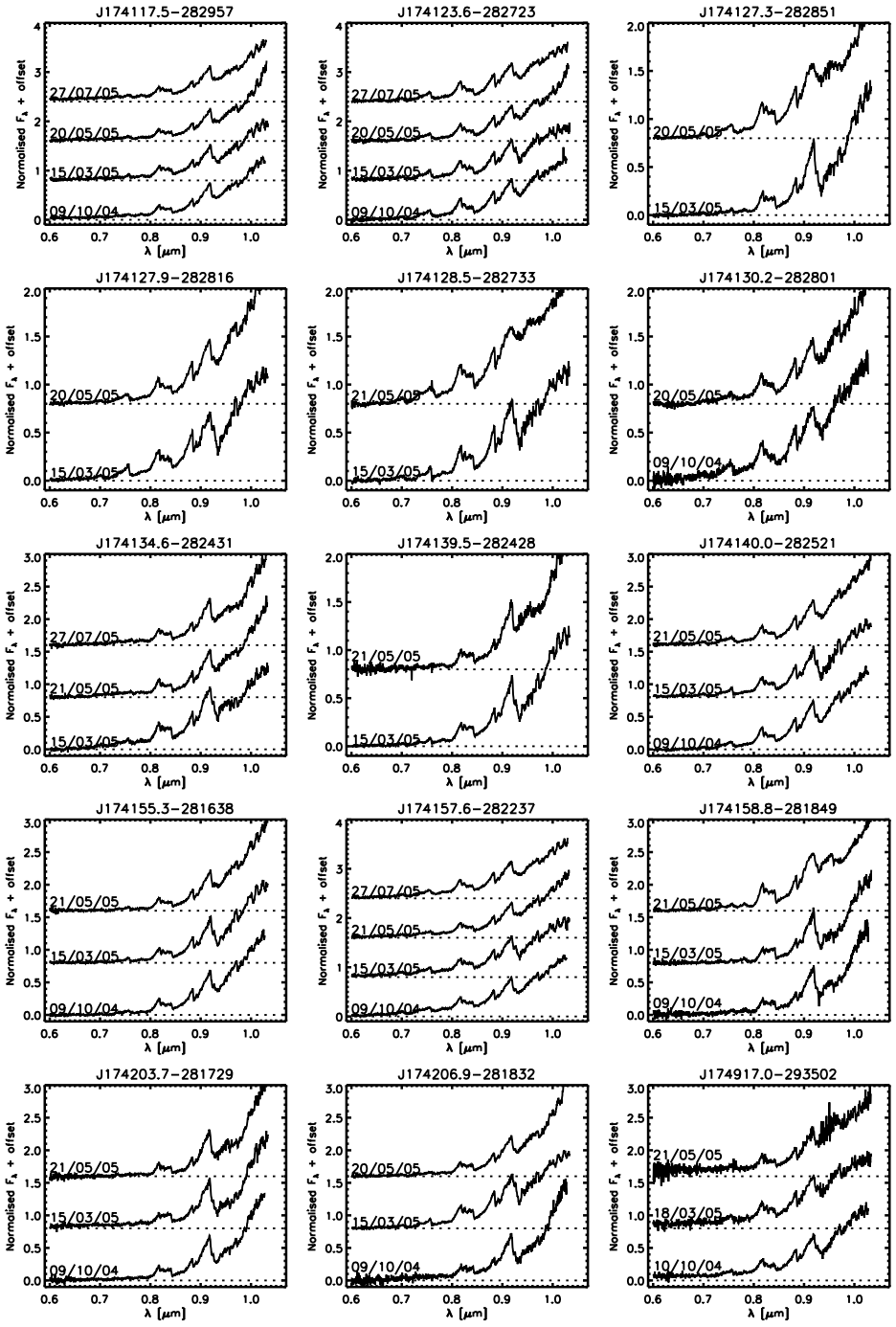

Figure 4.17: Optical spectroscopy. Relative F_λ is plotted against λ. The dotted lines indicate the zero-flux level and also the observation date is given for each spectrum.

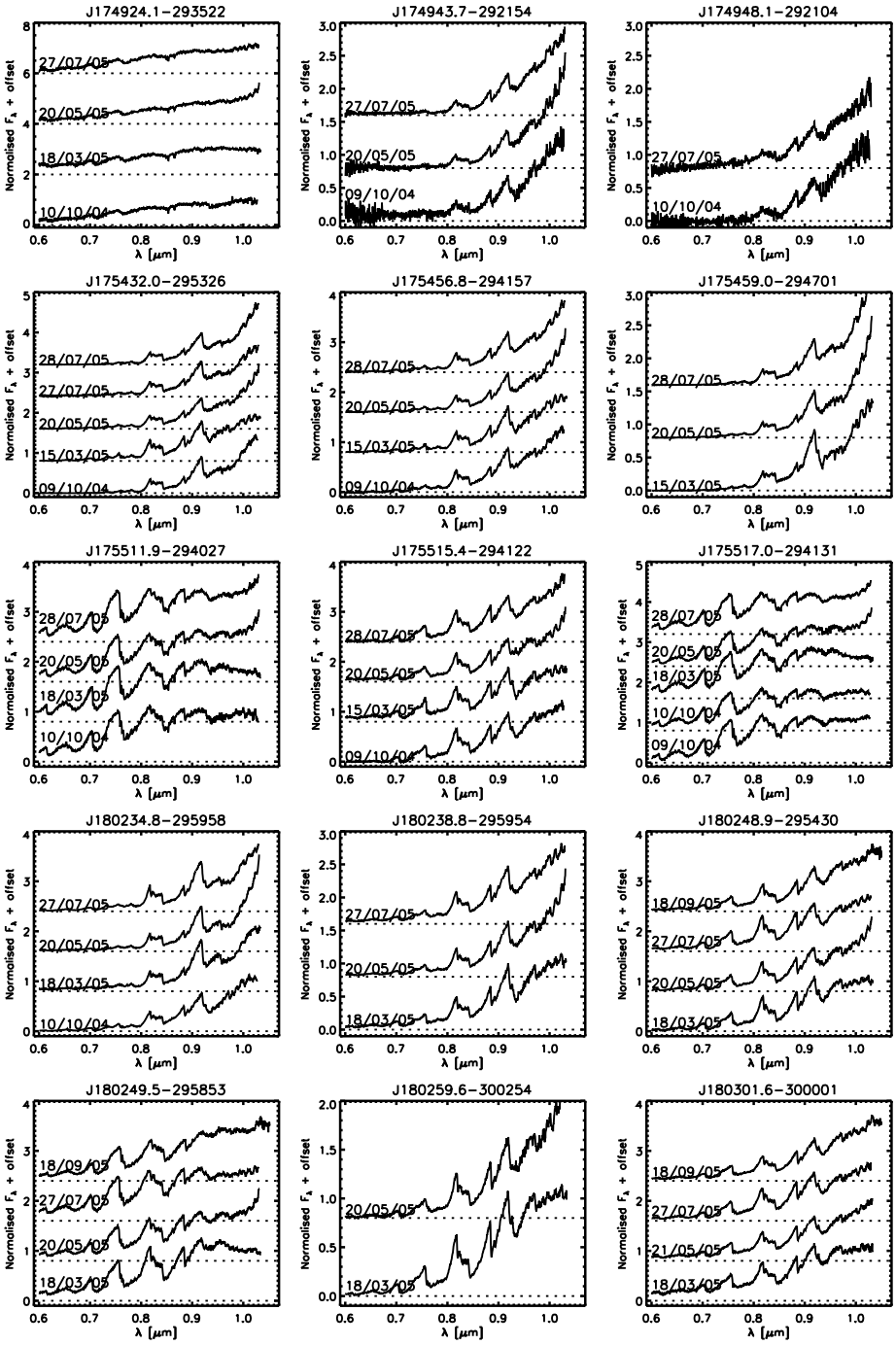

Figure 4.18: Optical spectroscopy – continued.

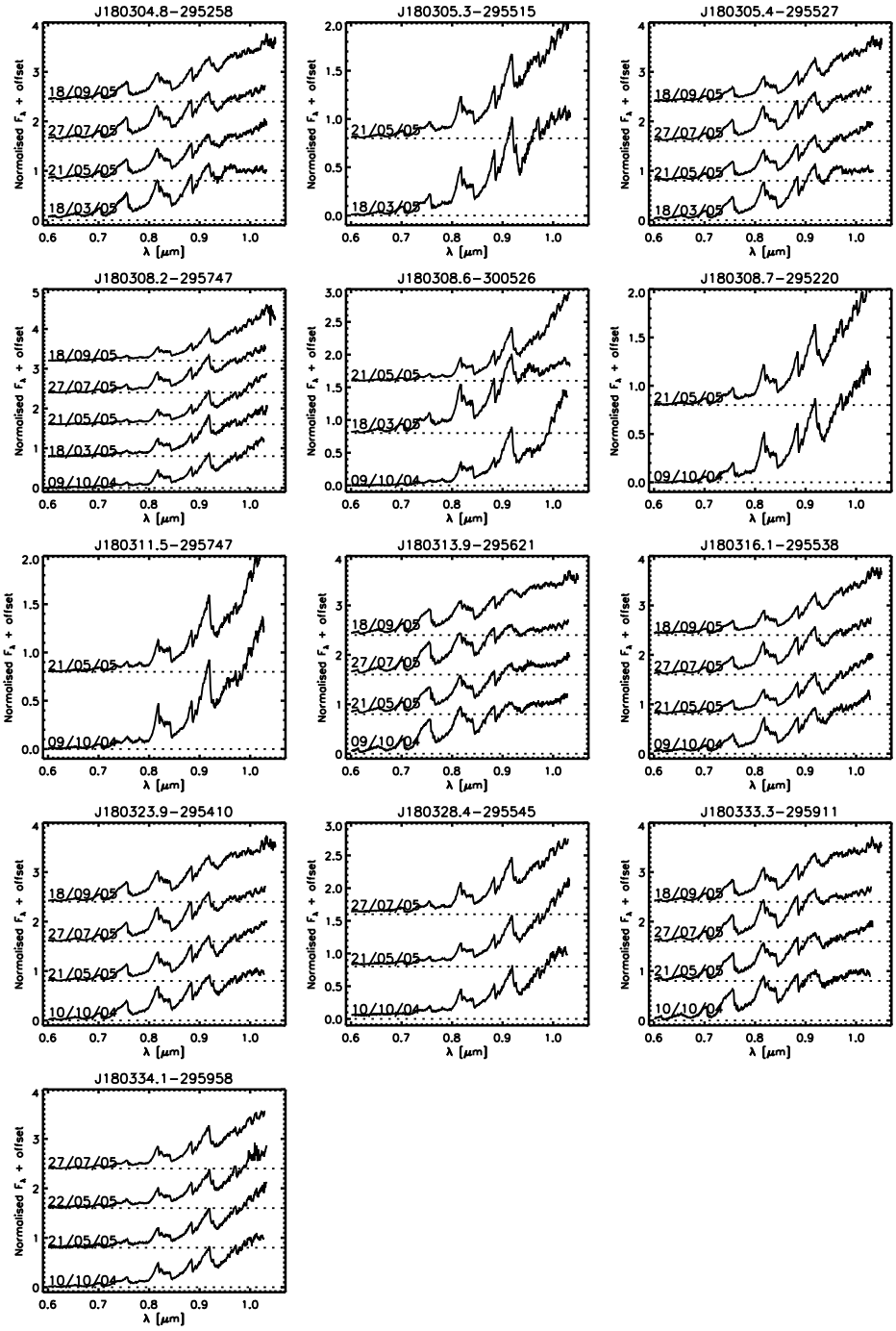

Figure 4.19: Optical spectroscopy – continued.

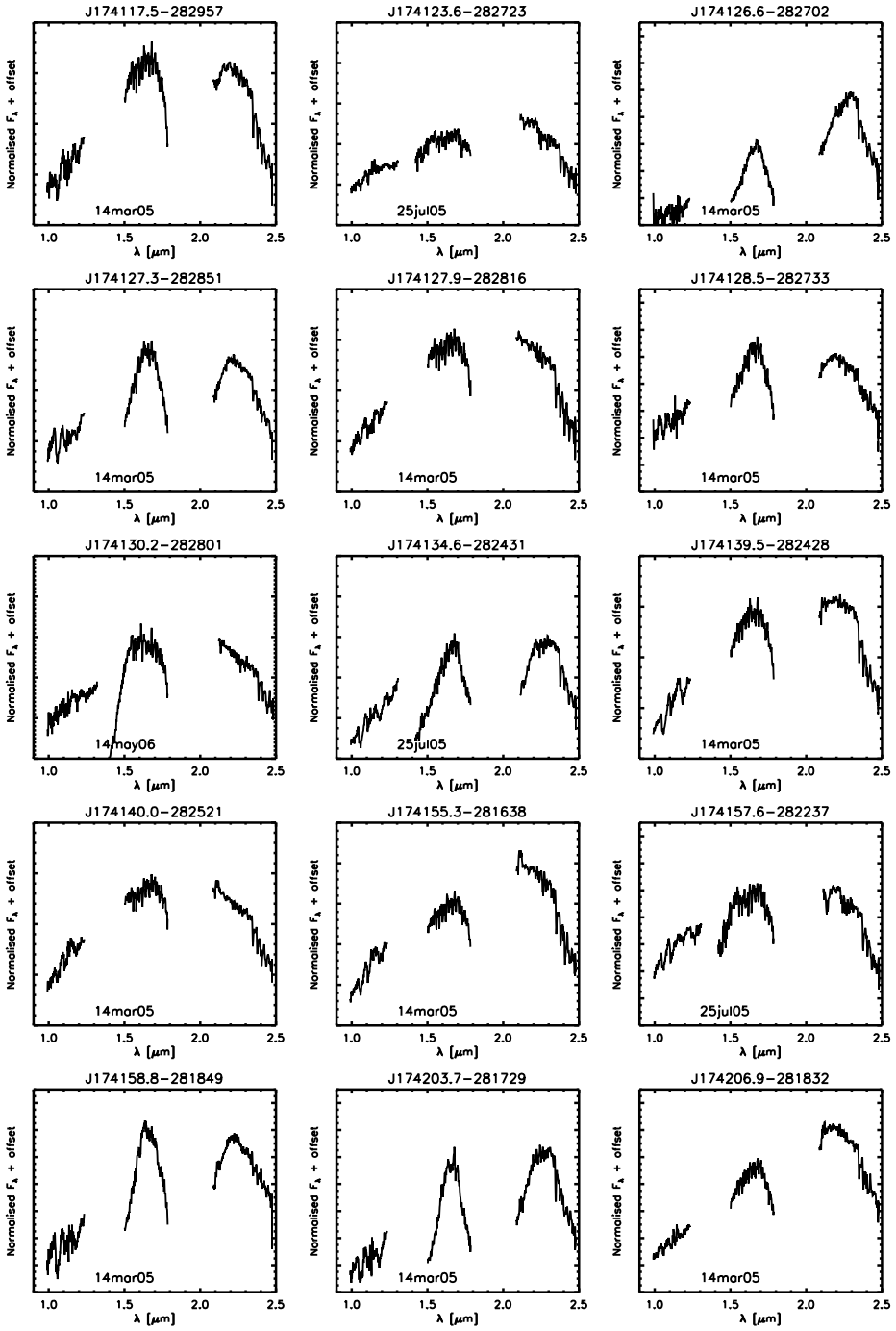

Figure 4.20: Near-IR spectroscopy. Relative F_λ is plotted against λ.

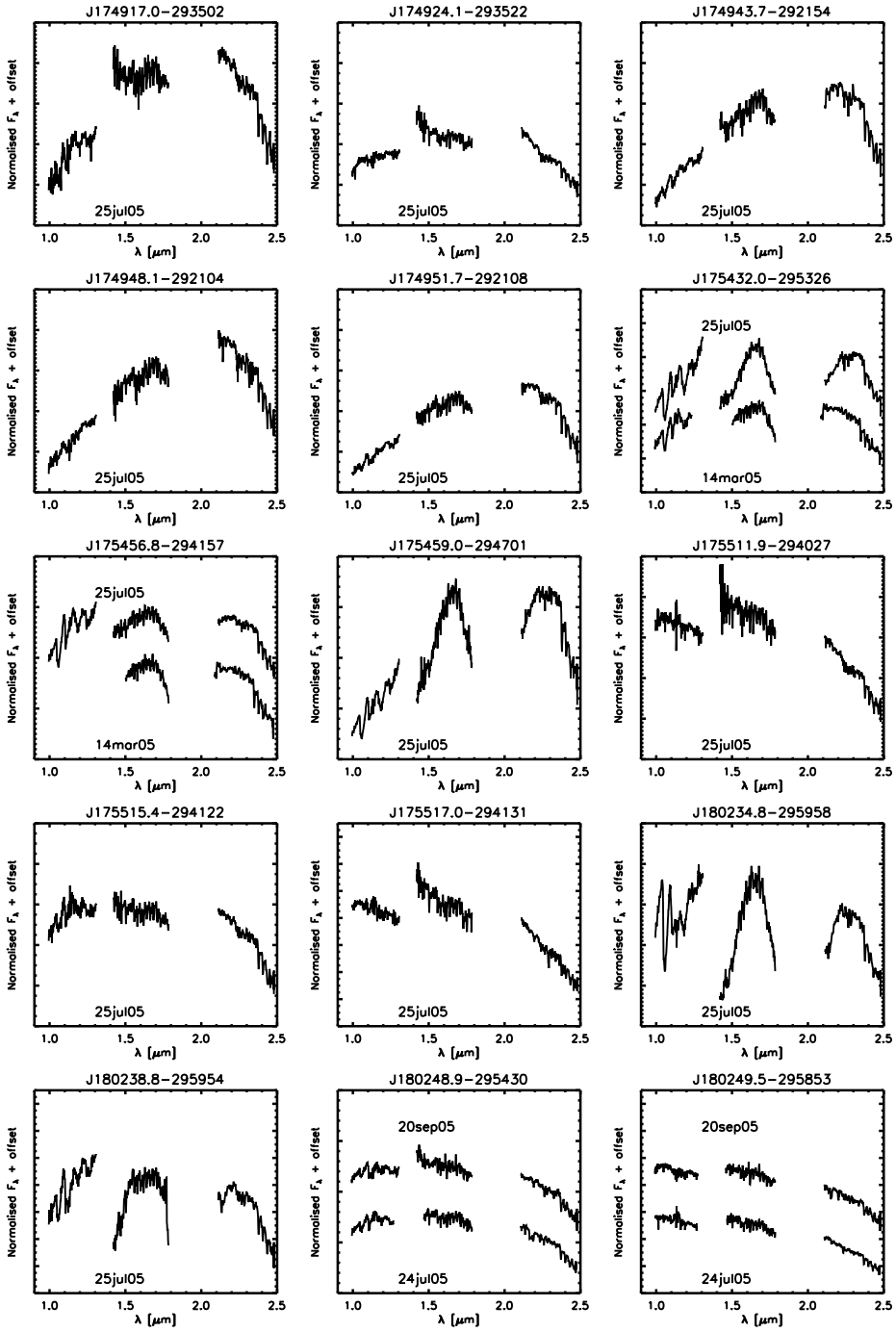

Figure 4.21: Near-IR spectroscopy – continued.

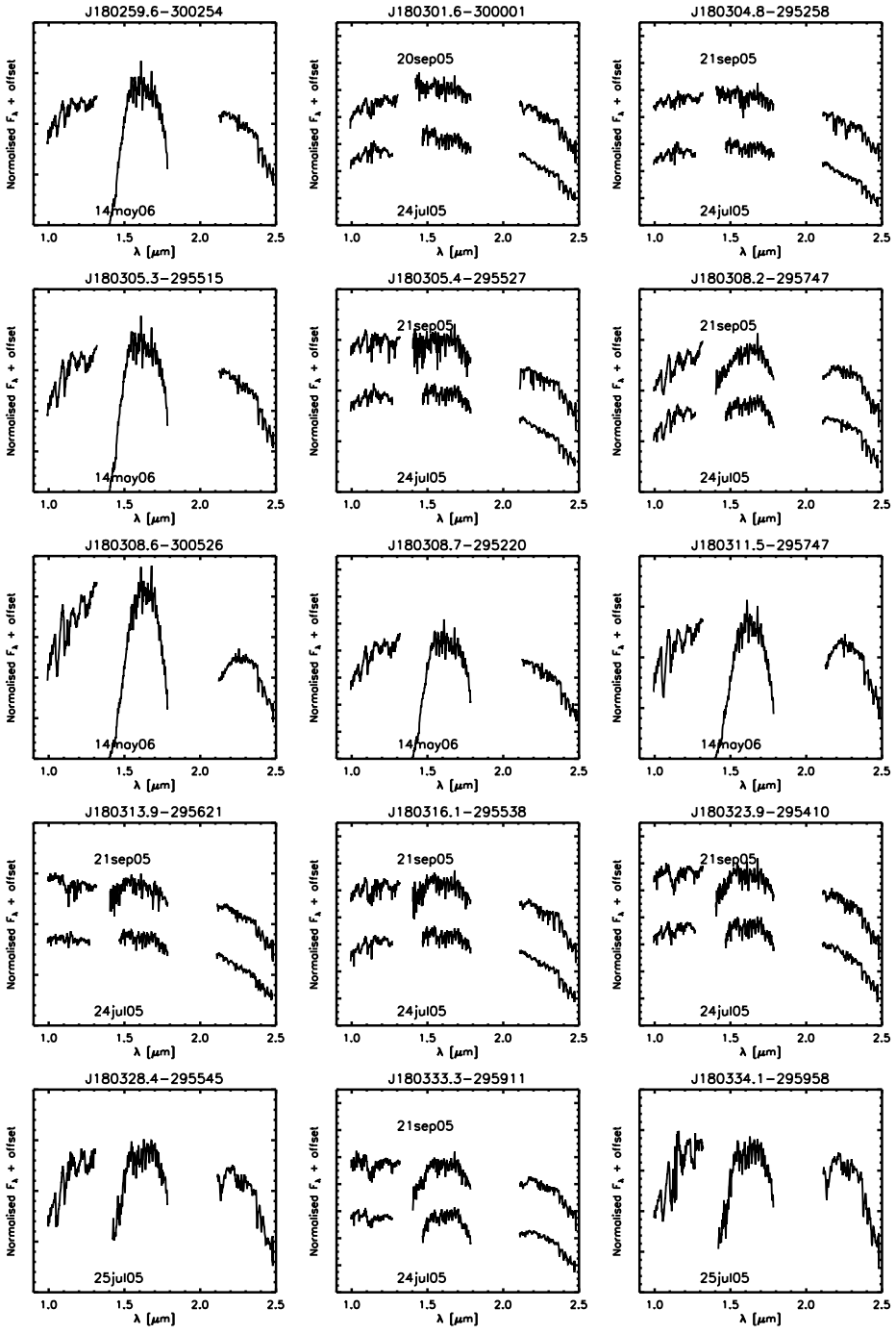

Figure 4.22: Near-IR spectroscopy – continued.

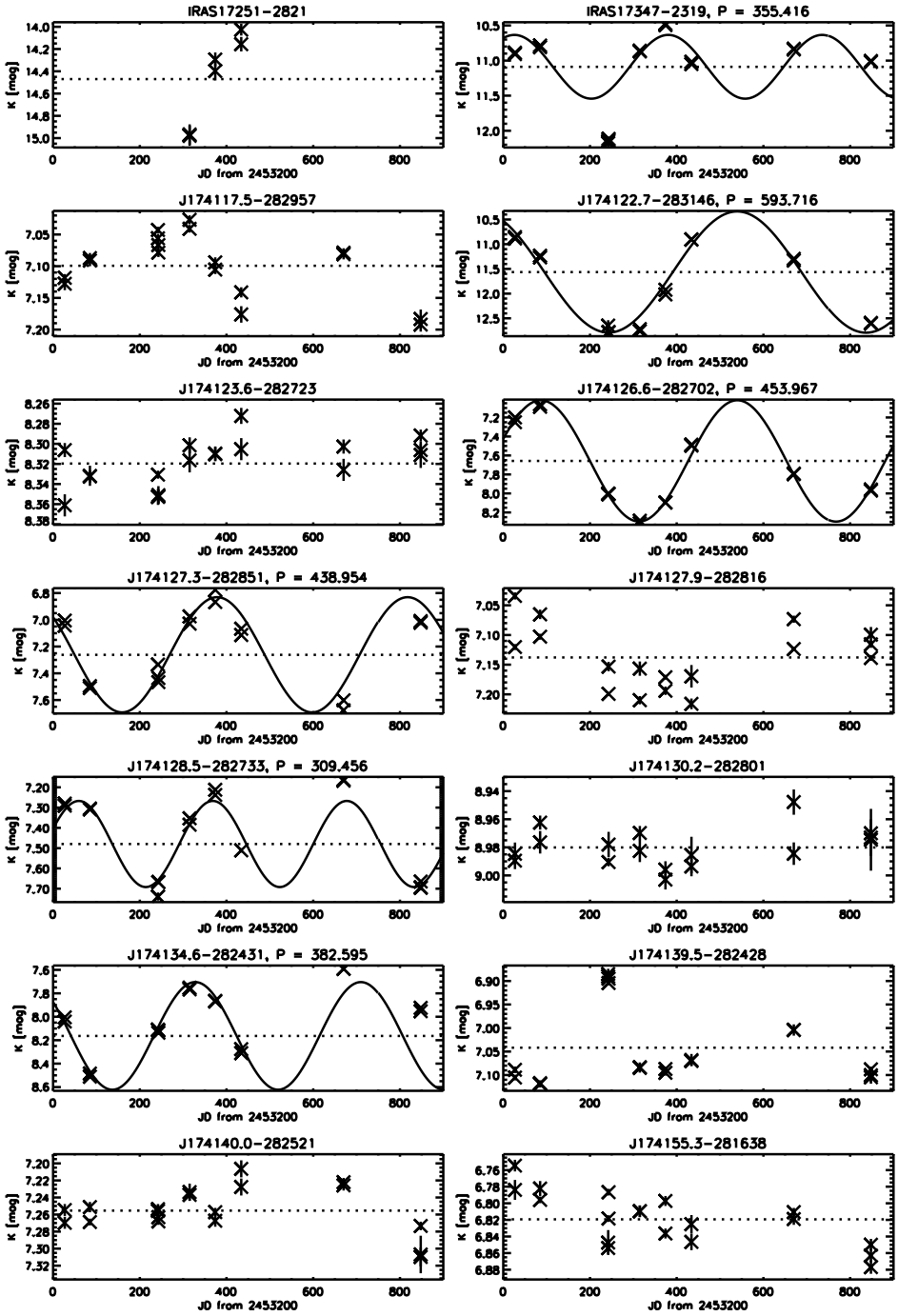

Figure 4.23: *K*–band light-curves.

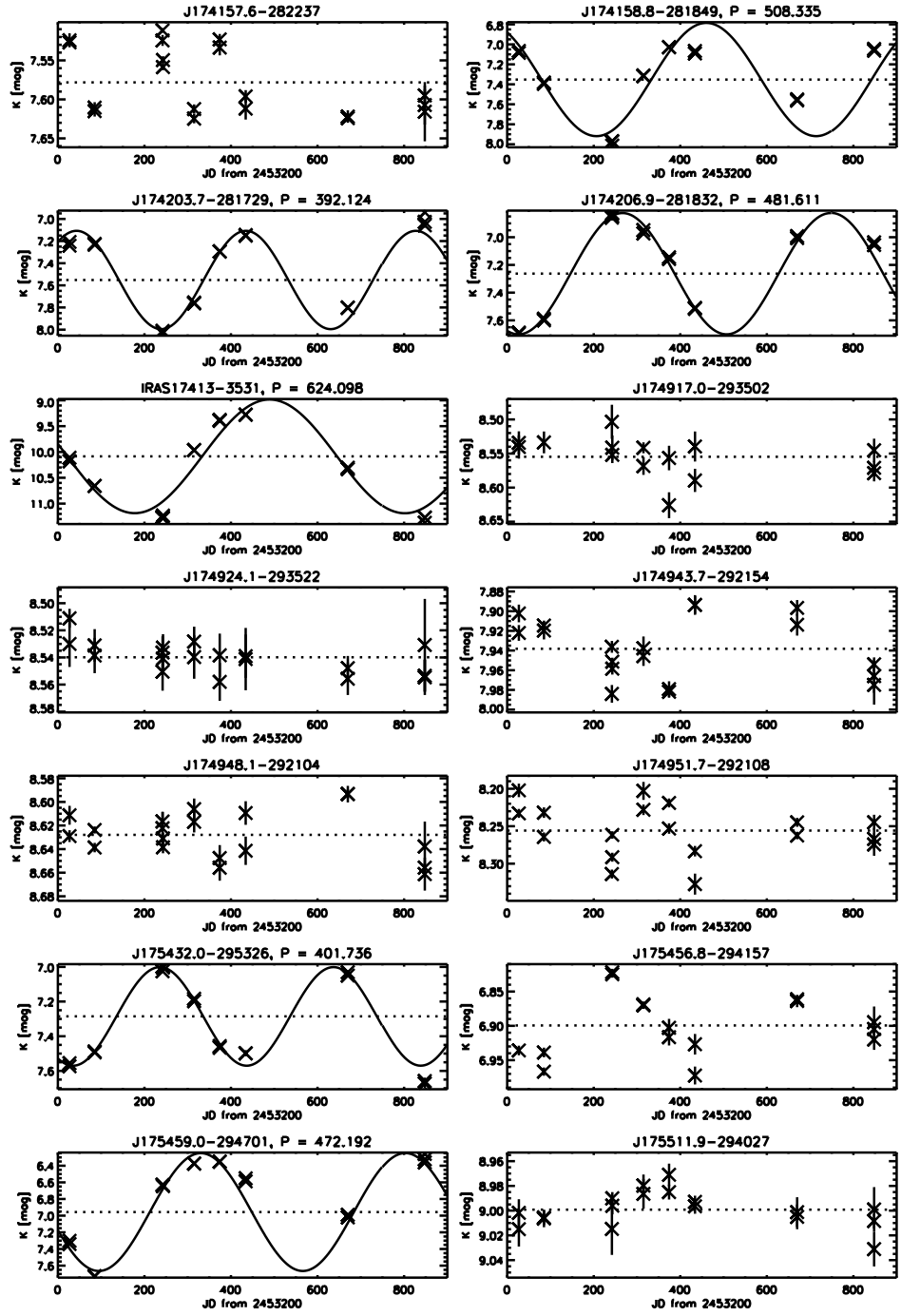

Figure 4.24: *K*–band light-curves – continued.

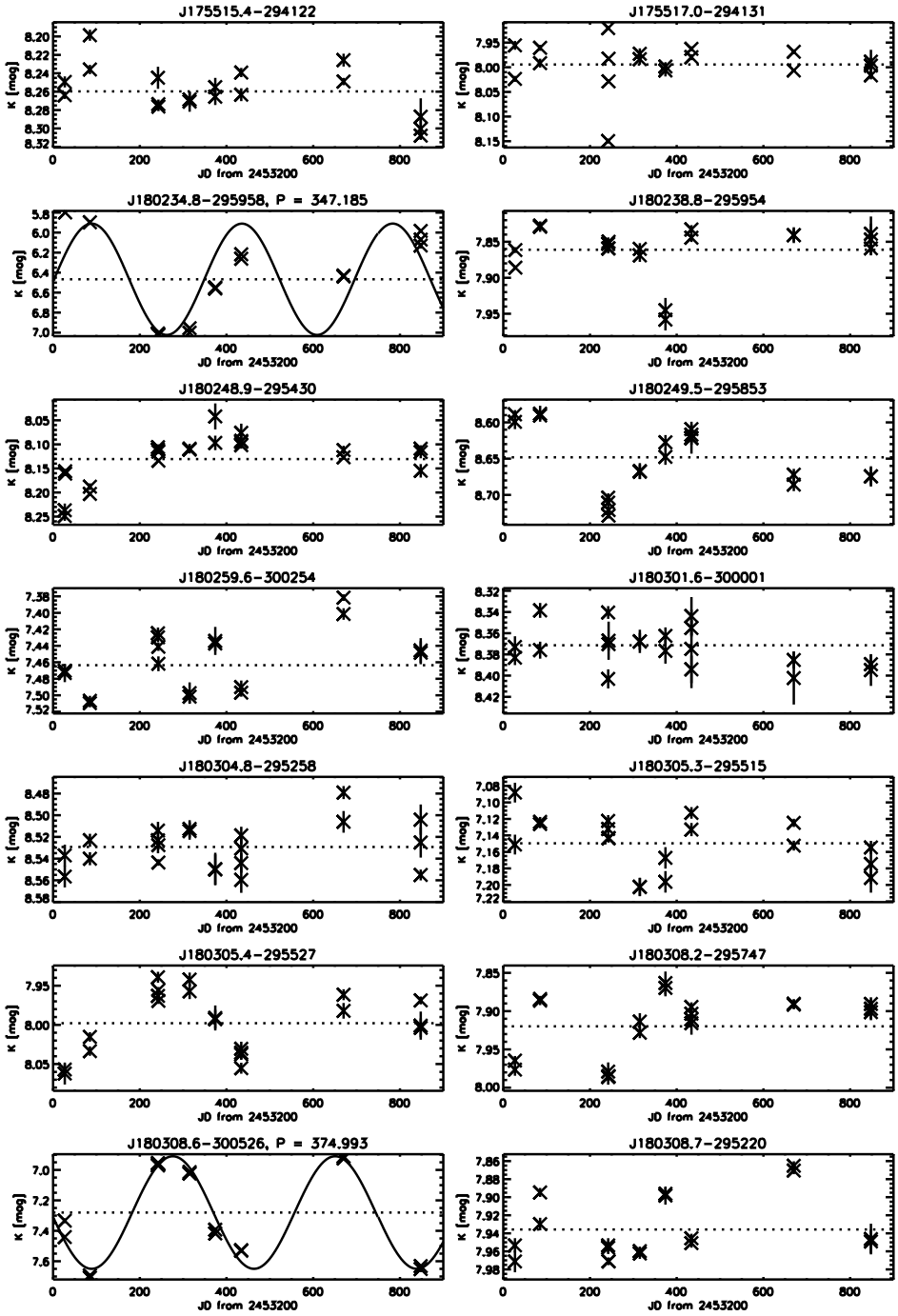

Figure 4.25: *K*–band light-curves – continued.

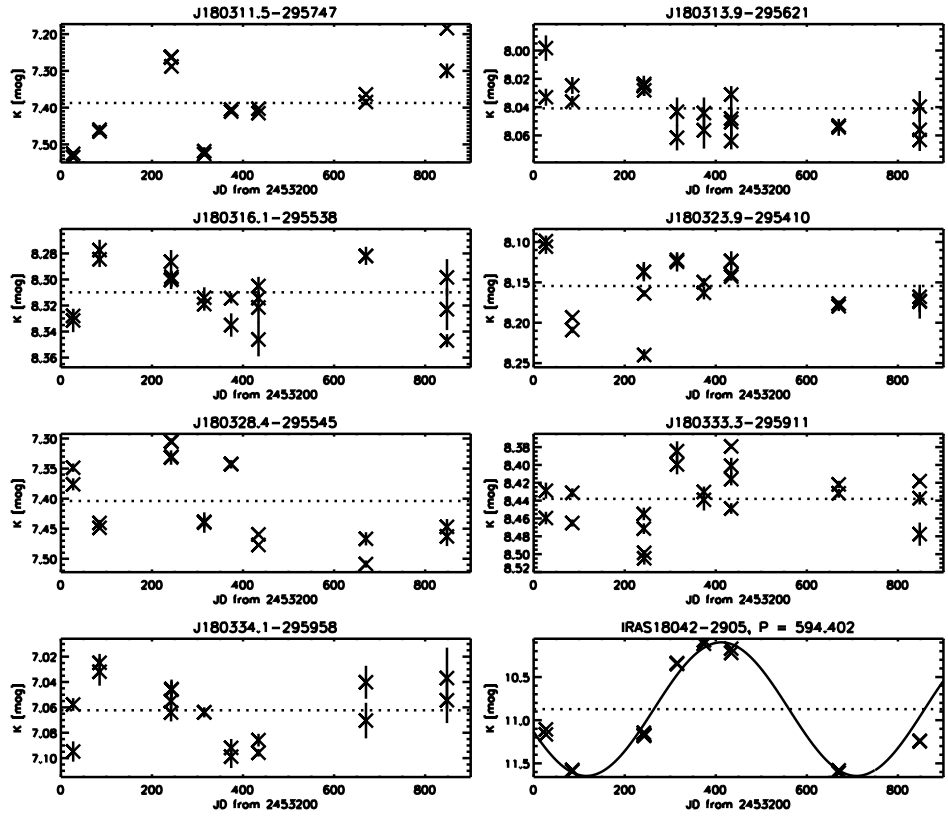

Figure 4.26: *K*–band light-curves – continued.

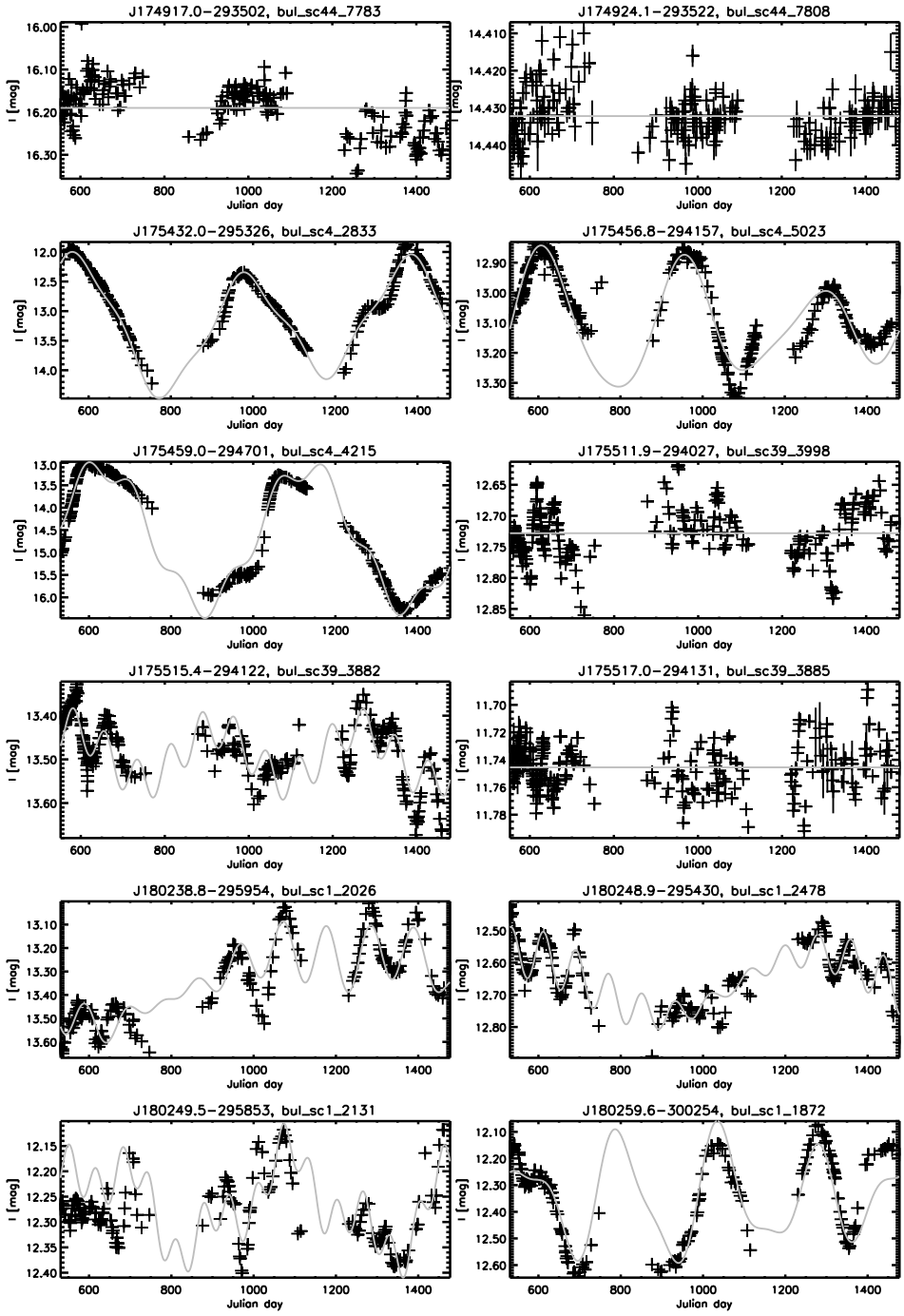

Figure 4.27: OGLE *I*-band light-curves.

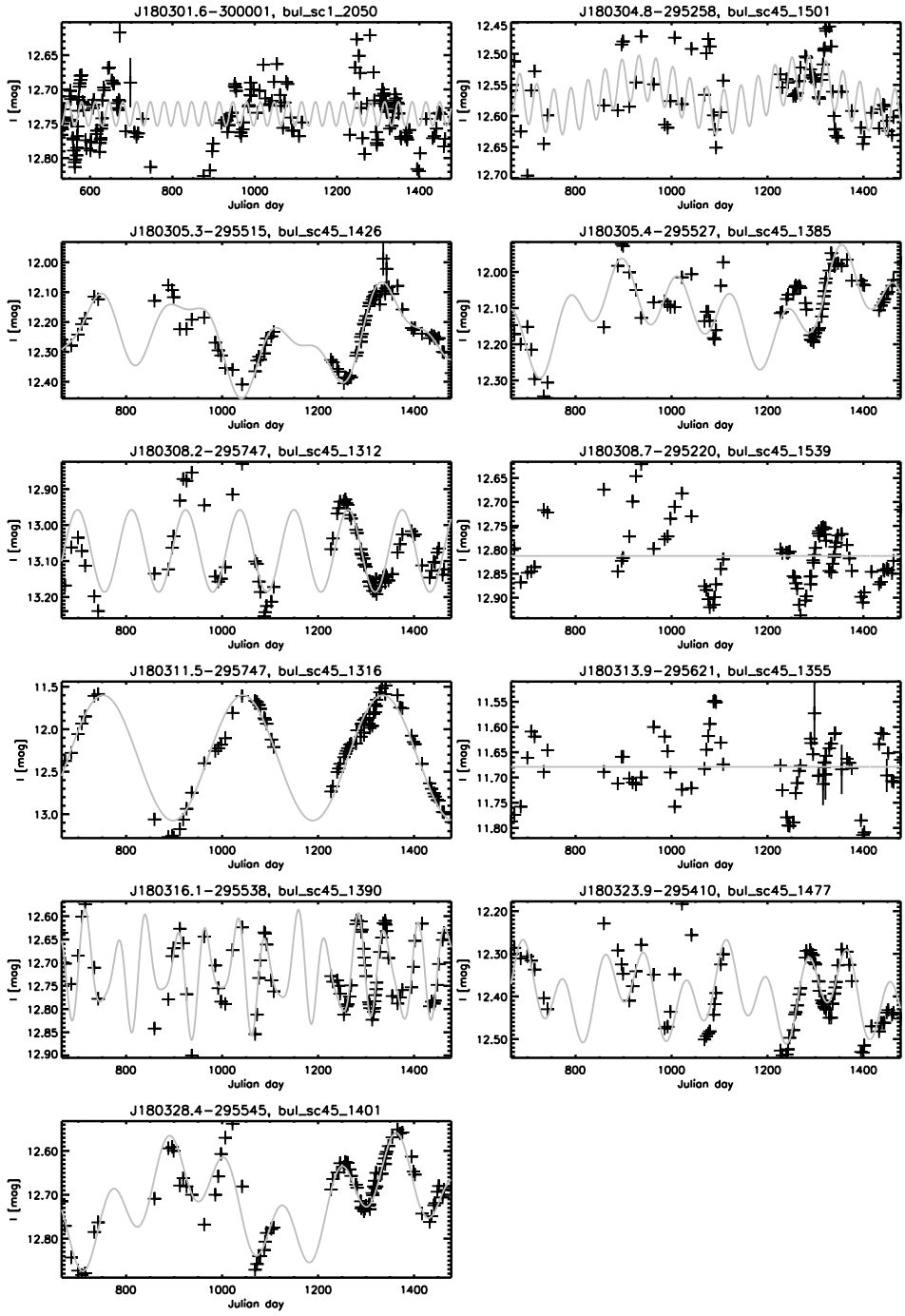

Figure 4.28: OGLE *I*-band light-curves – continued.

CHAPTER 5

Crystalline material in the circumstellar envelope around OH/IR stars in the Galactic Bulge

This chapter is based on the paper:
Vanhollebeke, E., Waters, L.B.F.M., Blommaert, J.A.D.L., and Markwick-Kemper, F.: 2007, "Crystalline material in the circumstellar envelope around OH/IR stars in the Galactic Bulge", Astron. Astrophys., to be submitted

OH/IR stars are AGB stars in the final stage on the AGB and are believed to be the progenitors of Planetary Nebulae (see e.g. Habing 1996; Dijkstra et al. 2003; Cohen et al. 2005). They are characterised by huge amounts of mass-loss, the so-called superwind phase, which results in optically-thick dust envelopes which largely obscure the central star.

Min et al. (2007) studied the composition and shape distribution of silicate dust grains in the interstellar medium (ISM) towards the Galactic Centre. They found that the interstellar silicates are highly magnesium rich and not perfect homogeneous spheres as has often been assumed. They also confirmed the low presence (about 1%) of crystalline material in the ISM. They state that the high magnesium content in crystalline silicates in cometary and circumstellar grains is a natural consequence to the high amount of magnesium in amorphous silicates in the ISM. As AGB stars are known to be one of the major contributors to the dust in the interstellar medium, it is therefore important to study the amorphous and the crystalline dust around oxygen-rich AGB stars.

Apart from amorphous silicates, OH/IR stars also show evidence for crystalline silicates (Waters et al. 1996; Waters and Molster 1999). Crystalline silicates in late type stars have

been first detected with the Infrared Space Observatory (ISO) (Waters et al. 1996). It was believed that the presence of crystalline material must be directly linked to the dust formation process, possibly to the high densities in the circumstellar envelopes since there are no AGB stars with lower mass-loss rates found which also exhibit these crystalline features.
Several studies showed that this does not necessarily have to be the case as only iron-free magnesium silicates can account for the observed band position in astronomical spectra showing silicate features. Jäger et al. (1998) studied the correlation between the band position and the Fe-content and found that only very Mg-rich crystalline silicates can explain the ISO-SWS spectrum of AFGL 4106, an evolved binary. Molster et al. (2002b) obtained ISO-SWS observations of 17 oxygen-rich circumstellar dust shells surrounding evolved stars. In 14 of these 17 objects Molster et al. (2002c) studied the crystalline silicates and found that these crystalline silicates are colder than the amorphous silicates. This is probably due to the difference in chemical composition: Fe is not present in the crystalline silicates, while in the amorphous silicates, it is expected to explain the higher absorptivity. They also state that this difference in temperature must also imply that the crystalline and amorphous grains are two distinct grain populations (see also Kemper et al. 2001). Because of the large temperature difference in the inner parts of the optically thin dust shells around low mass-loss rate AGB stars, the warm amorphous silicate emission dominates the spectrum as amorphous dust containing Fe absorbs more efficiently the stellar radiation than the Fe-poor crystalline dust. When the dust becomes optically thick, the radiation from the central star will be absorbed and re-radiated by the dust several times. Therefore the dust in the outer layers receives a relatively red radiation field that peaks in the mid-IR. In this region, both crystalline and amorphous silicates absorb equally well the IR radiation and therefore the two dust species have the same temperature. Since the shell is optically thick, only the outer layers are visible, which leads to a high contrast of the crystalline silicate features.

A problem accompanying the question to why we do not see crystalline features in AGB stars with lower mass-loss rates than OH/IR stars, is the question to the formation of these crystalline silicates. Sylvester et al. (1999) detected in OH/IR stars studied with ISO-SWS crystalline features in emission in the same wavelength region as where the amorphous silicates are in absorption. This suggests a different spatial distribution of the two species.

Sloan et al. (2006) studied the dust around HV 2310, an evolved star located in the Large Magellanic Cloud. The dust emission of this star shows a narrow 9.7 μm component and an 11.2 μm shoulder superimposed on the amorphous 10 μm silicate emission feature. Compared to evolved Galactic sources, this is very unusual. The most plausible explanation Sloan et al. (2006) found is the presence of crystalline silicates (particularly forsterite). No stars with lower mass-loss rates than OH/IR stars have been found to show crystalline features in the present Galactic sample. If HV 2310, which is not an OH/IR star, shows crystalline silicate grains, then the generally lower metallicities in the Magellanic Clouds should lead to a higher degree of crystallinity (Sloan et al. 2006). Therefore, the metallicity could be an extra parameter playing a role in the presence or absence of crystalline features in evolved stars.

The Mira population in the Galactic Bulge (GB) all originate from the same population with an initial mass of about 1.5 $M_{\odot}$ (Groenewegen and Blommaert 2005). In addition, AGB stars in the GB are all located at about the same distance which makes them directly com-

parable in terms of different evolutionary stadia. Therefore AGB stars in the GB are the ultimate sample to study dust formation in a homogeneous way. Because of the homogeneity of this sample, it is ideal to study the dust around evolved stars and the parameters the dust formation depends on, while this is harder with an inhomogeneous sample like e.g. a sample selected in the Solar neighbourhood. With this sample, we can now address questions on how the amount of crystalline silicates depend on the properties of the central star.

This chapter is organised as follows: in Section 5.1 we discuss the sample and show the Spiter-IRS observations. Section 5.2 is dedicated to the analysis of the amorphous and crystalline features and the 11.3 μm, also the 33.6 μm feature are studied in more detail. Section 5.3 is dedicated to a discussion about the central position of the 11.3 μm feature and the degree of crystallinity. Finally in Section 5.4 we will summarise and come to conclusions.

5.1 Sample

Table 5.1 gives an overview on the OH/IR stars in the sample which are part of the larger sample selected in Chapter 3. The numbers in the first column refer to the object numbering in Table 3.2.

The data-reduction has been performed using SMART (Higdon et al. 2004) and started from the pipeline level of Basic Calibrated Data S12.4.0. Data-reduction consisted of background subtraction, cleaning the images for bad pixels and cosmic-ray hits, column extraction of the observed object, correcting for fringes at the longer wavelengths, and extinction correction.

For weak objects, the highly varying background in the GB can severely hamper data-reduction and can leave fingerprints on the final spectrum. Because the OH/IR stars in this sample are very bright and as most of them are located a bit higher above the plane than the other AGB stars in the sample, varying background levels do not leave any residuals in the final spectra.
Due to crowdedness in the slit, we could not always use all the pixels belonging to the object. This does not influence the general shape of the spectra, but the absolute flux calibration is therefore not trustworthy. In this sample of OH/IR stars, there is only one object suffering from this (J174122.7-283146). As we do not study the OH/IR stars in terms of their absolute fluxes, the spectra shown in Figure 5.1 are normalised to overcome this effect.
Most of the spectra also still show residuals of fringes in the region between 20 and 22 μm, thus the "features" in this region are not genuine, but are due to artefacts from data-reduction issues (see also Chapter 3). Also the bump at about 14 μm (seen in some objects) is not genuine, but originates from the so-called "14 μm teardrop" and is believed to originate from scattered light (see also 3.3.3).
To correct for extinction originating from dust in the ISM, the law by Chiar and Tielens (2006) for extinction originating from the local ISM has been used. The A_K extinction values come from Marshall et al. (2006) except for J174122.7-283146 for which we used the extinction map from Schultheis et al. (1999) and J175517.0-294131 for which we used the

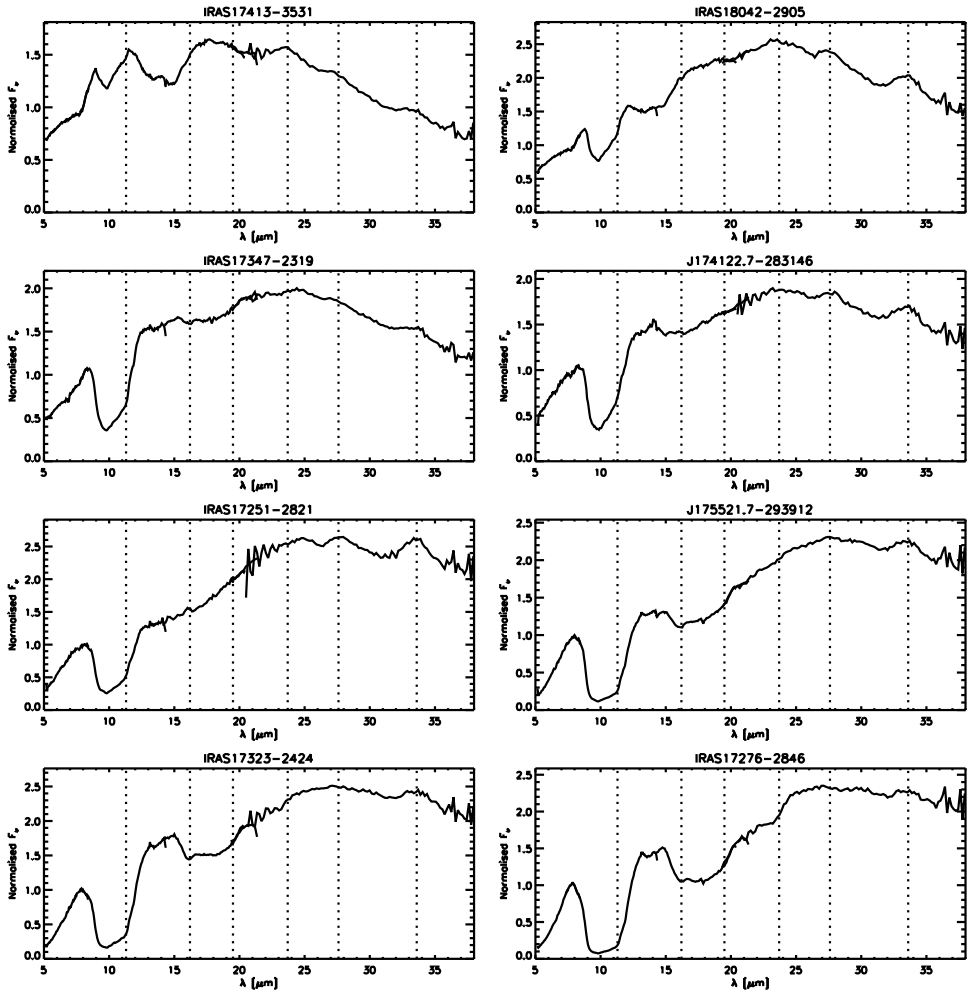

Figure 5.1: Spectra of the stars ordered with increasing $\dot{M}$ from left to right and top to bottom. The spectra are normalised to their flux at 8 μm. The dotted lines at 11.3, 16.2, 19.5, 23.7, 27.6, and 33.6 μm indicate the mean forsterite wavelength positions (Molster et al. 2002a). The spectra are normalised at 8 μm.

values from Sumi (2004). The used A_K values are 0.368 mag for IRAS 17251-2821, 0.495 mag for IRAS 17276-2846, 0.574 mag for IRAS 17323-2424, 0.498 mag for IRAS 17347-2319, 0.602 mag for J174122.7-283146, 0.283 mag for IRAS 17413-3531, 0.302 mag for J175517.0-294131, and 0.172 mag for IRAS 18042-2905.
For more information on the data-reduction, the extinction correction, and a first analysis, we refer the reader to Chapter 3.

Table 5.1: Appearance of the forsterite features in the OH/IR stars and the enstatite feature at 9.3 μm. The objects are arranged for increasing mass-loss rate $\dot{M}$ from top to bottom. "–" indicates the feature was found in absorption, "+" in emission, and "0" when there was no feature seen. A question mark indicates that the label might be spurious. The numbers in the first column refer to the numbering given in Table 3.2.

Number	Name	9.3	10.1	11.3	11.9	16.2	19.5	23.7	27.6	33.6
21	IRAS 17413-3531	0	0	–	–?	0	0	+	+	+
53	IRAS 18042-2905	0?	–	–	–	–	–	+	+	+
4	IRAS 17347-2319	0	–	–	–	–	0	+	+	+
6	J174122.7-283146	0	–	–	–	+	0	+	+	+
1	IRAS 17251-2821	–	0?	–	–?	+	0	+	+	+
33	J175521.7-293912	–	0	–	–	–	–	–?	+	+
3	IRAS 17323-2424	0	–	–	–	–	–	0	+	+
2	IRAS 17276-2846	0	–?	–	–	–	–	–	–	+

5.2 Analysis

Figure 5.1 shows the normalised OH/IR star spectra. The most prominent features seen in all these spectra are the 10 and 18 μm complex and several crystalline features at longer wavelengths (see dashed lines in Figure 5.1). The 10 and 18 μm complex originate from amorphous silicates and will be discussed in Section 5.2.1. The feature at 33.6 μm is the only crystalline feature seen in emission in all spectra. The crystalline features will be discussed in Section 5.2.2.

5.2.1 Amorphous silicate features

The amorphous silicate features at 9.7 and 18 μm can be clearly seen in the spectra shown in Figure 5.1. Only the first two stars still show their 10 μm complex in emission with a central reversal which is the beginning of self-absorption. For the other six stars, their 10 μm complex appears completely in self-absorption. Most AGB stars show these features in emission, but due to the high mass-loss rate, the super-wind, the dust column density is very large which results in optical thick dust shells and amorphous silicate features seen in absorption rather than emission.

The relative depth of the 10 μm absorption feature is not equal in all objects. Sylvester et al. (1999) and Justtanont et al. (2006) showed that the depth of the 9.7 μm silicate feature correlates very well with the mass-loss rate. The optical depth of the 10 μm complex τ_{10}, the mass-loss rate $\dot{M}$, and the luminosity L_* will be derived in Section 5.2.3. The objects in Figure 5.1 are organised in order of increasing mass-loss rate $\dot{M}$.

To have a better idea on what happens in the 10 μm complex, we also plot an optical depth τ of the 10 μm complex using the following equation:

$$F_{obs} = F_{cont} e^{-\tau}, \tag{5.1}$$

with F_{obs} the observed flux and F_{cont} the continuum flux. The continuum has been defined by a straight line above the 10 μm complex and therefore τ only represents the optical depth of

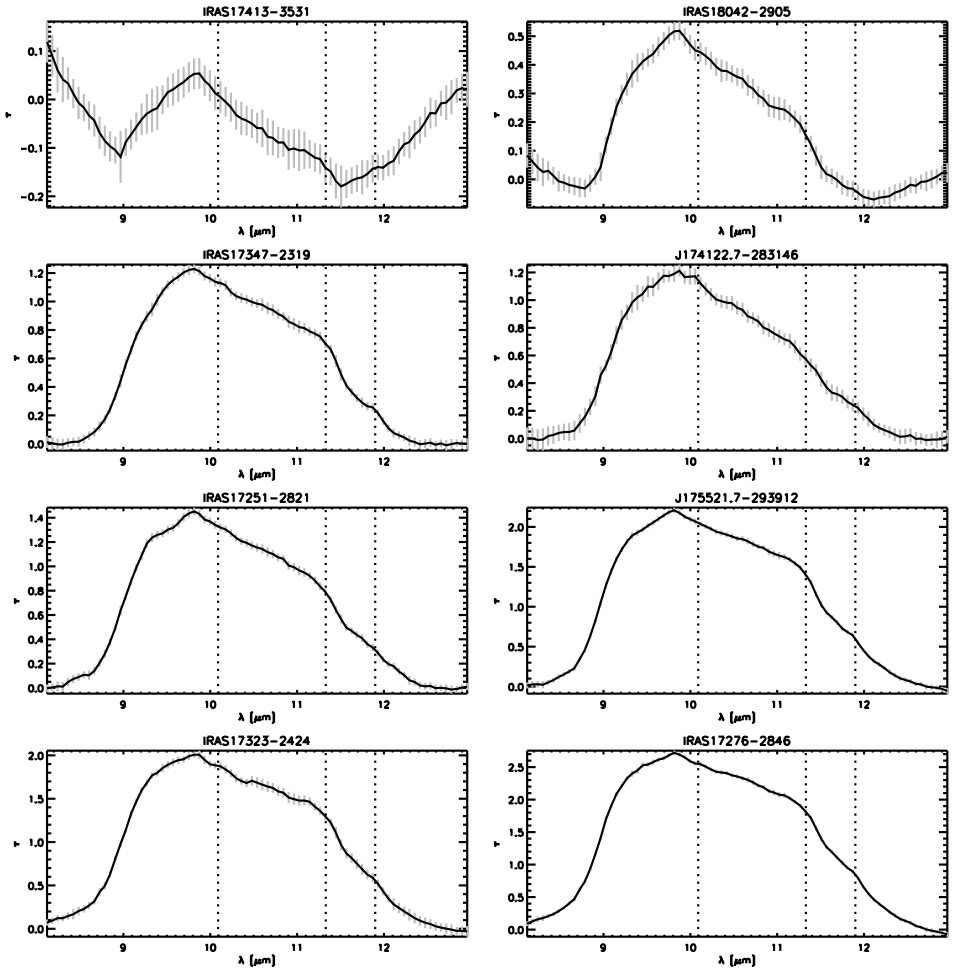

Figure 5.2: τ in the 10 μm wavelength region for our sample of OH/IR stars. The stars are again ordered with increasing $\dot{M}$. The dotted lines indicate the positions of stronger forsterite bands in this region (10.09, 11.33, and 11.9 μm).

the 10 μm complex itself and not the overall absorption of amorphous silicates in this region: the continuum in this wavelength region is for the objects showing complete self-absorption of the 10 μm complex expected to be located at higher flux levels than where we placed the continuum. The results are shown in Figure 5.2. This figure shows that the peak of this complex is located around 9.8 μm. Based on Figure 5.2 and also Figure 5.1 we see that not only the 10 μm complex changes from partly self-absorbed to complete self-absorption for increasing mass-loss rate, but these figures also show that the shape of the 10 μm complex itself changes: as the mass-loss rate increases, the 10 μm complex becomes broader and several sub-structures seem to appear. These sub-structures are caused by crystalline material and will be discussed in the following subsection.

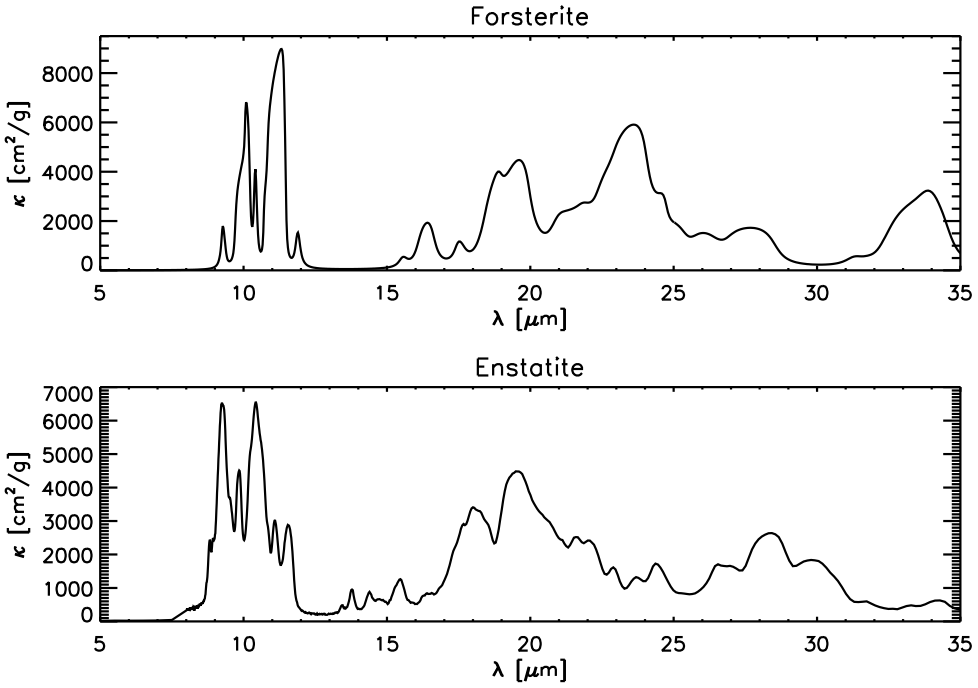

Figure 5.3: The opacity κ in function of wavelength for forsterite (Servoin and Piriou 1973, upper panel) and enstatite (Jäger et al. 1998, lower panel).

Not only the 9.7 μm silicate feature changes from emission in the stars with the lowest mass-loss rates to absorption in objects with the highest mass-loss rates, also the 18 μm silicate feature shows the same trend: the 18 μm feature is still seen in emission in IRAS 17413-3531 and IRAS 18042-2905 (the two objects which also show their 10 μm complex in partial self-absorption), the 18 μm feature is hard to detect in J174122.7-283146 and IRAS 17251-2821, but it is clearly seen in absorption in IRAS 17347-2319, IRAS 17323-2424, J175521.7-293912, and IRAS 17276-2846 (the OH/IR stars with the deepest 10 μm complexes).

5.2.2 Crystalline silicate features

Molster et al. (2002a) studied ISO-SWS data of a sample of 17 oxygen-rich dust shells surrounding evolved stars. For this sample Molster et al. (2002a) studied 7 complexes (the 10, 18, 23, 28, 33, 40, and 60 μm complexes) and derived average properties for the individual bands. The dashed lines in Figure 5.1 show the wavelength positions for forsterite (Mg_2SiO_4, the magnesium-rich end member of the olivines) as derived by Molster et al. (2002a).

The most prominent crystalline silicate features in our sample of OH/IR stars can be found at the longest wavelengths. For the stars with the lowest mass-loss rates in this sample, we see that the forsterite features longwards of 20 μm all appear in emission. For the sources with higher mass-loss rates, the emission features disappear and finally for the objects with the highest mass-loss rates, some of the features appear in absorption. Table 5.1 gives an overview of the forsterite features in the OH/IR star spectra. This table does not give a quantitative measurement of the features, but lists if the features are visible by eye or not. From Table 5.1 it becomes clear that the 33.6 μm feature is the only feature that appears in emission for every star in our sample.

Figure 5.2 shows that as we already noticed from the spectra in Figure 5.1, the 10 μm complex broadens for increasing mass-loss rate. This broadening is mainly caused by the amorphous silicates, but amorphous silicates alone are not responsible for the change in shape of the feature, also crystalline silicates influence the shape of the 10 μm complex. The dotted lines in Figure 5.2 indicate the positions of stronger forsterite features in this wavelength region. The upper panel in Figure 5.3 shows the opacity κ for forsterite. This figure shows how strong we can expect the different forsterite features to be in comparison with each other and shows that the 11.3 μm is the strongest and broadest forsterite feature in this region. All τ–spectra show a bump in this region, indicating that the forsterite is in absorption in the spectra. In Section 5.2.4.1 we will analyse this feature in more detail.
The laboratory spectra of forsterite show, in addition to the strong peak at 11.3 μm, two additional features, one fairly strong band at 10.1 and a weak band at 11.9 μm (see Figure 5.3). Inspection of our data (see Figure 5.1 and Table 5.1) shows that we detect the 11.9 μm band in almost all sources, but the 10.1 μm band is visible in only a few stars. This is probably due to the fact that the 10.1 μm band coincides with the maximum in the opacity of the amorphous silicate band, while the weaker 11.9 μm band is located in the wing of the amorphous silicate band, and is thus easier to detect against the amorphous silicate.

Forsterite is not the only crystalline material in the spectra of OH/IR stars, also enstatite ($MgSiO_3$, the Mg-rich end member of the pyroxenes) can be detected. Enstatite has it strongest features at 9.3 and 10.4 μm (see lower panel in Figure 5.3). The enstatite feature at 9.3 μm becomes very clear for the highest mass-loss rates: there is a distinguishable kink in the spectra at 9.3 μm. For IRAS 17276-2846 the star with the highest mass-loss rate, the kink in the spectrum seems to have shifted a bit to the blue.

5.2.3 Modelling

To derive luminosities and mass-loss rates for these objects, as well as to investigate the optical thickness of the dust shell at different wavelengths, we used the radiative transfer model of Groenewegen (1993, 1995). The used method to model our spectra is described in Blommaert et al. (2006). In later sections we discuss the degrees of crystallinity for the OH/IR stars based on the analysis of Kemper et al. (2001) who derive a grid of models for AGB stars with different mass-loss rates. To allow a direct comparison with our modelling we use the so-called astronomical or dirty silicates of which the optical constants were observationally determined from observed spectra of AGB stars by Suh (1999), as was done in Kemper et al.

Table 5.2: For the stars in this sample this table lists the mass-loss rate $\dot{M}$, the optical depth at 10 and 33.6 μm (τ_{10} and $\tau_{33.6}$), the luminosity L_*, the characteristics of the 11.3 μm feature, and the relative strength of the 33.6 μm feature ($S_{33.6}$).

Name	$\dot{M}$	τ_{10}	$\tau_{33.6}$	L_*	11.3 μm feature			$S_{33.6}$
	[10^{-4}M$_\odot$/yr]			[L$_\odot$]	height	peak [μm]	σ [μm]	
IRAS 17413-3531	0.3	4.7	0.6	7000	–	–	–	0.069
IRAS 18042-2905	0.6	8.6	1.1	6700	0.07	11.19	0.15	0.142
IRAS 17347-2319	0.4	10.2	1.3	7000	0.15	11.24	0.18	0.074
J174122.7-283146	0.8	10.7	1.4	7000	0.07	11.19	0.18	0.122
IRAS 17251-2821	1.5	17.9	2.3	7000	0.12	11.18	0.18	0.122
J175521.7-293912	2.0	22.3	2.8	6000	0.26	11.20	0.18	0.079
IRAS 17323-2424	2.0	23.8	3.0	7000	0.24	11.21	0.18	0.067
IRAS 17276-2846	3.0	32.3	4.1	5500	0.29	11.21	0.18	0.039

(2001).

Further input parameters for the modelling are the gas-to-dust ratio which was taken to be 200 (as was assumed in Blommaert et al. 2006). A typical grain density for amorphous silicates of 3.3 g cm^{-3} (e.g. Draine and Lee 1984) was assumed. The outflow velocity was taken from the expansion velocities derived from the OH spectra. For all IRAS sources these values were taken from van der Veen and Habing (1990) and for J174122.7-283146 from Sevenster et al. (1997) and J175521.7-293912 from David et al. (1993). These values are mostly around 15 km/s, which is a typical value for what is found in Galactic Bulge. The sources have been put at a distance of 8.5 kpc. The dust condensation temperature was assumed to be 1000 K. For the central stars we used the photospheric spectrum of a M10 giant from Fluks et al. (1994) and a $T_{\rm eff}$ = 2500K. The luminosities and mass-loss rates of the OH/IR stars are the remaining free parameters.

Additional photometry used in the modelling process has been derived from different sources: *K*, *L*, *M*, *N*1, *N*2, and *N*3-band photometry from van der Veen and Habing (1990), *H*, *K*, and *nbL* photometry from Chapter 4, 7 and 15 μm photometry from ISOGAL, MSX photometry at 8.28, 12.12, 14.65, and 21.34 μm, and IRAS fluxes at 12, 25, 60, and 100 μm. The fluxes have been dereddened in the same manner as the spectra (see Section 5.1). Since OH/IR stars are variable AGB stars exhibiting large amplitudes, it is important to keep in mind that the obtained photometric results were not observed at the same time. Therefore, a shift in the photometry between the different used catalogues due to the variability of the object is likely to occur.

The photometry has been used to model the overall energy distribution in order to obtain the luminosity. Based on the Spitzer-IRS spectrum, the mass-loss rates were determined. Figure 5.4 shows an example of the modelling. Table 5.2 lists the derived parameters for each object. All objects have mass-loss rates between 3×10^{-5} and 3×10^{-4}M$_\odot$/yr. The next column in Table 5.2 lists the derived optical depths of the 10 μm complex for each object. Based on the shape of the amorphous silicate 9.7 μm absorption features, it was already clear that the shells are optical thick at this wavelength and equivalent have a $\tau_{10} > 1$. This is confirmed by our modelling. The luminosities of the objects in our sample range between 5500 and 7000L$_\odot$, which compare well with the values given in van der Veen and Habing (1990).

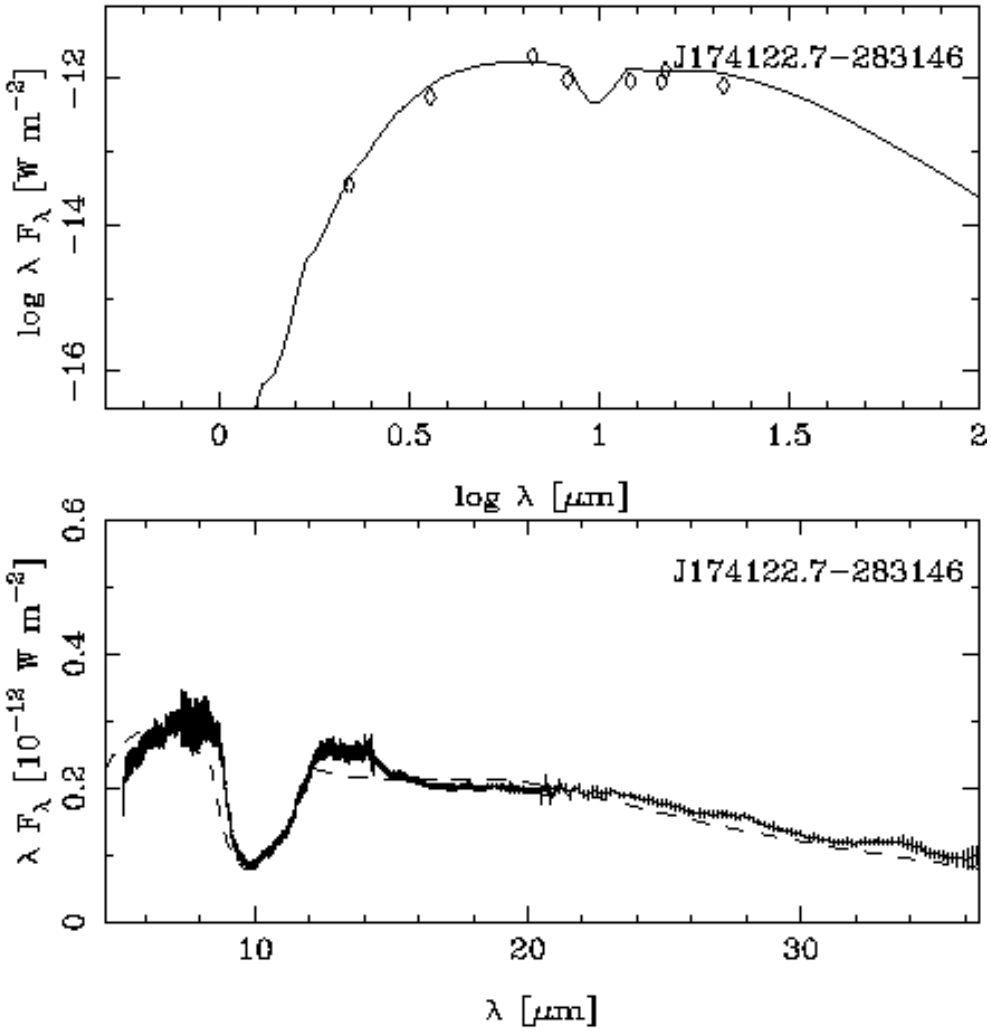

Figure 5.4: Example of the model fit to the photometry (upper panel) and Spitzer-IRS spectroscopy for J174122.7-283146.

This narrow range in luminosities confirms that the OH/IR stars in this sample originate from a population of similar initial masses.

5.2.4 Derivation of the fraction of crystalline dust

In this section we analyse the forsterite bands seen in our spectra. We wish to determine the amount of crystalline silicates produced, and the spatial distribution of the crystalline dust. A full analysis of the spectra would require fitting detailed radiative transfer models to the in-

dividual spectra including not only amorphous silicate dust as was done in Section 5.2.3, but also crystalline material would have to be included. This is beyond the scope of the present study. Instead, we will use the model calculations by Kemper et al. (2001) who provide a relation between mass-loss rate, crystallinity and the strength of the 33.6 μm forsterite band. In order to measure the spatial distribution of crystalline silicates, it is important to include as many bands as possible covering a wide wavelength range, and again using full radiative transfer model. Here we will focus on the 11.3 μm forsterite band, which should probe material located much closer to the star than the 33.6 μm forsterite band. Unfortunately no easy calibration of the strength of the 11.3 μm forsterite band as a function of crystallinity exists in the literature. Nevertheless, we will be able to establish if the trends seen in the strength of the 33.6 μm band are similar to those seen in the 11.3 μm band.

5.2.4.1 The 11.3 μm feature

In order to study the degree of crystallinity in Section 5.3.2 we analyse the 11.3 μm feature in more detail. Figure 5.5 shows how this was done. Using the τ spectra in the 10 μm region a local continuum has been defined close to the 11.3 μm. The continuum bands were chosen at 10.6 – 10.9 μm and 11.5 – 11.7 μm and a straight line has been fitted to these bands (see dashed lines in Figure 5.5). On top of this local continuum, a Gaussian has been fitted. The resulting Gaussian curves are shown on top of the τ spectra in grey in Figure 5.2, the parameters for these curves are listed in Table 5.2. Due to the partial self-absorption that just started in IRAS 17413-3531, this star has been excluded from this analysis.

5.2.4.2 The 33.6 μm feature

Kemper et al. (2001) used the strength of the 33.6 μm feature to derive an estimate for the degree of crystallinity in O-rich AGB stars. The relative strength of the 33.6 μm feature $S_{33.6}$ is given by:

$$S_{33.6} = \frac{F_{33.6}}{F_{cont}} - 1, \tag{5.2}$$

with $F_{33.6}$ the flux at 33.6 μm and F_{cont} the continuum flux at 33.6 μm under the feature. The continuum bands chosen to derive the local continuum are 31.0 – 31.5 μm and 35.0 – 35.5 μm. The results of this analysis are given in Table 5.2.

5.3 Discussion

5.3.1 The wavelength position of the 11.3 μm feature

Figure 5.2 showed that the 11.3 μm feature can be seen in all τ-spectra and Table 5.2 indicates that the peak position of the 11.3 μm feature in this sample is located around 11.2 μm. The 11.3 μm feature is also often seen in young stars such as Herbig Ae/Be stars and T Tauri stars (Bouwman et al. 2003; van Boekel et al. 2005; Kessler-Silacci et al. 2006). In these young stars the 11.3 μm feature is seen at 11.3 μm and not at 11.2 μm. Different grain sizes between

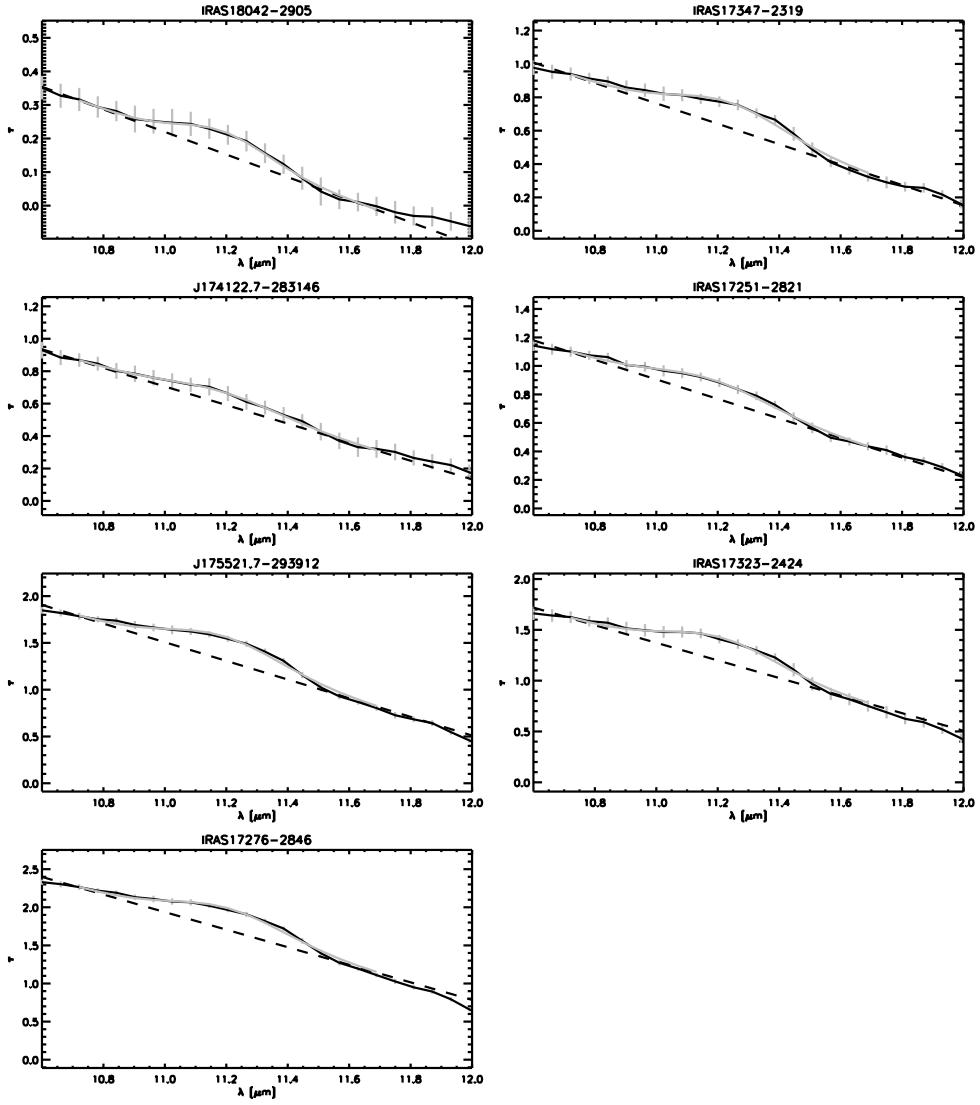

Figure 5.5: Gaussian fit on top of a local continuum to derive the characteristics of the 11.3 μm feature. The τ spectrum is given by the black line and grey error bars. The dashed line is a fit to the continuum and the full grey line gives the Gaussian fit on top of the local continuum.

the crystalline dust around young stars and these OH/IR stars could be responsible for the different wavelength positions. Smaller grain sizes make the feature shift towards the blue, indicating that the grain sizes of crystalline forsterite around OH/IR stars could be smaller than the crystalline dust around young stars.

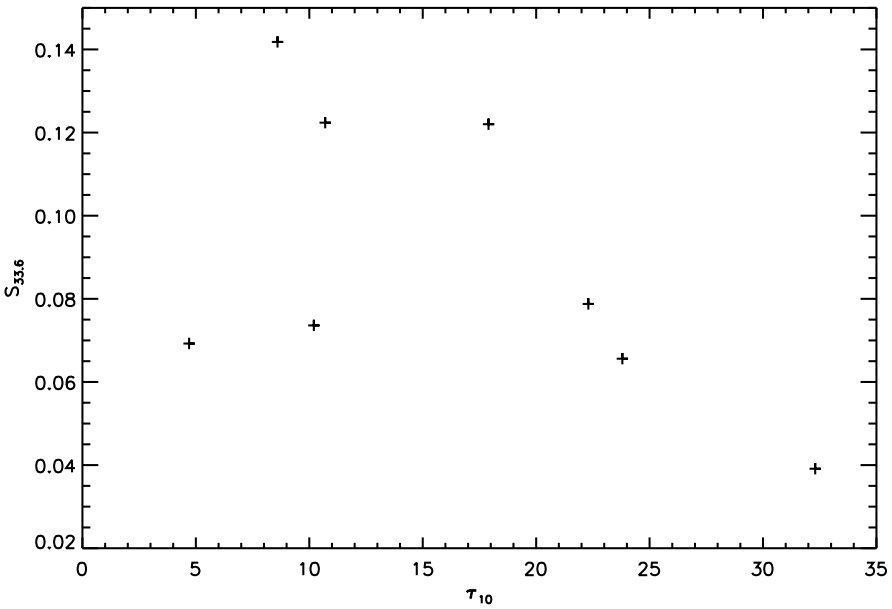

Figure 5.6: Relative strength of the crystalline 33.6 μm forsterite feature ($S_{33.6}$) vs τ_{10}, a mass-loss indicator..

Tamanai et al. (2006) performed for the first time laboratory measurements of the 10 μm band profiles of non-embedded (free-flying) particles of amorphous and crystalline forsterite. This study shows that the extinction efficiency for crystalline silicates has considerably different band positions in comparison to the band positions measured in a comparison study using classical measurements were the particles are not free-flying but embedded in a KBr pellet. In comparison to the study using the KBr pellet technique the wavelength position of the forsterite 11.3 μm band has shifted toward the blue to 11.06 μm. Tamanai et al. (2006) show that the true wavelength position of the 11.3 μm forsterite band is located more toward the blue than observations in young stars suggest, which might indicate that what is observed in young stars is not pure forsterite but has been contaminated by some material. This could also indicate that the forsterite formed in this sample of OH/IR stars is more pure forsterite than what is found in young stars.

5.3.2 Degree of crystallinity

Using the method of Kemper et al. (2001) we derived relative strengths of the 33.6 μm feature (see Section 5.2.4.2). Figure 5.6 shows the strength of the 33.6 μm forsterite features versus τ_{10}, which is equivalent with the mass-loss rate (see Table 5.2). There exists a clear trend between the mass-loss indicator τ_{10} and the relative strength of the 33.6 μm feature. The feature loses strength, as the mass-loss rate increases.

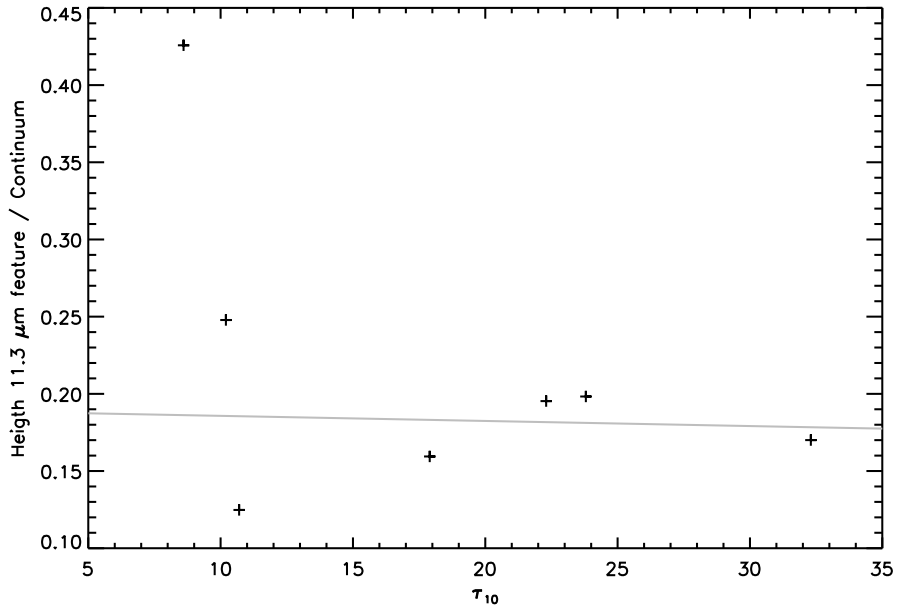

Figure 5.7: Relative strength of the 11.3 μm forsterite feature versus τ_{10}. The grey line indicates the best linear fit to the data excluding the objects in partial self-absorption.

Kemper et al. (2001) use the strength of the 33.6 μm forsterite feature to estimate the degree of crystallinity. Their Fig. 7 shows the relations between the degree of crystallinity, the mass-loss rate and the strength of the 33.6 μm feature. If we place our objects in their Fig. 7, our objects are situated in the area where the strength of the 33.6 μm feature decreases again with increasing mass-loss rate. Half of our objects also have higher mass-loss rates than the mass-loss rates given in their Fig. 7. Therefore we cannot estimate the degree of crystallinity based on their method. Nevertheless the parabolic trend in their Fig. 7 seems to indicate that the decreasing trend seen in Figure 5.6 is correlated with radiative transport effects. Based on the models derived for the OH/IR stars in this sample, we can confirm this. In Table 5.2 we list the optical depths at 33.6 μm ($\tau_{33.6}$). Only one object has an optical depth smaller than 1 and 3 other objects have an optical depth close to 1, the other values are larger than 2. This table shows that especially the objects with the highest mass-loss rates have optically thick dust shells even at this wavelength region. Because of this we can not look through the shell, as we can for optical thin dust envelopes, and therefore not all forsterite is seen in the spectrum. This causes the apparent decreasing trend of the amount of forsterite with increasing mass-loss rate seen in Figure 5.6.

Alternatively we can also use the relative strength of the 11.3 μm feature to estimate the degree of forsterite. In Section 5.2.1 we derived the τ spectra in the 10 μm region. Since $\tau \sim \kappa$ the relative strength of the 11.3 μm feature correlates directly with the amount of forsterite.

Figure 5.7 shows the height of the 11.3 μm feature normalised by the continuum flux at the peak position of the feature versus τ_{10}. In contrast to the strength of the 33.6 μm feature, the relative strength of the 11.3 μm feature is constant in comparison with the depth of the 9.7 μm silicate feature. The grey line gives the best linear fit to the data and reveals no dependence between the relative strength of the 11.3 μm feature and τ_{10}. IRAS 18042-2905 is the only star not following the constant trend. As could be seen from Figure 5.1 this is the second star still in partial self-absorption, although the partial self-absorption is not as obvious as for IRAS 17413-3531 (which we already excluded from this analysis), this is possibly the reason why this star is an outlier in Figure 5.7. To derive the linear fit to the data we excluded the objects in partial self-absorption, similar to what we did for the relative strength of the 33.6 μm feature in function of the mass-loss rate. The relative strength of the 11.3 μm feature suggest no differences in degree of crystallinity between the different stars in function of their mass-loss.

5.4 Conclusions

In this chapter we have studied a sample of Galactic Bulge OH/IR stars observed with Spitzer-IRS. We studied the characteristics of the crystalline material.

For the OH/IR stars in this sample, we showed that the peak position of the 11.3 μm forsterite feature is actually located at 11.2 μm. This could be due to smaller particle sizes in the OH/IR stars than in the young stars or, based on the laboratory work of Tamanai et al. (2006), this could indicate that the forsterite found in these targets is more pure than the typical forsterite found in young stars.

We also showed that there is no relation between the relative strength of the 11.3 μm feature and τ_{10}, a mass-loss indicator. This shows that the OH/IR stars in this sample must produce relatively the same amount of crystalline forsterite.

We determined the relative strength of the 33.6 μm forsterite feature and showed that the relative strength of this feature decreases with increasing mass-loss rates. We compared our results with the model calculations of Kemper et al. (2001) and found that this is most likely caused by optical depth effects. This has been confirmed by simple radiative transfer modelling using only amorphous silicate dust. When the mass-loss rate increases, the peak of the spectral energy distribution shifts to longer wavelengths and therefore the optical depth at these wavelengths also increases. The higher the optical depth at 33.6 μm the less deep we can see in the circumstellar envelope and therefore we see relative less forsterite particles compared to the amorphous silicate particles and the relative strength of the 33.6 μm forsterite feature decreases.

CHAPTER 6

The dust sequence along the AGB

In the previous 3 chapters, we studied a sample of Galactic Bulge AGB stars with respect to their dust formation (see Chapter 3 and 5) and their stellar characteristics and variability (see Chapter 4). In this Chapter, we combine this information and analyse the dust spectra in view of the stellar characteristics and the variability of the objects.

Stars on the Asymptotic Giant Branch (AGB) are known to lose substantial amounts of their mass through a dust-driven outflow. One of the primary observational consequences of such mass-loss is the formation of an expanding circumstellar envelope (CSE). Depending on the chemical composition of the star, oxygen-rich or carbon-rich dust is formed in the CSE (see also Section 1.2). Lebzelter et al. (2006) showed that in general the dust mineralogy and the position on the AGB are related. For a sample of AGB stars located in 47 Tuc, they show that stars at the onset of dust formation on the AGB show dust that is mainly consisting of Mg, Al, and Fe oxides. When the star evolves on the AGB, amorphous silicates become more important and become the dominant species. Nevertheless Lebzelter et al. (2006) find inconsistencies in the composition of the dust spectra when the stars are placed on an evolutionary sequence.

Lebzelter and Wood (2005) and Lebzelter et al. (2006) use the position of the stars in a (log P, K)-diagram to trace the evolution of the star on the AGB. Lebzelter et al. (2006) show for a sample of 11 objects, observed with Spitzer-IRS, that as the AGB star evolves (i.e. the dust spectrum of the star becomes more and more dominated by amorphous silicates), the star moves from sequence B to sequence C in the period-luminosity diagram. This is to be expected as it was already known that stars located on sequences A, B, and the lower part of sequence C are mainly semi-regular variables and the stars located on the upper half of sequence C are believed to be Mira variables (see also Section 1.2.3). Two stars in their study fall out of this sequence and seem to be located at the wrong position in the period-luminosity diagram considering their dust spectrum. For one of these objects Lebzelter et al. (2006) suggest that the star might be undergoing a thermal pulse event. The strange combination of

position in the period-luminosity diagram and the dust spectrum for the other object could be attributed to a long secondary period. All this suggests that there is no simple one-to-one relation between the displayed dust spectrum of an AGB star and its evolutionary position on the AGB.

In Section 6.1 we discuss the dust spectra of our bulge sample in terms of their position in the (log *P*, *K*)-diagram. In Section 6.2 we discuss the oxygen-rich dust condensation sequence with respect to variability on the AGB. In Section 6.3 we perform a principal component analysis on all the quantities derived in Chapters 3 and 4. Finally we summarise and come to the conclusions in Section 6.4. The numbers given to the stars in this chapter are identical to the numbers given to the objects in Table 3.2.

6.1 $(K_0, \log P)$-diagram

A $(K_0, \log P)$-diagram gives the mean absolute magnitude in the *K*-band versus the logarithm of the period in days. Several different sequences can be identified in such a diagram of which four are important to this work: sequences A, B, C, and D (see also Section 1.2.3).

6.1.1 Pulsation models versus observed sequences

In Chapter 1 we already briefly discussed the physical interpretation of the sequences seen in $(K_0, \log P)$-diagrams. We mentioned that sequence C in the diagram is occupied by Mira variables and semi-regular variables at the lower half of the sequence. Sequences A and B are occupied by semi-regular variables. In the next section we will discuss the dust spectra from Chapter 3 in terms of the variability of the objects and positions in the PL-diagram as discussed in Chapter 4. As an introduction to this discussion, we present here a more general background on the sequences in the $(K_0, \log P)$-diagram (based on Lattanzio and Wood 2003, unless mentioned otherwise).

Xiong et al. (1998) computed linear pulsation models for LPVs taking the dynamical and thermal coupling between pulsation and convection into account. Previously this coupling had not been taken into account, due to the complexity of the problem. The stability and growth rates of pulsation are determined by energy transport which is dominated by convection. Convection is still a physical problem not yet fully understood and often treated in a simplified way with the mixing-length theory. Therefore the growth rates resulting from published models need to be treated with caution, though the periods are probably reasonably accurate.

The model for a 1 $M_\odot$ object shown in Fig. 2.51 in Lattanzio and Wood (2003) indicates the general characteristic of pulsation on the AGB: as the star evolves to higher luminosities, it first becomes unstable in the second or third overtone, then switches to lower overtones, and eventually to the fundamental mode. The models described in Lattanzio and Wood (2003) and the results given in their Fig. 2.53 show that the fundamental mode is able to accurately

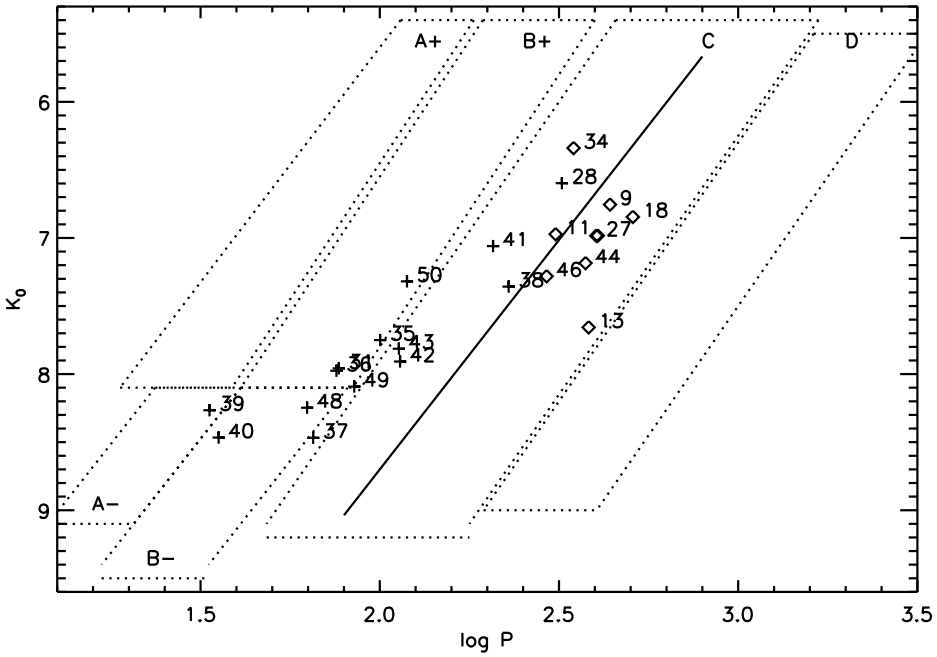

Figure 6.1: Period-luminosity diagram (see also Figure 4.10). The plus-signs represent the semi-regular variables, the diamonds are Mira variables with $(J-K)_0 < 2$.

account for the period-luminosity (PL) relation of sequence C. This sequence contains Mira variables and some semi-regular variables. Semi-regulars located on sequences A and B are first, second, or third overtone pulsators.

Pulsation modes higher than the third overtone are not seen in AGB stars. This is in agreement with theoretical expectations: pulsations with higher modes are not reflected at the stellar surface back into the interior (Fox and Wood 1982), they travel from the interior out into the photosphere and are damped there by energy and momentum loss, and therefore are not unstable. Fig. 2.53 in Lattanzio and Wood (2003) shows the shortest pulsation period for which waves will be reflected back and it corresponds reasonably well with the highest observed mode of pulsation in AGB stars.

6.1.2 Dust spectra versus variability

In Figure 4.10 the PL-diagram for this sample of stars is shown. We repeat this figure in Figure 6.1 for the ease of the reader; the identification numbers of the objects corresponding to the different symbols have been included. In this section we will study the different dust spectra belonging to the objects located on the different sequences.

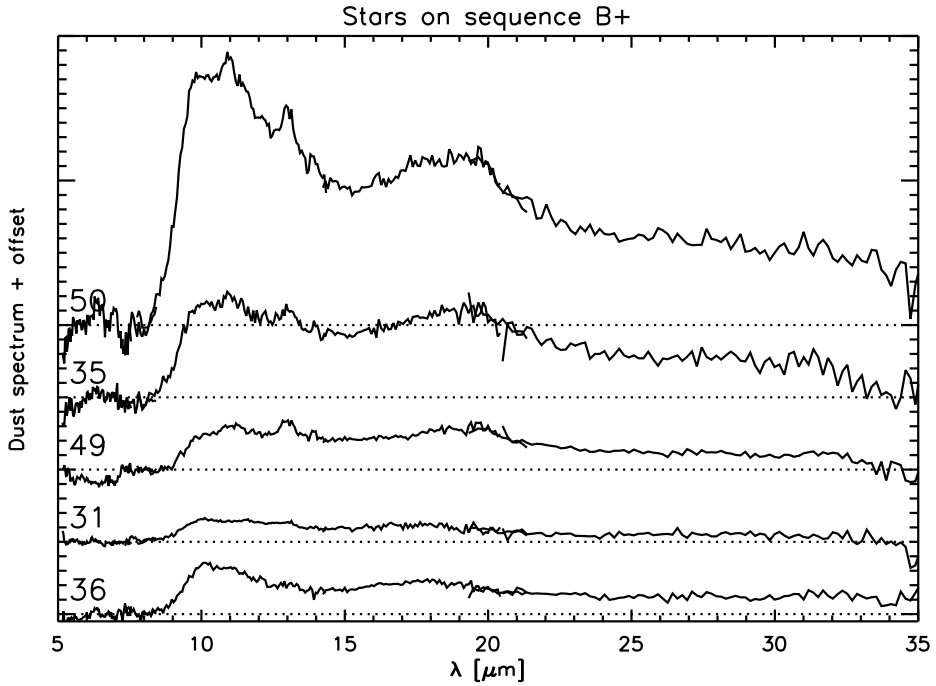

Figure 6.2: Dust spectra for the objects on sequence B+ in the PL diagram. The dust spectra are shown with increasing period from bottom to top.

Based on the period analysis derived in Chapter 4 we only found one object located on sequence A. This object (J180301.6-300001, number 39) is an object which shows no sign of a dust contribution yet and has therefore been treated as a naked star. Both sequences A and B are divided into two boxes in Figure 6.1. The dividing line is the tip of the RGB (at about 8 mag in K_0): objects in boxes A– and B– are located below the tip of the RGB, while objects in boxes A+ and B+ are located above the tip of the RGB. Also the three objects in box B– (J180249.5-295853, J180304.8-295258, and J180316.1-295538, numbers 37, 40, and 48) show no sign of dust contribution and were labelled as naked stars.

The five objects located in box B+ all show signs of dust, there are no naked stars above the tip of the RGB. The dust spectra for these objects are shown in Figure 6.2. Based on the analysis in Chapter 3 we showed that object 36 is the only object in this sequence without clear signs of alumina and with no clear 13 μm feature. All the other dust spectra from objects in this sequence show signs of amorphous silicates. Only object 49 shows (minor) indications for a 19.5 μm feature.

Shown in Figure 6.3 are the dust spectra for stars located on sequence C in the PL-diagram. All the objects with periods belonging to this sequence show clear dust features.

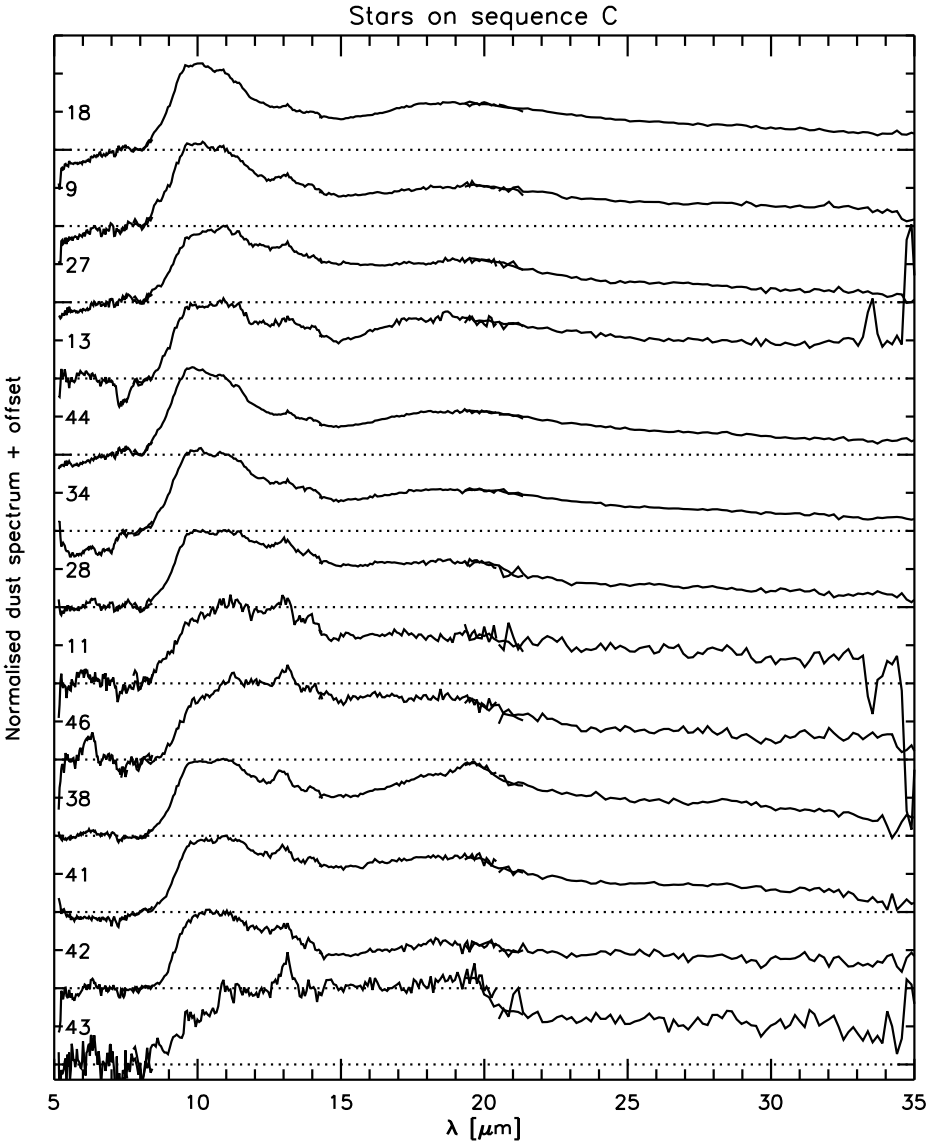

Figure 6.3: Dust spectra for stars located on sequence C, arranged for increasing period from bottom to top. The dust spectra are normalised at 11 μm.

The stars are displayed according to increasing periods from bottom to top and the spectra are normalised at 11 μm. Most of the dust spectra in this figure show evidence for amorphous silicate bands around 10 and 18 μm. Stars J174128.5-282733, J180308.2-295747, and J180308.2-295747 (respectively numbers 11, 43 and 46 in the figure) mainly show evidence for aluminum-oxides and no clear evidence for amorphous silicates. All stars shown in this

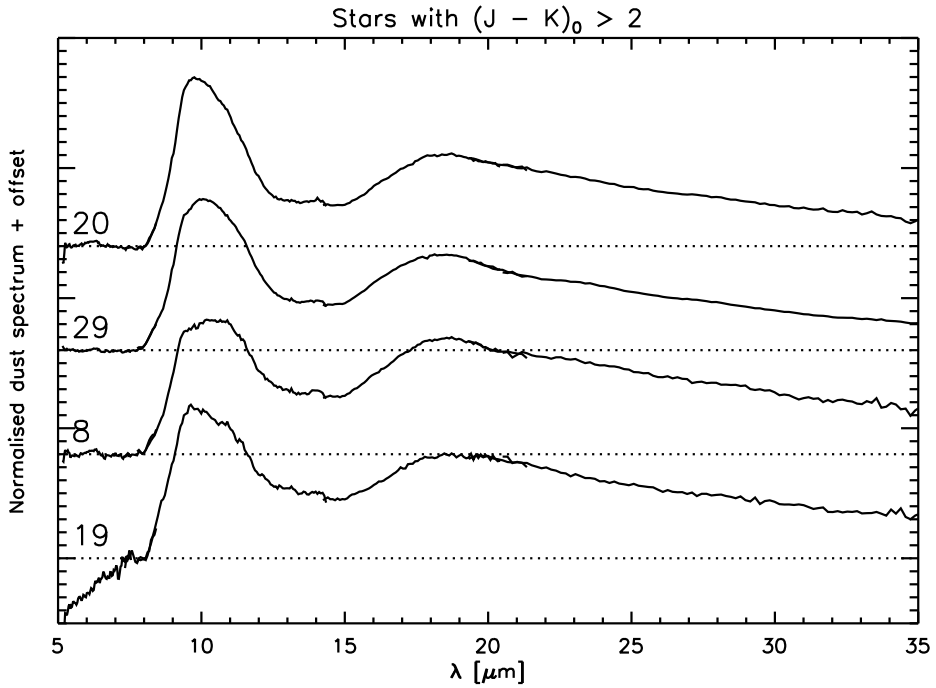

Figure 6.4: Dust spectra for stars located with $(J-K)_0 > 2$, arranged for increasing period from bottom to top and are normalised at 11 μm.

sequence show evidence for a 13 μm feature in their dust spectrum (see also Table 3.4). Based on the position of J180305.4-295527 and J180308.2-295747 (objects number 42 and 43) in the $(K_0, \log P)$-diagram it is more likely that these objects belong to sequence B+ rather than to sequence C.

The $(K_0, \log P)$-diagram shown in Figure 6.1 does not contain any objects for which $(J-K)_0 > 2$. As explained in Chapter 4, these objects are too much affected by circumstellar extinction in their K-band and are therefore left out of these diagrams. The dust spectra for such objects is shown in Figure 6.4. The OH/IR stars are not included in this plot as we did not derive dust spectra for those objects. The objects with $(J-K)_0 > 2$ are supposed to have higher mass-loss rates than the objects seen in sequence C. Figure 4.12 shows that these objects are located at the end of the mass-loss sequence in the $(K_s - [15])_0$ versus $[15]_0$ CMD. The dust spectra for these objects are clearly dominated by amorphous silicates. Except for the artefact at 14 μm (the "14 micron teardrop", see also Section 3.3.3), these spectra do not seem to indicate the presence of any other feature.

Fig. 4 in Lebzelter and Wood (2005) shows that the variable stars in 47 Tuc seem to evolve along sequences B and the lower half of sequence C to eventually switch to the upper half of sequence C. This switch seems to correspond to a transition in pulsation from a low order

radial overtone mode to the fundamental radial mode (Wood et al. 1999; Lebzelter and Wood 2005). We showed that the Mira variables in our sample are only located on sequence C, indicating that there is also a switch in pulsation mode noticeable in this sample from radial overtone pulsators to radial fundamental mode pulsators. One has to keep in mind that the spread in K_0 around the sequences could be due to the finite thickness of the bulge (see e.g Glass and Schultheis 2002, who found a dispersion of 0.35 mag from the K_s-log P relation for M giants in the bulge).

6.2 The oxygen-rich dust condensation sequence

Based on the analysis in Chapter 3 and the analysis in the previous section we can conclude that we can study the oxygen-rich dust condensation sequence using this sample of stars by two different, but of course related, methods.

The first method is described in Chapter 3 and uses the $(K_s - [15])_0$ colour to trace the mass-loss rate. Using $(K_s - [15])_0$ as a mass-loss rate indicator, the spectra were arranged according to increasing mass-loss rate. This revealed that *(1)* no obvious clear trend between the composition of the dust and $(K_s - [15])_0$ could be seen, as could be expected based on the oxygen-rich dust condensation sequence; *(2)* no linear correlation between the mass-loss rate and the decreasing abundance of alumina with respect to amorphous silicates has been found; and *(3)* most of the 10 μm complexes can be explained by using a mixture of alumina and amorphous silicates: only one object was found to be completely dominated by alumina.

The second method used to trace the evolution along the AGB is described in Chapter 4 and in the previous section. This method is based on the position of the objects in the period-luminosity diagram. The dust spectra have been studied as a function of the evolution on the AGB with respect to the stellar variability. Lebzelter et al. (2006) showed that stars at the onset of dust formation exhibit dust that is mainly consisting of Mg, Al, and Fe oxides. These objects are supposed to be located on sequences A, B, and the lower part of sequence C (the semi-regular variables).

The objects located below the tip of the RGB (around $K_0 = 8$ mag, indicated by the horizontal lines dividing sequence A and B in two parts) are categorised as naked stars in Chapter 3 and show no sign of dust contribution. All the objects above the tip of the RGB show a dust contribution.

The next group of objects seems to be formed by the objects in box B+ as well as two objects in box C (numbers 42 and 43). The dust spectra for these objects shown in Figures 6.2 and 6.3 show no obvious similarities, although all objects except J180248.9-295430 (number 36) show a 13 μm feature. The relative amount of alumina to amorphous silicates derived in Chapter 3 (see Table 3.4) is about 0.3 except for J180308.2-295747 and J180323.9-295410 (numbers 43 and 49). These two stars are among the 4 objects with a relative abundance of alumina with respect to amorphous silicates higher than 0.5. J174943.7-292154 (object number 24) is the only object which has a dust spectrum dominated by amorphous alumina and is

labelled as a small-amplitude variable in Chapter 4. Therefore this object is not shown in the PL-diagram. The other object with a relative high amount of alumina (J180311.5-295747, number 46) is a Mira variable and is located on sequence C.

Most of the objects located on the upper half of sequence C are Mira variables. Only three objects (numbers 28, 38, and 41) were categorised as semi-regular variables in Chapter 4. Most of the dust spectra for these objects (see Figure 6.3) are dominated by amorphous silicate dust and all objects exhibit a 13 μm feature.

The stars with the reddest $(J-K)_0$ colours are not shown in the PL-diagram, but these objects show a dust spectrum dominated by amorphous silicates, none of these objects exhibits a 13 μm feature.

Based on the comparison between the position of the objects in the PL-diagram shown in Figure 6.1 and their dust spectra, a clear one-to-one relation between the dust composition and the objects place on the PL-diagram cannot be found. There exist however indications for a sequence. The objects below the tip of the RGB show no dust. Concerning the objects above the RGB tip, there are two objects with high amounts of alumina with respect to amorphous silicates as well as a 13 μm feature and a possible 19.5 μm feature. The other objects on sequence B and the objects on sequence C show a mixture of alumina and amorphous silicate dust as well as a 13 μm feature, while the objects with the highest $(J-K)_0$ colours, which are not shown in the PL-diagram, are dominated by amorphous silicate dust without signs of any other feature.

6.3 Principal component analysis

In this section we will use a principal component analysis to study in a statistical and objective manner the possible correlations and dependencies between the different derived quantities for this sample. As well will we look for physical interpretations inducing the variance seen in this sample.

A principal component analysis (PCA) aims at reducing multi-dimensional data sets into fewer dimensions. From a mathematical point of view it is defined as an orthogonal linear transformation that transforms the data into a new coordinate system such that the greatest variance by any projection of the data comes to lie on the first coordinate (called the first principal component – PC), the second greatest variance on the second coordinate, and so on. In general, a PCA is used to reduce the dimensionality of the parameter set by looking for linear correlations and identifying (new) meaningful underlying variables.

6.3.1 Introduction to the principal component analysis

For a data matrix $\mathbf{Y} = (y_{ij})_{n\times p}$ with n the amount of objects and p the amount of parameters, a PCA first consists of seeking a linear combination $Z_1 = a_{11}Y_1 + \ldots + a_{1p}Y_p$ with $\sum_{k=1}^{p} a_{1k}^2 = 1$

for which the observations Z_{1i} possess the largest variance. With this new linear combination, we can define the vector OZ_1 (with O describing the origin of the parameter space). If we now consider the $p-1$ subspace orthogonal to OZ_1, we can again look for a linear combination Z_2 for which the dispersion of the n points obtained by projection is maximal. This process is continued until all p mutually orthogonal axes OZ_j are defined as $Z_j = a_{j1}Y_1 + \ldots + a_{jp}Y_p$, with $\sum_{k=1}^{p} a_{jk}^2 = 1$ and $\sum_{k=1}^{p} a_{jk}a_{lk} = 0$ if $j \neq l$ with $1 \leq j, l \leq p$. These p new variables are called the principal components.

The data are now equally well represented by the derived p-dimensional scatter plot in the Z-coordinate system as it was before. The contribution of each principal component to the total variability of the scatter plot is given by the corresponding eigenvalue. Based on how the different PCs were defined, the first PC has the largest eigenvalue λ_1 and the eigenvalues decrease for the next found PC: $\lambda_1 > \lambda_2 > \ldots > \lambda_p$. To reduce the p-dimensional problem to an r-dimensional problem with $r < p$, the r principal components which have the most significant contribution to the problem are retained. The eigenvalues are used to determine how many PCs will be considered. The PCs considered significant are those which have eigenvalues larger or equal to one. The information retained with r principal components is expressed in terms of cumulative percentages and given by $100\frac{\sum_{j=1}^{r}\lambda_j}{\sum_{j=1}^{p}\lambda_j}$.

6.3.2 Principal component analysis and discussion

In the beginning of a PCA analysis, as much information as possible is included, i.e. all the derived parameters. We choose to retain only the objects for which we could derive all parameters; the drawback to this is that this results in a reduced sample. The following parameters will be used: $(K_s - [15])_0$, $(J - K_s)_0$, M_{K_0}, the normalised dust luminosity, the relative amount of alumina to amorphous silicates, $T_{\rm eff}$, the equivalent line widths of Na I, Ca I, and ^{12}CO(2,0), the amount of water absorption, and the period. Because the SE index is a discrete parameter, it is not included in the PCA. No information is lost however as this parameter correlates very well with the relative abundance of alumina with respect to amorphous silicates (see Figure 3.38). Using these 11 parameters, 31 objects can be retained.

A PCA searches for linear correlations between all the parameters. From Chapter 4 we know that a linear relation with the amount of water can only be found if we take the logarithm of the negative amount of water, which will be done in this PCA analysis.

The PCA has been performed on the standardised matrix of all the variables for each object, so that each variable has an equal weight in the analysis. The results for the first 4 principal components are given in Table 6.1. As a general rule of thumb, one only keeps the PCs with eigenvalues larger than one. In this case this means that only the first three components, which explain 71% of the variance in the data, are considered.

Table 6.1 shows that the equivalent line width measurement of Na I does not contribute to the first PC and that all the other parameters have comparable contributions to the PC. Based on the sign of the coefficients in this PC, we can arrange the parameters in two groups. The group with the negative sign seems to be related to the characteristics of the central star, while

Table 6.1: Results of the first principal component analysis.

	Variable	PC 1	PC2	PC3	PC4
0	$(K_s - [15])_0$	0.41	-0.04	-0.09	0.18
1	$(J - K_s)_0$	0.32	0.08	0.25	0.56
2	M_{K_0}	-0.33	-0.19	0.34	-0.24
3	normalised dust luminosity	0.26	-0.26	-0.55	-0.11
4	percentage alumina	-0.20	0.52	0.30	-0.06
5	T_{eff}	-0.28	-0.23	0.02	0.60
6	EW(Na)	-0.00	0.63	-0.19	0.17
7	EW(Ca)	-0.22	0.30	-0.55	-0.09
8	EW(CO)	-0.30	-0.17	-0.20	0.33
9	log(-water absorption)	0.40	0.19	0.06	0.06
10	period	0.36	-0.07	0.20	-0.27
	Eigenvalues	4.64	1.88	1.33	0.98
	Cumulative variance	0.42	0.59	0.71	0.80

the group with positive coefficients may be linked to the dust characteristics.

Figure 6.5 shows the biplots for the three considered PCs. In each panel, the arrows with the large bold numbers at the end show the vector defined by the coefficient of a parameter in the PC given in the *x*-axis and the coefficient belonging to the same parameter but then for the PC given at the *y*-axis. The crosses with in accordance the small numbers, indicate the position of the objects defined by the two shown PCs (the numbers given to the objects are identical to the numbers in Table 3.2). Inspecting the spectra based on their position in the biplot of PC1 vs PC2 (see upper left panel Figure 6.5) helps understanding the physical nature of PC1. The stars on the left of the figure are e.g. objects number 47, 36, 24, 49, and 31. These objects belong to the objects with the bluest $(K_s - [15])_0$ colours while the objects on the right side of the diagram (see e.g. 9, 18, 19, and 20) have the reddest $(K_s - [15])_0$ colour. This is also reflected in the coefficients of PC1, as $(K_s - [15])_0$ has the largest contribution to this PC. Also the amount of water absorption and the period have a large influence on this PC. Both these variables were found in Chapter 4 to correlate with $(K_s - [15])_0$ (see Figures 4.13 and 4.16). Although $(K_s - [15])_0$ might not be a perfect mass-loss indicator (see Chapter 3), it can still be used as a first indication of the mass-loss rate. Therefore it is very plausible that the first PC traces the mass-loss rates of these objects.

Table 6.1 shows that there are three parameters that can be ignored in the second principal component: the $(K_s - [15])_0$ colour, $(J - K_s)_0$, and the period. Similarly to what we did for PC1 we can again divide the remaining parameters in two groups based on their sign. The parameters with the positive signs are the relative amount of alumina to amorphous silicates, the equivalent line widths of Na I and Ca I, and the amount of water absorption. The parameters with negative signs are M_{K_0}, the normalised dust luminosity, the effective temperature, and the equivalent line width of ^{12}CO(2,0). At first sight it is not obvious what connects the parameters in these groups, although the very strong contribution of the relative amount of alumina suggest that the physical nature of the second PC is related to the shape of the 10 μm

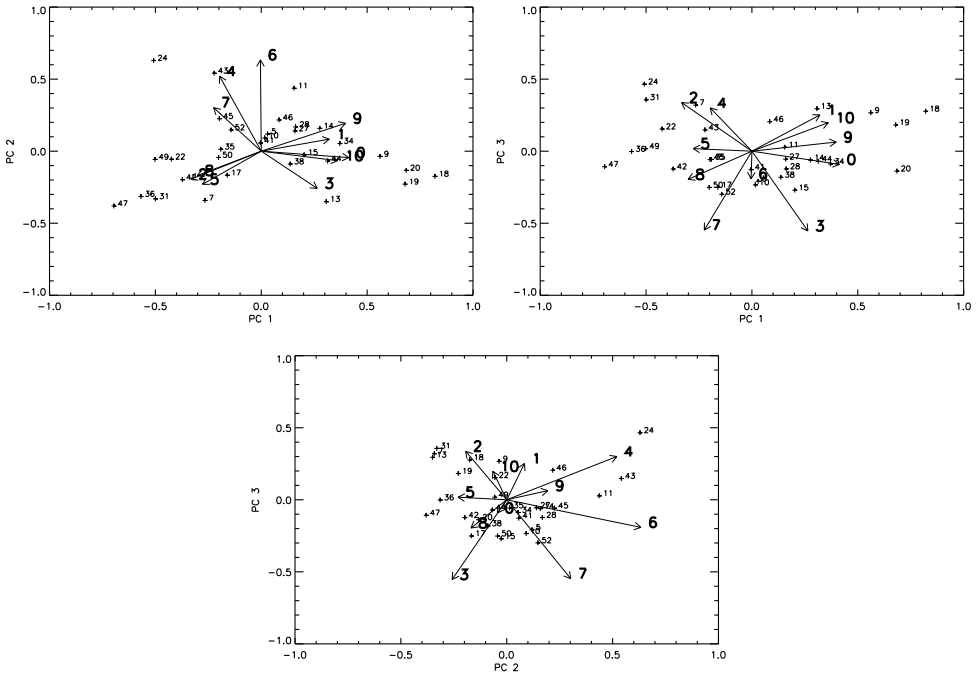

Figure 6.5: Biplots for the 3 significant principal components. The upper left panel shows the biplot for PC1 vs PC2, the upper right panel shows the biplot for PC1 vs PC3, and the lower panel for PC2 vs PC3. In both figures the arrows indicate the coefficients of the eigenvectors that belong to the same parameter. This parameter is indicated by the large bold number at the end of the arrow. The plus-signs indicate the data projected along the principal components and the small numbers indicate the numbers of the objects as given in Table 3.2.

complex.
The upper left panel in Figure 6.5 shows that the objects 24, 43, and 11 have the highest positive value for PC2, while objects 47, 13, and 7 have the most negative PC2 value. Inspecting the shape of the 10 μm complexes of objects 47, 13, and 7 shows that these objects are dominated by amorphous silicates, while object 24 can be explained using only alumina and objects 43 and 11 have of the highest alumina contributions (see also Table 3.4).
The coefficients in PC2 also show that the equivalent line width of Na I is the most important parameter in this PC. The equivalent line width of Na I is a very dominant factor to determine the metallicity using eq. (4.1).
We conclude that PC2 traces two properties: the shape of the 10 μm complex or equivalent the dust composition, and because of the high contribution of the equivalent line width of Na I to the PC, also the metal abundance of the central star.

With respect to principal component 3 there are three parameters that can be ignored: $K_{s,0}$ – [15], $T_{\rm eff}$, and the water absorption. All the other parameters have negative signs ex-

Table 6.2: Results of the second principal component analysis.

	Variable	PC 1	PC2	PC3	PC4
0	$(K_s - [15])_0$	0.51	0.10	0.12	-0.33
1	M_{K_0}	-0.41	-0.34	0.13	-0.53
2	normalised dust luminosity	0.43	-0.11	-0.50	-0.37
3	percentage alumina	-0.35	0.43	0.31	-0.50
4	EW(Na)	-0.06	0.69	-0.02	0.28
5	EW(Ca)	-0.24	0.34	-0.71	-0.26
6	log(-water absorption)	0.44	0.30	0.34	-0.27
	Eigenvalues	3.07	1.73	1.05	0.58
	Cumulative variance	0.44	0.69	0.84	0.92

cept $(J-K)_0$, M_{K_0}, the relative amount of alumina with respect to amorphous silicates, and the period. The two parameters contributing the most to PC3 are the normalised dust luminosity and the equivalent line width Ca I. After inspection of the spectra it is not clear what physical parameter PC3 traces.

Based on the biplots in Figure 6.5 we can look for correlations between the different parameters. These parameters would then span the same region in the biplot. In the lower and upper right panel, no obvious correlations can be found. Based on the upper left panel in Figure 6.5 we found that $(K_s - [15])_0$ and the period correlate very well (see also Figure 4.13 in Chapter 4). Also $(J-K)_0$ and the amount of water absorption correlate. Water absorption lines are known to influence the near-IR spectra of AGB stars severely (see Chapter 2). These water lines can suppress the continuum in the K-band region, resulting in a lower observed flux and a larger $(J-K)_0$ colour. The upper left panel in Figure 6.5 shows three other parameters spanning the same region: M_{K_0}, the effective temperature, and the equivalent line width of ^{12}CO(2,0). M_{K_0} and CO are known to be sensitive to the effective temperature (see e.g. Decin 2000).
It is sufficient if one of the parameters that correlates with other parameters is considered. In this way, we reduce the dimensionality of the problem. We choose to retain the parameters with the largest influence in PC1.

Having reduced the dimensionality of the problem, we have to investigate if we did not leave out any important information. This is done by performing a new principal component analyses on the reduced dataset. The results are listed in Table 6.2. Using the first 3 components, which have eigenvalues larger than 1, we keep 84% of the variance. Figure 6.6 shows the biplots for the 3 significant principal components. If we compare the distribution of objects in these biplots with the distribution of the objects in Figure 6.5, then one can see that the objects have about the same distribution. Therefore our parameter reduction was valid. Using this reduced parameter space, PC1 still traces the mass-loss rate and PC2 the composition of the dust or the shape of the 10 μm complex as well as the metallicity.

The lower panel in Figure 6.6 and Table 6.2 shows that the equivalent line width of Ca I is

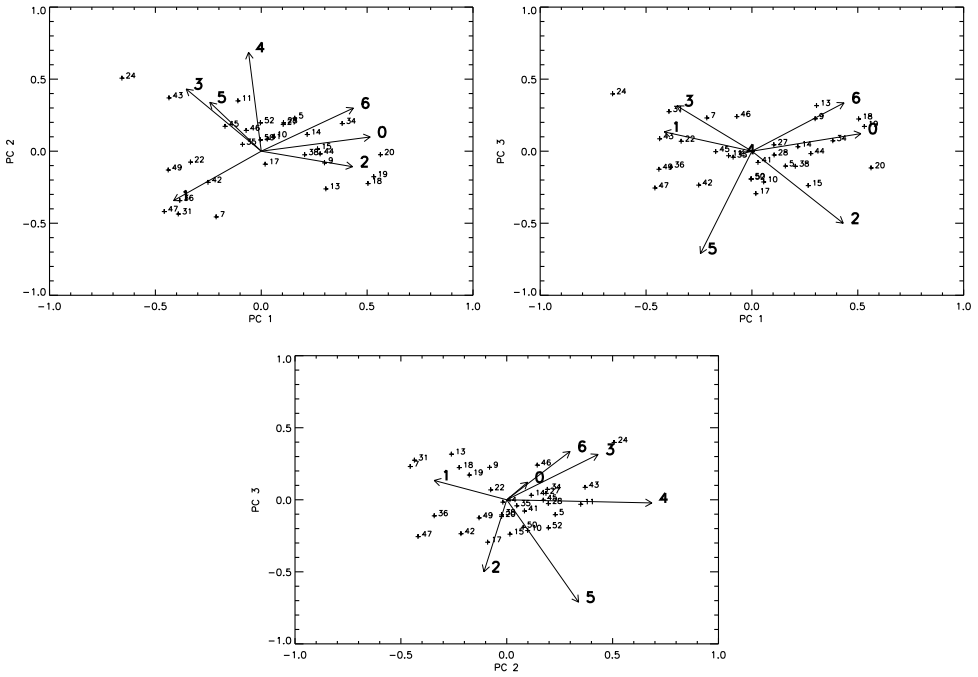

Figure 6.6: Biplots for the 3 significant principal components for the second PCA. The symbols for the objects are identical as in Figure 6.5, the numbers at the end of each arrow refer to the parameters in Table 6.2.

the dominating parameter in PC3. Whereas in the first PCA the normalised dust luminosity had an equal importance in PC3 as the equivalent line width of Ca I, this parameter has now become the second most important in this PC. The biplots in Figures 6.5 and 6.6 show a very small variance with respect to PC3, all objects are clustered with respect to PC3 in the same area. It is not obvious which physical parameter(s) PC3 traces.

This principal component analysis revealed relations between the different parameters derived in Chapters 3 and 4. It also showed us that the variance in our parameter space can be described in terms of 3 principal components. The first PC traces the mass-loss rate, the second the composition of the dust and the characteristics of the central star. It is not clear what PC3 traces.
Since the different PCs are orthogonal by definition (see Section 6.3.1), this indicates that the dust composition and the mass-loss rate are statistically unrelated. This emphasises what we already found in Chapter 3: no clear one-to-one relation between the mass-loss rate indicator $(K_s - [15])_0$ and the dust composition can be revealed in this sample. There is a very large variance concerning the dust composition of the bluest objects in this sample. This is in contrast to the dust composition of the reddest sources showing amorphous silicate dominated dust spectra.

6.4 Summary and conclusions

In this chapter we have analysed the dust spectra for a sample of Galactic Bulge AGB stars already discussed in Chapter 3 in function of the additional characteristics derived in Chapter 4, such as the variability and parameters describing the central star.

Based on the position of the stars in the period-luminosity diagram in Figure 4.10 (see also Figure 6.1), we discussed the dust spectra in terms of the pulsation sequence they belong to. We showed that the objects located below the tip of the RGB show no signs of dust, while all the objects above the tip of the RGB show a dust contribution. AGB stars are expected to form aluminum rich dust at the onset of dust mass-loss. The objects with the highest amounts of alumina dust (except one Mira object) are located just above the tip of the RGB. All the other objects shown in the PL-diagram show a mixture of alumina and amorphous silicate dust as well as a 13 μm feature. The objects with the reddest $(J-K)_0$ colour, which are not shown in the PL-diagram, only shown indications for amorphous silicate dust.

Using a PCA, all the derived parameters for these objects were analysed simultaneously, searching linear relations. We could reduce the parameter space from 11 to 7 parameters. We showed that the variance in the data can be described in terms of three principal components. The first PC, responsible for the largest part of the variance in the data, is the mass-loss rate. The second PC is linked to the shape of the 10 μm complex, and therefore also to the composition of the dust, as well as to the metallicity. This indicates a relation between the dust composition and the metallicity. It is unknown which parameter(s) PC3 traces. The analysis described in this chapter endorses the results found in Chapter 3.

CHAPTER 7

Stellar populations in the Galactic Bulge

This chapter is based on the paper:
Vanhollebeke, E., Groenewegen, M.A.T., Girardi, L.: 2007, "Stellar populations in the Galactic Bulge. Modelling the Galactic Bulge with TRILEGAL", submitted to Astron. and Astrophys.

As already mentioned in the introduction to this thesis, the central parts of our Milky Way Galaxy (MWG) consists of the Galactic Bulge (GB), the central part of the halo, and the Galactic Centre (GC). Over the years, several studies have tried to understand the characteristics of these parts of the MWG. Questions addressed in studies to these characteristics are questions about the formation history, star formation, relations between different stellar components, and kinematics (Wyse 1995).

Understanding the formation history of galactic spheroids (i.e. elliptical galaxies and the bulges of spiral galaxies) is crucial in understanding galaxy formation in general as these spheroids contain a large fraction of all stellar mass in the local universe (Zoccali et al. 2003, and references therein). Our GB, due to its proximity, is the spheroid for which the most information is accessible. Issues that can be addressed in the GB are e.g. the initial mass function, the distribution of stellar ages, and the 3D structure. For more distant spheroids, this sort of information is accessible just by very indirect means based on the study of the integrated light.

Many different approaches exists to study galaxy formation. Often galaxy models are used to study the entire content of a galactic component such as the bulge (Dwek et al. 1995; Binney et al. 1997; Freudenreich 1998; Bissantz and Gerhard 2002; Robin et al. 2003; Merrifield 2004), but studies to the same kinds of stars can also reveal a wealth of information.

Examples of this are e.g. the use of red clump stars (Stanek et al. 1997; Paczynski and Stanek 1998; Udalski 1998; Babusiaux and Gilmore 2005; Nishiyama et al. 2006; López-Corredoira et al. 2007; Rattenbury et al. 2007), RR Lyrae stars (Fernley et al. 1987; Feast 1997; Udalski 1998), masers (Reid et al. 1988; Sevenster et al. 1999), and Mira variables (Whitelock 1992; Groenewegen and Blommaert 2005). Our target is both to perform a calibration of the bulge geometry and to explore the distribution of ages that can be inferred from these data.

This chapter is organised as follows: in Section 7.1 we give a resume on the models and parameters generally used to study the GB, the star formation rate, and the metallicity distribution of the GB. In Section 7.2 we will give a brief introduction to the galaxy model used in this work. Section 7.3 is dedicated to the observational data used. Section 7.4 explains the method used and Section 7.5 discusses the results derived using this method. Section 7.6 discusses the results using the same method if we only used red clump stars. In Section 7.7 we summerise and come to the conclusions.

7.1 The Galactic Bulge

7.1.1 Models describing the Galactic Bulge and its bar

Many different geometries can be assumed for the GB. Oblate spheroidal models can be a good start, providing a first order estimate of the bulge luminosity and minor to major axis ratios (Dwek et al. 1995). As became clear over the past decades, there is a triaxial part, the bar, which needs a triaxial model. There are three types of triaxial models proposed: Gaussian-type function, exponential-type function, and power-law functions (see Dwek et al. 1995, and references therein). Dwek et al. (1995) find that the best model to fit the COBE/DIRBE data for the bulge is an exponential-type function with a modified spheroid included. Robin et al. (2003) use the same parameter set as Dwek et al. (1995) introduced to fit the bulge. They used a boxy Gaussian type function, but did not model the inner parts of the bulge. Binney et al. (1997) and also Bissantz and Gerhard (2002) used a truncated power-law to model the bulge. In this paper, we will use the Binney et al. (1997) formalism to model the number density of stars $f(b)$, which is given by:

$$f(b) = f_0 \frac{e^{-a^2/a_m^2}}{(1+a/a_0)^{1.8}} \text{ and} \tag{7.1}$$

$$a = \left(x^2 + \frac{y^2}{\eta^2} + \frac{z^2}{\zeta^2} \right)^{1/2} . \tag{7.2}$$

In these formulae, a_m represents the scale length, a_0 the inner truncation length, and f_0 is the stellar density per kpc^3. The axis-ratios of the bar are given by: $1 : \eta : \zeta$.

7.1.2 Parameters describing the Galactic Bulge

The typical parameters needed to describe the GB (see previous section) are the scale length (a_m) and inner truncation length (a_0) of the bulge, the axis-ratios ($1 : \eta : \zeta$) of the bar, the an-

Table 7.1: A not complete overview on recent values of parameters describing the GB, its bar and the distance to the GC.

Reference	R_0 [kpc]	a_m [kpc]	a_0 [pc]	$1:\eta:\zeta$	ϕ [°]	Based on
Fernley et al. (1987)	8.0 ± 0.65					RR Lyrae stars
Reid et al. (1988)	7.1 ± 1.5					H_2O maser spots
Whitelock (1992)	9.1			1:0.25:0.25	45	Mira variables
Dwek et al. (1995)				1:0.33±0.11:0.23±0.08	20 ± 10	*COBE*/DIRBE surface brightness map
Binney et al. (1997)		1.9	100	1:0.6:0.4	20	*COBE*/DIRBE surface brightness map
Feast (1997)	8.1 ± 0.4					RR Lyrae stars
Stanek et al. (1997)				1:0.43:0.29	20 – 30	red clump stars
Freudenreich (1998)		2.6				DIRBE full-sky surface brightness map
Paczynski and Stanek (1998)	8.4 ± 0.4					red clump stars
Udalski (1998)	8.1 ± 0.15					RR Lyrae stars
Udalski (1998)	8.1 ± 0.06					red clump stars
Sevenster et al. (1999)		2.5			44	OH/IR stars (OASP)
Bissantz and Gerhard (2002)		2.8	100	1:(0.3 – 0.4):0.3	20 – 25	*COBE*/DIRBE *L*-band map
Eisenhauer et al. (2003)	7.94 ± 0.42					stars orbiting black hole
Robin et al. (2003)				1:0.27:0.27	11.1 ± 0.7	Hipparcos data
Merrifield (2004)				1:0.6:0.4	25	H I gas and *COBE*/DIRBE surface brightness map
Babusiaux and Gilmore (2005)	7.7 ± 0.15				22 ± 5.5	red clump stars
Eisenhauer et al. (2005)	7.62 ± 0.32					stars orbiting black hole
Groenewegen and Blommaert (2005)	8.8 ± 0.4				47	Mira variables
López-Corredoira et al. (2005)				1:0.5:0.4	20 – 35	2MASS star counts
Nishiyama et al. (2006)	7.51 ± 0.10 ± 0.35					red clump stars
López-Corredoira et al. (2007)					43	red clump stars
Rattenbury et al. (2007)				1:0.35:0.26	24 – 27	red clump stars

gle between the Sun-Centre line and the major axis of the bar (ϕ), and the scaling parameter (f_0). Of course also the Sun's distance to the Galactic Centre (R_0) is an important parameter in this context.

One of the most studied types of stars in the GB are the red clump stars. The red clump stars are considered as standard candles to determine distances. They can also be used to estimate the axis ratios of the bulge and the angle ϕ. Using these red clump stars, values between 7.4 and 8.4 kpc for R_0 have been found (see e.g. Paczynski and Stanek 1998; Udalski 1998; Babusiaux and Gilmore 2005; Nishiyama et al. 2006). Values for ϕ derived from red clump stars are situated either around 20° or around 45° (see e.g. Stanek et al. (1997, $\phi = 20° - 30°$), Babusiaux and Gilmore (2005, $\phi = 22° \pm 5.5°$), and López-Corredoira et al. (2007, $\phi = 43°$)). Recent work on the red-clump stars in the GB comes from Cabrera-Lavers et al. (2007) and Rattenbury et al. (2007). Cabrera-Lavers et al. (2007) claim two very different large-scale triaxial structures in the inner Galaxy. A first component is a long thin stellar bar ($|b| < 2°$) with a position angel of 43.0°± 1.8°. The second component is a distinct triaxial bulge that extends to at least $|b| \leq 7.5°$ and has a position angle of 12.6°± 3.2°. Rattenbury et al. (2007) study the red clump stars observed with OGLE in the OGLE-II phase and find that the bar's major axis is oriented at 24° – 27° to the Sun-Galactic centre line-of-sight.
Another kind of stars that is considered a standard candle are the RR Lyrae stars. Using these stars typical values for R_0 of $\sim$ 8.0 kpc have been found (see e.g. Fernley et al. 1987; Feast 1997; Udalski 1998).
Other types of stars that have been studied to characterise the GB are e.g. Mira variables (see e.g. Groenewegen and Blommaert (2005, $R_0 = 8.8$ kpc and $\phi = 43°$) and Whitelock (1992, $1 : \eta : \zeta = 1 : 0.25 : 0.25$, $\phi = 45°$)), H_2O masers (see Reid et al. 1988, $R_0 = 7.1$ kpc), and OH/IR stars (see Sevenster et al. 1999, $a_m = 2500$ pc and $\phi = 44°$).

Studying one type of star is not the only method to reveal information on the characteristics of the Galactic Bulge and distance to the Galactic Centre. Eisenhauer et al. (2003) and Eisenhauer et al. (2005) studied stars orbiting the central black hole and found values for R_0 of respectively 7.94 ± 0.42 kpc and 7.62 ± 0.32 kpc. Also surveys like 2MASS and the surface brightness maps of *COBE*/DIRBE were used. Studies based on these databases find values for ϕ around 20°(see e.g. Dwek et al. 1995; Binney et al. 1997; Bissantz and Gerhard 2002; López-Corredoira et al. 2005), scale lengths a_m between 1900 pc and 2800 pc (see e.g. Binney et al. 1997; Freudenreich 1998; Bissantz and Gerhard 2002), and an axis-ratio of 1:0.5-0.6:0.4 (Merrifield 2004; López-Corredoira et al. 2005), except Dwek et al. (1995) who find lower values for the axis-ratio (1:0.33:0.23). Robin et al. (2003) used HIPPARCOS data to model and obtained axis-ratios of 1:0.27:0.27 and an angle ϕ of 11.1° ± 0.7°.

The Milky Way Galaxy consists not only of stars, there is also an amount of gas present. The location of H I gas in the galaxy (see Figure 2 in Merrifield 2004) immediately reveals the non-axisymmetric distribution of the gas. This non-axisymmetric distribution can also be seen when one measures the velocities of the interstellar CO molecule (Dame et al. 2001). Using the distribution of the H I gas Merrifield (2004) found an angle ϕ of 25°.

Table 7.1 gives an overview on these studies and the parameters found. Concerning the angle between the Sun-Centre line and the bar ϕ, Table 7.1 clearly shows two groups of val-

ues: a low value around 20° and a higher value around 45°. According to Sevenster et al. (1999) the lower values found for ϕ arise when the longitude range used is too narrow or when low latitudes are excluded. Groenewegen and Blommaert (2005) point out that this could also be due to the fact that these studies trace different populations, which may be distributed differently.

7.1.3 Star formation rate and metallicity distribution

Besides the uncertainty in literature on the parameters describing the GB geometry and its bar, also the characteristics of the stars located in the GB are debated.

Lately, studies show traces of an intermediate age population in the GB. Before, it was believed that the GB consisted only of an old population (more then 10 Gyr). Recent studies still reveal that the GB is dominated by this old population, but traces of a smaller intermediate population can no longer be ignored.
Holtzman et al. (1993) studied a field in Baade's Window and concluded that based on the luminosity function there exist not only old stars in the GB, but also a significant, although unquantified, number of intermediate age stars (less then 10 Gyr). Ortolani et al. (1995) conclude that there is no age difference between the majority of bulge stars and the halo globular clusters and no more than $\sim$ 10% of the bulge population can be represented by intermediate age stars (Ortolani et al. 2001; Zoccali et al. 2003, see also). Feltzing and Gilmore (2000) found no significant young stellar population in the GB, but emphasise that it is still possible to have an age range of several Gyr. van Loon et al. (2003) found that in addition to the dominant old population ($\geq$ 7 Gyr), there is also an intermediate-age population ($\sim$ 200 Myr – 7 Gyr) and possibly even younger ($\leq$ 200 Myr) stars are found across the inner bulge (although the latter could be attributed to foreground stars). Concerning an intermediate age population, Groenewegen and Blommaert (2005) found that the Mira variables in the studied OGLE bulge fields have ages of a few Gyr. Also Uttenthaler et al. (2007) found some AGB stars that might be tracers of a younger population: some of their selected AGB stars in the GB show Technetium, which indicates that these AGB stars must originate from a younger population.

The detection of a metallicity spread or absence of it and the metallicity distribution reveals information on the formation history. During the last decade, there were several papers studying the metallicity in the GB. McWilliam and Rich (1994) obtained for 14 M giants in the GB high resolution spectroscopy. They found a mean metallicity of <[Fe/H]>= -0.19 ± 0.02. Sadler et al. (1996) studied K and M giants in Baade's Window and found a mean abundance of <[Fe/H]>= -0.11 ± 0.04. Feltzing and Gilmore (2000) studied HST images and found that the metallicity of the bulge is equal to that of the old disk and that there is only a marginal evidence for a central metallicity gradient. Also Ramírez et al. (2000) studied M giants in the GB. They found a mean metallicity <[Fe/H]>= -0.21 ± 0.30 and no evidence for a metallicity gradient along the minor or major axes of the inner bulge ($R < 560$ pc). van Loon et al. (2003) found a mean metallicity [M/H] $\sim$ 0.5, but also stars with a metallicity of +0.5 and -2 are common, but not dominant. The old stars in the population ($\geq$ 7 Gyr) tend to have higher metallicities (see their Figure 18). They propose that the metallicity distribution

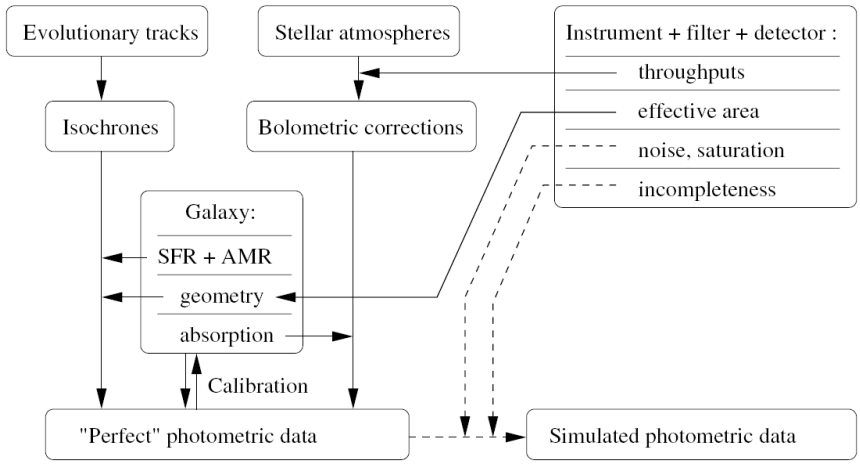

Figure 7.1: Schematic overview on the TRILEGAL code. Taken from Girardi et al. (2005).

of the old stars might be bimodal: one component of super-solar metallicity and another of subsolar metallicity. Zoccali et al. (2003) found that most of the bulge stars have a metallicity [M/H] between +0.1 and -0.6 with a peak at -0.1.

7.2 TRILEGAL

In this study, we use the code TRILEGAL (TRIdimensional modeL of thE GALaxy) (Girardi et al. 2005), a population synthesis code to simulate the stellar content towards any direction on the sky. In this paper the model will be used to compute colour-magnitude diagrams (CMD) towards the GB. This means that we simulate the photometric properties of stars located towards a given direction (ℓ, b) and complete down to a given limiting magnitude.

Figure 7.1 shows the general scheme of the TRILEGAL code. As is shown in this figure the input to the model consists of four main elements:

– a library of stellar evolutionary tracks. It is essentially composed by the Girardi et al. (2000) tracks with some updating at low metallicities (Girardi 2002, unpublished), and now complemented with the TP-AGB models by Marigo and Girardi (2007). These latter are expected to describe the TP-AGB phase with much more realistic lifetimes and luminosities than in the original Girardi et al. (2000) isochrones.

– a library of synthetic spectra, which is used to compute bolometric corrections and extinction coefficients for the simulated stars. They are described in detail by Girardi et al. (2002).

– the instrumental setup, describing the settings of the telescope to be used, e.g. filters, detectors and the effective sky area to be simulated.

– a detailed description of the Galaxy components, being the Galactic thin and thick disk, the Halo and the Bulge. For each component a Star Formation Rate (SFR), Age–Metallicity Relation (AMR), and space densities are assumed. These parameters are different for every Galaxy component, therefore the Galactic components are treated separately by the code. Also the Initial Mass Function (IMF) and interstellar absorption belong to this group of input parameters.

The TRILEGAL code itself performs a Monte Carlo simulation to generate stars in accordance with the input (see above). The SFR, AMR and IMF define a stars age, metallicity, and mass. An interpolation in the grids of evolutionary tracks (see Girardi 1996) results in the absolute photometry, which is then converted to apparent magnitudes based on the bolometric corrections, distance modulus, and extinction.

The output of the TRILEGAL code is a catalogue of stars that contains for each star the Galactic component in which they are located, stellar age, metallicity [M/H], initial mass, luminosity L, effective temperature $T_{\rm eff}$, gravity g, distance modulus $m - M_0$, visual extinction A_V, core mass and the *perfect* photometric data in each of the wanted filters. To be able to compare the output in CMDs with observational data one has to perform some extra calculations which are not included in the TRILEGAL code such as adding photometric errors, saturation of the bright stars in real observations, and completeness.

A more detailed description of the TRILEGAL code and the parameters used concerning the disk and halo can be found in Girardi et al. (2005).

Concerning the calculation of the extinction in TRILEGAL, there is a small change with regard to Girardi et al. (2005). Not only can we now give the extinction value A_V as an input parameter to the code, but a spread on the A_V has also been used in this work. The extinction values and their sigma used can be found in Table 7.2 and are based on Sumi (2004).

An important point is that we have used TRILEGAL with the original filter curves provided for 2MASS (Skrutskie et al. 2006) and OGLE-II (Udalski et al. 1997), so simulating as far as possible the original photometric systems[1]. The bolometric corrections for 2MASS have already been described in detail by Bonatto et al. (2004). Those for OGLE-II have been newly computed, and apart from being used in TRILEGAL have also been incorporated into the Padova database of isochrones. Extensive tables of bolometric corrections and isochrones in the OGLE-II system are now made available at the web sites `http://pleiadi.pd.astro.it/isoc_photsys.02` (static tables) and `http://stev.oapd.inaf.it/~lgirardi/cmd` (interactive web form).

[1] Our experience is that the simulation of the 2MASS photometric system presents zero-point offsets of just a few 0.01 mag. Zero-point errors of similar magnitude are just expected in synthetic photometry applied to present-day libraries of synthetic spectra, and are also likely present in our simulations of the OGLE-II system.

Furthermore, extinction coefficients in the several 2MASS and OGLE-II passbands have been computed for a G2V star using the Cardelli et al. (1989) extinction curve with $R_V = 3.1$. The extinction coefficients turn out to be $A_{U_{\rm OGLE}}/A_V = 1.524$, $A_{B_{\rm OGLE}}/A_V = 1.308$, $A_{V_{\rm OGLE}}/A_V = 1.021$, $A_{I_{\rm OGLE}}/A_V = 0.571$, $A_{J_{\rm 2MASS}}/A_V = 0.290$, $A_{H_{\rm 2MASS}}/A_V = 0.183$, and $A_{K_{\rm s,2MASS}}/A_V = 0.118$.

These numbers would be fine to simulate extinction in the nearby disk, but do not apply to a bulge with an anomalous ratio of total to selective extinction (see Udalski 2003). Since the reasons for such anomalous ratios are still not understood, one does not know really how to properly simulate extinction for the bulge. Our choice has been very pragmatic: we assume that the generalised Cardelli et al. (1989) extinction curve still applies, and just change its input R_V value until the mean $R_{VI} = 1.964$ value for the bulge (Sumi 2004) is recovered. Therefore, we find that the anomalous extinction is reproduced with a $R_V = 2.4$, which produces $A_{U_{\rm OGLE}}/A_V = 1.715$, $A_{B_{\rm OGLE}}/A_V = 1.386$, $A_{V_{\rm OGLE}}/A_V = 1.017$, $A_{I_{\rm OGLE}}/A_V = 0.506$, $A_{J_{\rm 2MASS}}/A_V = 0.256$, $A_{H_{\rm 2MASS}}/A_V = 0.162$, $A_{K_{\rm s,2MASS}}/A_V = 0.101$. These values are assumed in this work.

7.3 Observational Data

Sky surveys have as ultimate goal to unravel the mysteries of our Universe. They come in different shapes and packages. Every sky survey has its own specific aim and often – if ground based – the project can make use of its own telescope facility. Sky surveys are very useful for very different kind of astronomers. One can use them to probe galaxy formation and trace galaxy structure, to study star formation, one can look for variable stars, micro lensing events, extra-solar planets and so on... Sky surveys often can also be used for things they were not designed for. Sky surveys looking for micro lensing events e.g. produce huge amounts of observational data on very interesting stars and star regions. Which is exactly what we need to study stellar populations in the GB: large amounts of observational data on as much as possible different regions in the GB. To perform this study, we selected data from 2MASS and OGLE.

7.3.1 Two Micron All Sky Survey – 2MASS

The Two Micron All Sky Survey (2MASS) project was set up as a result of the success of the Two Micron Sky Survey (TMSS) and the InfraRed Astronomical Satellite (IRAS). It is a collaboration between The University of Massachusetts and the Infrared Processing and Analysis Center (JPL/ Caltech). Survey operations began in Spring 1997 and concluded in Spring 2001. The resulting 2MASS project made uniformly-calibrated observations of the entire sky in the J (1.24 μm), H (1.66 μm) and K_s (2.16 μm) near-infrared bands with a pixel size of 2.0".
The observations for this project were made using almost two identical telescopes and cameras, one located in the northern hemisphere at the Whipple Observatory and one in the southern hemisphere at the Cerro Tololo Inter-American Observatory. In this way almost full

sky coverage (99.998%) could be obtained.
In this paper, we will use the 2MASS Point Source Catalog (PSC). It contains astrometry and photometry in the three survey bandpasses for 470 992 970 sources. For every source, position, magnitude, astrometric and photometric uncertainties and flags indicating the quality of the source characterisations are provided.

7.3.2 Optical Gravitation Lensing Experiment – OGLE

The Optical Gravitational Lensing Experiment (OGLE) aims at detecting dark matter using micro lensing phenomena. This idea was first proposed by Paczynski (1986) (see also Paczynski 1991). In order to draw any conclusions about the nature of dark matter one needs a massive, long term survey and one needs to detect a significant amount of micro lensing events. Crowded regions are a suited place to conduct this survey. During the first phase of the program (OGLE-I) (1992-1995), the 1m Swope telescope at the Las Campanas Observatory, Chile, operated by Carnegie Institution of Washington has been used. The second phase of OGLE (OGLE-II) started in January 1997. A telescope for the OGLE project (the 1.3m Warsaw telescope) was build which is dedicated for long-term photometric surveys of the dense stellar fields. The telescope is located at Las Campanas Observatory in Chili and is described in Udalski et al. (1997). The telescope has a 1.5° field of view. The Large Magellanic Cloud (LMC) was the first target in the second phase. Later on additional targets were added among 10 deg^2 in the GB. On June 11, 2001 the third phase of OGLE started (OGLE-III). Observations are still done from Las Campanas Observatory, Chile, but are now using a so called second generation CCD mosaic camera. The total field of view is now 35' x 35'.
In this paper, we will use data from Udalski et al. (2002) from OGLE-II who present the *VI* photometric maps of the GB as a natural by-product of large micro lensing surveys. These maps contain the mean *VI*-photometry and astrometry of about 30 million stars, covering about 11 deg^2 in different parts of the GB. Each field covers $14.2' \times 57'$.

7.3.3 Selected fields

The fields selected to perform this study are shown in Table 7.2. The fields are chosen based on the OGLE fields from Udalski et al. (2002) and are as much as possible spread in longitude and latitude around the Galactic Centre. The data from 2MASS has been downloaded according to the positions of the OGLE fields, using Gator on the IRSA web site (`http://irsa.ipac.caltech.edu/`).

7.4 Analysis

When calculating a set of models of any kind, one always needs an objective method to determine why one model is better than an other model. One also wants to know the error bars and/or confidence intervals for the derived parameters.

Table 7.2: Properties of the selected fields.

Ogle field (bul_sc)	l	b	A_V [a]	σ_{A_V} [a]	# stars	
					OGLE	2MASS
2	2.23	-3.46	1.51	0.024	803 269	26 147
7	-0.14	-5.91	1.34	0.025	462 748	19 304
8	10.48	-3.78	2.14	0.042	401 813	19 411
13	7.91	-3.58	2.05	0.042	569 850	20 704
14	5.23	2.81	2.49	0.048	619 028	24 851
17	5.28	-3.45	1.92	0.031	687 019	22 241
25	-2.32	-3.56	2.33	0.042	622 326	26 328
27	-4.92	-3.65	1.69	0.025	690 785	23 623
29	-6.64	-4.62	1.53	0.024	491 941	20 692
40	-2.99	-3.14	2.92	0.066	630 774	26 169
47	-11.19	-2.60	2.58	0.056	300 705	20 099

[a]Based on Sumi (2004)

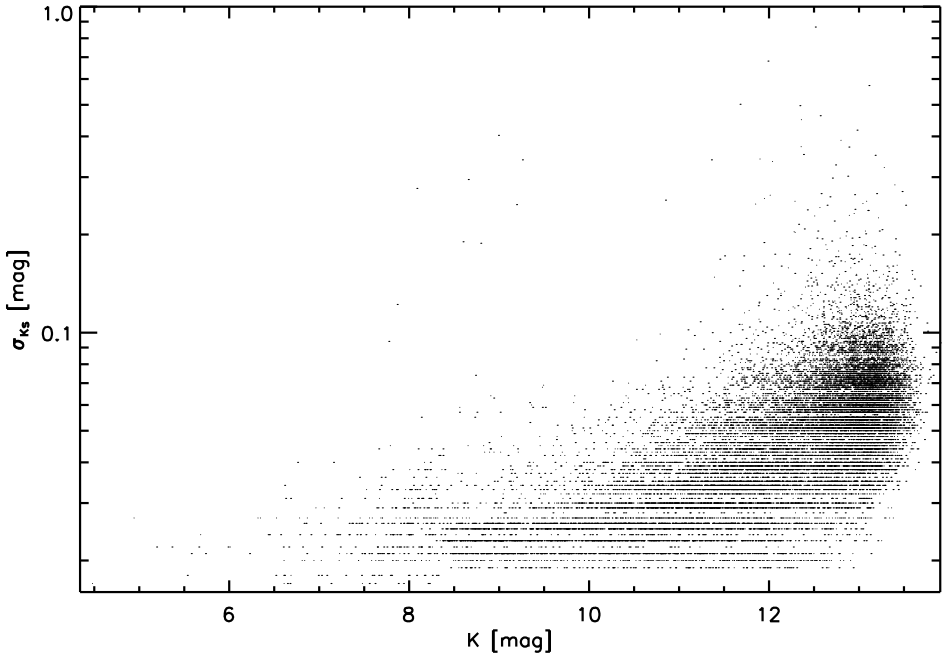

Figure 7.2: Example on the photometric errors of the *K*-band 2MASS data for field bul_sc40.

7.4.1 Method

The output of the TRILEGAL code consists of *perfect* photometric data (see Section 7.2). In order to be able to compare the output of the code with real observations, we need to add

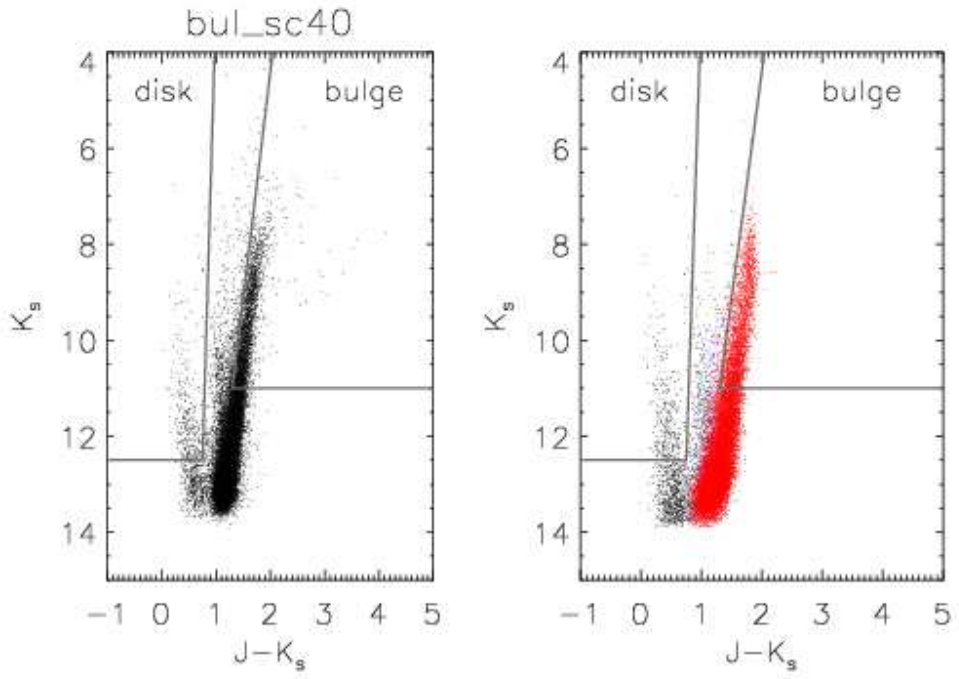

Figure 7.3: $J - K_s$ vs K_s CMD for field bul_sc40. The figure on the left are the observations, the figure on the right is a model with $R_0 = 8.60$ kpc, $a_m = 2.67$ kpc, $a_0 = 96.6$ pc, $\eta = 0.68$, $\zeta = 0.30$, $\phi = 14.4°$, and $f_0 = 427.3$. The black dots in the model (right panel) are stars that originate from the disk, the dark blue dots originate from the halo and the red dots are bulge stars. This colour code will be used in all figures of this type. The grey lines indicate the boxes used to compute the model with the observations. The 2MASS CMDs for all the selected fields using this model are shown in Figure 7.11.

photometric errors to the output of TRILEGAL.
Both 2MASS and OGLE-II give individual errors on the observations. These individual errors are shown in Figure 7.2 as an example for the 2MASS K_s-band data in field bul_sc40 in function of the K_s-band magnitude. Using this data a density profile has been generated: for each bin in K_s (size 0.1 mag) we calculated how likely it is for a star to have an error σ_{K_s}. Each bin in σ_{K_s} (size 0.01 mag) is then given a number between 0 and 1 representing the relative amount of stars in this bin with respect to all stars with a similar K_s-band magnitude. For each star in the output file of TRILEGAL a random number has been generated between 0 and 1. The assigned error is then the closest σ_{K_s} with respect to the assigned density profile. This method has been used to generate photometric errors in all the observed magnitude bands from both 2MASS as OGLE-II for each field individually.

With the observational data and the data calculated with TRILEGAL, CMDs have been constructed. For the 2MASS data these CMDs are in $J - K_s$ vs K_s (see Figure 7.3), for

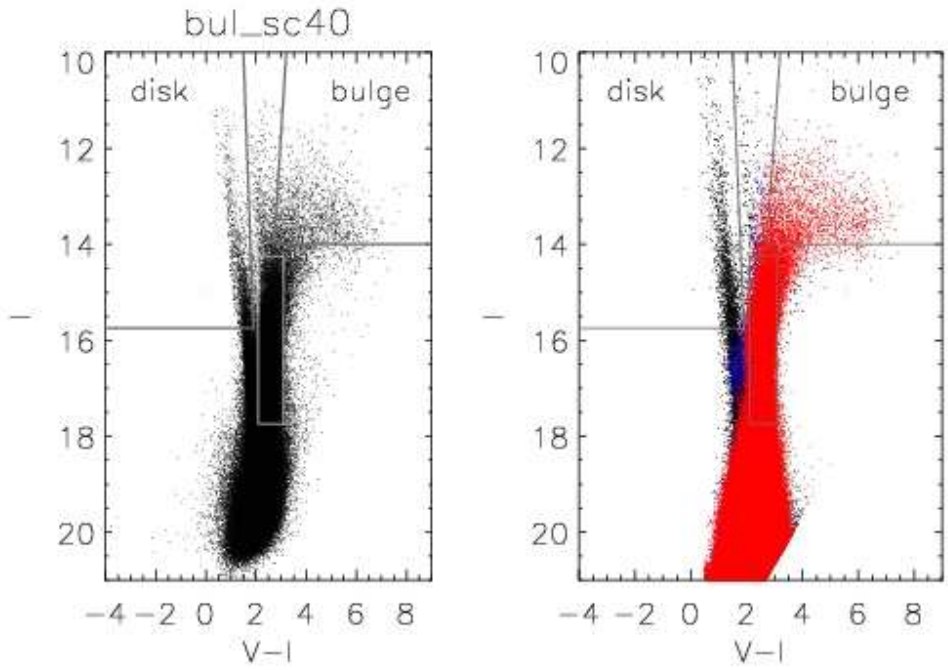

Figure 7.4: Same figure and colour code as Figure 7.3 for the same model but now for a $V-I$ vs I CMD. The additional box which is not seen in Figure 7.3 is used to compare the red clump stars. The OGLE CMDs for all the selected fields using this model are shown in Figure 7.13.

the OGLE data the CMDs are $V-I$ vs I (see Figure 7.4). To be able to compare a CMD constructed with observational data to a CMD constructed with modelled data, the CMDs have been divided into regions. For both the 2MASS data and OGLE data, we define a disk region and a bulge region in the dereddened CMDs as follows:

$$K_{s,0} \leq 12.2 \quad \text{and} \quad (J-K_s)_0 \leq 0.25 \text{ (for 2MASS disk)} \tag{7.3}$$

$$I_0 \leq 14.1 \quad \text{and} \quad (V-I)_0 \leq 1.4 \text{ (for OGLE disk)} \tag{7.4}$$

$$K_{s,0} \leq 10.7 \quad \text{and} \quad K_{s,0} \geq -10.4(J-K_s)_0 + 18.9 \text{ (for 2MASS bulge)} \tag{7.5}$$

$$I_0 \leq 12.4 \quad \text{and} \quad I_0 \geq -8.2(V-I)_0 + 24.0 \text{ (for OGLE bulge)} \tag{7.6}$$

For the OGLE data we defined additionally a clump region which contains the red clump stars, as $16.1 \leq I_0 \leq 12.6$ and $0.8 \leq (V-I)_0 \leq 1.8$.

The regions are defined on a model with no extinction. Based on the assumed extinction for a field, these boxes are also reddened, in this way, these boxes include for every field the same part of the CMD. The boxes are defined in such a way that there is only a very small contamination of disk stars in the bulge region and the other way around. Therefore,

if we want to study the bulge parameters, the only part of interest is the bulge region. The histograms for the disk and bulge regions are probably not affected by incompleteness and are used to compare the number counts in each bin.

The stars in the selected regions, are used to create histograms. All histograms were created in one magnitude (K_s for 2MASS and I for OGLE) and not in the colours. The histograms for the disk and bulge region are used to compare the number counts in each bin.

The histogram for the stars in the red clump region are not used for number counts, but to derive the red clump magnitude both from observations and modelled data. To derive the $I_{0,m}$ magnitude for the red clump, the method described in Stanek and Garnavich (1998) has been used. This method fits a 2D polynomial to the underlying population, with on top of this a Gaussian function to determine the magnitude of the red clump. The formula is given by:

$$n(I_0) = a \quad + \quad b(I_0 - I_{0,m}) + c(I_0 - I_{0,m})^2 + \frac{N_{RC}}{\sigma_{RC}\sqrt{2\pi}} \exp\left(-\frac{(I_0 - I_{0,m})^2}{2\sigma_{RC}^2}\right), \qquad (7.7)$$

with the first tree terms corresponding to the underlying population with coefficients a, b, and c for the second degree polynomial. The last term refers to the red clump population itself, with parameters corresponding to a Gaussian fit: scaling factor N_{rc}, sigma σ_{RC} and peak of the observed red clump stars $I_{0,m}$. Figure 7.5 shows a fit using this method to the I-band observations in the bul_sc40 field. Using this fit to the red clump, we will compare the peak position of the red clump stars in the observations to the peak position of the red clump in the model. The expected magnitude of the red clump M_I^{RC} is often compared to the peak position in the magnitude distribution of the red clump in order to estimate the distance to these stars.

7.4.2 Poisson distributed maximum likelihood

For the stars in the selected disk and bulge areas (see Figure 7.3 and Figure 7.4) the constructed histograms are used to compare number counts. The typical errors on the amount of stars in these histogram bins are Poisson errors ($\sim \frac{1}{\sqrt{n_i}}$ with n_i the total amount of stars in bin i). Therefore the selected test to perform on these histogram is a log likelihood test for Poisson statistics (Eidelman et al. 2004):

$$-2\ln(\lambda(\theta)) = 2\sum_{i=1}^{N}\left(\nu_i(\theta) - n_i + n_i \ln\frac{n_i}{\nu_i(\theta)}\right). \qquad (7.8)$$

In this formula θ is the set of unknown parameters one wants to derive, $n = (n_1, n_2, \ldots, n_N)$ is the data vector containing the observations with N the number of bins in a histogram. ν are the expected values, which are derived from the histograms of the modelled data and are therefore dependent on θ. When $n_i = 0$, the last term in Eq. (7.8) is set to zero.

As already mentioned, for each field, there are 4 histograms (one for the disk region and one for the bulge region, both for the comparison with 2MASS and OGLE). When determining the parameters for the bulge, we only use the histograms based on the stars in the bulge

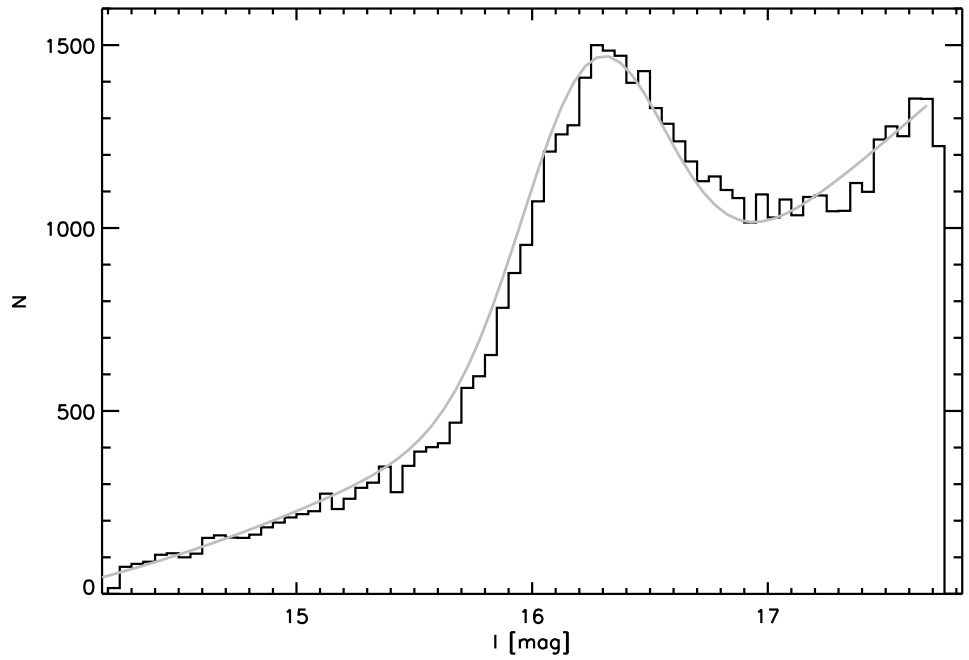

Figure 7.5: Example showing how the red clump stars are fitted using the method described by Stanek and Garnavich (1998). The black histogram are the stars selected from the "red clump box" in the $V-I$ vs I CMD and the grey line is the Gaussian fit with underlying second degree polynomial.

boxes. This means that for each field, 2 histograms remain. Table 7.2 shows that we selected 11 fields. Including all this gives us a value l for each model, which we want to minimise:

$$l = \sum_{j=1}^{11} \sum_{k=1}^{2} -2 \ln(\lambda_{kj}(\theta)). \tag{7.9}$$

7.4.3 Gaussian distributed log-likelihood

In addition to a box for the disk and bulge stars, Figure 7.4 also shows a box in which the red clump stars are expected to be. When evaluating calculated models based on the position of the red clump, we cannot use the Poisson distributed maximum likelihood (see Section 7.4.2). In this case the errors are not Poisson distributed, but normal $N(0, \sigma^2)$, with $\sigma = 0.025$ which is the half of the bin size used to construct the histograms to determine the peak of the red clump distribution. To determine the appropriateness of a model concerning its position of

the red clump, the log-likelihood function l can be used (Decin et al. 2007):

$$l = \sum_{j=1}^{11} \sum_{i=1}^{N_j} -\ln(\sigma) - \ln(\sqrt{2\pi}) - \frac{1}{2}\left(\frac{n_{ij} - \nu_{ij}(\theta)}{\sigma}\right)^2 . \tag{7.10}$$

The used symbols in this equation have the same meaning as the symbols used in Eq. (7.8). Because of the definition of this log-likelihood, to find the best model, l has to be maximised and not minimised as Eq. (7.8).

7.4.4 Minimisation procedure

The minimisation procedure used in this work is the *Broyden – Fletcher – Goldfarb – Shanno (BFGS) method* (Broyden 1970; Fletcher 1970; Goldfarb 1970; Shanno 1970) which can be used to solve a non-linear optimisation problem. By analysing gradient vectors, the method constructs an approximated Hessian matrix allowing a quasi-Newton fitting method to move towards the minimum in parameter space. The parameters were normalised in the minimisation procedure so they have an equal influence on the choice of the next set of parameters.

To significantly decrease the amount of computing time, the simulations made during the minimisation runs adopt a shallower limiting magnitude, at $I = 18$. This does not influence our results as the stars fainter than this limit have no relevance to our analysis (see Section 7.4.1). Because these areas are chosen well above the completeness limits for both the 2MASS and OGLE data, we did not include completeness, again to speed up calculations.

The model calculations and minimisation procedure have been performed using Python. The program has been written as such that the 11 different fields, that need to be calculated to evaluate one model (see Section 7.3.3), were calculated simultaneously over 11 different CPU's. We could make use of 18 Dell PowerEdge PC's: half of them with 2 Pentium 4 processors of 3400MHz and the other half with 4 Xeon processors (7 processors of 3400MHz and 2 of 3800MHz). In total we could thus make use of 54 processors, which makes it possible to evaluate about 5 models at the same time. In total we evaluated 37 606 models in a time span of about 35 weeks.

7.4.5 Uncertainties on the model parameters

As explained by Decin et al. (2007) the log-likelihood function can be used to estimate the uncertainties on the model parameters. A model with a likelihood value l is equally good as the best model if $\min(l) - l > N_{\rm crit}$ in the case of Eq. (7.9) and $\max(l) - l < N_{\rm crit}$ in the case of Eq. (7.10). For both cases, these critical values $N_{\rm crit}$ follow a χ^2_p-distribution with p the degrees of freedom (Eidelman et al. 2004; Decin et al. 2007). A table with these values for $p \in [1, 20]$ can be found in Decin et al. (2007, and references therein).

Another way of determining uncertainties on the parameters can come from the observations. Both the 2MASS and OGLE data come with errors on the observed photometry. We

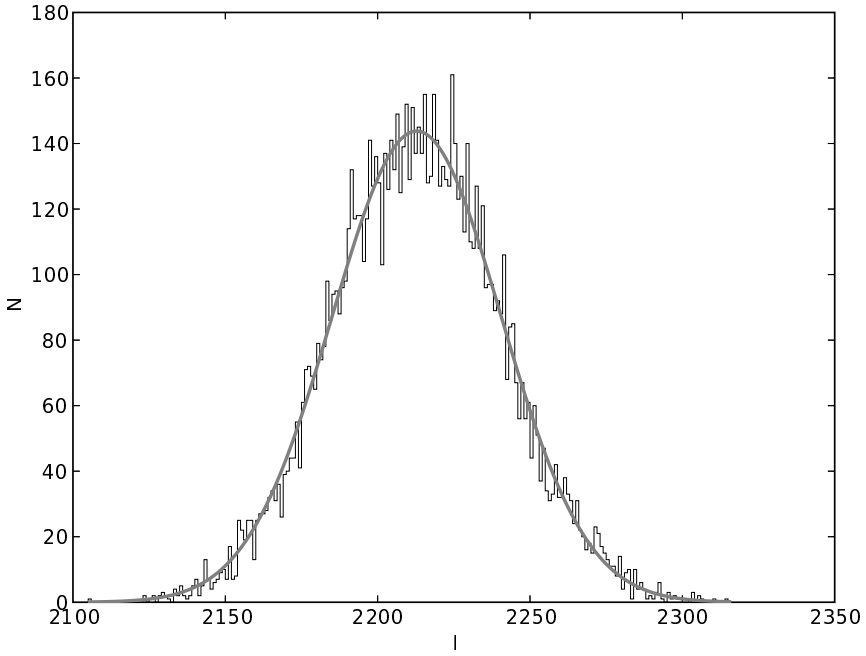

Figure 7.6: This figure shows how an estimate of $N_{\rm crit}$ based on the observations can be obtained. The parameter on the x-axis is l, the log-likelihood value. The observations have been altered 10 000 times and compared to a model (histogram). The standard deviation σ of the Gaussian fit through this histogram (full grey line) gives then $N_{\rm crit}$. In this case $\sigma = 27.75$. This figure is based on a model with the following parameters: $R_0 = 8.60$ kpc, $a_m = 2.67$ kpc, $a_0 = 96.6$ pc, $\eta = 0.68$, $\zeta = 0.30$, $\phi = 14.4°$, and $f_0 = 427.3$. The SFR is based on Zoccali et al. (2003) and the metallicity distribution is shifted with 0.3 dex in comparison to Zoccali et al. (2003).

can alter the photometry by adding a value defined by a Gaussian function with as dispersion the given error. If we do this for all the observations we have a different set of observations, but that still lies within the errors given. If we compare a perfect model (i.e. no errors added the outputs of the TRILEGAL code) a huge amount of times (e.g. 10 000 times) with the observations that we adapt based on the errors for every comparison, we get a reliable estimate of the possible spread in l for this model. The standard deviation σ that comes out of this method, can then be used as a critical value to look for equally good models and estimate uncertainties (see Figure 7.6).

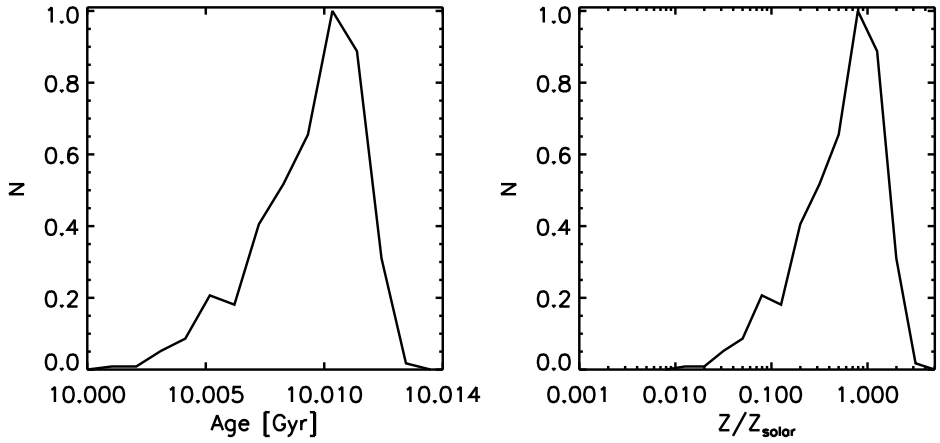

Figure 7.7: The left panel shows the SFR normalised to 1 and the right panel shows the metallicity distribution normalised to 1 (based on Zoccali et al. 2003).

7.5 Results

The SFR and AMR chosen to start the minimisation process with are based on Zoccali et al. (2003) and are shown in Figure 7.7. The left figure shows a bulge formed by a single star burst about 10 Gyr ago and the right figure indicates that the majority of the stars have a metallicity slightly lower than solar ($Z_\odot = 0.019$).

The start values for the minimisation procedure have been chosen in accordance with Binney et al. (1997, see also Table 7.1): $R_0 = 8.00$ kpc, $a_m = 1.90$ kpc, $a_0 = 100$ pc, $\eta = 0.6$, $\zeta = 0.4$, $\phi = 20°$, and $f_0 = 624$. The output of this minimisation procedure is a model with following parameters: $R_0 = 8.60$ kpc, $a_m = 2.69$ kpc, $a_0 = 97.0$ pc, $\eta = 0.69$, $\zeta = 0.30$, $\phi = 20.0°$, and $f_0 = 422.3$.

The constructed histograms for this model are shown for field bul_sc40 in Figure 7.8. As mentioned in Section 7.4.1 we only used the histograms constructed with the I and K_s magnitude to compare the model with the observations. The histograms in $V - I$ and $J - K_s$ illustrate the fit between the model and the data for the colours. The minimisation procedure uses only the stars in the bulge box. The stars in the disk box were used prior to the minimisation process to set the scale parameter for the disk stars and to check the contamination of disk and halo objects in the "bulge box". For field bul_sc40 adopting the same model as in Figure 7.8, we find that out of a total of 2731 objects in the bulge box for the 2MASS data only 127 originate from the disk and halo. Concerning the 2110 objects in the bulge box for the OGLE data, only 105 originate from the disk and halo. Since this is already a very modest fraction (about 5% for both CMDs), possible errors in our representation of the disk and halo geometry are expected to have a negligible impact in the star counts inside the bulge box.

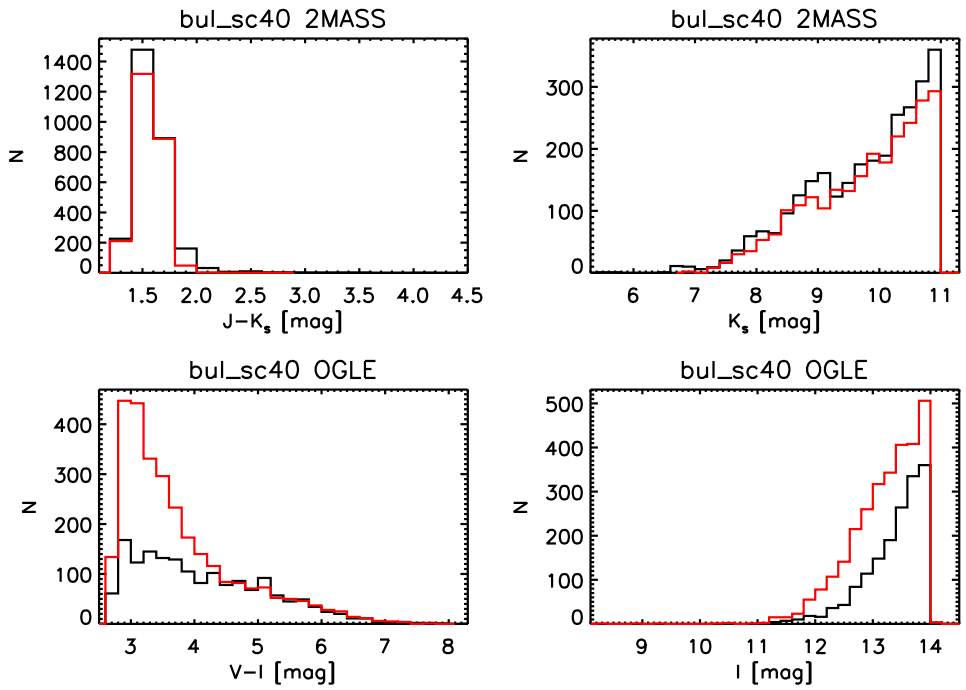

Figure 7.8: Histograms showing the distribution of selected bulge stars for field bul_sc40. The black line represents the observations, the red line the model. The left panel shows the 2MASS data, the right panel the OGLE data. The model has the following parameters: R_0 = 8.60 kpc, a_m = 2.69 kpc, a_0 = 97.0 pc, η = 0.69, ζ = 0.30, ϕ = 20.0°, and f_0 = 422.3. The star formation rate is a 10 Gyr burst and the metallicity distribution is based on Zoccali et al. (2003).

Figure 7.8 shows the distribution of stars for the observations and the model for the selected bulge stars for field bul_sc40. Also for all the other fields this model overestimates the amount of bulge stars in the 2MASS data and underestimates the amount of bulge stars in the OGLE data, therefore this model can still be improved, but not by adapting the parameters already in the minimisation procedure.

7.5.1 Varying the metallicity distribution

One of the parameters not in the minimisation procedure is the metallicity. The metallicity distribution in Zoccali et al. (2003), which has been used for the previous model calculations, is based on photometric results and is slightly less metal-rich in comparison with metallicity distributions derived from spectroscopic results from e.g.
McWilliam and Rich (1994), Sadler et al. (1996), and Ramírez et al. (2000) (see Fig. 14 in

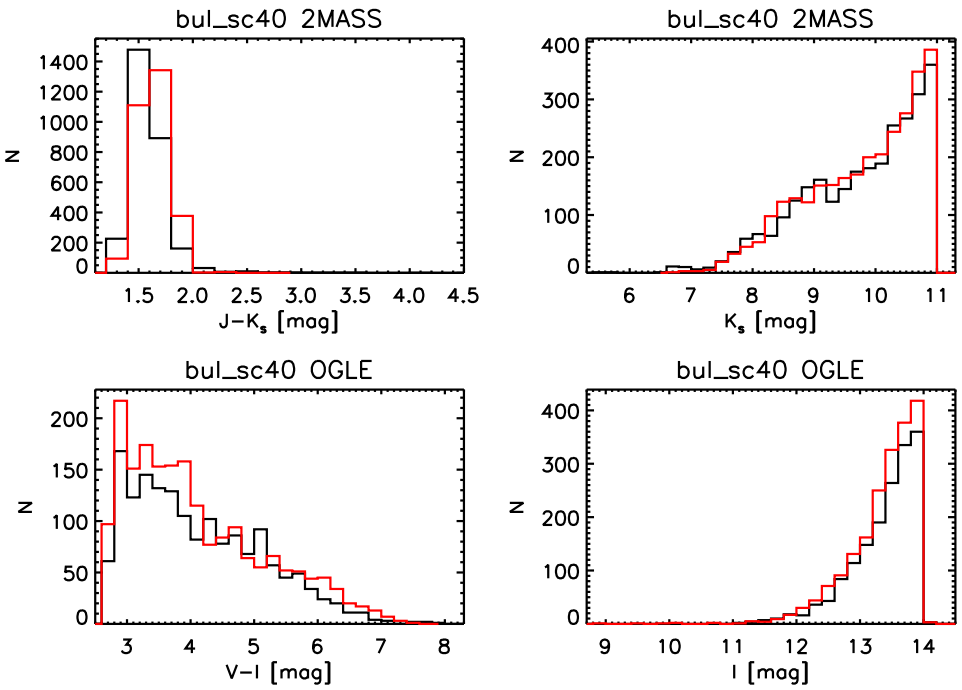

Figure 7.9: Histograms showing the distribution of selected bulge stars for field bul_sc40. The black line represents the observations, the red line the model. The left panel shows the 2MASS data, the right panel the OGLE data. The model has the following parameters: R_0 = 8.60 kpc, a_m = 2.67 kpc, a_0 = 96.6 pc, η = 0.68, ζ = 0.30, ϕ = 14.4°, and f_0 = 427.3. The star formation rate is a 10 Gyr burst and the metallicity distribution is based on Zoccali et al. (2003) but shifted with 0.3 dex. (This figure is also given for all the modelled fields, see Figures 7.15 and 7.16).

Zoccali et al. 2003). Therefore we shifted the metallicity towards a more metal-rich population and used the parameters of the model found after the minimisation process (model 1) to run some new models with the shifted metallicity distribution. Already when we shift [Fe/H] with 0.1 dex our fit improves. We obtained the best fit with a shift of 0.3 dex for [Fe/H] (see Table 7.3, model 4). Fig. 14 in Zoccali et al. (2003) shows that a shift with 0.3 dex in [Fe/H] is consistent with the noticed differences between the metallicity distribution they derived and metallicity distributions derived based on spectroscopy.

Although the fit with the slightly metal-rich population improves the fit, we need to be sure that this is also the best model using a more metal-rich population. Therefore, we ran a new minimisation procedure with starting values R_0 = 8.60 kpc, a_m = 2.69 kpc, a_0 = 97 pc, η = 0.69, ζ = 0.30, ϕ = 20°, and f_0 = 422.3. The resulting model from this minimisation procedure has the following parameters: R_0 = 8.60 kpc, a_m = 2.67 kpc, a_0 = 96.6 pc, η = 0.68, ζ = 0.30, ϕ = 14.4°, and f_0 = 427.3 (model 7). Figures 7.11 and 7.12 show all the CMDs

based on the 2MASS data, Figures 7.13 and 7.14 show the CMDs based on the OGLE data, Figures 7.15 and 7.16 show the histograms for the selected bulge stars for all the modelled fields, and Figure 7.17 shows all the fits using the red clump stars for both observations and model.

The parameters for this new model do not differ much from the initial model (model 4). Also the maximum-likelihood values are very similar (see Table 7.3). Section 7.4.5 describes two methods to estimate errors on the model parameters and therefore also discuss how to decide if one model is significantly better than another model. If we use the method described in Decin et al. (2007) then the critical value is given by $N_{\rm crit} = 14.07$ and the new model is significantly better then the initial one. The other method described in Section 7.4.5 gives a critical value of $N_{\rm crit} = 27.76$ (see also Figure 7.6). In this case the two models are equally good. We will continue with the new model (model 7).

To derive the error bars on these model parameters, we used both methods described in Section 7.4.5. For each parameter we explored the parameter space around the value found by the minimisation procedure and rounded the found parameters within the found error bars. Using the first method, all models that fall within the critical value of $N_{\rm crit} = 14.07$ from our model are equally good. This results in the following error bars: $R_0 = 8.60\pm^{0.15}_{0.10}$ kpc, $a_m = 2.70\pm^{0.04}_{0.08}$ kpc, $a_0 = 96.6\pm^{1.1}_{3.5}$ pc, $\eta = 0.68\pm^{0.01}_{0.07}$, $\zeta = 0.30\pm^{0.01}_{0.01}$, $\phi = 14.4^\circ\pm^{5.6}_{9.6}$, and $f_0 = 427.3\pm^{10.8}_{25.7}$.
Using the second method, we find a $N_{\rm crit} = 27.76$ (see also Figure 7.6). Using this critical value, we derive the following error bars on our parameters: $R_0 = 8.60\pm^{0.15}_{0.11}$ kpc, $a_m = 2.70\pm^{0.004}_{0.01}$ kpc, $a_0 = 96.6\pm^{1.1}_{4.1}$ pc, $\eta = 0.68\pm^{0.01}_{0.07}$, $\zeta = 0.30\pm^{0.01}_{0.01}$, $\phi = 14.4^\circ\pm^{5.7}_{10.3}$, and $f_0 = 427.3\pm^{11.0}_{25.7}$.
As was expected the error bars using the second method are larger then using the first method. Nevertheless the differences are very small.

7.5.2 Varying the age distribution

The star formation rate is also still quite uncertain (see also Section 7.1.3). Therefore we also tested other SFR's. First we start with shifting the star burst to a different age in steps of 0.5 Gyr from a star burst 9 Gyr ago till 13 Gyr ago. Table 7.3 gives an overview of this and shows that we could not improve our fit by changing the age of the star burst.
Changing the age of the star burst is not the only possibility to alter the SFR. Section 7.1.3 describes that most likely there are also intermediate aged stars in the GB and maybe also some younger stars. In order to check these possibilities, we used the SFR given in van Loon et al. (2003) (see their Figure 28). The metallicity distribution used is the metallicity distribution of Zoccali et al. (2003) shifted with 0.3 dex. Young stars as well as intermediate aged stars are included in the SFR by van Loon et al. (2003). To check the possibility of an intermediate aged population on top of the dominant old population, the metallicity distribution of van Loon et al. (2003) has been used, but without the stars younger than 0.1 Gyr and a SFR without the stars younger than 1 Gyr. The metallicity distribution used in these scenarios is again the shifted distribution found by Zoccali et al. (2003). The results are again shown in Table 7.3.

Table 7.3 shows that we do not get a significant better fit if we use the SFR by van Loon et al. (2003) and the shifted metallicity distribution by Zoccali et al. (2003). Because the SFR has changed drastic, and therefore also the colour distribution of the stars in the resulting models, a new minimisation procedure is necessary to check if no better model can be found using the SFR by van Loon et al. (2003). The previous best model found (model 7), has been chosen to start the minimisation procedure with. This resulted in the following model: $R_0 = 10.27$ kpc, $a_m = 3.19$ kpc, $a_0 = 95.0$ pc, $\eta = 0.62$, $\zeta = 0.31$, $\phi = 11.0°$, and $f_0 = 370.8$. All parameters except R_0, a_m, and f_0 fall within the defined error bars of the best model with a star burst of 10 Gyr as SFR. The differences seen between R_0, a_m, and f_0 are huge and do not fall within the previously defined error bars. Additionally, based on the method to compare different models, this new model is significantly better than the models previously found. In Section 7.6 we explain based on the analysis of the red clump stars why we prefer the previous model 7 over this new model although based on the comparison of the stars located in the bulge box in the CMDs, this model is significantly better.

Also for the two SFR's including only intermediate aged stars based on the SFR by van Loon et al. (2003) a new minimisation procedure was set up. Using the SFR by van Loon et al. (2003) for stars older than 0.1 Gyr, the minimisation procedure ended with the following model: $R_0 = 9.00$ kpc, $a_m = 2.67$ kpc, $a_0 = 95.3$ pc, $\eta = 0.69$, $\zeta = 0.28$, $\phi = 8.7°$, and $f_0 = 424.8$. Almost all parameters found using this SFR are within the error bars derived on the previous model, except R_0 and ζ. Nevertheless this model is not significantly better than the former model 7. Using the SFR for stars older than 1 Gyr, the minimisation procedure ended with: $R_0 = 8.70$ kpc, $a_m = 2.57$ kpc, $a_0 = 96.4$ pc, $\eta = 0.68$, $\zeta = 0.28$, $\phi = 15.7$, and $f_0 = 423.7$. Almost all parameters for this model are consistent with the parameters and their error bars derived using the star burst of 10 Gyr and a metallicity distribution of Zoccali et al. (2003) shifted with 0.3 dex. The parameters a_m and ζ are the only two that are not consistent with the previously derived parameters, although the differences are very small. But again this model is significantly worse than the previous found model 7.

7.6 Red Clump stars

The red clump stars can be used as a distance indicator as well as an estimator to the angle ϕ between the bar and the Sun-Centre line (see also Section 7.1.2). Using the red clump stars, a new minimisation procedure as described in Section 7.4.4 was set up. In this scenario, there are only two variable parameters: R_0 and ϕ, the other parameters have been kept constant ($a_m = 2.67$ kpc, $a_0 = 96.6$ pc, $\eta = 0.68$, $\zeta = 0.30$, and $f_0 = 427.3$). An age of 10 Gyr and a metallicity distribution based on Zoccali et al. (2003) and shifted with 0.3 dex has been used. The minimisation process started with $R_0 = 8.60$ kpc and $\phi = 14.4°$ and ended with $R_0 = 8.60$ kpc and $\phi = 24.8°$. This model is also listed in Table 7.3.

Using the first method to derive error bars on these parameters, with $N_{\rm crit} = 5.99$, the following error bars were calculated: $R_0 = 8.60 \pm^{0.33}_{0.11}$ kpc and $\phi = 24.8° \pm^{25.7}_{13.0}$. Using the second method a critical value $N_{\rm crit} = 4.36$ has been derived, which resulted in the following error bars: $R_0 = 8.60 \pm^{0.16}_{0.11}$ kpc and $\phi = 24.8° \pm^{5.9}_{12.5}$. Therefore the model derived based on the red

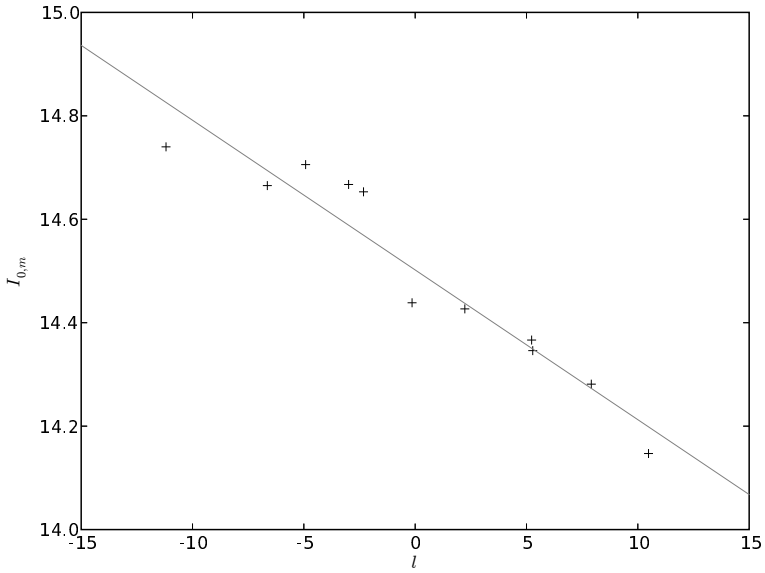

Figure 7.10: Peak positions I_0 of the red clump stars corrected for extinction in function of the longitude ℓ.

clump stars for R_0 and ϕ falls within the previously defined error bars for the model derived on the stars located in the bulge box. Nevertheless the derived model is significantly better if we only consider the red clump stars.

In Section 7.5 other SFR's have been tested (see Table 7.3). Also for these other models, we compared the red clump stars. Based on the red clump stars, Table 7.5 shows that the models with a star burst of 10 Gyr as SFR but with shifted metallicity distributions are equally good. There is based on the critical value N_{crit} no difference between these models. If the age of the star burst has changed, one notices that not all models are equally good. The best model that comes out of the comparison based on only the red clump star is a model with a star burst of $11\pm^{2.0}_{1.0}$ Gyr, with the model derived using the minimisation procedure based on the red clump stars included.

Concerning the models with a SFR based on van Loon et al. (2003) the comparison with the red clump stars shows that our fit could not be improved adapting this SFR. Although the model with $R_0 = 10.27$ kpc, $a_m = 3.19$ kpc, $a_0 = 95.0$ pc, $\eta = 0.62$, $\zeta = 0.31$, $\phi = 11.0°$, and $f_0 = 370.8$ is significantly better based on the stars in the bulge box, the comparison with the red clump stars shows that this is the worst fit made for the red clump stars.

We did not compare the observed clump with estimates derived from independent formulae that describe how M_I^{RC} changes with age and metallicity (see e.g. Udalski 2000; Girardi

and Salaris 2001). Instead, we completely model the luminosity function of the red clump, and hence derive its expected $M_I^{\rm RC}$ in the same way as $I^{\rm RC}$ is derived from real data. Using the distance to the GC R_0 and the peak positions of the red clump in the observations, we can calculate $M_I^{\rm RC}$ in the following way:

$$M_I^{\rm RC} = I_{0,m} - (5 \log R_0 - 5) \tag{7.11}$$

with $I_{0,m}$ the peak of the red clump corrected for extinction.

Figure 7.10 shows the peak positions of the red clump in function of the longitude. These peak positions are corrected for extinction using the extinction values given in Table 7.2. The full line is a linear least-squares fit through these peak positions and is given by: $I_{0,m} = (14.502 \pm 0.018) + (-0.029 \pm 0.003)l$. Therefore, the peak position $I_{0,m}$ in the GC ($\ell = 0$) is then given by 14.502 ± 0.018. If we assume that $R_0 = 8600 \pm^{155}_{110}$, which we found using the minimisation process, Eq. (7.11) gives then $M_I^{\rm RC} = -0.170 \pm^{0.069}_{0.066}$. Due to the rather large errors on R_0 the error bars for $M_I^{\rm RC}$ are also rather large.

Girardi and Salaris (2001) study the possible effects of systematic magnitude differences between the local red clump revealed by Hipparcos and the red clump stars in distant galaxies. They constructed detailed models for the red clump population and took star formation rates and chemical enrichment histories from literature. Their Table 4 gives an overview on the found results, and indicates that the value we found is consistent with the value found for the Solar neighbourhood using the SFR of Rocha-Pinto et al. (2000b) and the AMR of Rocha-Pinto et al. (2000a). Our value is also consistent with the value for Baade's Window if α-enhancement is included in the models. Also Paczynski and Stanek (1998) studied the red clump stars for which detailed Hipparcos parallaxes are available in the solar neighbourhood and found that $M_I^{\rm RC} = -0.279 \pm 0.088$. Although our found value resembles better the values found by Girardi and Salaris (2001), this value is also consistent within the given error bars with our value.

7.7 Summary and conclusions

In this chapter we have studied the characteristics of the Galactic Bulge based on CMD comparisons between OGLE and 2MASS data an the results from the galactic model TRILEGAL (Girardi et al. 2005). Several star formation rates and metallicity distributions have been tested. Over all these different SFR's and metallicity distributions the model parameters give within the error bars the same results except for the angle ϕ between the Sun-Centre line and the Bar. Concerning the other parameters we found a distance to the Galactic Centre $R_0 = 8.60 \pm^{0.16}_{0.11}$ kpc, a scale length for the Bulge a_m of $2.70 \pm^{0.04}_{0.10}$ kpc, an inner truncation length for the Bulge a_0 of $96.6 \pm^{1.1}_{4.1}$ pc, and a scaling factor $f_0 = 427.3 \pm^{11.0}_{25.7}$. Concerning the characteristics of the Bar, we found the ratio of the major axis to be $1 : 0.68 \pm^{0.01}_{0.07} : 0.30 \pm^{0.01}_{0.01}$ and an angle ϕ of $14.4^\circ \pm^{5.5}_{10.3}$. The largest scatter in the found model parameters is found for the angle ϕ. Nevertheless the found values are all rather small and around 15°. The present best model of the bulge is provided as the default in the interactive web interface to TRILEGAL (`http://trilegal.ster.kuleuven.be/`).

If we compare our results to the results found in literature and listed in Table 7.1 our parameters fall within the listed range of parameters except for the axial ratio η. Concerning the distance to the GC, our value resembles the values found by Paczynski and Stanek (1998) based on red clump stars and Groenewegen and Blommaert (2005) based on Mira variables. Our results disagree with e.g. Udalski (1998) based on red clump stars in the GB. If we compute the mean observed magnitude I_0 from the distance modulus listed in Udalski (1998) using M_I^{RC} from Stanek and Garnavich (1998) as they did, than this is consistent with the observed mean magnitude we derived in this work. The other two studies deriving the distance to the GC based on red clump stars which are inconsistent with this work are Babusiaux and Gilmore (2005) and Nishiyama et al. (2006). These two studies are consistent with each other and use a very similar method: both define an "extinction-free" magnitude. It is not exactly clear why the results of these methods are not consistent with our results. As these studies are performed using K-band observations, we cannot compare the expected magnitude as we could do for Udalski (1998). For the scale length of the bulge, we found the same value as Freudenreich (1998) and similar values as Sevenster et al. (1999) and Bissantz and Gerhard (2002). The inner truncation length for the Bulge is similar to the two values listed in Table 7.1 by Binney et al. (1997) and Bissantz and Gerhard (2002). The value η we found is higher than the values found in literature. Concerning the other ratio of the major axis ζ we found similar results as Whitelock (1992), Dwek et al. (1995), and Stanek et al. (1997). For the last parameter ϕ, we found values consistent with the group of studies finding lower values for ϕ (see e.g. Dwek et al. 1995; Binney et al. 1997; Stanek et al. 1997; Bissantz and Gerhard 2002; Robin et al. 2003; Merrifield 2004; Babusiaux and Gilmore 2005; López-Corredoira et al. 2005; Rattenbury et al. 2007). As already mentioned by Groenewegen and Blommaert (2005) the different results found in literature with respect to the angle between the bar and the Sun-Centre line (see e.g. our results in contrast to Whitelock 1992; Sevenster et al. 1999; Groenewegen and Blommaert 2005; López-Corredoira et al. 2007) could originate from a different spatial distribution of the stellar population these studies trace.

We also tested different star formation rates and metallicity distributions. A model with a star burst of 10 Gyr based on Zoccali et al. (2003) gave the best results together with a metallicity distribution also based on Zoccali et al. (2003) but shifted by 0.3 dex. We could not improve our fits including intermediate and/or young stars if we compared both the stars we selected in the defined bulge box and the red clump stars. Therefore we conclude that based on 2MASS and OGLE data comparisons with the TRILEGAL model we find best results for a population of 10 Gyr. Nevertheless it is still possible that there are also intermediate aged stars located in the GB, although we could not trace them using our described method (see e.g. Groenewegen and Blommaert 2005; Uttenthaler et al. 2007).

Using the peak positions of the red clump stars and the distance to the Galactic Centre obtained by our minimisation procedures, we found that $M_I^{\mathrm{RC}} = -0.170 \pm^{0.069}_{0.066}$. This value is consistent with recent values found in literature, although it resembles best the values found by Girardi and Salaris (2001) using red clump stars in the solar neighbourhood ($M_I^{\mathrm{RC}} = -0.171$) or using red clump stars in Baade's Window if α-enhancement is taken into account ($M_I^{\mathrm{RC}} = -0.161$).

Table 7.3: Overview on the different models described in the text.

Number	R_0 [kpc]	a_m [kpc]	a_0 [pc]	η	ζ	ϕ [$^\circ$]	f_0	SFR	[Fe/H]	l_{bulge}	l_{RC}
1	8.60	2.69	97.0	0.69	0.30	20.0	422.3	Zoccali et al. (2003), 10 Gyr	Zoccali et al. (2003)	2 185	-10.6
2	8.60	2.69	97.0	0.69	0.30	20.0	422.3	Zoccali et al. (2003), 10 Gyr	Zoccali et al. (2003) + 0.1 dex	1 768	-9.2
3	8.60	2.69	97.0	0.69	0.30	20.0	422.3	Zoccali et al. (2003), 10 Gyr	Zoccali et al. (2003) + 0.2 dex	1 597	-8.8
4	8.60	2.69	97.0	0.69	0.30	20.0	422.3	Zoccali et al. (2003), 10 Gyr	Zoccali et al. (2003) + 0.3 dex	1 519	-9.2
5	8.60	2.69	97.0	0.69	0.30	20.0	422.3	Zoccali et al. (2003), 10 Gyr	Zoccali et al. (2003) + 0.4 dex	1 597	-8.7
6	8.60	2.69	97.0	0.69	0.30	20.0	422.3	Zoccali et al. (2003), 10 Gyr	Zoccali et al. (2003) + 0.5 dex	1 657	-9.0
7	8.60	2.67	96.6	0.68	0.30	14.4	427.3	Zoccali et al. (2003), 10 Gyr	Zoccali et al. (2003) + 0.3 dex	1 442	-13.3
8	8.60	2.67	96.6	0.68	0.30	14.4	427.3	Zoccali et al. (2003), 9 Gyr	Zoccali et al. (2003) + 0.3 dex	1 735	-13.0
9	8.60	2.67	96.6	0.68	0.30	14.4	427.3	Zoccali et al. (2003), 9.5 Gyr	Zoccali et al. (2003) + 0.3 dex	1 593	-13.2
10	8.60	2.67	96.6	0.68	0.30	14.4	427.3	Zoccali et al. (2003), 10.5 Gyr	Zoccali et al. (2003) + 0.3 dex	1 563	-11.2
11	8.60	2.67	96.6	0.68	0.30	14.4	427.3	Zoccali et al. (2003), 11 Gyr	Zoccali et al. (2003) + 0.3 dex	1 657	-7.1
12	8.60	2.67	96.6	0.68	0.30	14.4	427.3	Zoccali et al. (2003), 11.5 Gyr	Zoccali et al. (2003) + 0.3 dex	1 518	-10.5
13	8.60	2.67	96.6	0.68	0.30	14.4	427.3	Zoccali et al. (2003), 12 Gyr	Zoccali et al. (2003) + 0.3 dex	1 851	-25.1
14	8.60	2.67	96.6	0.68	0.30	14.4	427.3	Zoccali et al. (2003), 12.5 Gyr	Zoccali et al. (2003) + 0.3 dex	2 023	-7.4
15	8.60	2.67	96.6	0.68	0.30	14.4	427.3	Zoccali et al. (2003), 13 Gyr	Zoccali et al. (2003) + 0.3 dex	2 342	-7.4
16	8.60	2.67	96.6	0.68	0.30	14.4	427.3	van Loon et al. (2003)	Zoccali et al. (2003) + 0.3 dex	3 832	-21.4
17	10.27	3.19	95.0	0.62	0.31	11.0	370.8	van Loon et al. (2003)	Zoccali et al. (2003) + 0.3 dex	1 355	-75.7
18	8.60	2.67	96.6	0.68	0.30	14.4	427.3	van Loon et al. (2003), older than 0.1 Gyr	Zoccali et al. (2003) + 0.3 dex	3 779	-21.6
19	9.00	2.67	95.3	0.68	0.28	8.7	424.8	van Loon et al. (2003), older than 0.1 Gyr	Zoccali et al. (2003) + 0.3 dex	1 768	-18.9
20	8.60	2.67	96.6	0.68	0.30	14.4	427.3	van Loon et al. (2003), older than 1.0 Gyr	Zoccali et al. (2003) + 0.3 dex	4 430	-14.6
21	8.70	2.57	96.4	0.68	0.28	15.7	423.7	van Loon et al. (2003), older than 1.0 Gyr	Zoccali et al. (2003) + 0.3 dex	3 222	-13.1
22	8.60	2.67	96.6	0.68	0.30	24.8	427.3	Zoccali et al. (2003), 10 Gyr	Zoccali et al. (2003) + 0.3 dex	1 550	-7.3

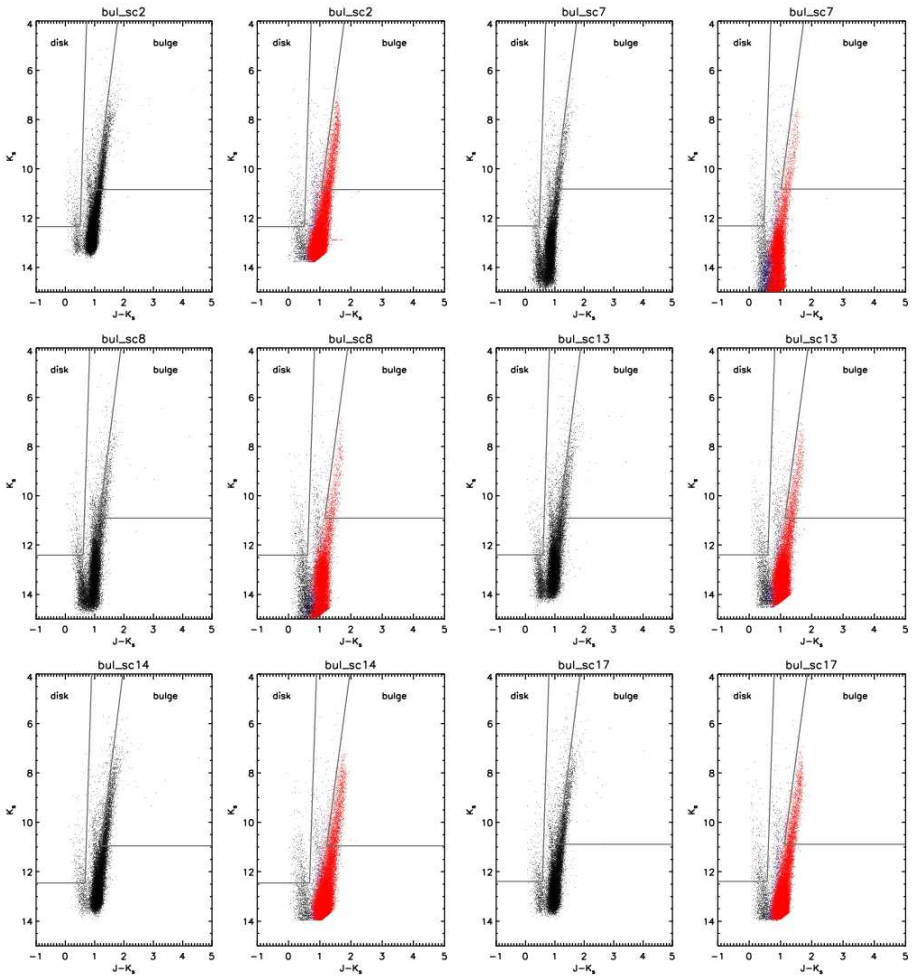

Figure 7.11: $J-K_s$ vs K_s CMD for all selected fields. For each field there are two panels given, the left panel give the 2MASS observations, the right panel is the model with $R_0 = 8.60$ kpc, $a_m = 2.67$ kpc, $a_0 = 96.6$ pc, $\eta = 0.68$, $\zeta = 0.30$, $\phi = 14.4°$, and $f_0 = 427.3$. The black dots in the model (right panel) are stars that originate from the disk, the dark blue dots originate from the halo and the red dots are bulge stars. This colour code will be used in all figures of this type. The light grey lines indicate the boxes used to compute the model with the observations.

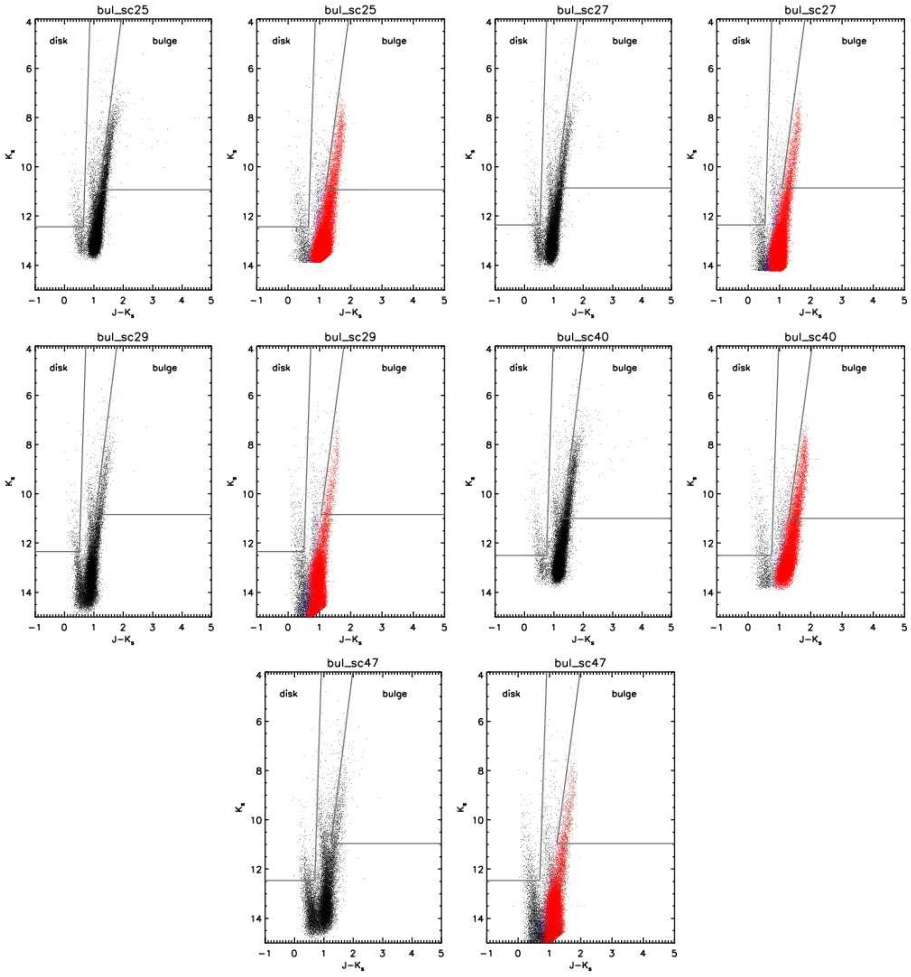

Figure 7.12: $J - K_s$ vs K_s CMD for all selected fields – continued.

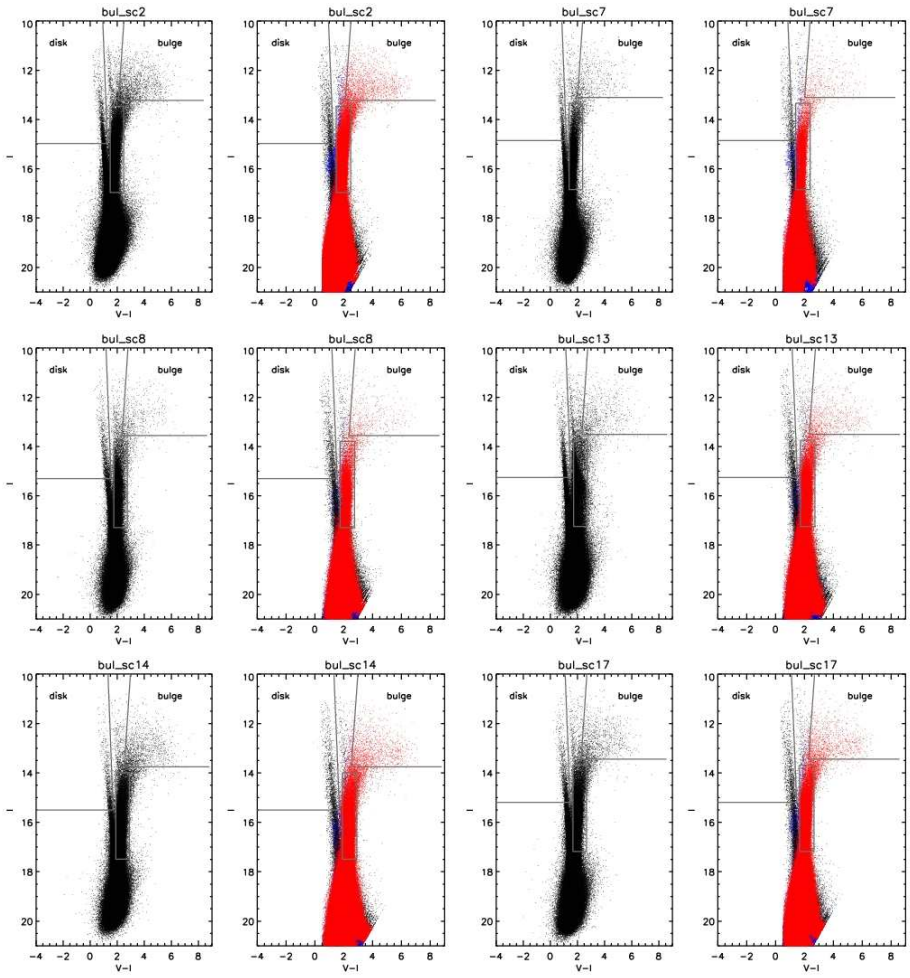

Figure 7.13: $V-I$ vs I CMD for all selected fields. For each field there are two panels given, the left panel give the OGLE observations, the right panel is the model with $R_0 = 8.60$ kpc, $a_m = 2.67$ kpc, $a_0 = 96.6$ pc, $\eta = 0.68$, $\zeta = 0.30$, $\phi = 14.4°$, and $f_0 = 427.3$. The black dots in the model (right panel) are stars that originate from the disk, the dark blue dots originate from the halo and the red dots are bulge stars. This colour code will be used in all figures of this type. The light grey lines indicate the boxes used to compute the model with the observations.

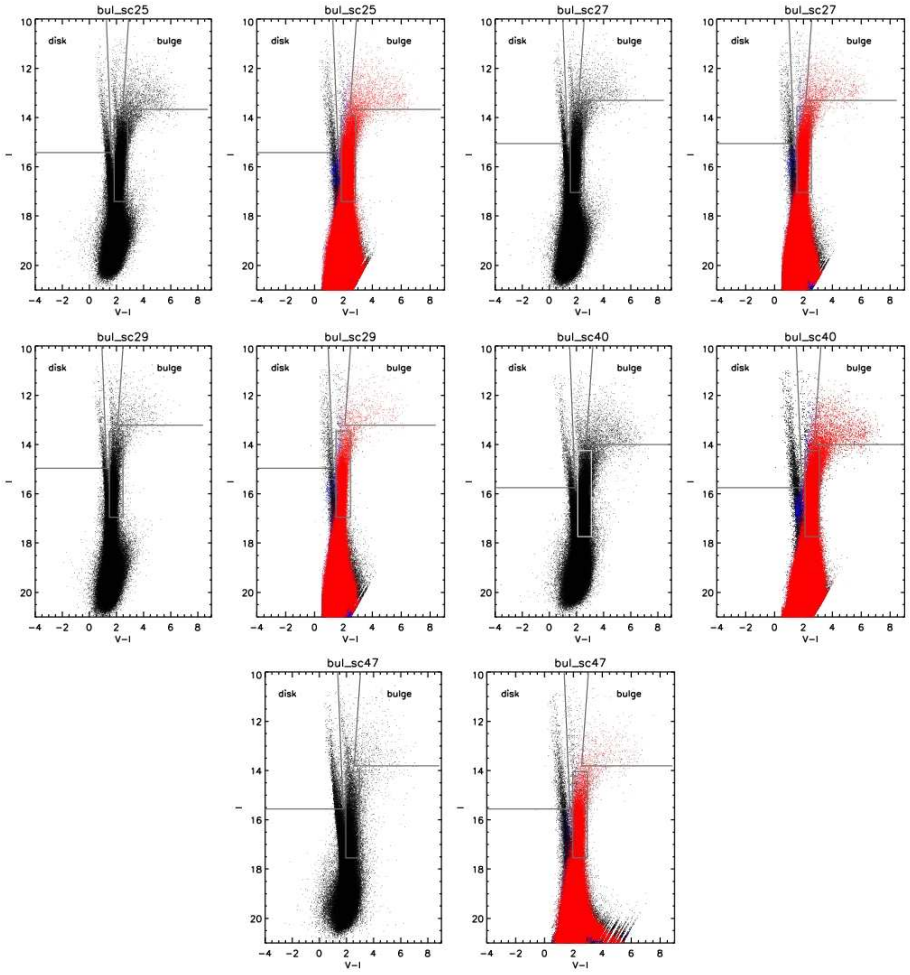

Figure 7.14: $V - I$ vs I CMD for all selected fields – continued.

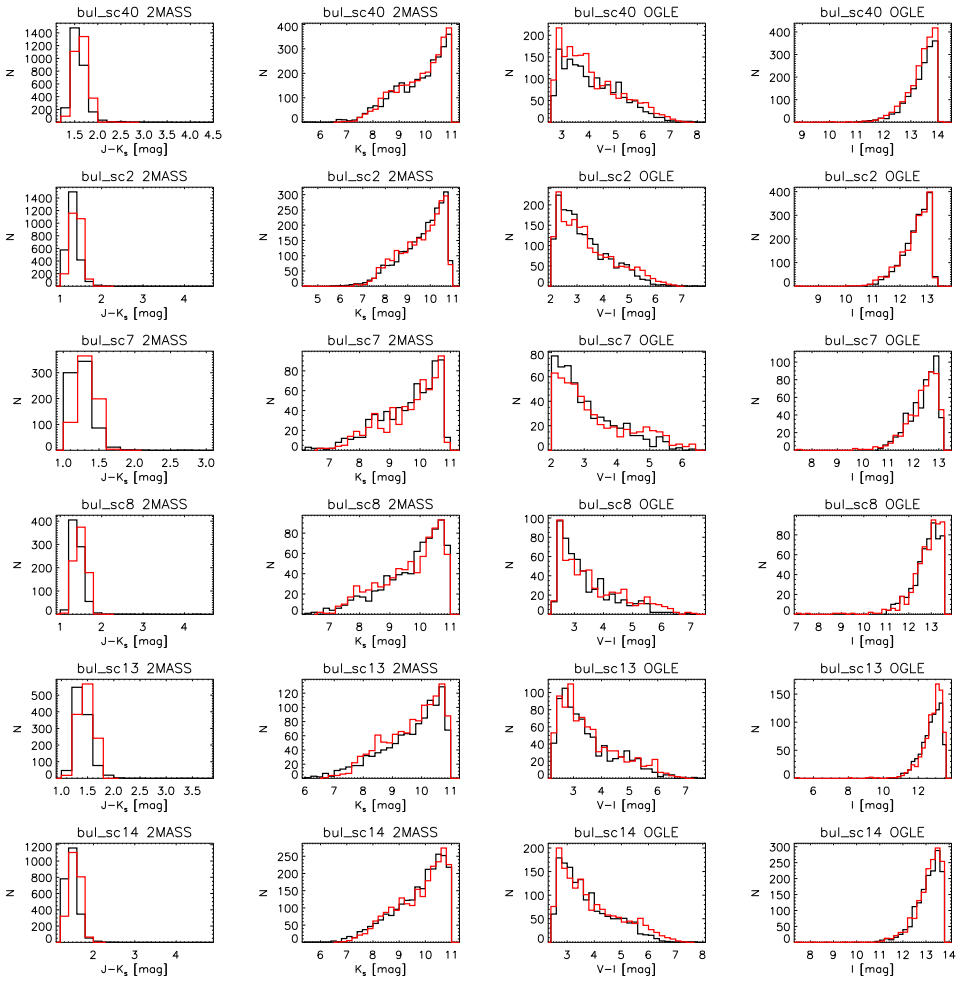

Figure 7.15: Histograms showing the distribution of selected bulge stars for all the modelled fields. The black line is the histogram for the observational data, the red line represents the model. For each field there are two panels, the panel on the left shows the 2MASS data and the panel on the right shows the OGLE data. The model has the following parameters: $R_0 = 8.60$ kpc, $a_m = 2.67$ kpc, $a_0 = 96.6$ pc, $\eta = 0.68$, $\zeta = 0.30$, $\phi = 14.4°$, and $f_0 = 427.3$. The star formation rate is a 10 Gyr burst and the metallicity distribution is based on Zoccali et al. (2003) but shifted with 0.3 dex.

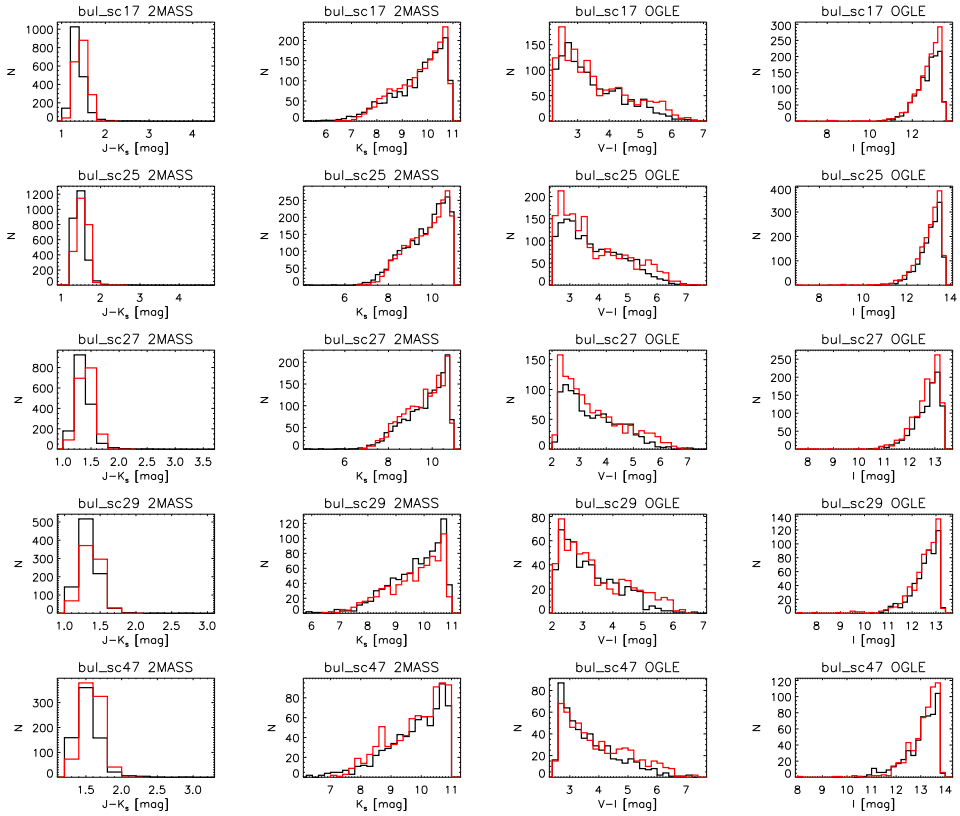

Figure 7.16: Histograms showing the distribution of selected bulge stars for all the modelled fields – continued.

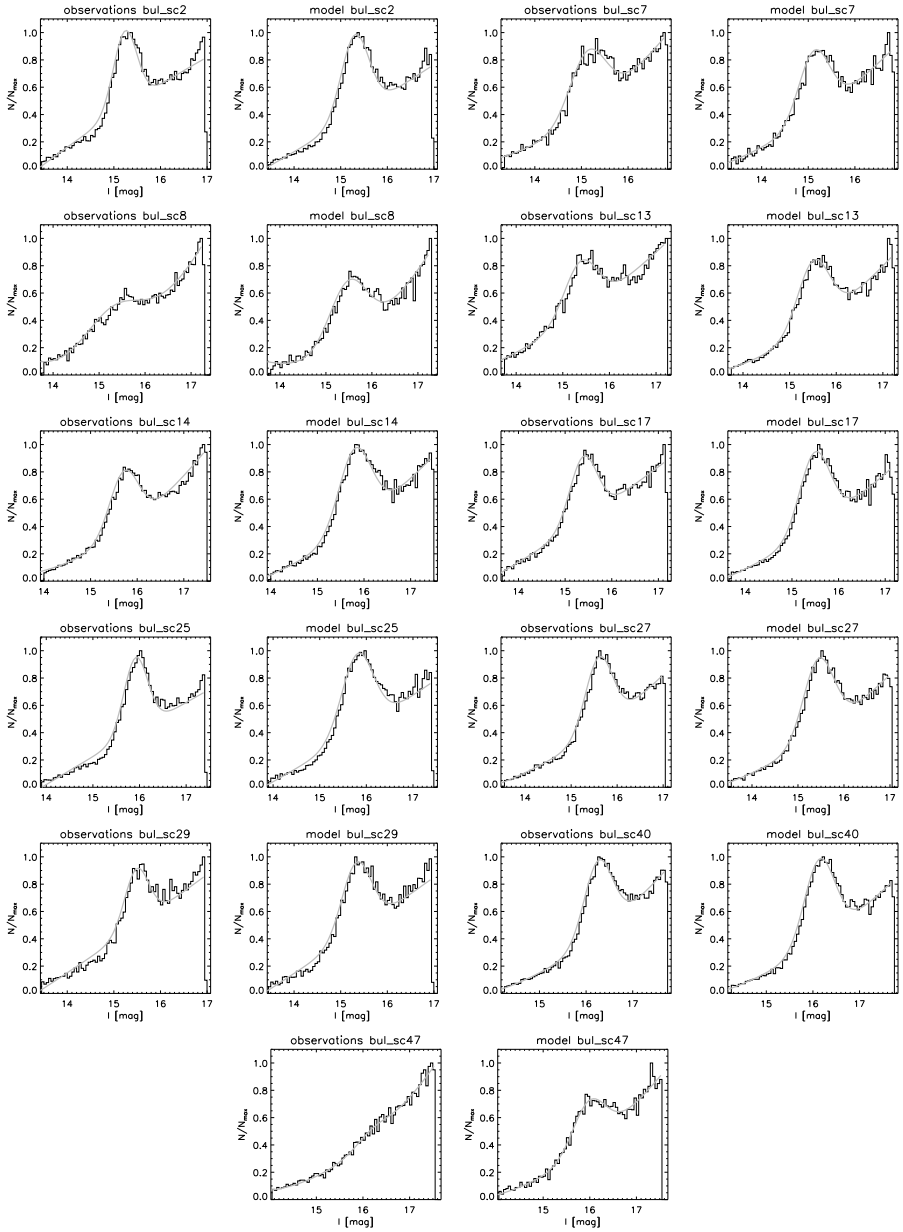

Figure 7.17: Fits to the red clump stars using the method described by Stanek and Garnavich (1998). The black histogram are the stars selected from the "red clump box" in the $V - I$ vs I CMD and the grey line is the Gaussian fit with underlying second degree polynomial.

CHAPTER 8

Conclusions and prospects

In this thesis we studied several aspects related to the final stages of stellar evolution of low-mass stars. We studied OH/IR stars in the Galactic Centre, investigated the late stages of evolution of low-mass stars located in the Galactic Bulge, as well did we trace the stellar content in, and the geometry of the Galactic Bulge. In this final chapter, we want to summarise the main conclusions presented in this thesis and propose possible research plans for the near future.

8.1 OH/IR stars in the Galactic Centre

The OH/IR stars located in the Galactic Centre are believed to originate from two different populations. The first population has a low expansion velocity, a larger spread in latitude, and a larger velocity dispersion with respect to the Galactic rotation than the OH/IR stars in the second group with higher expansion velocities. The stars in the first group with the lowest expansion velocities are believed to be older objects, while the stars in the second group may have a more recent formation history. Based on this assumption, it is expected that the stars in the first group, the "older" objects, have lower luminosities than the stars in the second group. This could not be confirmed in earlier studies, the differences in the luminosities between the two groups, if these differences exist, are not very big. Another expected difference between these two groups of stars is the gas-to-dust ratio in the expansion velocities which is correlated to the metallicity of the star. It is in this context that we discussed in Chapter 2 our attempt to study the metallicity of this sample of OH/IR stars based on medium-resolution near-IR spectroscopy.

Due to several reasons (the dust surrounding the OH/IR stars, the water content of these objects, and their variability) we were unable to determine the metallicity based on the obtained medium resolution near-IR spectroscopy. We showed that because of the mentioned

physical effects the equivalent line widths of the molecules and atoms in the near-IR are altered. Determining the metallicity of these objects in order to look for an additional distinction between these two groups of OH/IR stars, might in near feature still be hard. High-resolution spectroscopy of these objects is needed to determine accurate metallicity estimates. Because of the variability of these objects, dynamical model atmospheres will be needed. These models account for the effects induced by the variability of the object when calculating a model spectrum. Since these models are only recently being developed, it will take a while until the general astronomical community will have access to these models, as well as the models converge in a short time span.

8.2 The oxygen-rich dust condensation sequence along the AGB

In Chapters 3 to 6 we studied a sample of Galactic Bulge AGB stars in order to obtain more insight on the dust condensation sequence along the AGB. Chapter 3 is dedicated to the analysis of the dust around these stars based on Spitzer-IRS observations. Chapter 4 studies ground based optical and near-IR spectroscopy and near-IR photometry to gather more information about the central star. In Chapter 5 we study the crystalline material around the OH/IR stars in the sample and in Chapter 6 we look for correlations between the characteristic parameters for the central star and the dust content.

8.2.1 Stellar characteristics and variability in function of $(K_s - [15])_0$

Using the ground based observations for this sample of GB AGB stars, we obtained information on the characteristics and the variability of the central star. We showed that the AGB stars in our sample have a spectral type of M4 or later. The 6 bluest stars in $(K_s - [15])_0$ were the only objects in which a Ca-triplet could be detected, indicating the early spectral type of these objects. We also derived a metallicity distribution for the objects in this sample and found it to be consistent with recent literature studying the metallicity in the Galactic Bulge. Based on an estimate of the amount of water we found that the amount of water increases with decreasing effective temperature. The Mira variables in our sample have the largest amounts of water. We also showed correlations between the pulsation amplitude and period and the $(K_s - [15])_0$ colour.

We could not derive periods for the objects with the smallest amplitudes (the bluest $(K_s - [15])_0$ colours) and could therefore not place these objects in the PL-diagram. Therefore it might be interesting to monitor these objects more frequently as the expected periods for these objects is about 30 days.

8.2.2 Dust characteristics

Spitzer-IRS spectra were obtained for the AGB stars in our sample, selected based on the $(K_s - [15])_0$ colour, a mass-loss indicator (Ojha et al. 2003; Blommaert et al. 2006). For the naked stars in our sample we showed that there exists a large spread in $(K_s - [15])_0$ colour, although these objects are expected to have similar mass-loss rates ($\sim 10^{-8}$M$_\odot$/yr). A difference in colour temperature, which could be induced by the presence of a water layer, is able to explain this observed spread in $(K_s - [15])_0$.

For the objects showing a dust contribution (except the OH/IR stars) dust spectra were created and analysed. To study the characteristics of the dust composition and its expected relation to the mass-loss rate, several parameters were determined. The normalised dust luminosity was calculated and we searched the dust spectra for indications of alumina, amorphous silicates, a 13, and a 19.5 μm feature. Based on the 10 μm complexes of these dust spectra, SE indexes have been derived as well as an estimate of the relative abundance of alumina with respect to amorphous silicates.

Only one object seems to be dominated by alumina, most of the other objects have a relative abundance of alumina with respect to amorphous silicates between 0.1 and 0.4. Only minor indications can be found for a decreasing trend for the relative amount of alumina with increasing $(K_s - [15])_0$, a mass-loss indicator. This is reflected in the derived SE indexes. Very few objects have small or high SE indexes, the majority has an SE index of 4 or 5. The SE index correlates very well with the relative abundance of alumina with respect to amorphous silicates.

Based on the analysis of the dust spectra, we concluded that no clear trend between $(K_s - [15])_0$, a mass-loss indicator, and the dust composition can be found. This indicates that although $(K_s - [15])_0$ is a mass-loss indicator, it is most likely not precise enough to study the oxygen-rich dust condensation sequence. The large spread shown in the different figures of Chapter 3 is however not expected to disappear completely if independent estimates for the mass-loss rates are used. This indicates that the oxygen-rich dust condensation sequence as it is derived at this moment is not sufficient to explain dust formation around oxygen-rich AGB stars. Detailed radiative transfer modelling of these objects is therefore required to obtain mass-loss estimates and to derive a more detailed dust composition. These mass-loss estimates can then be used to rearrange the dust spectra in order to evaluate the obtained dust compositions with respect to the oxygen-rich dust condensation sequence.

8.2.3 Crystalline material around OH/IR stars

We studied the OH/IR stars in this sample in function of their crystalline material very clearly detected throughout the entire Spitzer-IRS spectrum. Based on the crystalline forsterite feature at 11.3 μm we showed that the OH/IR stars in this sample relatively produce equal amounts of crystalline material. When measuring the relative strength of the 33.6 μm forsterite feature, this revealed that as the mass-loss rate increases the relative strength of this feature decreases. With a radiative transfer model only using amorphous silicate, we showed that

this decreasing trend in relative strength with increasing mass-loss rate, is related to optical thickness effects. For the objects with the highest mass-loss rates, the dust shells are still optically thick at these wavelengths.

This collection high signal to noise Spitzer-IRS spectra for 8 OH/IR stars located in the GB, is an ideal homogenous sample. With this sample detailed radiative transfer modelling, not only including amorphous silicates, but also crystalline material, metallic iron, and other dust species, will reveal more information on the detailed composition of the dust surrounding these objects. It might help understanding why we do not detect crystalline material in AGB stars with lower mass-loss rates and it might even reveal new insights on the geometry of the dust around OH/IR stars.

8.2.4 The oxygen-rich dust condensation sequence

Using a period-luminosity diagram, this sample can also be analysed in terms of variability. We showed that all the objects below the tip of the RGB are naked stars, while the objects above the tip of the RGB show a dust contribution. Based the position of the objects in the PL-diagram, a clear one-to-one relation with the dust composition can not be found, although there exists clear indications for such a trend. The objects with the highest relative amounts of alumina dust are located just above the tip of the RGB. These objects show also a 13 μm feature and possibly also a 19.5 μm feature. All the other objects on sequences B and C show a mixture of alumina and amorphous silicate dust and also a 13 μm feature. The objects with the reddest $(J-K)_0$ colour only show indications of amorphous silicate dust.

A principal component analysis on the derived parameters in Chapters 3 and 4 showed that the variance between the objects can be described in terms of three principal components. The first principal component reflects the mass-loss rate, the second the dust composition and the characteristics of the central star, it is not clear which parameter(s) the third principal component traces. We were also able to reduce the dimensionality of the problem from 11 to 7 dimensions.

Detailed radiative transfer modelling of the dust spectra is also needed to continue this research project. This will enable us to search for a relation between the evolution on the AGB based on the position of the object in the PL-diagram and a more detailed dust composition then derived in this work.

8.3 Stellar populations in the Galactic Bulge

In Chapter 7 we aimed at studying the characteristics, the stellar populations, and the metallicity distribution in the Galactic Bulge using the galaxy model TRILEGAL. By comparing CMDs based on 2MASS and OGLE-II observations with calculated CMDs, we search for a model that explains the observations best. The found model has a distance to the GC of $8.6\pm^{0.15}_{0.11}$ kpc, major axis of the bar of $1 : 0.68\pm^{0.01}_{0.07} : 0.30\pm^{0.1}_{0.1}$, and an angle between the bar

and the Sun-Centre line of $14.4° \pm^{5.5}_{10.3}$. The population of the GB is mainly an old population which formed about 10 Gyr ago in a star burst. We could not improve our models significantly by adding an intermediate and/or young population, which does not imply that there does not exist such a population. The found metallicity distribution is slightly more metal rich than the metallicity distribution in Zoccali et al. (2003) based on photometry, but consistent with metallicity distributions derived based on spectroscopic results (see e.g. McWilliam and Rich 1994; Sadler et al. 1996; Ramírez et al. 2000).

Using the OGLE-II *I*-band photometry, we also compared the observed and the modelled red clump stars. Based on this comparison, we could derive an expected magnitude for the objects of $M_I^{\mathrm{RC}} = -0.170 \pm^{0.069}_{0.066}$, consistent with values in recent literature.

Based on the calibration of the parameters for the geometry, the stellar population, and metallicity distribution performed in this thesis with respect to the 11 selected fields in the Galactic Bulge using OGLE-II and 2MASS photometry, we are now ready to compare the results of this model with other observations, such as e.g. the ISOGAL catalogue. Studying the stellar content of the Galactic Bulge at different wavelengths will allow us to trace different populations and in this way we might be able to also detect an intermediate age population as well as obtain more insight on the formation history of the bulge.

Nederlandse samenvatting

Sterpopulaties en stofvorming in de binnenste delen van de Melkweg

Hoewel we het maar zelden beseffen doet ook het universum aan “recyclage”. Sterren worden geboren uit wolken en doorlopen verschillende levensfases. Tijdens één van deze levensfases produceren sommige sterren grote hoeveelheden stof die terug de interstellaire ruimte ingeblazen worden, terwijl anderen ontploffen als supernova en op deze manier het interstellair medium verrijken. Niet alleen stof verrijkt het interstellair medium, ook het gas wordt verrijkt door bijvoorbeeld de sterrenwinden van massieve sterren. Wanneer nu een nieuwe generatie sterren geboren wordt, zal dat gebeuren met onder andere de restanten van de vorige generatie. Deze “levenscyclus” wordt in de loop der tijd doorlopen en opnieuw doorlopen…

Deze thesis bestudeert sterpopulaties en stofvorming in de binnenste delen van de Melkweg. In hoofdstuk 2 bestuderen we OH/IR sterren in het centrum van de Melkweg. Hoofdstukken 3 tot 6 zijn gewijd aan een steekproef AGB sterren die zich in de bulge bevinden. Van deze sterren zullen we in hoofdstuk 3 het stof bestuderen, in hoofdstuk 4 eigenschappen die de centrale ster karakteriseren en de variabiliteit, in hoofdstuk 5 zullen we het kristallijn stof rond OH/IR sterren bestuderen en in hoofdstuk 6 zullen we al de gevonden stofeigenschappen bestuderen in functie van de karakteristieke eigenschappen van de ster. In hoofdstuk 7 zullen we door middel van een “galaxymodel” de geometrie van en de sterpopulatie in de bulge bestuderen. Deze hoofdstukken zullen samen met de belangrijkste besluiten in de verschillende secties van deze samenvatting aan bod komen.

N.1 Inleiding

In deze sectie wordt een korte inleiding gegeven over de relevante onderwerpen die in deze thesis aan bod komen (gebaseerd op Habing en Olofsson 2003, tenzij anders vermeld).

N.1.1 Sterpopulaties

"Sterpopulaties" is een van de sleutelwoorden in de titel van deze thesis. Een sterpopulatie is een groep sterren die op een of andere manier samenhoort. De meest gebruikte definitie van "sterren die samenhoren" is die van een populatie die bestaat uit sterren met dezelfde massa, die allemaal ongeveer tegelijk geboren zijn en die dus eenzelfde leeftijd hebben en een vergelijkbare chemische samenstelling.
Een andere definitie van sterpopulaties heeft het over de ruimtelijke verdeling van deze sterren. Als we de ruimtelijke verdeling van al de sterren opdelen in blokken die we bij elkaar kunnen optellen om al de sterren in een bepaalde omgeving te beschrijven, dan kunnen deze "blokken" ook als een sterpopulatie beschouwd worden.

N.1.2 AGB sterren

Een belangrijk deel van deze thesis is gewijd aan AGB sterren. In de volgende secties zullen we dan ook iets meer in detail beschrijven wat een AGB ster is en hoe haar evolutie verloopt.

N.1.2.1 Pre-AGB evolutie

De verschillende levensfases die een ster doorloopt zijn afhankelijk van haar initiële massa. Figuur 1.1 toont twee Hertzsprung-Russel (HR) diagrammen. Afhankelijk van de temperatuur en lichtkracht van een ster krijgt deze een plaats in het diagram. Het linkse HR diagram toont enkele evolutiesporen afhankelijk van de initiële massa van de ster.

In deze thesis worden hoofdzakelijk lage-massa sterren bestudeerd. Ze hebben massa's vergelijkbaar aan die van onze Zon. De evolutie hier beschreven, is dus ook geldig voor onze Zon. Onze Zon bevindt zich momenteel op de "hoofdreeks" (*Main Sequence: MS*). In deze fase van haar leven zet de ster waterstof (H) om in helium (He). Het rechterpaneel in Figuur 1.1 toont het evolutiespoor voor deze laag-massieve sterren.
Wanneer alle waterstof in de kern opgebrand is, verlaat de ster de hoofdreeks. De kern produceert geen energie meer om de zwaartekracht tegen te werken en de ster trekt samen. Hierdoor stijgt de temperatuur en op een gegeven moment is de temperatuur hoog genoeg om in een schil rond de kern waterstof om te zetten in helium. Nu is de ster een rode reus en bevindt ze zich op de rode reuzentak (*Red Giant Branch: RGB*).
Door de waterstofschilverbranding stijgt de temperatuur in de binnenste delen van de ster nog steeds. Op een gegeven moment is de temperatuur in de kern hoog genoeg om nu ook de helium-kern om te zetten in zuurstof en koolstof. Wanneer dit gebeurt is de RGB fase voorbij en bevindt de ster zich op de horizontale tak (*Horizontal Branch: HB*).

Wanneer in de kern alle helium opgebruikt is, trekt de ster weer samen waardoor de temperatuur stijgt. Door deze temperatuursverhoging is het weer mogelijk om in een schil waterstof te gaan verbranden. De waterstofschilverbranding is op dit moment de grootste energieleverancier van de ster. De HB fase is ten einde en de ster bevindt zich nu op de asymptotische reuzentak (*Asymptotic Giant Branch: AGB*).

N.1.2.2 Structuur en evolutie van een AGB ster

Een AGB ster kan ruwweg in vier delen verdeeld worden: een kleine, heel hete en dichte kern; een grote, hete en minder dichte stellaire enveloppe; een ijle warme atmosfeer en een heel grote, heel ijle en koele circumstellaire enveloppe (zie ook Figuur 1.2).

In het begin van de AGB fase, de vroege-AGB (*Early-AGB: E-AGB*), zorgt zoals reeds vermeld de waterstofschilverbranding voor de meeste energie. De lichtkracht van de ster en temperatuur van de kern blijven toenemen. Op een gegeven ogenblik is de temperatuur hoog genoeg om ook aan heliumschilverbranding te doen. Op dit ogenblik zijn er dus twee schillen die voor energie zorgen: de waterstofschil en de heliumschil. Door de grote hoeveelheid energie die op deze manier vrijkomt wordt de heliumschilverbranding onstabiel, waardoor helium heel snel wordt omgezet in koolstof. Dit veroorzaakt een heliumflits ook wel een thermische puls genoemd. De ster is nu in de zogenoemde thermisch pulserende AGB fase (*Thermally pulsing AGB phase: TP-AGB*).

De steratmosfeer is zeer gevoelig voor deze fysische processen die dieper in de ster gebeuren. Door de variabiliteit van de ster kunnen schokgolven onstaan waardoor korrelvorming kan optreden. Een ander effect van deze schokken is massaverlies. In het begin van de AGB fase is dit nog heel laag (10^{-8} $M_\odot$/yr, zonsmassa's per jaar), maar aan het einde van de AGB fase kan dit oplopen tot 10^{-4} $M_\odot$/yr.

Door het massaverlies wordt er een circumstellaire enveloppe (CSE) van ontsnappend gas en stofdeeltjes gevormd. De moleculen bevinden zich dicht bij de ster in lagen, waarvan de grootste een water laag en een CO laag zijn. De stofdeeltjes daarentegen bevinden zich verder weg van de ster waar de temperatuur laag genoeg is opdat ze zouden kunnen blijven bestaan. Stof kan gevormd worden vanaf ongeveer 1800 K (ongeveer 1530°C). Het soort stof dat gevormd wordt is afhankelijk van de samenstelling van de ster, zuurstofrijk of koolstofrijk. In deze thesis bestuderen we zuurstofrijke sterren en de stofvorming rond deze sterren zal dan ook vnl. zuurstofrijk zijn.

Figuur 1.6 toont de verschillende karakteriserende parameters voor AGB sterren. Bovenaan de figuur zien we de effectieve temperatuur, daarna de lichtkracht relatief aan de zonslichtkracht, de periode in dagen, het massaverlies (in grootheden van 10^{-6} $M_\odot$/yr) en de totale massa. Deze figuur toont hoe de grootheden veranderen tijdens de AGB evolutie fase. De effectieve temperatuur daalt naarmate de tijd verstrijkt en de AGB ster evolueert, maar de andere grootheden nemen toe. In het begin van de AGB fase gebeurt dit allemaal vrij continue, maar wanneer de TP-AGB fase aanbreekt, zien we ten gevolge van de thermische pulsen plotse en grote veranderingen in deze grootheden. Op het einde van de AGB fase verliest de

ster een significant deel van haar massa ten gevolge van de zogenaamde “superwind” fase. Tijdens deze periode zijn de massa-verliezen heel hoog ($\sim 10^{-4} M_{\odot}$/yr).

Op het einde van de AGB fase domineert het massaverlies de evolutie van de ster. De straal wordt steeds kleiner en hierdoor verplaatst de ster zich in het HR diagram naar links. De AGB fase is ten einde en de ster wordt nu een post-AGB ster genoemd. Bij sommige post-AGB sterren wordt de materie die zich nog in de omgeving van de ster bevindt, geïoniseerd. Hierdoor wordt dit materiaal zichtbaar. Zo’n object wordt een planetaire nevel (*Planetary Nebula: PN*) genoemd.

N.1.2.3 Variabiliteit

AGB sterren worden ook vaak geclassificeerd op basis van hun variabiliteit. Vanuit historisch perspectief worden ze vaak in vier klassen opgedeeld: de onregelmatig pulserende, de semi-regelmatig pulserende, de Mira variabelen en de door stof omhulde variabelen (*dust-enshrouded variables*).

Op basis van de variabiliteit wordt voor AGB sterren vaak een periode-lichtkracht diagram gemaakt (zie Figuur 1.4). Op dit diagram kunnen we verschillende parallelle reeksen ontdekken die belangrijk zijn in dit werk. Op reeks A, B en het onderste deel van reeks C bevinden zich de semi-regelmatig pulserende variabelen. De Mira variabelen bevinden zich op reeks C. De oorsprong van de sterren op reeks D is nog niet helemaal begrepen.

N.1.2.4 Stofvorming en de zuurstofrijke stofcondensatiereeks

Zoals reeds vermeld verliezen AGB sterren gedurende deze fase in hun evolutie grote hoeveelheden van hun massa door middel van een trage massieve sterrenwind. In deze wind kan stof gevormd worden. De zuurstofrijke stofcondensatiereeks beschrijft op basis van theoretische studies de volgorde waarin dit stof gevormd kan worden. We zullen de condensatiereeks beschrijven te vertrekken van aluminium en silicaat (SiO) (gebaseerd op Tielens et al. 1997; Cami 2002).

Aluminium (Al) is in zuurstofrijke AGB sterren een relatief veel aanwezig element, daarom is het belangrijk om de Al condensatiereeks te bekijken voor zuurstofrijke omgevingen. Corundum (α-Al_2O_3, de kristalijne vorm van aluminiumoxyde, ook wel alumina genoemd – Al_2O_3) is het eerste stofdeeltje dat volgens de zuurstofrijke condensatiereeks gevormd wordt en dit rond ongeveer 1760 K. Wanneer corundum afkoelt, reageert het met SiO, Ca en Mg in de gasfase en vormt meliliet (een Ca-Na-Al-Mg-Fe-silicaat), eerst in de vorm van puur gehleniet ($Ca_2Al_2SiO_7$). Later wordt dit gehleniet gedeeltelijk omgevormd in akermaniet ($Ca_2MgSi_2O_7$) rond 1550 K, alumina (boven 1510 K) en spinel ($MgAl_2O_4$) onder 1510 K. Rond temperaturen van 1450 K wordt uit meliliet diopsiet ($CaMgSi_2O_6$) gevormd en spinel. Deze laatste twee reageren dan weer tot anorthiet ($CaAl_2Si_2O_8$).

De meeste mineralen die silicium (Si) bevatten worden gevormd via een andere condensatiereeks. Het meeste silicaat condenseert eerst rond 1440 K in forsteriet (Mg_2SiO_4). Forsteriet behoort tot de familie van de olivijnen ($a_{2x}b_{2-2x}SiO_4$ met a en b: Mg, Fe, Mn, Co of Zn). Het overtollig SiO wordt dan gebruikt om forsteriet om te zetten in enstatiet ($MgSiO_3$, een pyroxeen) rond 1350 K.

Waar ijzer (Fe) in deze reeksen thuishoort is op dit ogenblik nog niet duidelijk. Hoogstwaarschijnlijk word metallisch ijzer gevormd, maar Fe kan ook gebruikt worden om forsteriet en fayaliet (Fe_2SiO_4) te vormen rond 1100 K. Daarnaast worden magnesium-ijzer-oxides vaak waargenomen in AGB sterren, vnl. $Mg_{0.1}Fe_{0.9}O$, maar deze molecule heeft geen plaats in de condensatiereeks.

Zuurstofrijke AGB sterren vertonen veel verschillende soorten stof. Bijna al deze stofsoorten komen voor in de zojuist beschreven condensatiereeksen. AGB sterren die per jaar grote hoeveelheden massa verliezen, vertonen stofspectra gedomineerd door amorf silicaat en ook kristallijne olivijnen en pyroxenen kunnen erin aangetroffen worden. De stofspectra van AGB sterren die niet veel massa verliezen per jaar, vertonen voornamelijk alumina en magnesium-ijzer-oxides. Welk stof gevormd wordt is afhankelijk van de dichtheid van de deeltjes en daardoor dus ook van de grootte van het massaverlies. De “freeze out” is de term die aanduidt dat de dichtheid in het stofvormingsgebied te laag is zodat de condensatie van een volgende stofsoort in de condensatiereeks niet meer kan plaatsvinden. Op dit ogenblik stopt dus de condensatie van stofsoorten in een andere stofsoort. Wanneer we een verzameling AGB sterren bestuderen met verschillende massaverliezen, zien we dus deze “freeze out” voorkomen op verschillende tijdstippen en kunnen we dus bestuderen of het stof gevormd wordt in de volgorde die de stofvormingsreeksen aangeven.

N.1.2.5 OH/IR sterren

OH/IR sterren zijn zuurstofrijke-AGB sterren aan het einde van hun levensfase op de AGB. Ze verliezen grote hoeveelheden massa en daardoor wordt het stof in de circumstellaire enveloppe optisch dik. De ster kan daardoor in het optisch golflengtebereik niet meer gedetecteerd worden. OH/IR sterren worden dus bestudeerd op langere golflengten zoals in het infrarode- of radiogebied van het elektromagnetisch spectrum.

OH/IR sterren zijn niet alleen AGB sterren aan het einde van hun AGB fase, ze behoren ook tot één van de subklasses van de masers. Doordat ze OH maseren zijn ze makkelijk identificieerbaar op radio golflengtes (de OH maser kan o.a. waargenomen worden op 1612 MHz). Wanneer grote gebieden aan de hemel afgezocht worden op zoek naar OH/IR sterren, gebeurt dat dan ook het vaakst via radiotelescopen.
Masering is een vorm van gestimuleerde emissie: wanneer een foton geabsorbeerd wordt door een molecule, komt deze molecule in een hoger energie stadium, de molecule wordt geëxiteerd. Wanneer nu een foton in de buurt van de al geëxiteerde molecule komt, kan deze passerende foton een de-exitatie stimuleren. De molecule verliest dan zijn extra energie in de vorm van een foton. Dit foton heeft dezelfde energie en richting als het foton dat de de-extitatie stimuleerde. In normale omgevingen is dit een uitzonderlijk fenomeen. Wanneer

er echter sprake is van "populatie-inversie" is het een frequent voorkomend fenomeen. We spreken van populatie-inversie wanneer er zich meer moleculen in een hoger energieniveau bevinden dan in een lager energieniveau.

Het sterkste masering effect kunnen we waarnemen wanneer we het grootste aantal hoeveelheden deeltjes met dezelfde snelheid zien bewegen. In praktijk komt dit dus voor wanneer onze gezichtslijn door de centrale ster gaat, dan zien we een maximaal aantal deeltjes met eenzelfde snelheid richting ons bewegen en een maximaal aantal deeltjes met dezelfde snelheid van ons weg bewegen (zie ook Figuur 1.7). De deeltjes die met deze gelijke snelheid, maar in tegenovergestelde richting bewegen, zorgen voor het typische dubbel gepiekte snelheidsprofiel bij maser objecten. Het snelheidsverschil tussen deze twee pieken ΔV is een indicator van de initiële massa van de ster en ook van de gasexpansiesnelheid ($v_{\rm exp}$).

N.1.3 De Melkweg

Onze Melkweg is een spiraalvormig melkwegstelsel en kan in vier delen opgesplitst worden: de schijf, een centrale verdikking (de *bulge*), de halo en het centrum. Figuur 1.8 toont een samengestelde figuur van onze Melkweg in het nabij-infrarood (nabij-IR). Op de figuur kunnen we duidelijk het vlak of de schijf herkennen en in het midden de bulge met de halo.

Vermits we deel uitmaken van ons eigen melkwegstelsel kunnen we geen beelden maken van de Melkweg als geheel. Maar toch beschikken we, doordat we er zelf deel van zijn, over drie-dimensionele informatie. Dit soort informatie kunnen we voor andere melkwegstelsels enkel indirect verkrijgen.

Deze thesis bestudeert sterren in de binnenste delen van de Melkweg, in de bulge en in het centrum. Door de grote hoeveelheid sterren die zich in de binnenste delen van de Melkweg bevinden en omdat we van deze sterren kunnen veronderstellen dat ze zich ongeveer even ver van ons bevinden, is dit gedeelte van onze Melkweg een heel interessante omgeving om te bestuderen. Maar er zijn ook nadelen aan, net door het grote aantal sterren die zich hier bevinden is het vaak moeilijk om de sterren te identificeren die men wil observeren. Daarnaast bevindt er zich ook heel veel stof in deze gebieden wat voor verroding van de sterren zorgt. Gelukkig zijn er ook een aantal gebieden waar deze verroding kleiner is. Drie van deze gebieden werden geselecteerd door Baade: het *Sgr I-venster*, het *Sgr II-venster* en het *NGC 6522-venster*. Dit laatste wordt ook vaak *Baade's venster* genoemd.

In de binnenste regionen van de Melkweg kunnen we ook heel wat substructuren ontdekken. Figuur 1.9 toont de binnenste delen van de Melkweg. Deze figuur bevat ook de bulge en een van de substructuren die we kunnen zien is die van een balk (*bar*). De laatste decennia is de discussie omtrent deze balk hevig gevoerd en bewijs ervoor komt van verschillende onafhankelijke studies. Daarom is het hoogstwaarschijnlijk dat deze balk effectief bestaat, maar over de exacte bepaling ervan (massa, vorm, de hoek die de balk maakt met de lijn tussen de Zon en het centrum van de Melkweg, leeftijd,...) is nog geen consensus bereikt. Het is zelfs nog niet duidelijk of men een onderscheid moet maken tussen de bulge en de balk: soms wordt met de bulge de balk genoemd, soms bedoelt men met de balk een substructuur

in de bulge. In deze thesis zullen we het formalisme aannemen dat beschreven is in Sevenster (1999): bulge gebruiken we voor de galactische component in de richting van $|\ell| \leq 10^\circ$ en met balk bedoelen we de substructuur in de bulge.

N.2 Nabij-IR spectroscopie van OH/IR sterren in het centrum van de Melkweg

OH/IR sterren in het centrum van de Melkweg worden opgesplitst in twee populaties. De eerste populatie zijn sterren die een lagere expansiesnelheid hebben ($v_{\rm exp} < 18.0$ km/s), een grotere spreiding in galactische breedte en een grotere snelheidsdispersie in vergelijking met de galactische rotatie dan de sterren in de tweede populatie. De sterren uit de eerste populatie worden verondersteld ouder te zijn dan de sterren uit de tweede populatie. Tot op dit moment is de expansiesnelheid de enige parameter die de twee groepen echt onderscheidt. Als de sterren uit de eerste populatie ouder zijn, verwachten we dat deze sterren een lagere metalliciteit hebben dan de sterren in de tweede populatie. Daarom zullen we in het tweede hoofdstuk van deze thesis, nabij-IR spectra bestuderen van OH/IR sterren uit deze beide groepen.

N.2.1 Metalliciteit

Ramírez et al. (2000) tonen hoe men op basis van de equivalente lijnbreedtes van Na I, Ca I en ^{12}CO(2,0) de metalliciteit kan bepalen. Deze relatie is gebaseerd op reuzen in bolvormige sterrenhopen, maar werd ook gebruikt op een groep van ISOGAL bronnen in de bulge (Schultheis et al. 2003). In dit onderzoek werd aangetoond dat de metalliciteitsverdeling van een groep sterren in de bulge op basis van deze metalliciteitsbepaling, niet significant verschilde van vroegere metalliciteitsbepalingen op basis van chemische studies (Schultheis et al. 2003).

Naast de equivalente lijnbreedtes van Na I, Ca I en ^{12}CO(2,0), werd ook een maat voor absorptie van water bepaald op basis van de kromming van de spectra rond 1.6 μm.

Naast de OH/IR sterren in de bulge, werden ook andere sterren waargenomen die reeds door andere groepen bestudeerd werden. Dit om onze spectra en de methode om de equivalente lijnbreedtes te bepalen te kunnen vergelijken. Figuren 2.3 tot 2.6 en Tabellen 2.5 tot 2.7 tonen aan dat we dezelfde resultaten bekomen als Schultheis et al. (2003), Ramírez et al. (1997), Ramírez et al. (2000) en Lançon en Wood (2000). Toch kon in heel wat spectra de equivalente lijnbreedtes van Ca I en Na I niet bepaald worden (zie ook Tabellen 2.9 tot 2.11). Figuur 2.9 is een duidelijk voorbeeld van een spectrum waarvoor Ca I en Na I niet konden gemeten worden, vnl. voor de Ca I lijn lijkt het alsof deze lijn in het continuüm verdwijnt. In de rest van dit hoofdstuk bestuderen we mogelijke verklaringen voor dit fenomeen.

N.2.2 Stof

Zoals vermeld in de inleiding van deze samenvatting, zijn OH/IR sterren AGB sterren aan het einde van deze levensfase. Ze verliezen grote hoeveelheden massa (tussen de 10^{-6} en 10^{-4} zonsmassa's per jaar) en vormen daardoor dikke stofschillen. Het is hoogstwaarschijnlijk dat dit stof het nabij-IR spectrum beïnvloedt (Tej et al. 2003).

Om de invloed van het stof op onze spectra te berekenen werd een model uitgerekend dat het radiatief transport oplost voor het stof (Groenewegen 1993). Via dit model konden we inderdaad aantonen dat wanneer het massaverlies groter wordt (dus de hoeveelheid stof neemt toe), de equivalente lijnbreedtes van zowel Na I als Ca I afnemen tot zelfs verdwijnen in het continuüm (zie Figuur 2.10).

N.2.3 Aanwezigheid van water in OH/IR sterren

Water heeft een groot aantal spectrallijnen in het bestudeerde golflengtegebied (Wallace en Hinkle 1996). Niet alleen kan het water voor een depressie van het continuüm zorgen, de invloed van het water is ook verwacht te veranderen tijdens de pulsatie periode van de OH/IR sterren (Tej et al. 2003). Figuur 2.11 toont aan dat de equivalente lijnbreedte van zowel Na I als Ca I afneemt wanneer de maat voor de hoeveelheid water toeneemt. Dit effect is het grootst voor Ca I.

N.2.4 Variabiliteit

Van de waterabsorptie wordt verwacht dat ze correleert met de fase tijdens de pulsatie periode (Bessell et al. 1996; Lançon en Wood 2000; Tej et al. 2003). Voor 41 van de 50 OH/IR sterren in onze groep, bepaalde Wood et al. (1998) een periode. Deze periodes werden gebruikt om de waarnemingen te linken aan de fase van de pulsatie (zie Figuur 2.12). Figuur 2.13 toont de correlatie zoals ze verwacht wordt, maar vermits de sterren niet allen identiek zijn, zit er heel wat spreiding op de relatie.

N.2.5 Expansiesnelheden

Desondanks we niet via de equivalente lijnbreedtes van Na I, Ca I en ^{12}CO(2,0) de metalliciteit van deze sterren kunnen bepalen, is het toch van belang om te zoeken naar verschillen tussen de twee groepen. Figuur 2.14 toont de expansiesnelheden in functie van de gemeten equivalente lijnbreedtes. Uit deze figuur en Tabel 2.8 blijkt dat de sterren uit de eerste groep (met een lagere expansiesnelheid) kleinere equivalente lijnbreedtes voor Na I hebben en een grotere spreiding op de maat voor de hoeveelheid water. Wat betreft ^{12}CO(2,0) zien we geen verschil tussen beide groepen. Een logisch gevolg van de grotere hoeveelheid water in de eerste groep is dat voor deze groep nauwelijks equivalente lijnbreedtes van Ca I gemeten konden worden.

N.2.6 Besluit

Voor de in het nabij-IR waargenomen OH/IR sterren in het Galactisch Centrum, kunnen we op basis van de equivalente lijnbreedtes van Na I, Ca I en ^{12}CO(2,0) geen conclusies trekken over de metalliciteit van deze sterren. Wel is in deze studie naar voor gekomen wat de mogelijke invloed is van stof, de aanwezigheid van water in de sterren en de variabiliteit op dit deel van het spectrum. Al deze elementen hebben gelijktijdig invloed op het nabij-IR spectrum van een ster. Vermits we voor deze sterren niet de temperatuur van het stof en het massaverlies kennen, kunnen we deze verschillende effecten niet van elkaar onderscheiden. We kunnen via deze methode geen duidelijk onderscheid vinden tussen de twee groepen OH/IR sterren.

N.3 Stofvorming in de circumstellaire envellopes van AGB sterren

Door middel van dit project willen we de stofvorming bestuderen rond zuurstofrijke AGB sterren in functie van de AGB evolutie om zo de theoretisch voorspelde zuurstorijke stofcondensatiereeksen te toetsen aan de realiteit. Door de lancering van de Spitzer Space Telescoop in 2003 kunnen we nauwkeurige waarnemen maken van AGB sterren in het infrarood op grotere afstanden dan voorheen. Vroegere studies naar de stofvorming rond zuurstofrijke AGB sterren konden enkel AGB sterren waarnemen in onze nabije omgeving, waardoor geen homogene steekproef samengesteld kon worden. Indien de steekproef echter homogeen is, moet het verschil gezien in de stofsamenstelling van de verschillende sterren te wijten zijn aan de leeftijd van de ster op de AGB en kunnen we dus op deze manier de stofvorming bestuderen in functie van de AGB evolutie.

N.3.1 Selectie en waarnemingen

De AGB sterren die we in dit onderzoeksproject bestuderen zijn geselecteerd op basis van de ISOGAL waarnemingen. ISOGAL was het tweede grootste project met de ISO satelliet (Infrared Space Observatory). ISOGAL bestudeerde velden in de galactic bulge d.m.v. waarnemingen op 7 en 15 μm. Deze waarnemingen werden dan gecombineerd met nabij-IR waarnemingen van DENIS (*I*-, *J*- en K_s-band fotometrie). Ojha et al. (2003) en ook Blommaert et al. (2006) toonden aan dat de $(K_s - [15])_0$ kleur een goede indicator is voor het massaverlies van de AGB sterren. Gebruik makend van bronnen gedetecteerd met ISOGAL kunnen we AGB sterren selecteren met massaverliezen van 10^{-8} tot 10^{-4} $M_\odot$/yr. Daarenboven toonden Groenewegen en Blommaert (2005) aan dat de Mira variabelen in de bulge dezelfde oorsprong hebben en een initiële massa van ongeveer 1.5 tot 2 $M_\odot$. Door de objecten zo te selecteren verkrijgen we een homogene steekproef AGB sterren.

Op basis van de AGB sterren die met ISOGAL gedetecteerd waren hebben we 47 AGB sterren geselecteerd op die manier dat we de volledige massaverlies evolutie tijdens de AGB kunnen bestuderen: we selecteerden sterren met heel weinig massaverlies die nog geen stof

vormen of er pas mee begonnen zijn tot sterren met grote massaverliezen zoals de OH/IR sterren.

Deze steekproef AGB sterren werd waargenomen met Spitzer-IRS in het golflengte gebied van 5.2 tot 38 μm. Tijdens dezelfde periode als de Spitzer-IRS waarnemingen gebeurden, werd deze steekproef AGB sterren ook waargenomen vanop aarde d.m.v. optische en nabij-IR spectroscopie en nabij-IR fotometrie. Met deze extra informatie willen we zoveel mogelijk eigenschappen van de centrale ster en de variabiliteit te weten komen.

N.3.2 Eigenschappen van de centrale ster

Op basis van de waarnemingen met DBS (*Dual-Beam Spectrograph*) en CASPIR (*Cryogenic Array Spectrometer and Imager*) proberen we zoveel mogelijk informatie te verzamelen over de centrale ster.

Figuur 4.1 toont de optische spectra voor 3 AGB sterren uit onze steekproef. De onderste is een ster met nog weinig massaverlies, de middelste heeft een hoger massaverlies en de bovenste heeft het grootste massaverlies. Op deze figuur zijn ook de belangrijkste TiO en VO banden aangeduid en de golflengte positie van het Ca-triplet.
Van de TiO en VO banden weten we dat ze zeer gevoelig zijn voor de temperatuur en dus ook voor het spectraal type van de ster. Op basis van deze banden hebben we voor iedere ster het spectrale type bepaald en de effectieve temperatuur d.m.v. de calibratie in Fluks et al. (1994). De meeste objecten in onze steekproef hebben een spectraal type M5 of later en er zijn geen sterren met een spectraal type vroeger dan M4. Ook Glass et al. (1999) kwamen tot dit besluit op basis van ISOGAL bronnen in Baades venster.
Naast de TiO en de VO banden, is ook het Ca-triplet heel gevoelig aan de effectieve temperatuur. Het Ca-triplet wordt enkel waargenomen in objecten van een vroeg type. In onze steekproef hebben we dan ook slechts 3 objecten gevonden die het Ca-triplet heel duidelijk in al hun waarnemingen toonden en nog eens 3 andere sterren die het ook vertoonden, maar minder duidelijk. Deze 6 sterren zijn de 6 blauwste sterren in $(K_s - [15])_0$ uit onze steekproef en hebben dus de kleinste massaverliezen.

Vermits we de effectieve temperatuur afgeleid hebben op basis van de TiO banden in het spectrum, kunnen we door middel van modellen voor pulserende rode reuzen de intrinsieke (theoretische) $J - K$ kleur berekenen (Bessell et al. 1989). Wanneer we deze intrinsieke kleur vergelijken met de waargenomen $J - K$ kleur, krijgen we een afschatting voor de verroding van de ster. Deze verroding wordt dan veroorzaakt zowel door het circumstellair stof als door het interstellair stof. Via deze methode kunnen we dus geen afschatting maken voor de interstellaire extinctie, maar het toont ons wel aan dat de fout of de K-magnitude ongeveer 0.1 tot 0.2 mag is.

Figuren 4.2 tot 4.4 tonen voor dezelfde 3 sterren als in Figuur 4.1 de J-, H- en K-band spectroscopie. De belangrijkste moleculen die in dit golflengtegebied waargenomen kunnen worden zijn TiO, VO en CO. Water is ook een belangrijke molecule die zijn invloed laat merken op dit deel van het spectrum. Water zorgt ervoor dat het spectrum van de H-band een

kromming vertoont (zie bovenste spectrum van Figuur 4.3 t.o.v. de andere twee spectra). De sterkte van de waterband is afhankelijk van de preciese structuur van de buitenste lagen van de atmosfeer en er wordt van verwacht dat ze correleert met de variabiliteit van de ster (zie ook Sectie N.2.3). Figuur 4.4 toont ook de positie van Na I en Ca I. Deze twee lijnen zullen we later gebruiken om de metalliciteit af te schatten.

Naast nabij-IR spectroscopie hebben we met CASPIR ook nabij-IR fotometrie van onze bronnen verzamelt. De bronnen werden over 820 dagen tijdens 8 periodes voornamelijk in de *K*-band waargenomen en af in toe in de *J*-, *H*- en *nbL*-band. Op basis van de *K*-band fotometrie konden we voor 15 sterren uit onze steekproef periodes bepalen die dan gebruikt werden om ook de *J*-, *H*- en *nbL*-band te fitten. Via de *K* band fotometrie konden we enkel periodes vinden voor de Mira variabelen die een volledige amplitude hebben groter dan 0.4 mag. Voor 17 andere bronnen uit onze steekproef konden we op basis van deze data aantonen dat ze wel degelijk variabel zijn, maar de spreiding van de waarnemingen was te groot om periodes te kunnen vinden. De bronnen in deze steekproef werden vergeleken met de objecten in OGLE-II. 23 van onze bronnen hebben in OGLE-II *I*-band lichtcurves. Op basis van deze lichtcurves hebben we voor 5 objecten een periode gevonden waar we op basis van de *K*-band fotometrie geen variabiliteit konden detecteren. Voor 10 sterren waar we wel variabiliteit in *K* vonden maar geen periode, konden we op basis van deze *I*-band fotometrie wel een periode bepalen. Voor slechts 6 sterren vonden we geen periode op basis van deze *I*-band fotometrie, maar de lichtcurves vertonen duidelijk variabiliteit.
Op basis van de variabiliteit delen we onze objecten in in drie groepen: de Mira variabelen (met een volledige amplitude in *K* groter dan 0.4 of in *I* groter dan 0.9), de semi-regelmatige variabelen (variabelen met een amplitude kleiner dan die van de Mira's, maar waarvoor we nog steeds een periode konden vinden) en de variabelen met een kleine amplitude (dit zijn de variabelen waar we op basis van de *K*-band geen variabiliteit konden detecteren, in de *I*-band kon wel variabiliteit gedetecteerd worden, maar konden we geen periode afleiden).

Figuur 4.7 toont de waterabsorptie in functie van de effectieve temperatuur. Op deze figuur wordt duidelijk dat wanneer de effectieve temperatuur daalt, de hoeveelheid waterabsorptie toeneemt. Op deze figuur duiden de verschillende symbolen de verschillende variabiliteitstypes aan, gedefinieerd op basis van de *K* of *I*-band amplitude. Deze figuur toont duidelijk dat de Mira variabelen de grootste hoeveelheid waterabsorptie hebben. Vermits de hoeveelheid water correleert met de effectieve temperatuur, verwachten we dat de hoeveelheid water toeneemt naarmate de ster verder evolueert, dus verwachten we ook een correlatie tussen de hoeveelheid water en de amplitude waarmee de ster pulseert. Figuur 4.8 toont dit verband.

Op basis van de equivalente lijnbreedtes van Na I, Ca I en ^{12}CO(2,0) bepaalden Frogel et al. (2001) een manier om de metalliciteit af te schatten op basis van mediumresolutie nabij-IR spectroscopie. De gemiddelde metalliciteit die we op deze manier berekenen voor onze steekproef is [Fe/H]= -0.38 ± 0.18. Deze waarde is in overeenstemming met de metalliciteit voor de bulge gevonden door Rich en Origlia (2005) en Rich et al. (2007) op basis van hoge-resolutie spectroscopie van M-giants in de bulge.

Heel vaak worden voor dit soort sterren periode-lichtkracht (PL) diagrammen gemaakt.

Figuur 4.10 toont dit PL-diagram voor deze groep AGB sterren. Onze sterren bevinden zich in de reeksen A, B en C. De onregelmatig pulserende variabele worden niet getoond in deze figuur (voor deze objecten konden we geen periode afschatten), en ook de objecten met $(J-K)_0 > 2$ worden niet getoond (voor deze objecten heeft het circumstellaire stof een te grote invloed op de $(J-K)$ kleur). Dit PL-diagram toont aan dat de semi-regelmatige variabelen zich vnl. op reeksen A en B bevinden, terwijl de Mira variabelen allemaal op reeks C liggen. Dit is ook wat verwacht wordt op basis van de evolutie tijdens de AGB.

Deze steekproef is geselecteerd op basis van $(K_s - [15])_0$ kleur, een massaverliesindicator. Figuur 4.12 toont het Kleur-Magnitude Diagram (*Colour-Magnitude Diagram, CMD*) voor deze steekproef AGB sterren. Deze figuur toont duidelijk het verband tussen variabiliteit en massaverlies. De onregelmatig pulserende variabelen hebben de blauwste $(K_s - [15])_0$ kleur en dus de laagste massaverliezen. De semi-regelmatige variabelen bezitten een intermediaire $(K_s - [15])_0$ kleur en de Mira variabelen hebben de roodste $(K_s - [15])_0$ kleur en dus de hoogste massaverliezen.

Vermits massaverlies bij AGB sterren kan omschreven worden als een door pulsatie versterkte stofgedreven wind, verwachten we dat het massaverlies van de AGB ster correleert met de periode van de ster. Figuur 4.13 toont $(K_s - [15])_0$ in functie van de periode en geeft inderdaad aan dat naarmate de pulsatieperiode toeneemt de $(K_s - [15])_0$ kleur roder wordt, of equivalent dat het massaverlies toeneemt. Ditzelfde effect wordt ook getoond in het verband tussen het massaverlies en de pulsatieamplitude (zie Figuren 4.14 en 4.15).

N.3.3 Stofeigenschappen

Het licht dat we van de sterren in onze steekproef waarnemen is afkomstig van de centrale ster, een eventuele moleculaire laag en voor de objecten met stof, de stofschil. In dit hoofdstuk willen we de kenmerken van het stof rond deze sterren bestuderen. Daarom is het belangrijk om een goede afschatting te maken voor het licht dat we ontvangen van de centrale ster en de eventuele moleculaire laag. Hiermee kunnen we dan het spectrum voor de sterren met stof corrigeren zodat we het stof kunnen bestuderen.

Op basis van het selectiecriterium wordt verwacht dat de blauwste sterren in $(K_s - [15])_0$, de sterren zonder stof zijn. Figuur 3.22 toont dat er sterren zijn zonder stof die roder zijn dan de blauwste ster met stof. Daarom hebben we een objectieve manier nodig om de sterren zonder stof te selecteren. Om dit te bereiken werd een Planck-curve gefit aan de sterren die geen aanwijzingen vertoonden voor enig stoffeature. Door deze spectra te vergelijken met een zwarte straler d.m.v. de curve van Planck, kunnen we onze sterren zonder stof objectiever selecteren. Op deze manier hebben we 10 sterren gevonden die geen aanwijzingen van stof vertonen op basis van hun Spitzer-IRS spectrum. Voor deze sterren zonder stof ligt de temperatuur die bepaald is d.m.v. de Planck-curve tussen de 1360 en 3000 K. Deze spreiding in temperaturen is voldoende om de spreiding in waargenomen $(K_s - [15])_0$ te verklaren. Deze relatief lage temperaturen kunnen waarschijnlijk verklaard worden door de aanwezigheid van een moleculaire laag rond deze sterren.

Deze sterren zonder stof kunnen we nu gebruiken als templates om de emissie van de centrale ster en de waterlaag te verwijderen van de geobserveerde spectra voor de sterren met stof. Op deze manier creëren we stofspectra (zie Figuren 3.29 tot 3.31).

In deze stofspectra kunnen we een heel aantal features herkennen: amorfe silicaten, alumina, het 13 en het 19.5 μm feature. De efficiencies voor deze stof soorten worden getoond in Figuur 3.32. Amorfe silicaten vertonen twee kenmerkende banden: één rond 9.7 μm en één rond 18 μm. Dit profiel kan in heel wat stofspectra herkend worden. Alumina heeft in het golflengtebereik dat met Spitzer-IRS bestudeerd wordt, enkel een feature rond 11 μm. Het wordt onderscheiden van het amorfe silicaatfeature doordat het verloop van de rode vleugel van het feature veel minder stijl is dan dat van amorfe silicaten. De efficiencies voor het 13 μm feature worden niet getoond in Figuur 3.32. Op dit ogenblik is het nog niet gekend wat dit feature veroorzaakt. In recente studies worden corundum, spinel en silica als mogelijke stofcomponenten gegeven die dit feature zouden kunnen veroorzaken. Het 19.5 μm feature is een scherp gepiekt feature (zie Figuur 3.32). $Mg_{0.1}Fe_{0.9}O$ is in staat dit feature te veroorzaken. Alhoewel dit feature in heel veel AGB sterren waargenomen wordt, wordt het in deze steekproef maar 1 keer duidelijk waargenomen, voor twee andere sterren zijn er aanwijzigen dat ze het feature vertonen. Tabel 3.3 geeft de objecten in volgorde van stijgende $(K_s - [15])_0$ kleur weer. Voor ieder object in de lijst dat geen object zonder stof is, wordt aangegeven welke features in de stofspectra gezien kunnen worden.

Als verondersteld wordt dat de eigenschappen van de stofschillen voor ieder object dezelfde zijn, behalve de hoeveelheid massa die erin zit, dan geeft de flux onder het stofspectrum de hoeveelheid stof weer. De integraal onder het stofspectrum noemen we de stoflichtkracht. Vermits de spectra van de objecten in onze steekproef niet abosluut flux-gecalibreerd konden worden, delen we deze stoflichtkracht door de integraal van het geobserveerde spectrum. Op deze manier berekenen we de genormaliseerde stoflichtkracht.

Figuur 3.33 geeft de genormaliseerde stoflichtkracht in functie van $(K_s - [15])_0$. De grootte van de symbolen duidt de onzekerheid op de parameters aan. De fout op $(K_s - [15])_0$ wordt bepaald door de fout op de fotometrie, maar ook de variabiliteit van het object heeft een invloed. De fout weergegeven in Figuur 3.33 toont enkel de fout op de fotometrie. De sterren met de roodste $(K_s - [15])_0$ kleur zijn de sterren met de grootste variabiliteit en dit kan een verschuiving in de $(K_s - [15])_0$ kleur veroorzaken. Vermits de blauwste sterren heel kleine amplitudes hebben, is de fout die daar veroorzaakt wordt door de variabiliteit verwaarloosbaar.
De figuur toont een stijgende trend voor de genormaliseerde stoflichtkracht in functie van $(K_s - [15])_0$, een massaverliesindicator. Als we aannemen dat het enige verschil tussen de stofschillen van deze objecten de massa is, dan verwachten we inderdaad deze stijgende trend: als het massaverlies groter is, wordt er meer stof gevormd en neemt de genormaliseerde stoflichtkracht toe. Ondanks dat we deze trend verwachtten is er een hele grote spreiding waarneembaar: voor objecten met een $(K_s - [15])_0$ kleur van ongeveer 1 zien we zowel sterren zonder stof als objecten met een genormaliseerde stoflichtkracht van ongeveer 0.4. Ook wanneer we objecten bekijken met een ongeveer gelijke genormaliseerde stoflichtkracht, zien we een hele grote spreiding op de $(K_s - [15])_0$ kleur.

Op basis van de efficiencies voor alumina en amorf silicaat, hebben we de 10 μm complexen gefit. De resultaten worden weergegeven in Tabel 3.4. Figuur 3.35 toont de afgeleidde relatieve abondantie van alumina ten opzichte van de amorfe silicaten in functie van $(K_s - [15])_0$. Deze figuur toont aan dat er maar één object gevonden werd dat volledig door alumina verklaard kan worden. De meeste objecten hebben een relatieve abondantie van alumina tussen 0.1 en 0.4. Er zijn aanwijzingen voor een dalende trend in deze figuur, maar de trend is niet zo sterk als verwacht. Er is duidelijk ook geen eenduidige relatie tussen $(K_s - [15])_0$ en de vorm van het 10 μm stofcomplex.

Sloan en Price (1995) classificeren zuurstofrijke AGB sterren in 8 SE (silicaatemissie) indices. Sterren met een SE index van 1 vertonen het breedste 10 μm complex. De breedte van dit complex neemt af naarmate de SE index hoger wordt en de objecten met de smalste profielen hebben een SE index van 8. Gebasseerd op de zuurstofrijke stofcondensatiereeksen, worden AGB sterren verwacht deze 8 indices te doorlopen. Figuur 3.37 toont de verdeling van objecten volgens hun SE index. Daarin zien we dat de meerderheid van de objecten een SE index van 4 of 5 heeft. Op basis van de selectiemethode werd echter verwacht dat er meer objecten een kleinere SE index zouden hebben. Op basis van de stofspectra kunnen we echter geen reden vinden waarom de meeste AGB sterren in deze steekproef een SE index hebben van 4 of 5.

N.3.4 Kristallijn materiaal in de circumstellaire enveloppe van OH/IR sterren

De steekproef AGB sterren die we in de bulge selecteerden, bevat ook AGB sterren aan het einde van de AGB fase, de OH/IR sterren. Deze OH/IR sterren hebben door het grote massaverlies een optisch dikke stof enveloppe. Het infrarode spectrum van deze sterren ziet er anders uit dan van de andere AGB sterren in de steekproef. De meeste AGB sterren in onze selectie vertonen amorf silicaat in emissie. Doordat het circumstellair materiaal zo dicht is, worden deze amorfe silicaten niet meer in emissie, maar in (gedeeltelijke) zelfabsorptie waargenomen. Daarenboven kunnen we in deze sterren ook kristallijn materiaal waarnemen (forsteriet en enstatiet).

De spectra van deze objecten worden getoond in Figuur 5.1. De sterren zijn geordend volgens stijgend massaverlies. Het eerste twee objecten (IRAS 17413-3531 en IRAS 18042-2905) zijn objecten die het 10 μm complex nog niet volledig in absorptie hebben. Ook de 18 μm silicaatband vertoont zich ook nog in emissie. De bulten op langere golflengten worden veroorzaakt door forsteriet en enstatiet. De belangrijkste forsteriet banden worden aangegeven door stippellijnen in Figuur 5.1. De andere zes sterren vertonen hun 10 en 18 μm band in absorptie. Wanneer het 10 μm complex sterker wordt, wordt het ook breder en begint het meer substructuren te vertonen. Ook deze sterren vertonen kristallijn materiaal, alhoewel de sterkte ervan op de langste golflengtes lijkt af te nemen wanneer de sterkte van het 10 μm complex toeneemt.

Om een betere afschatting van het massaverlies en lichtkracht voor deze OH/IR sterren te hebben, werden deze sterren gemodeleerd met behulp van het radiatief transportmodel van

Groenewegen (1993, 1995). Een voorbeeld van zo'n model wordt getoond in Figuur 5.4 en de resultaten zijn gegeven in Tabel 5.2. De lichtkrachten voor deze objecten bevinden zich tussen de 5 500 en 7 000 $L_\odot$, wat nog eens de homogeniteit van de steekproef bevestigt. De massaverliezen liggen tussen 0.3 en 3.0×10^{-4} $M_\odot$/yr.

Om de kristalliniteitsgraad van deze objecten te bestuderen, werd het 11.3 en 33.6 μm forsteriet feature in meer detail bestudeerd. Voor beide features werd de relatieve sterkte gemeten. Voor het 11.3 μm feature werd daarenboven ook nog de centrale positie van het feature bepaald. Deze gegevens zijn terug te vinden in Tabel 5.2.

Wat betreft de positie van het 11.3 μm feature vonden we dat dit feature eigenlijk op 11.2 μm ligt i.p.v. op 11.3 μm zoals het in jonge sterren waargenomen wordt. Dit zou kunnen betekenen dat de forsterietdeeltjes die dit feature veroorzaken kleiner zijn dan de forsterietdeeltjes rond jonge sterren. Recent onderzoek naar de golflengtepositie van dit feature door Tamanai et al. (2006) toonde aan dat de golflengtepositie van dit feature ook opschuift naar kortere golflengtes wanneer het feature in een zuivere vorm voorkomt. Dit zou dus ook kunnen aantonen dat de forsterietdeeltjes rond AGB sterren minder vervuild zijn door andere elementen dan de forsterietdeeltjes rond jonge sterren.

Figuren 5.6 en 5.7 tonen de relatieve sterktes van het 11.3 en het 33.6 μm forsterietfeature in functie van de optische diepte τ van het 10 μm complex, een maat voor het massaverlies. Deze figuur toont dat naarmate het massaverlies toeneemt de relatieve sterkte van het 33.6 μm feature afneemt. Deze dalende trend met stijgend massaverlies kan verklaard worden d.m.v. de optische diepte op 33.6 μm. Voor alle sterren behalve 1, is de optische diepte groter dan 1: voor 3 objecten is de optische diepte ongeveer 1 en voor al de andere objecten is de optische diepte groter dan 2. Dit geeft aan dat de stofschil niet optisch dun wordt op 33.6 μm voor de objecten met de hoogste massaverliezen. Hierdoor kunnen we dus niet meer door de stofschil kijken en zien we minder forsteriet, waardoor de sterkte van het feature afneemt. Dit wil dus niet zeggen dat er ook effectief minder forsteriet aanwezig is.
Op basis van het 11.3 μm feature wordt geen trend waargenomen tussen massaverlies en sterkte van dit feature. Dit geeft aan dat de OH/IR sterren relatief gezien dezelfde hoeveelheid kristallijn materiaal vormen.

N.3.5 De zuurstofrijke stofcondensatie

In hoofdstuk 6 willen we de stofspectra bestuderen in functie van de eigenschappen van de centrale ster en in functie van de variabiliteit van de objecten. Op basis van de variabiliteit van de sterren, werden de objecten in een $(K_0, \log P)$-diagram geplaatst (zie Figuur 6.1). De horizontale streep die de reeksen A en B in twee verdeeld is de tip van de rode reuzentak (RGB). De objecten onder deze tip zijn sterren zonder stof (zie hoofdstuk 3). Figuren 6.2 tot 6.4 geven de stofspectra van de objecten weer naargelang de reeks waarop ze gevonden werden. Op basis van pulsatiemodellen weten we dat de semi-regelmatige variabelen radiële boventoon pulsators zijn in tegenstelling tot de objecten op reeks C. Deze objecten pulseren in de fundamentele radiële mode. De Mira variabelen bevinden zich allen op deze reeks. Op basis van de stofspectra en op basis van het $(K_0, \log P)$-diagram kunnen we bestluiten dat de

objecten met de grootste hoeveelheid alumina teruggevonden worden vlak boven de tip van de RGB. Er is echter 1 Mira variabele die ook een grote hoeveelheid alumina bezit die hier niet aan voldoet. De andere objecten op reeksen B en C vertonen allemaal stofspectra die gekenmerkt worden door zowel alumina als amorfe silicaten. Deze objecten bezitten bovendien een 13 μm feature. De objecten waarvoor $(J-K)_0$ groter is dan 2 worden in deze figuur niet getoond, maar worden verondersteld al verder geëvolueerd te zijn dan de objecten die wel in deze figuur gegeven zijn. De stofspectra van de objecten met $(J-K)_0$ wordt gedomineerd door amorfe silicaten, tekenen van andere stofsoorten kunnen in deze spectra niet teruggevonden worden. De sterren met de grootste massaverliezen, de OH/IR sterren, vertonen een door amorfe silicaten gedomineerd stofspectrum met daarenboven duidelijke kristallijne features. Ook in deze objecten wordt geen 13 μm feature waargenomen.

Op basis van de parameters afgeleidt in de vorige hoofdstukken, voeren we een principaal componenten analyse (PCA) uit. Een PCA heeft als doel het zoeken naar lineaire verbanden tussen de verschillende parameters, waardoor de dimensionaliteit van een probleem verkleint. Ze kan ook onderliggende (eventueel nog onbekende) grootheden aan het daglicht brengen. Op basis van deze analyse konden we de dimensionaliteit van het geschetste probleem van 11 tot 7 parameters terugbrengen. De variatie in de dataset kan door middel van 3 principaal componenten (PC) verklaard worden. Het massaverlies is de achterliggende grootheid van de eerste PC, de stofsamenstelling en de metalliciteit zijn de fysische interpretatie van de tweede PC. Wat de fysische interpretatie van de derde component is, blijft vooralsnog onduidelijk.

N.3.6 Besluit

Op basis van de optische en de nabij-IR waarnemingen voor deze steekproef van AGB sterren in de bulge, hebben we voor onze groep sterren een afschatting van het spectraal type en dus ook van de effectieve temperatuur. We maakten ook een schatting voor de metalliciteit op basis van de equivalente lijnbreedtes van Na I, Ca I en ^{12}CO(2,0). De metalliciteitsverdeling die we op deze manier afgeleid hebben is in overeenstemming met recente literatuur. Gebruikmakend van de fotometrie konden we de variabiliteit voor deze sterren bestuderen. Daarenboven gebruikmakend van de massaverliesindicator $(K_s-[15])_0$ werd een duidelijk verband aangetoond tussen de pulsatieperiode en -amplitude en het massaverlies.

Op basis van de analyse in hoofdstuk 3, vinden we geen eenduidige relatie tussen $(K_s-[15])_0$, een massaverliesindicator, en de stofeigenschappen van de AGB sterren. Reeds voor de sterren zonder stof hebben we aangetoond dat $(K_s-[15])_0$ geen perfecte massaverliesindicator is: er zijn objecten met stof die dezelfde kleur hebben als objecten zonder stof. Daarnaast vonden we voor de sterren met stof dat er geen duidelijke relatie is tussen $(K_s-[15])_0$ en de relatieve abondantie van alumina en $(K_s-[15])_0$ en de SE index. Dit wijst erop dat alhoewel $(K_s-[15])_0$ in eerste instantie gebruikt kan worden als een massaverlies indicator, we een betere afschatting van het massaverlies voor deze objecten nodig hebben. Dit zouden we kunnen verkrijgen via gedetailleerde modellering van deze spectra. Op basis van deze massaverliezen, kunnen we de spectra opnieuw ordenen en opnieuw de stofsamenstelling bekijken in functie van het massaverlies. Vermits de spreiding op de correlaties tussen de verschillende parameters en $(K_s-[15])_0$ echter zo groot is, is het heel onwaarschijnlijk

dat deze correlaties veel duidelijker worden wanneer onafhankelijke massaverliezen bepaald worden. Dit geeft aan dat de zuurstofrijke stofcondensatiereeksen zoals beschreven in N.1.2.4 niet voldoende zijn om het waargenomen stof rond zuurstofrijke AGB sterren te voorspellen. Daarenboven toonden we in hoofdstuk 6 d.m.v. een principaal componenten analyse aan dat het massa-verlies statistisch onafhankelijk is van de stofsamenstelling, maar de stofsamenstelling is wel gerelateerd met de metalliciteit.

N.4 Sterpopulaties in de bulge

Het laatste hoofdstuk van deze thesis is gewijd aan het bestuderen van de geometrie van, de sterpopulatie in en de metalliciteitsverdeling van sterren in de bulge. Zoals vermeld in de inleiding is er op dit ogenblik nog lang geen conscencus bereikt over de eigenschappen van dit deel van de Melkweg.

Om de eigenschappen van de bulge en zijn sterpopulatie te bestuderen kunnen verschillende methodes gebruikt worden. Wij kiezen in dit werk voor een populatie-synthese-model TRILEGAL (Girardi et al. 2005). Deze code berekent voor iedere positie aan de hemel de verwachte sterpopulatie op basis van enkele parameters. De code verwacht van de gebruiker de volgende parameters:

- een verzameling evolutiesporen. Deze evolutiesporen beschrijven het levensverloop van een ster afhankelijk van haar initiële massa en metalliciteit.
- een verzameling synthetische spectra. Deze spectra worden gebruikt om bollometrische correcties en verrodingscoëfficiënten uit te rekenen.
- de eigenschappen van het instrument dat in de code nagebootst wordt (zoals eigenschappen van de gebruikte filters en detectoren) en het gebied aan de hemel dat men wil simuleren.
- een gedetailleerde omschrijving van de verschillende componenten van de Melkweg. Voor iedere component wordt een stervormingsgeschiedenis (*star formation rate, SFR*), een metalliciteitsverdeling en een maat voor de verdeling/dichtheid van de sterren in die component gegeven.

Met de uitvoer van deze code kunnen we dan kleur-magnitude diagrammen (CMDs) maken, die we kunnen vergelijken met waarnemingen. De waarnemingen die voor dit project gekozen zijn, zijn 11 velden uit de OGLE-II waarneemcampagne. Voor deze 11 velden hebben we V- en I-band fotometrie van OGLE-II en J-, H- en K_s-band fotometrie van 2MASS. Voor ieder veld, creëren we twee CMDs: een (I,$V-I$) diagram en een (K_s,$J-K_s$) diagram. In ieder CMD definiëren we twee gebieden: een gebied dat bestaat uit sterren die zich in de schijf bevinden “schijf gebied” en een gebied dat bestaat uit sterren in de bulge “bulge gebied” (zie Figuur 7.3 en 7.4). In Figuur 7.4, het CMD voor de OGLE data, zien we nog een derde gebied aangeduid. Dit is de plaats waar we de *red clump* sterren zien. Red clump sterren zijn rode reuzen die zich op de horizontale tak bevinden. Deze sterren worden vaak gebruikt om afstanden te schatten: de waargenomen magnitude wordt voor deze sterren vergeleken met

de verwachtte magnitude en zo kan men de afstand bepalen.

Om het model en de waarnemingen te vergelijken worden histogrammen gemaakt van de sterren in de twee geselecteerde gebieden uit het CMD. De statistische test die gebruikt werd om de histogrammen te vergelijken is een Poisson verdeelde maximum-likelihood. Uit deze methode krijgen we voor ieder model een getal l dat omschrijft hoe goed of hoe slecht de fit is. Het beste model wordt dan gegeven door het minimum van al deze getallen l. De modellen die "even goed" zijn of equivalent waarvan we niet kunnen zeggen dat ze significant slechter zijn, bepalen dan de foutenbalken op de gevonden parameters. Met behulp van 54 processoren werd om dit vraagstuk op te lossen een minimalisatieprocedure opgezet. Het beste model dat we op deze manier vinden is een model met de volgende parameters:

- $R_0 = 8.6 \pm^{0.15}_{0.11}$kpc, de afstand van onze Zon tot aan het centrum van de Melkweg,
- $a_m = 2.7 \pm^{0.04}_{0.10}$kpc, de schaallengte van de bulge,
- $a_0 = 96.6 \pm^{1.1}_{4.1}$pc, de schaallengte die beschrijft vanaf waar de bulge begint,
- $1 : \eta : \zeta = 1 : 0.68 \pm^{0.01}_{0.07} : 0.30 \pm^{0.01}_{0.01}$, de verhouding van de grote assen van de balk,
- $\phi = 14.4^\circ \pm^{5.5}_{10.3}$, de hoek die de balk maakt met de lijn gevormd door het centrum van de Melkweg en onze Zon,
- $f_0 = 427.3 \pm^{11.0}_{25.7}$, de schaalfactor die de hoeveelheid sterren in de bulge bepaalt.

Tabel 7.1 geeft een beknopt overzicht van studies die deze parameters willen bepalen. De parameters die wij op basis van onze methode vinden, vallen binnen de verscheidenheid aan waarden tot nu toe gevonden. Wat betreft de afstand tot het galactisch centrum behoort onze waarde tot de grootste afstanden. Onze waarnemingen zijn consistent binnen de foutenbalken met studies gebaseerd op RR Lyrae sterren (Fernley et al. 1987; Feast 1997), red clump sterren (Paczynski en Stanek 1998) en Mira variabelen (Groenewegen en Blommaert 2005). Er zijn ook een aantal studies die significant kleinere waarden vinden dan wij: Eisenhauer et al. (2003, 2005) bestudeerden sterren in de nabijheid van het zwarte gat in het centrum van de Melkweg en vonden een gemiddelde afstand van ongeveer 7.8 kpc. Ook studies op basis van water masers, en de meeste studies die gebruik maken van red clump sterren vonden kleinere resultaten. Een verschillende verdeling van deze verschillende sterpopulaties zou aan de oorzaak kunnen liggen van deze soms nogal ver uiteenlopende onderzoeksresultaten.

Naast de afstandsbepaling tot het centrum van de Melkweg, is ook de hoek die de balk maakt een veel bediscussieerde parameter. Tabel 7.1 toont dat er twee groepen resultaten zijn. De ene groep vind kleine hoeken (rond de 20°), terwijl de andere groep grote hoeken vindt (rond de 40°). Sevenster et al. (1999) suggereert dat kleine waarden voor ϕ gevonden worden wanneer enkel dichtbij het centrum gekeken wordt, terwijl grotere waarden gevonden worden wanneer op grotere galactische lengte gekeken wordt. Groenewegen en Blommaert (2005) vermelden dat dit verschil waarschijnlijk te wijten is aan het verschil in bestudeerde sterpopulaties, die niet noodzakelijk dezelfde ruimtelijke verdeling hebben.

Naast de geometrie van de bulge, hebben we ook de metalliciteits- en leeftijdsverdeling bestudeerd. De metalliciteitsverdeling waarvan we gestart zijn is beschreven in Zoccali et al. (2003) (zie Figuur 7.7). Met deze metalliciteitsverdeling merkten we dat we de histogrammen gemaakt op basis van 2MASS data goed konden voorspellen, maar de histogrammen op basis van de OGLE data werden altijd overschat (zie Figuur 7.8). Dit zou kunnen veroorzaakt worden door de metalliciteitsverdeling. De metalliciteitsverdeling in Zoccali et al. (2003) is gebaseerd op fotometrische waarnemingen en is ietsje metaal-armer dan metalliciteitsverdelingen bepaald op basis van spectroscopische waarnemingen, maar is er nog steeds consistent mee. Om dit te onderzoeken hebben we de metalliciteitsverdeling verschoven naar een metaal-rijkere verdeling. We vonden een siginficant betere fit voor een metalliciteitsverdeling verschoven met +0.3 dex (zie Figuur 7.9).

De bulge wordt ook vaak geassocieerd met een oude populatie (ouder dan 10 Gyr). In de recente literatuur worden er echter meer en meer indicaties gevonden voor een bulge die gedomineerd wordt door een oude populatie, maar waar ook “intermediaire” (een aantal Gyr) en soms zelfs jonge (een aantal miljoen jaar) sterren worden in teruggevonden (Holtzman et al. 1993; Ortolani et al. 1995, 2001; Zoccali et al. 2003; van Loon et al. 2003). Om deze hypothese te testen gebruikten we de stervormingsgeschiedenis beschreven in van Loon et al. (2003). Hiermee simuleerden we een dominante oude populatie met daarenboven een groep jonge sterren en/of sterren met een intermediaire leeftijd. Hiermee konden we geen significant betere fit vinden. Dit wil niet zeggen dat er geen sterren aanwezig zijn in de bulge die jonger zijn dan de oude populatie. Dit toont enkel aan dat deze sterren een te kleine invloed hebben op het CMD om via onze methode opgespoord te worden. Op basis van onze resultaten moeten we besluiten dat de gemiddelde leeftijd van de bulge 10 Gyr is.

APPENDIX A

List of acronyms

2MASS	Two Micron All Sky Survey
AGB	Asymptotic Giant Branch
ATCA	Australia Telescope Compact Array
BCD	Basic Calibrated Data
BFGS	Broyden-Fletcher-Goldfarb-Shanno
CMD	Colour Magnitude Diagram
COBE	Cosmic Background Explorer
CSE	circumstellar envelope
CTA	Cryogenic Telescope Assembly
DDT	Director's Discretionary Time
DENIS	Deep Near-Infrared Survey
E-AGB	early-AGB
ESO	European Southern Observatory
FWHM	Full With Half Maximum
GB	Galactic Bulge
GC	Galactic Centre
GO	General Observers
GTO	Guaranteed Time Observers
HB	Horizontal Branch
HBB	Hot Bottom Burning
HR diagram	Hertzsprung-Russell diagram
IPAC	Infrared Processing and Analysis Center
IRAC	Infrared Array Camera
IR	Infrared
IRAF	Image Reduction and Analysis Facility
IRAS	Infrared Astronomical Satellite
IRS	Infrared Spectrograph

ISM	Interstellar Medium
ISO	Infrared Space Observatory
ISO-LWS	ISO's Long-Wavelength Spectrometer
ISO-SWS	ISO's Short-Wavelength Spectrometer
ISOCAM	ISO's Infrared Camera
ISOCAM-CVF	ISOCAM's Circular Variable Filters
ISOPHOT	ISO's Imaging Photo-polarimeter
LMC	Large Magellanic Cloud
LH	Long High
LL	Long Low
LPV	Long Period Variable
MIPS	Multiband Imaging Photometer for Spitzer
MIDAS	Munich Image Data Analysis System
MS	Main Sequence
MSX	Midcourse Space Experiment
MWG	Milky Way Galaxy
NASA	National Aeronotic and Space Administration
NTT	New Technology Telescope
OGLE	Optical Gravitational Lensing Experiment
OPZ	Operational Pointing Zone
PAH	Polycyclic Aromatic Hydrocarbon
PC	Principal Component
PCA	Principal Component Analysis
PCRS	Pointing Calibration Reference Sensor
PI	Principal Investigator
PL	Period-Luminosity
PN	Planetary Nebula
PSC	Point Source Catalog
RGB	Red Giant Branch
ROC	Reseved Observations Catalogue
SH	Short High
SIRTF	Space InfraRed Telescope Facility
SL	Short Low
SMART	Spectroscopic Modelling Analysis and Reduction Tool
SOFI	Son of Isaac
SOM	Spitzer Observer's Manual
SSC	Spitzer Science Center
SST	Spitzer Space Telescope
TP-AGB	thermally pulsing AGB
TMSS	Two Micron Sky Survey
VLA	Very Large Array
XSC	Extended Source Catalog
YSO	Young Stellar Object

BIBLIOGRAPHY

Aringer, B.: 2000, "*The SiO molecule in the atmospheres and circumstellar shells of AGB stars*", *Ph.D. thesis*, University of Vienna

Aringer, B., Jorgensen, U. G., and Langhoff, S. R.: 1997, "SiO rotation-vibration bands in cool giants. I. A grid of model spectra for different stellar parameters.", *Astron. Astrophys.* **323**, 202–210

Babusiaux, C. and Gilmore, G.: 2005, "The structure of the Galactic bar", *Mon. Not. Roy. Astron. Soc.* **358**, 1309–1319

Bahcall, J. N. and Soneira, R. M.: 1980, "The universe at faint magnitudes. I - Models for the galaxy and the predicted star counts", *Astrophys. J. Suppl.* **44**, 73–110

Ballero, S. K., Matteucci, F., Origlia, L., and Rich, R. M.: 2007, "Formation and evolution of the Galactic bulge: constraints from stellar abundances", *Astron. Astrophys.* **467**, 123–136

Baud, B., Habing, H. J., Matthews, H. E., and Winnberg, A.: 1981, "A systematic search at 1612 MHz for OH maser sources. III - The galactic distribution, kinematics, and emission properties of Type II OH/IR sources. IV Type II OH/IR sources in the central region of the Galaxy", *Astron. Astrophys.* **95**, 156–176

Begemann, B., Dorschner, J., Henning, T., Mutschke, H., Guertler, J., Koempe, C., and Nass, R.: 1997, "Aluminum Oxide and the Opacity of Oxygen-rich Circumstellar Dust in the 12–17 Micron Range", *Astrophys. J.* **476**, 199

Benjamin, R. A., Churchwell, E., Babler, B. L., Bania, T. M., Clemens, D. P., Cohen, M., Dickey, J. M., Indebetouw, R., Jackson, J. M., Kobulnicky, H. A., Lazarian, A., Marston, A. P., Mathis, J. S., Meade, M. R., Seager, S., Stolovy, S. R., Watson, C., Whitney, B. A., Wolff, M. J., and Wolfire, M. G.: 2003, "GLIMPSE. I. An SIRTF Legacy Project to Map the Inner Galaxy", *Pub. Astron. Soc. Pacific* **115**, 953–964

Bessell, M. S., Brett, J. M., Wood, P. R., and Scholz, M.: 1989, "Colors of extended static model photospheres of M giants", *Astron. Astrophys. Suppl.* **77**, 1–30

Bessell, M. S., Scholz, M., and Wood, P. R.: 1996, "Phase and cycle dependence of the photospheric structure and observable properties of Mira variables.", *Astron. Astrophys.* **307**, 481–499

Binney, J., Gerhard, O., and Spergel, D.: 1997, "The photometric structure of the inner Galaxy", *Mon. Not. Roy. Astron. Soc.* **288**, 365–374

Bissantz, N. and Gerhard, O.: 2002, "Spiral arms, bar shape and bulge microlensing in the Milky Way", *Mon. Not. Roy. Astron. Soc.* **330**, 591–608

Blommaert, J. A. D. L., Cami, J., Szczerba, R., and Barlow, M. J.: 2005, "Late Stages of Stellar Evolution", *Space Science Reviews* **119**, 215–243

Blommaert, J. A. D. L., Groenewegen, M. A. T., Okumura, K., Ganesh, S., Omont, A., Cami, J., Glass, I. S., Habing, H. J., Schultheis, M., Simon, G., and van Loon, J. T.: 2006, "ISO mid-infrared spectroscopy of Galactic Bulge AGB stars", *Astron. Astrophys.* **460**, 555–563

Blommaert, J. A. D. L., van der Veen, W. E. C. J., and Habing, H. J.: 1993, "Candidate OH/IR stars in the outer parts of our Galaxy", *Astron. Astrophys.* **267**, 39–53

Blommaert, J. A. D. L., van der Veen, W. E. C. J., van Langevelde, H. J., Habing, H. J., and Sjouwerman, L. O.: 1998, "The nature of OH/IR stars in the galactic centre", *Astron. Astrophys.* **329**, 991–1009

Bonatto, C., Bica, E., and Girardi, L.: 2004, "Theoretical isochrones compared to 2MASS observations: Open clusters at nearly solar metallicity", *Astron. Astrophys.* **415**, 571–576

Bouwman, J., de Koter, A., Dominik, C., and Waters, L. B. F. M.: 2003, "The origin of crystalline silicates in the Herbig Be star HD 100546 and in comet Hale-Bopp", *Astron. Astrophys.* **401**, 577–592

Brett, J. M.: 1990, "Astrophysical oscillator strengths for TiO and VO bands from spectrum synthesis of spectral types M1 III to M7 III", *Astron. Astrophys.* **231**, 440–452

Broyden, C. G.: 1970, "The convergence of a class of double-rank minimization algorithms. I: General considerations", *Journal of the Institute of Mathematics and Its Applications* **6**, 76–90

Cabrera-Lavers, A., Hammersley, P. L., González-Fernández, C., López-Corredoira, M., Garzón, F., and Mahoney, T. J.: 2007, "Tracing the long bar with red-clump giants", *Astron. Astrophys.* **465**, 825–838

Cami, J.: 2002, "*Molecular gas and dust around evolved stars*", *Ph.D. thesis*, University of Amsterdam

Cardelli, J. A., Clayton, G. C., and Mathis, J. S.: 1989, "The relationship between infrared, optical, and ultraviolet extinction", *Astrophys. J.* **345**, 245–256

Chiar, J. E. and Tielens, A. G. G. M.: 2006, "Pixie Dust: The Silicate Features in the Diffuse Interstellar Medium", *Astrophys. J.* **637**, 774–785

Cohen, M., Parker, Q. A., and Chapman, J.: 2005, "A circular planetary nebula around the OH/IR star OH354.88-0.54 (V1018 Sco)", *Mon. Not. Roy. Astron. Soc.* **357**, 1189–1196

Couch, P. A., Lloyd Evans, T., and Sarre, P. J.: 2003, "The cool circumstellar environment of IRAS 08182-6000: radiative transfer modelling of TiO absorption bands", *Mon. Not. Roy. Astron. Soc.* **346**, 153–162

Dame, T. M., Hartmann, D., and Thaddeus, P.: 2001, "The Milky Way in Molecular Clouds: A New Complete CO Survey", *Astrophys. J.* **547**, 792–813

David, P., Lesqueren, A. M., and Sivagnanam, P.: 1993, "An OH Satellite Line Maser Survey of Cool IRAS Sources and Circumstellar Envelope Evolution", *Astron. Astrophys.* **277**, 453

Decin, L.: 2000, "*Synthetic spectra of cool stars observed with the Short-Wavelength Spectrometer: improving the models and the calibration of the instrument*", *Ph.D. thesis*, Katholieke Universiteit Leuven

Decin, L., Hony, S., de Koter, A., Molenberghs, G., Dehaes, S., and Markwick-Kemper, F.: 2007, "The variable mass loss of the AGB star WX Psc as traced by the CO J=1-0 through 7-6 lines and the dust emission", *ArXiv e-prints* 708

DePew, K., Speck, A., and Dijkstra, C.: 2006, "Astromineralogy of the 13 μm Feature in the Spectra of Oxygen-rich Asymptotic Giant Branch Stars. I. Corundum and Spinel", *Astrophys. J.* **640**, 971–981

Dijkstra, C., Speck, A. K., Reid, R. B., and Abraham, P.: 2005, "The 10 μm Feature of M-Type Stars in the Large Magellanic Cloud and the Dust Condensation Sequence", *Astrophys. J. Lett.* **633**, L133–L136

Dijkstra, C., Waters, L. B. F. M., Kemper, F., Min, M., Matsuura, M., Zijlstra, A., de Koter, A., and Dominik, C.: 2003, "The mineralogy, geometry and mass-loss history of IRAS 16342-3814", *Astron. Astrophys.* **399**, 1037–1046

Draine, B. T.: 1989, *Interstellar extinction in the infrared*, 93, Infrared Spectroscopy in Astronomy, Proceedings of the 22nd Eslab Symposium held in Salamanca, Spain, 7-9 December, 1988. Edited by B.H. Kaldeich. ESA SP-290. European Space Agency, 1989., p.93

Draine, B. T. and Lee, H. M.: 1984, "Optical properties of interstellar graphite and silicate grains", *Astrophys. J.* **285**, 89–108

Dutra, C. M., Santiago, B. X., Bica, E. L. D., and Barbuy, B.: 2003, "Extinction within 10° of the Galactic centre using 2MASS", *Mon. Not. Roy. Astron. Soc.* **338**, 253–262

Dwek, E., Arendt, R. G., Hauser, M. G., Kelsall, T., Lisse, C. M., Moseley, S. H., Silverberg, R. F., Sodroski, T. J., and Weiland, J. L.: 1995, "Morphology, near-infrared luminosity, and mass of the Galactic bulge from COBE DIRBE observations", *Astrophys. J.* **445**, 716–730

Eidelman, S., Hayes, K., Olive, K., Aguilar-Benitez, M., Amsler, C., Asner, D., Babu, K., Barnett, R., Beringer, J., Burchat, P., Carone, C., Caso, C., Conforto, G., Dahl, O., D'Ambrosio, G., Doser, M., Feng, J., Gherghetta, T., Gibbons, L., Goodman, M., Grab, C., Groom, D., Gurtu, A., Hagiwara, K., Hernández-Rey, J., Hikasa, K., Honscheid, K., Jawahery, H., Kolda, C., Y., K., Mangano, M., Manohar, A., March-Russell, J., Masoni, A., Miquel, R., Mönig, K., Murayama, H., Nakamura, K., Navas, S., Pape, L., Patrignani, C., Piepke, A., Raffelt, G., Roos, M., Tanabashi, M., Terning, J., Törnqvist, N., Trippe, T., Vogel, P., Wohl, C., Workman, R., Yao, W.-M., Zyla, P., Armstrong, B., Gee, P., Harper, G., Lugovsky, K., Lugovsky, S., Lugovsky, V., Rom, A., Artuso, M., Barberio, E., Battaglia, M., Bichsel, H., Biebel, O., Bloch, P., Cahn, R., Casper, D., Cattai, A., Chivukula, R., Cowan, G., Damour, T., Desler, K., Dobbs, M., Drees, M., Edwards, A., Edwards, D., Elvira, V., Erler, J., Ezhela, V., Fetscher, W., Fields, B., Foster, B., Froidevaux, D., Fukugita, M., Gaisser, T., Garren, L., Gerber, H.-J., Gerbier, G., Gilman, F., Haber, H., Hagmann, C., Hewett, J., Hinchliffe, I., Hogan, C., Höhler, G., Igo-Kemenes, P., Jackson, J., Johnson, K., Karlen, D., Kayser, B., Kirkby, D., Klein, S., Kleinknecht, K., Knowles, I., Kreitz, P., Kuyanov, Y., Lahav, O., Langacker, P., Liddle, A., Littenberg, L., Manley, D., Martin, A., Narain, M., Nason, P., Nir, Y., Peacock, J., Quinn, H., Raby, S., Ratcliff, B., Razuvaev, E., Renk, B., Rolandi, G., Ronan, M., Rosenberg, L., Sachrajda, C., Sakai, Y., Sanda, A., Sarkar, S., Schmitt, M., Schneider, O., Scott, D., Seligman, W., Shaevitz, M., Sjöstrand, T., Smoot, G., Spanier, S., Spieler, H., Spooner, N., Srednicki, M., Stahl, A., Stanev, T., Suzuki, M., Tkachenko, N., Trilling, G., Valencia, G., van Bibber, K., Vincter, M., Ward, D., Webber, B., Whalley, M., Wolfenstein, L., Womersley, J., Woody, C., Zenin, O., and Zhu, R.-Y.: 2004, "Review of Particle Physics", *Physics Letters B* 592

Eisenhauer, F., Genzel, R., Alexander, T., Abuter, R., Paumard, T., Ott, T., Gilbert, A., Gillessen, S., Horrobin, M., Trippe, S., Bonnet, H., Dumas, C., Hubin, N., Kaufer, A., Kissler-Patig, M., Monnet, G., Ströbele, S., Szeifert, T., Eckart, A., Schödel, R., and Zucker, S.: 2005, "SINFONI in the Galactic Center: Young Stars and Infrared Flares in the Central Light-Month", *Astrophys. J.* **628**, 246–259

Eisenhauer, F., Schödel, R., Genzel, R., Ott, T., Tecza, M., Abuter, R., Eckart, A., and Alexander, T.: 2003, "A Geometric Determination of the Distance to the Galactic Center", *Astrophys. J. Lett.* **597**, L121–L124

Elitzur, M., Ivezić, Ž., and Vinković, D.: 2003, "The structure of winds in AGB stars", in *ASSL Vol. 283: Mass-Losing Pulsating Stars and their Circumstellar Matter*, 265–273

Epchtein, N., Deul, E., Derriere, S., Borsenberger, J., Egret, D., Simon, G., Alard, C., Balázs, L. G., de Batz, B., Cioni, M.-R., Copet, E., Dennefeld, M., Forveille, T., Fouqué, P., Garzón, F., Habing, H. J., Holl, A., Hron, J., Kimeswenger, S., Lacombe, F., Le Bertre, T., Loup, C., Mamon, G. A., Omont, A., Paturel, G., Persi, P., Robin, A. C., Rouan, D., Tiphène, D., Vauglin, I., and Wagner, S. J.: 1999, "A preliminary database of DENIS point sources", *Astron. Astrophys.* **349**, 236–242

Fabian, D., Posch, T., Mutschke, H., Kerschbaum, F., and Dorschner, J.: 2001, "Infrared optical properties of spinels. A study of the carrier of the 13, 17 and 32 mu m emission features observed in ISO-SWS spectra of oxygen-rich AGB stars", *Astron. Astrophys.* **373**, 1125–1138

Feast, M. W.: 1997, "RR Lyraes, Galactic and extragalactic distances, and the age of the oldest globular clusters", *Mon. Not. Roy. Astron. Soc.* **284**, 761–766

Feast, M. W., Glass, I. S., Whitelock, P. A., and Catchpole, R. M.: 1989, "A period-luminosity-colour relation for Mira variables", *Mon. Not. Roy. Astron. Soc.* **241**, 375–392

Feast, M. W., Robertson, B. S. C., Catchpole, R. M., Evans, T. L., Glass, I. S., and Carter, B. S.: 1982, "The infrared properties of Mira-type variables and other cool stars as determined from JHKL photometry", *Mon. Not. Roy. Astron. Soc.* **201**, 439–450

Feltzing, S. and Gilmore, G.: 2000, "Age and metallicity gradients in the Galactic Bulge. A differential study using HST/WFPC2", *Astron. Astrophys.* **355**, 949–965

Fernley, J. A., Jameson, R. F., Longmore, A. J., Watson, F. G., and Wesselink, T.: 1987, "The absolute magnitude of RR Lyraes and the distance to the Galactic Centre", *Mon. Not. Roy. Astron. Soc.* **226**, 927–942

Fletcher, R.: 1970, "A New Approach to Variable Metric Algorithms.", *Comput. J.* **13(3)**, 317–322

Fluks, M. A., Plez, B., The, P. S., de Winter, D., Westerlund, B. E., and Steenman, H. C.: 1994, "On the spectra and photometry of M-giant stars", *Astron. Astrophys. Suppl.* **105**, 311–336

Fox, M. W. and Wood, P. R.: 1982, "Theoretical growth rates, periods, and pulsation constants for long-period variables", *Astrophys. J.* **259**, 198–212

Fraser, O. J., Hawley, S. L., Cook, K. H., and Keller, S. C.: 2005, "Long-Period Variables in the Large Magellanic Cloud: Results from MACHO and 2MASS", *Astron. J.* **129**, 768–775

Freudenreich, H. T.: 1998, "A COBE Model of the Galactic Bar and Disk", *Astrophys. J.* **492**, 495

Frogel, J. A., Stephens, A., Ramírez, S., and DePoy, D. L.: 2001, "An Accurate, Easy-To-Use Abundance Scale for Globular Clusters Based on 2.2 Micron Spectra of Giant Stars", *Astron. J.* **122**, 1896–1915

Fulbright, J. P., McWilliam, A., and Rich, R. M.: 2007, "Abundances of Baade's Window Giants from Keck HIRES Spectra. II. The Alpha and Light Odd Elements", *Astrophys. J.* **661**, 1152–1179

Gail, H.-P. and Sedlmayr, E.: 1999, "Mineral formation in stellar winds. I. Condensation sequence of silicate and iron grains in stationary oxygen rich outflows", *Astron. Astrophys.* **347**, 594–616

Girardi, L.: 1996, "*Propriedades integradas de populações estelares simples (Integrated properties of single stellar populations)*", *Ph.D. thesis*, Instituto de Física, UFRGS, Porto Alegre, Brazil

Girardi, L., Bertelli, G., Bressan, A., Chiosi, C., Groenewegen, M. A. T., Marigo, P., Salasnich, B., and Weiss, A.: 2002, "Theoretical isochrones in several photometric systems. I. Johnson-Cousins-Glass, HST/WFPC2, HST/NICMOS, Washington, and ESO Imaging Survey filter sets", *Astron. Astrophys.* **391**, 195–212

Girardi, L., Bressan, A., Bertelli, G., and Chiosi, C.: 2000, "Evolutionary tracks and isochrones for low- and intermediate-mass stars: From 0.15 to 7 $M_{\odot}$, and from Z=0.0004 to 0.03", *Astron. Astrophys. Suppl.* **141**, 371–383

Girardi, L., Groenewegen, M. A. T., Hatziminaoglou, E., and da Costa, L.: 2005, "Star counts in the Galaxy. Simulating from very deep to very shallow photometric surveys with the TRILEGAL code", *Astron. Astrophys.* **436**, 895–915

Girardi, L. and Salaris, M.: 2001, "Population effects on the red giant clump absolute magnitude, and distance determinations to nearby galaxies", *Mon. Not. Roy. Astron. Soc.* **323**, 109–129

Glass, I. S.: 1999, "Handbook of Infrared Astronomy", *Highlights of Astronomy*

Glass, I. S., Ganesh, S., Alard, C., Blommaert, J. A. D. L., Gilmore, G., Lloyd Evans, T., Omont, A., Schultheis, M., and Simon, G.: 1999, "ISOGAL survey of Baade's Windows in the mid-infrared", *Mon. Not. Roy. Astron. Soc.* **308**, 127–139

Glass, I. S. and Schultheis, M.: 2002, "M giants in MACHO, DENIS and ISOGAL", *Mon. Not. Roy. Astron. Soc.* **337**, 519–528

Goebel, J. H., Bregman, J. D., and Witteborn, F. C.: 1994, "A 7 micron dust emission feature in oxygen-rich circumstellar shells", *Astrophys. J.* **430**, 317–322

Goldfarb, D.: 1970, "A Family of Variable-Metric Methods Derived by Variational Means", *Mathematics of Compuation* **24(109)**, 23–26

Groenewegen, M. A. T.: 1993, "*On the evolution and properties of AGB stars*", *Ph.D. thesis*, University of Amsterdam

Groenewegen, M. A. T.: 1995, "Dust shells around infrared carbon stars.", *Astron. Astrophys.* **293**, 463–478

Groenewegen, M. A. T.: 2004, "Long Period Variables in the Magellanic Clouds: OGLE + 2 MASS + DENIS", *Astron. Astrophys.* **425**, 595–613

Groenewegen, M. A. T. and Blommaert, J. A. D. L.: 2005, "Mira variables in the OGLE bulge fields", *Astron. Astrophys.* **443**, 143–156

Groenewegen, M. A. T., de Jong, T., and Gaballe, T. R.: 1994, "The 3 micrometer spectra of candidate carbon stars", *Astron. Astrophys.* **287**, 163–174

Habing, H. J.: 1996, "Circumstellar envelopes and Asymptotic Giant Branch stars", *Astron. Astrophys. Rev.* **7**, 97–207

Habing, H. J., Olnon, F. M., Winnberg, A., Matthews, H. E., and Baud, B.: 1983, "OH/IR stars within one degree of the galactic centre", *Astron. Astrophys.* **128**, 230–244

Habing, H. J. and Olofsson, H. (Eds.): 2003, *Asymptotic giant branch stars*

Habing, H. J., Tignon, J., and Tielens, A. G. G. M.: 1994, "Calculations of the outflow velocity of envelopes of cool giants", *Astron. Astrophys.* **286**, 523–534

Harris, W. E.: 1996, "A Catalog of Parameters for Globular Clusters in the Milky Way", *Astron. J.* **112**, 1487

Heras, A. M. and Hony, S.: 2005, "Oxygen-rich AGB stars with optically thin dust envelopes", *Astron. Astrophys.* **439**, 171–182

Higdon, S. J. U., Devost, D., Higdon, J. L., Brandl, B. R., Houck, J. R., Hall, P., Barry, D., Charmandaris, V., Smith, J. D. T., Sloan, G. C., and Green, J.: 2004, "The SMART Data Analysis Package for the Infrared Spectrograph on the Spitzer Space Telescope", *Pub. Astron. Soc. Pacific* **116**, 975–984

Höfner, S. and Andersen, A. C.: 2007, "Winds of M- and S-type AGB stars: an unorthodox suggestion for the driving mechanism", *Astron. Astrophys.* **465**, L39–L42

Holtzman, J. A., Light, R. M., Baum, W. A., Worthey, G., Faber, S. M., Hunter, D. A., O'Neil, Jr., E. J., Kreidl, T. J., Groth, E. J., and Westphal, J. A.: 1993, "Wide field camera observations of Baade's Window", *Astron. J.* **106**, 1826–1838

Houck, J. R., Roellig, T. L., van Cleve, J., Forrest, W. J., Herter, T., Lawrence, C. R., Matthews, K., Reitsema, H. J., Soifer, B. T., Watson, D. M., Weedman, D., Huisjen, M., Troeltzsch, J., Barry, D. J., Bernard-Salas, J., Blacken, C. E., Brandl, B. R., Charmandaris, V., Devost, D., Gull, G. E., Hall, P., Henderson, C. P., Higdon, S. J. U., Pirger, B. E., Schoenwald, J., Sloan, G. C., Uchida, K. I., Appleton, P. N., Armus, L., Burgdorf, M. J., Fajardo-Acosta, S. B., Grillmair, C. J., Ingalls, J. G., Morris, P. W., and Teplitz, H. I.: 2004, "The Infrared Spectrograph (IRS) on the Spitzer Space Telescope", *Astrophys. J. Suppl.* **154**, 18–24

Houdashelt, M. L., Bell, R. A., Sweigart, A. V., and Wing, R. F.: 2000, "Synthetic Spectra and Color-Temperature Relations of M Giants", *Astron. J.* **119**, 1424–1447

Hron, J., Aringer, B., and Kerschbaum, F.: 1997, "Semiregular variables of types SRa and SRb. Silicate dust emission features.", *Astron. Astrophys.* **322**, 280–290

Hughes, S. M. G. and Wood, P. R.: 1990, "Long-period variables in the Large Magellanic Cloud. II - Infrared photometry, spectral classification, AGB evolution, and spatial distribution", *Astron. J.* **99**, 784–816

Indebetouw, R., Mathis, J. S., Babler, B. L., Meade, M. R., Watson, C., Whitney, B. A., Wolff, M. J., Wolfire, M. G., Cohen, M., Bania, T. M., Benjamin, R. A., Clemens, D. P., Dickey, J. M., Jackson, J. M., Kobulnicky, H. A., Marston, A. P., Mercer, E. P., Stauffer, J. R., Stolovy, S. R., and Churchwell, E.: 2005, "The Wavelength Dependence of Interstellar Extinction from 1.25 to 8.0 μm Using GLIMPSE Data", *Astrophys. J.* **619**, 931–938

IRS Data Handbook: 2006, *Infrared Spectrograph Data Handbook*, Spitzer Science Center – California Institute of Technology, 2.0 edition

Ita, Y., Tanabé, T., Matsunaga, N., Nakajima, Y., Nagashima, C., Nagayama, T., Kato, D., Kurita, M., Nagata, T., Sato, S., Tamura, M., Nakaya, H., and Nakada, Y.: 2004, "Variable stars in the Magellanic Clouds - II. The data and infrared properties", *Mon. Not. Roy. Astron. Soc.* **353**, 705–712

Jäger, C., Molster, F. J., Dorschner, J., Henning, T., Mutschke, H., and Waters, L. B. F. M.: 1998, "Steps toward interstellar silicate mineralogy. IV. The crystalline revolution", *Astron. Astrophys.* **339**, 904–916

Jones, T. J., McGregor, P. J., Gehrz, R. D., and Lawrence, G. F.: 1994, "OH/IR stars near the Galactic Center: Pulsation periods, luminosities, and polarimetry", *Astron. J.* **107**, 1111–1119

Joyce, R. R., Hinkle, K. H., Wallace, L., Dulick, M., and Lambert, D. L.: 1998, "Spectra of Cool Stars in the J Band (1.0-1.3 μm) at Medium Resolution", *Astron. J.* **116**, 2520–2529

Justtanont, K., Feuchtgruber, H., de Jong, T., Cami, J., Waters, L. B. F. M., Yamamura, I., and Onaka, T.: 1998, "Discovery of CO_2 emission in AGB stars with the 13mu M dust feature", *Astron. Astrophys.* **330**, L17–L20

Justtanont, K., Olofsson, G., Dijkstra, C., and Meyer, A. W.: 2006, "Near-infrared observations of water-ice in OH/IR stars", *Astron. Astrophys.* **450**, 1051–1059

Kemper, F., Waters, L. B. F. M., de Koter, A., and Tielens, A. G. G. M.: 2001, "Crystallinity versus mass-loss rate in asymptotic giant branch stars", *Astron. Astrophys.* **369**, 132–141

Kessler, M. F., Mueller, T. G., Leech, K., Arviset, C., Garcia-Lario, P., Metcalfe, L., Pollock, A., Prusti, T., and Salama, A. (Eds.): 2003, *The ISO Handbook, Volume I - Mission & Satellite Overview*

Kessler-Silacci, J., Augereau, J.-C., Dullemond, C. P., Geers, V., Lahuis, F., Evans, II, N. J., van Dishoeck, E. F., Blake, G. A., Boogert, A. C. A., Brown, J., Jørgensen, J. K., Knez, C., and Pontoppidan, K. M.: 2006, "c2d Spitzer IRS Spectra of Disks around T Tauri Stars. I. Silicate Emission and Grain Growth", *Astrophys. J.* **639**, 275–291

Lamers, H. J. G. L. M. and Cassinelli, J. P.: 1999, *Introduction to Stellar Winds*, Introduction to Stellar Winds, by Henny J. G. L. M. Lamers and Joseph P. Cassinelli, pp. 452. ISBN 0521593980. Cambridge, UK: Cambridge University Press, June 1999.

Lançon, A. and Wood, P. R.: 2000, "A library of 0.5 to 2.5 mu m spectra of luminous cool stars", *Astron. Astrophys. Suppl.* **146**, 217–249

Lattanzio, J. C. and Wood, P. R.: 2003, *Asymptotic Giant Branc stars*, Chapt. 2, 23–104, Astron. and Ap. Library (Springer)

Lebzelter, T., Hinkle, K. H., and Aringer, B.: 2001, "4 μm spectra of AGB stars I. Observations", *Astron. Astrophys.* **377**, 617–630

Lebzelter, T., Posch, T., Hinkle, K., Wood, P. R., and Bouwman, J.: 2006, "Tracing the Development of Dust around Evolved Stars: The Case of 47 Tuc", *Astrophys. J. Lett.* **653**, L145–L148

Lebzelter, T. and Wood, P. R.: 2005, "Long period variables in 47 Tuc: direct evidence for lost mass", *Astron. Astrophys.* **441**, 1117–1127

Lindqvist, M., Habing, H. J., and Winnberg, A.: 1992a, "OH/IR stars close to the Galactic Centre. II - Their spatial and kinematic properties and the mass distribution within 5-100 PC from the galactic centre", *Astron. Astrophys.* **259**, 118–127

Lindqvist, M., Winnberg, A., Habing, H. J., and Matthews, H. E.: 1992b, "OH/IR stars close to the Galactic Centre. I - Observational data", *Astron. Astrophys. Suppl.* **92**, 43–62

Little-Marenin, I. R. and Little, S. J.: 1990, "Emission features in IRAS LRS spectra of M Mira variables", *Astron. J.* **99**, 1173–1186

López-Corredoira, M., Cabrera-Lavers, A., and Gerhard, O. E.: 2005, "A boxy bulge in the Milky Way. Inversion of the stellar statistics equation with 2MASS data", *Astron. Astrophys.* **439**, 107–110

López-Corredoira, M., Cabrera-Lavers, A., Mahoney, T. J., Hammersley, P. L., Garzón, F., and González-Fernández, C.: 2007, "The Long Bar in the Milky Way: Corroboration of an Old Hypothesis", *Astron. J.* **133**, 154–161

Lutz, D., Feuchtgruber, H., Genzel, R., Kunze, D., Rigopoulou, D., Spoon, H. W. W., Wright, C. M., Egami, E., Katterloher, R., Sturm, E., Wieprecht, E., Sternberg, A., Moorwood, A. F. M., and de Graauw, T.: 1996, "SWS observations of the Galactic center.", *Astron. Astrophys.* **315**, L269–L272

Marigo, P. and Girardi, L.: 2007, "Evolution of asymptotic giant branch stars. I. Updated synthetic TP-AGB models and their basic calibration", *Astron. Astrophys.* **469**, 239–263

Marshall, D. J., Robin, A. C., Reylé, C., Schultheis, M., and Picaud, S.: 2006, "Modelling the Galactic interstellar extinction distribution in three dimensions", *Astron. Astrophys.* **453**, 635–651

McGinn, M. T., Sellgren, K., Becklin, E. E., and Hall, D. N. B.: 1989, "Stellar kinematics in the Galactic center", *Astrophys. J.* **338**, 824–840

McGregor, P. and Hart, J. and Hoadley, D., and Bloxham, G.: 1994, *Infrared Astronomy with Arrays*, Kluwer

McWilliam, A. and Rich, R. M.: 1994, "The first detailed abundance analysis of Galactic bulge K giants in Baade's window", *Astrophys. J. Suppl.* **91**, 749–791

Merrifield, M. R.: 2004, "The Galactic Bar", in D. Clemens, R. Shah, and T. Brainerd (Eds.), *ASP Conf. Ser. 317: Milky Way Surveys: The Structure and Evolution of our Galaxy*, 289

Min, M., Waters, L. B. F. M., de Koter, A., Hovenier, J. W., Keller, L. P., and Markwick-Kemper, F.: 2007, "The shape and composition of interstellar silicate grains", *Astron. Astrophys.* **462**, 667–676

Miyata, T., Kataza, H., Okamoto, Y., Onaka, T., and Yamashita, T.: 2000, "A Spectroscopic Study of Dust around 18 Oxygen-rich Mira Variables in the N Band. I. Dust Profiles", *Astrophys. J.* **531**, 917–927

Molster, F. J., Waters, L. B. F. M., and Tielens, A. G. G. M.: 2002a, "Crystalline silicate dust around evolved stars. II. The crystalline silicate complexes", *Astron. Astrophys.* **382**, 222–240

Molster, F. J., Waters, L. B. F. M., Tielens, A. G. G. M., and Barlow, M. J.: 2002b, "Crystalline silicate dust around evolved stars. I. The sample stars", *Astron. Astrophys.* **382**, 184–221

Molster, F. J., Waters, L. B. F. M., Tielens, A. G. G. M., Koike, C., and Chihara, H.: 2002c, "Crystalline silicate dust around evolved stars. III. A correlations study of crystalline silicate features", *Astron. Astrophys.* **382**, 241–255

Nishiyama, S., Nagata, T., Sato, S., Kato, D., Nagayama, T., Kusakabe, N., Matsunaga, N., Naoi, T., Sugitani, K., and Tamura, M.: 2006, "The Distance to the Galactic Center Derived from Infrared Photometry of Bulge Red Clump Stars", *Astrophys. J.* **647**, 1093–1098

O'Donnell, J. E.: 1994, "R_v-dependent optical and near-ultraviolet extinction", *Astrophys. J.* **422**, 158–163

Ojha, D. K., Omont, A., Schuller, F., Simon, G., Ganesh, S., and Schultheis, M.: 2003, "Stellar sources in the ISOGAL intermediate bulge fields", *Astron. Astrophys.* **403**, 141–154

Omont, A., Ganesh, S., Alard, C., Blommaert, J. A. D. L., Caillaud, B., Copet, E., Fouqué, P., Gilmore, G., Ojha, D., Schultheis, M., Simon, G., Bertou, X., Borsenberger, J., Epchtein, N., Glass, I., Guglielmo, F., Groenewegen, M. A. T., Habing, H. J., Kimeswenger, S., Morris, M., Price, S. D., Robin, A., Unavane, M., and Wyse, R.: 1999, "ISOGAL-DENIS detection of red giants with weak mass loss in the Galactic bulge", *Astron. Astrophys.* **348**, 755–767

Omont, A., Gilmore, G. F., Alard, C., Aracil, B., August, T., Baliyan, K., Beaulieu, S., Bégon, S., Bertou, X., Blommaert, J. A. D. L., Borsenberger, J., Burgdorf, M., Caillaud, B., Cesarsky, C., Chitre, A., Copet, E., de Batz, B., Egan, M. P., Egret, D., Epchtein, N., Felli, M., Fouqué, P., Ganesh, S., Genzel, R., Glass, I. S., Gredel, R., Groenewegen, M. A. T., Guglielmo, F., Habing, H. J., Hennebelle, P., Jiang, B., Joshi, U. C., Kimeswenger, S., Messineo, M., Miville-Deschênes, M. A., Moneti, A., Morris, M., Ojha, D. K., Ortiz, R., Ott, S., Parthasarathy, M., Pérault, M., Price, S. D., Robin, A. C., Schultheis, M., Schuller, F., Simon, G., Soive, A., Testi, L., Teyssier, D., Tiphène, D., Unavane, M., van Loon, J. T., and Wyse, R.: 2003, "ISOGAL: A deep survey of the obscured inner Milky Way with ISO at 7 mu m and 15 mu m and with DENIS in the near-infrared", *Astron. Astrophys.* **403**, 975–992

Onaka, T., de Jong, T., and Willems, F. J.: 1989, "A study of M Mira variables based on IRAS LRS observations. I - Dust formation in the circumstellar shell", *Astron. Astrophys.* **218**, 169–179

Origlia, L., Moorwood, A. F. M., and Oliva, E.: 1993, "The 1.5-1.7 micrometer spectrum of cool stars: Line identifications, indices for spectral classification and the stellar content of the Seyfert galaxy NGC 1068", *Astron. Astrophys.* **280**, 536–550

Ortiz, R., Blommaert, J. A. D. L., Copet, E., Ganesh, S., Habing, H. J., Messineo, M., Omont, A., Schultheis, M., and Schuller, F.: 2002, "OH/IR stars in the inner bulge detected by ISOGAL", *Astron. Astrophys.* **388**, 279–292

Ortolani, S., Barbuy, B., Bica, E., Renzini, A., Zoccali, M., Rich, R. M., and Cassisi, S.: 2001, "HST NICMOS photometry of the reddened bulge globular clusters NGC 6528, Terzan 5, Liller 1, UKS 1 and Terzan 4", *Astron. Astrophys.* **376**, 878–884

Ortolani, S., Renzini, A., Gilmozzi, R., Marconi, G., Barbuy, B., Bica, E., and Rich, R. M.: 1995, "Near Coeval Formation of the Galactic Bulge and Halo Inferred from Globular Cluster Ages", *Nature* **377**, 701

Paczynski, B.: 1986, "Gravitational microlensing by the galactic halo", *Astrophys. J.* **304**, 1–5

Paczynski, B.: 1991, "Gravitational microlensing of the Galactic bulge stars", *Astrophys. J. Lett.* **371**, L63–L67

Paczynski, B. and Stanek, K. Z.: 1998, "Galactocentric Distance with the Optical Gravitational Lensing Experiment and HIPPARCOS Red Clump Stars", *Astrophys. J. Lett.* **494**, L219

Peeters, E., Allamandola, L. J., Hudgins, D. M., Hony, S., and Tielens, A. G. G. M.: 2004, "The Unidentified InfraRed Features after ISO", in A. N. Witt, G. C. Clayton, and B. T. Draine (Eds.), *Astrophysics of Dust*, Vol. 309 of *Astronomical Society of the Pacific Conference Series*, 141

Posch, T., Kerschbaum, F., Mutschke, H., Dorschner, J., and Jäger, C.: 2002, "On the origin of the 19.5 μ m feature. Identifying circumstellar Mg-Fe-oxides", *Astron. Astrophys.* **393**, L7–L10

Press, W. H., Flannery, B. P., Teukolsky, S. A., and Vetterling, W. T.: 1992, *Numerical Recipes in C: The Art of Scientific Computing*, Cambridge University Press, 2nd edition

Ramírez, S. V., Depoy, D. L., Frogel, J. A., Sellgren, K., and Blum, R. D.: 1997, "Luminosity and Temperature from Near-Infrared Spectra of Late-Type Giant Stars", *Astron. J.* **113**, 1411–1420

Ramírez, S. V., Stephens, A. W., Frogel, J. A., and DePoy, D. L.: 2000, "Metallicity of Red Giants in the Galactic Bulge from Near-Infrared Spectroscopy", *Astron. J.* **120**, 833–844

Rattenbury, N. J., Mao, S., Sumi, T., and Smith, M. C.: 2007, "Modelling the Galactic bar using OGLE-II red clump giant stars", *Mon. Not. Roy. Astron. Soc.* **378**, 1064–1078

Reid, M. J., Schneps, M. H., Moran, J. M., Gwinn, C. R., Genzel, R., Downes, D., and Roennaeng, B.: 1988, "The distance to the center of the Galaxy - H2O maser proper motions in Sagittarius B2(N)", *Astrophys. J.* **330**, 809–816

Rich, R. M. and Origlia, L.: 2005, "The First Detailed Abundances for M Giants in Baade's Window from Infrared Spectroscopy", *Astrophys. J.* **634**, 1293–1299

Rich, R. M., Origlia, L., and Valenti, E.: 2007, "The First Detailed Abundances for M Giants in the Inner Bulge from Infrared Spectroscopy", *Astrophys. J. Lett.* **665**, L119–L122

Robin, A. C., Reylé, C., Derrière, S., and Picaud, S.: 2003, "A synthetic view on structure and evolution of the Milky Way", *Astron. Astrophys.* **409**, 523–540

Rocha-Pinto, H. J., Maciel, W. J., Scalo, J., and Flynn, C.: 2000a, "Chemical enrichment and star formation in the Milky Way disk. I. Sample description and chromospheric age-metallicity relation", *Astron. Astrophys.* **358**, 850–868

Rocha-Pinto, H. J., Scalo, J., Maciel, W. J., and Flynn, C.: 2000b, "Chemical enrichment and star formation in the Milky Way disk. II. Star formation history", *Astron. Astrophys.* **358**, 869–885

Rodgers, A. W., Conroy, P., and Bloxham, G.: 1988, "A dual-beam Nasmyth spectrograph", *Pub. Astron. Soc. Pacific* **100**, 626–634

Román-Zúñiga, C., Lada, C., Muench, A., and Alves, J.: 2007, "The Infrared Extinction Law at Extreme Depth in a Dark Cloud Core", *ArXiv e-prints* 704

Ryde, N., Eriksson, K., Gustafsson, B., Lindqvist, M., and Olofsson, H.: 1997, "Tentative Detection of Circumstellar CO2 from the AGB Star R Crateris", *Astrophys. and Space Science* **255**, 301–302

Sadler, E. M., Rich, R. M., and Terndrup, D. M.: 1996, "K Giants in Baade's Window. II. The Abundance Distribution", *Astron. J.* **112**, 171

Schechter, P. L., Mateo, M., and Saha, A.: 1993, "DOPHOT, a CCD photometry program: Description and tests", *Pub. Astron. Soc. Pacific* **105**, 1342–1353

Schlegel, D. J., Finkbeiner, D. P., and Davis, M.: 1998, "Maps of Dust Infrared Emission for Use in Estimation of Reddening and Cosmic Microwave Background Radiation Foregrounds", *Astrophys. J.* **500**, 525

Schuller, F., Ganesh, S., Messineo, M., Moneti, A., Blommaert, J. A. D. L., Alard, C., Aracil, B., Miville-Deschênes, M.-A., Omont, A., Schultheis, M., Simon, G., Soive, A., and Testi, L.: 2003, "Explanatory supplement of the ISOGAL-DENIS Point Source Catalogue", *Astron. Astrophys.* **403**, 955–974

Schultheis, M., Ganesh, S., Simon, G., Omont, A., Alard, C., Borsenberger, J., Copet, E., Epchtein, N., Fouqué, P., and Habing, H.: 1999, "Interstellar extinction towards the inner Galactic Bulge", *Astron. Astrophys.* **349**, L69–L72

Schultheis, M., Lançon, A., Omont, A., Schuller, F., and Ojha, D. K.: 2003, "Near-IR spectra of ISOGAL sources in the inner Galactic Bulge", *Astron. Astrophys.* **405**, 531–550

Servoin, J. L. and Piriou, B.: 1973, "Infrared reflectivity and Ramman scattering of Mg_2SiO_4 single crystal", *Physica Status Solidi B* **55**, 667–686

Sevenster, M., Saha, P., Valls-Gabaud, D., and Fux, R.: 1999, "New constraints on a triaxial model of the Galaxy", *Mon. Not. Roy. Astron. Soc.* **307**, 584–594

Sevenster, M. N.: 1999, "Something about the structure of the Galaxy", *Mon. Not. Roy. Astron. Soc.* **310**, 629–644

Sevenster, M. N., Chapman, J. M., Habing, H. J., Killeen, N. E. B., and Lindqvist, M.: 1997, "The ATCA/VLA OH 1612 MHz survey. I. Observations of the galactic bulge Region", *Astron. Astrophys. Suppl.* **122**, 79–93

Shanno, D. F.: 1970, "Conditioning of Quasi-Newton Methods for Function Minimization", *Mathematics of Computation* **24(111)**, 647–656

Sjouwerman, L. O., van Langevelde, H. J., Winnberg, A., and Habing, H. J.: 1998, "A new sample of OH/IR stars in the Galactic center", *Astron. Astrophys. Suppl.* **128**, 35–65

Skrutskie, M. F., Cutri, R. M., Stiening, R., Weinberg, M. D., Schneider, S., Carpenter, J. M., Beichman, C., Capps, R., Chester, T., Elias, J., Huchra, J., Liebert, J., Lonsdale, C., Monet, D. G., Price, S., Seitzer, P., Jarrett, T., Kirkpatrick, J. D., Gizis, J. E., Howard, E., Evans, T., Fowler, J., Fullmer, L., Hurt, R., Light, R., Kopan, E. L., Marsh, K. A., McCallon, H. L., Tam, R., Van Dyk, S., and Wheelock, S.: 2006, "The Two Micron All Sky Survey (2MASS)", *Astron. J.* **131**, 1163–1183

Sloan, G. C., Devost, D., Bernard-Salas, J., Wood, P. R., and Houck, J. R.: 2006, "The Unusual Silicate Dust around HV 2310, an Evolved Star in the Large Magellanic Cloud", *Astrophys. J.* **638**, 472–477

Sloan, G. C., Kraemer, K. E., Goebel, J. H., and Price, S. D.: 2003, "Guilt by Association: The 13 Micron Dust Emission Feature and Its Correlation to Other Gas and Dust Features", *Astrophys. J.* **594**, 483–495

Sloan, G. C. and Price, S. D.: 1995, "Silicate Emission at 10 Microns in Variables on the Asymptotic Giant Branch", *Astrophys. J.* **451**, 758

SOM: 2005, *Spitzer Space Telescope Observer's Manual*, Spitzer Science Center – California Institute of Technology, 6.0 edition

Speck, A. K., Barlow, M. J., Sylvester, R. J., and Hofmeister, A. M.: 2000, "Dust features in the 10-mu m infrared spectra of oxygen-rich evolved stars", *Astron. Astrophys. Suppl.* **146**, 437–464

Stanek, K. Z. and Garnavich, P. M.: 1998, "Distance to M31 with the Hubble Space Telescope and HIPPARCOS Red Clump Stars", *Astrophys. J. Lett.* **503**, L131

Stanek, K. Z., Udalski, A., Szymanski, M., Kaluzny, J., Kubiak, M., Mateo, M., and Krzeminski, W.: 1997, "Modeling the Galactic Bar Using Red Clump Giants", *Astrophys. J.* **477**, 163

Suh, K.-W.: 1999, "Optical properties of the silicate dust grains in the envelopes around asymptotic giant branch stars", *Mon. Not. Roy. Astron. Soc.* **304**, 389–405

Sumi, T.: 2004, "Extinction map of the Galactic centre: OGLE-II Galactic bulge fields", *Mon. Not. Roy. Astron. Soc.* **349**, 193–204

Sylvester, R. J., Kemper, F., Barlow, M. J., de Jong, T., Waters, L. B. F. M., Tielens, A. G. G. M., and Omont, A.: 1999, "2.4-197 mu m spectroscopy of OH/IR stars: the IR characteristics of circumstellar dust in O-rich environments", *Astron. Astrophys.* **352**, 587–599

Tamanai, A., Mutschke, H., Blum, J., and Meeus, G.: 2006, "The 10 μm Infrared Band of Silicate Dust: A Laboratory Study Comparing the Aerosol and KBr Pellet Techniques", *Astrophys. J. Lett.* **648**, L147–L150

Tej, A., Lançon, A., Scholz, M., and Wood, P. R.: 2003, "Optical and near-IR spectra of O-rich Mira variables: A comparison between models and observations", *Astron. Astrophys.* **412**, 481–494

Tielens, A. G. G. M.: 1990, "Towards a circumstellar silicate mineralogy", in M. O. Mennessier and A. Omont (Eds.), *From Miras to Planetary Nebulae: Which Path for Stellar Evolution?*, 186–200

Tielens, A. G. G. M., Waters, L. B. F. M., Molster, F. J., and Justtanont, K.: 1997, "Circumstellar Silicate Mineralogy", *Astrophys. and Space Science* **255**, 415–426

Tsuji, T., Ohnaka, K., Aoki, W., and Yamamura, I.: 1997, "Warm molecular envelope of M giants and Miras: a new molecule forming region unmasked by the ISO SWS.", *Astron. Astrophys.* **320**, L1–L4

Udalski, A.: 1998, "The Optical Gravitational Lensing Experiment. The Distance Scale: Galactic Bulge – LMC – SMC.", *Acta Astronomica* **48**, 113–145

Udalski, A.: 2000, "The Optical Gravitational Lensing Experiment: Red Clump Stars as a Distance Indicator", *Astrophys. J. Lett.* **531**, L25–L28

Udalski, A.: 2003, "The Optical Gravitational Lensing Experiment: Is Interstellar Extinction toward the Galactic Center Anomalous?", *Astrophys. J.* **590**, 284–290

Udalski, A., Kubiak, M., and Szymanski, M.: 1997, "Optical Gravitational Lensing Experiment. OGLE-2 – the Second Phase of the OGLE Project", *Acta Astronomica* **47**, 319–344

Udalski, A., Szymanski, M., Kubiak, M., Pietrzynski, G., Soszynski, I., Wozniak, P., Zebrun, K., Szewczyk, O., and Wyrzykowski, L.: 2002, "The Optical Gravitational Lensing Experiment. BVI Maps of Dense Stellar Regions. III. The Galactic Bulge", *Acta Astronomica* **52**, 217–240

Uttenthaler, S., Hron, J., Lebzelter, T., Busso, M., Schultheis, M., and Käufl, H. U.: 2007, "Technetium and the third dredge up in AGB stars. II. Bulge stars", *Astron. Astrophys.* **463**, 251–259

van Boekel, R., Min, M., Waters, L. B. F. M., de Koter, A., Dominik, C., van den Ancker, M. E., and Bouwman, J.: 2005, "A 10 μm spectroscopic survey of Herbig Ae star disks: Grain growth and crystallization", *Astron. Astrophys.* **437**, 189–208

van der Veen, W. E. C. J. and Habing, H. J.: 1990, "Far evolved AGB stars in the Galactic bulge", *Astron. Astrophys.* **231**, 404–418

Van Kerckhoven, C., Hony, S., Peeters, E., Tielens, A. G. G. M., Allamandola, L. J., Hudgins, D. M., Cox, P., Roelfsema, P. R., Voors, R. H. M., Waelkens, C., Waters, L. B. F. M., and Wesselius, P. R.: 2000, "The C-C-C bending modes of PAHs: a new emission plateau from 15 to 20 μm", *Astron. Astrophys.* **357**, 1013–1019

van Langevelde, H. J., Brown, A. G. A., Lindqvist, M., Habing, H. J., and de Zeeuw, P. T.: 1992, "High-velocity OH/IR stars at the Galactic centre", *Astron. Astrophys.* **261**, L17–L20

van Loon, J. T., Gilmore, G. F., Omont, A., Blommaert, J. A. D. L., Glass, I. S., Messineo, M., Schuller, F., Schultheis, M., Yamamura, I., and Zhao, H. S.: 2003, "Infrared stellar populations in the central parts of the Milky Way galaxy", *Mon. Not. Roy. Astron. Soc*. **338**, 857–879

Van Malderen, R.: 2003, "*On the analysis of the IR spectra of cool giants: model atmospheres and time-dependent behaviour*", *Ph.D. thesis*, Katholieke Universiteit Leuven

Vardya, M. S., de Jong, T., and Willems, F. J.: 1986, "IRAS Low-Resolution Spectrograph observations of silicate and molecular SiO emission in Mira variables", *Astrophys. J. Lett.* **304**, L29–L32

Vassiliadis, E. and Wood, P. R.: 1993, "Evolution of low- and intermediate-mass stars to the end of the asymptotic giant branch with mass loss", *Astrophys. J.* **413**, 641–657

Volk, K. and Kwok, S.: 1988, "Spectral evolution of asymptotic giant branch stars", *Astrophys. J.* **331**, 435–462

Wallace, L. and Hinkle, K.: 1996, "High-Resolution Spectra of Ordinary Cool Stars in the K Band", *Astrophys. J. Suppl.* **107**, 312

Waters, L. B. F. M. and Molster, F. G.: 1999, "Crystalline silicates in AGB and post-AGB stars", in T. Le Bertre, A. Lebre, and C. Waelkens (Eds.), *Asymptotic Giant Branch Stars*, Vol. 191 of *IAU Symposium*, 209

Waters, L. B. F. M., Molster, F. J., de Jong, T., Beintema, D. A., Waelkens, C., Boogert, A. C. A., Boxhoorn, D. R., de Graauw, T., Drapatz, S., Feuchtgruber, H., Genzel, R., Helmich, F. P., Heras, A. M., Huygen, R., Izumiura, H., Justtanont, K., Kester, D. J. M., Kunze, D., Lahuis, F., Lamers, H. J. G. L. M., Leech, K. J., Loup, C., Lutz, D., Morris, P. W., Price, S. D., Roelfsema, P. R., Salama, A., Schaeidt, S. G., Tielens, A. G. G. M., Trams, N. R., Valentijn, E. A., Vandenbussche, B., van den Ancker, M. E., van Dishoeck, E. F., Van Winckel, H., Wesselius, P. R., and Young, E. T.: 1996, "Mineralogy of oxygen-rich dust shells.", *Astron. Astrophys.* **315**, L361–L364

Weinberg, M. D.: 1992a, "Constraints on the Galactic bulge using IRAS variable point sources", *Astrophys. J. Lett.* **392**, L67–L69

Weinberg, M. D.: 1992b, "Detection of a large-scale stellar bar in the Milky Way", *Astrophys. J.* **384**, 81–94

Werner, M. W., Roellig, T. L., Low, F. J., Rieke, G. H., Rieke, M., Hoffmann, W. F., Young, E., Houck, J. R., Brandl, B., Fazio, G. G., Hora, J. L., Gehrz, R. D., Helou, G., Soifer, B. T.,

Stauffer, J., Keene, J., Eisenhardt, P., Gallagher, D., Gautier, T. N., Irace, W., Lawrence, C. R., Simmons, L., Van Cleve, J. E., Jura, M., Wright, E. L., and Cruikshank, D. P.: 2004, "The Spitzer Space Telescope Mission", *Astrophys. J. Suppl.* **154**, 1–9

Whitelock, P.: 1992, "The Bar-Like Bulge of our Galaxy", in B. Warner (Ed.), *ASP Conf. Ser. 30: Variable Stars and Galaxies, in honor of M. W. Feast on his retirement*, 11

Woitke, P.: 2006, "Too little radiation pressure on dust in the winds of oxygen-rich AGB stars", *Astron. Astrophys.* **460**, L9–L12

Wood, P. R.: 2000, "Variable red giants in the LMC: Pulsating stars and binaries?", *Publications of the Astronomical Society of Australia* **17**, 18–21

Wood, P. R.: 2004, private communication

Wood, P. R., Alcock, C., Allsman, R. A., Alves, D., Axelrod, T. S., Becker, A. C., Bennett, D. P., Cook, K. H., Drake, A. J., Freeman, K. C., Griest, K., King, L. J., Lehner, M. J., Marshall, S. L., Minniti, D., Peterson, B. A., Pratt, M. R., Quinn, P. J., Stubbs, C. W., Sutherland, W., Tomaney, A., Vandehei, T., and Welch, D. L.: 1999, "MACHO observations of LMC red giants: Mira and semi-regular pulsators, and contact and semi-detached binaries", in T. Le Bertre, A. Lebre, and C. Waelkens (Eds.), *IAU Symp. 191: Asymptotic Giant Branch Stars*, 151

Wood, P. R., Habing, H. J., and McGregor, P. J.: 1998, "Infrared monitoring of OH/IR stars near the Galactic Center", *Astron. Astrophys.* **336**, 925–941

Wood, P. R., Olivier, E. A., and Kawaler, S. D.: 2004, "Long Secondary Periods in Pulsating Asymptotic Giant Branch Stars: An Investigation of their Origin", *Astrophys. J.* **604**, 800–816

Wood, P. R., Whiteoak, J. B., Hughes, S. M. G., Bessell, M. S., Gardner, F. F., and Hyland, A. R.: 1992, "OH/IR stars in the Magellanic Clouds", *Astrophys. J.* **397**, 552–569

Woolf, N. J. and Ney, E. P.: 1969, "Circumstellar Infrared Emission from Cool Stars", *Astrophys. J. Lett.* **155**, L181

Wozniak, P. R., Udalski, A., Szymanski, M., Kubiak, M., Pietrzynski, G., Soszynski, I., and Zebrun, K.: 2002, "Difference Image Analysis of the OGLE-II Bulge Data. III. Catalog of 200000 Candidate Variable Stars", *Acta Astronomica* **52**, 129–142

Wyse, R. F. G.: 1995, "Chemical Evolution of the Galactic Disk and Bulge", in P. C. van der Kruit and G. Gilmore (Eds.), *Stellar Populations*, Vol. 164 of *IAU Symposium*, 133

Xiong, D. R., Deng, L., and Cheng, Q. L.: 1998, "Turbulent Convection and Pulsational Stability of Variable Stars. I. Oscillations of Long-Period Variables", *Astrophys. J.* **499**, 355

Yamamura, I., de Jong, T., Onaka, T., Cami, J., and Waters, L. B. F. M.: 1999, "Detection of warm SO_2 gas in oxygen-rich AGB stars", *Astron. Astrophys.* **341**, L9–L12

Zoccali, M., Renzini, A., Ortolani, S., Greggio, L., Saviane, I., Cassisi, S., Rejkuba, M., Barbuy, B., Rich, R. M., and Bica, E.: 2003, "Age and metallicity distribution of the Galactic bulge from extensive optical and near-IR stellar photometry", *Astron. Astrophys.* **399**, 931–956